NOVEL ATOMIC COHERENCE AND INTERFERENCE EFFECTS IN QUANTUM OPTICS AND ATOMIC PHYSICS

A Dissertation

by

PANKAJ KUMAR JHA

Submitted to the Office of Graduate Studies of
Texas A&M University
in partial fulfillment of the requirements for the degree of

DOCTOR OF PHILOSOPHY

August 2012

Major Subject: Physics

NOVEL ATOMIC COHERENCE AND INTERFERENCE EFFECTS IN QUANTUM OPTICS AND ATOMIC PHYSICS

A Dissertation

by

PANKAJ KUMAR JHA

Submitted to the Office of Graduate Studies of
Texas A&M University
in partial fulfillment of the requirements for the degree of

DOCTOR OF PHILOSOPHY

Approved by:

Chair of Committee,	Marlan O. Scully
Committee Members,	George R. Welch
	M. Suhail Zubairy
	Goong Chen
Head of Department,	George R. Welch

August 2012

Major Subject: Physics

ABSTRACT

Novel Atomic Coherence and Interference Effects in Quantum Optics
and Atomic Physics. (August 2012)
Pankaj Kumar Jha, B.Sc. ; M.Sc., Indian Institute of Technology Kanpur
Chair of Advisory Committee: Dr. Marlan O. Scully

It is well known that the optical properties of multi-level atomic and molecular system can be controlled and manipulated efficiently using quantum coherence and interference, which has led to many new effects in quantum optics for e.g. lasing action without population inversion, ultraslow light, high resolution nonlinear spectroscopy etc. Recent experimental and theoretical studies have also provided support for the hypothesis that biological systems uses quantum coherence. Nearly perfect excitation energy transfer in photosynthesis is an excellent example of this.

In this dissertation we studied quantum coherence and interference effects in the transient and the continuous-wave regimes. This study led to (i) the first experimental demonstration of carrier-envelope phase effects on bound-bound atomic excitation in multi-cycle regime (~ 15 cycles), (ii) a unique possibility for standoff detection of trace gases using their rotational and vibrational spectroscopic signals and from herein called Coherent Raman Umklappscattering, (iii) several possibilities for frequency up-conversion and generation of short-wavelength radiation using quantum coherence (iv) the measurement of spontaneous emission noise intensity in Yoked-superfluorescence scheme.

Applications of the obtained results are development of XUV (X-Ray) lasers, controlled superfluorescent (superradiant) emission, carrier-envelope phase effects, coherent Raman scattering in the backward direction, enhancement of efficiency for generating radiation in XUV and X-Ray regime using quantum coherence with and without population inversion and to extend XUV and X-Ray lasing to ~ 4.023 nm in Helium-like carbon.

To my father Parmanand Jha

ACKNOWLEDGMENTS

The dissertation presented here is the result of a collaborative work performed at Texas A&M and Princeton Universities. No words can describe the enthusiasm of my advisor Prof. Marlan O. Scully who, all these years, has played a key role in shaping the graduate students into young and dynamic researchers. During my graduate research work at Texas A&M and Princeton Universities, I had the privilege to work with the pioneers of quantum optics and laser physics.

The work presented here could not have been accomplished without the guidance from Prof. Scully who has provided countless number of opportunities for my research and academic development. My sincere thanks to the unique team of theoreticians and experimentalists in our group at Institute for Quantum Science and Engineering (IQSE). I would like to acknowledge Y. V. Rostovtsev and V. A. Sautenkov for their endless effort since the beginning of my graduate work. The list of people who contributed to the present work includes G. R. Welch, S. Suckwer, A. M. Zheltikov, A. V. Sokolov, A. A. Svidzinsky, K. E. Dorfman, H. Li, H. Eleuch, S. Das, D. V. Voronine, L. Yuan, Z. Yi, E. Sete and A. Traverso. I would like to warmly thank them all.

My sincere appreciation for all the efforts of Prof. L.V. Keldysh with whom I had countless long discussions on different aspects of laser physics while his stay at Texas A&M University. It is my pleasure to acknowledge useful discussions with D. Herschbach, D. Lee, V. Pokrovsky, M. S. Zubairy, O. Kocharovskaya, V. Kocharovsky, P. Hemmer, R. Miles, W. Chow, A. Kalachev, A. Dogariu, H. Xia, and M. Zhi. I would also like to gratefully acknowledge financial support from the office of Naval Research, the Welch Foundation Graduate Fellowship, the HEEP Foundation Graduate Fellowship, the Texas A&M Research and Presentation Grant, and the American Physical Society Student Travel Grants.

Many thanks to K. R. Chapin and C. Holle at IQSE for their cheerful support. To all the members of the IQSE and my friends and colleagues in the Department of Physics and Astronomy (Texas A&M University) and Department of Mechanical and Aerospace Engineering (Princeton University), I thank you for your support and encouragement. Sincere thanks to the administrative staffs M. Hickey and C. P. Reed at Princeton University for their assistance during my frequent visits.

Finally I would like to acknowledge my wife Anamika Jha for her love, support and patience. I am grateful to my family members who have helped me in completing this path. I dedicate this dissertation to my father Parmanand Jha, who will always be a source of strength and inspiration for me.

TABLE OF CONTENTS

CHAPTER Page

CHAPTER Page

LIST OF TABLES

LIST OF FIGURES

FIGURE Page

FIGURE Page

FIGURE Page

FIGURE Page

FIGURE Page

FIGURE Page

FIGURE Page

FIGURE Page

FIGURE Page

CHAPTER I

INTRODUCTION

A. Motivation and Objectives

Interaction of light with matter is one of the major areas of research in quantum optics and atomic physics. Quantum coherence and interference[1] have led to many novel effects[2] for e.g. coherent population trapping [3], amplification or lasing without population inversion(LWI) [4, 2, 5, 6, 7], ultraslow light [8], enhancement of refractive index without absorption [9], yield high-sensitivity magnetometry [10], high resolution nonlinear spectroscopy[11], efficient solar cells[12] etc. Recent experimental and theoretical studies have also provided support for the hypothesis that even biological systems use quantum coherence[13, 14, 15]. Nearly perfect efficient excitation energy transfer in photosynthesis is an excellent example of this. Furthermore, during the past decade study of quantum interference(QI) effects has been extended to tailored semiconductor nanostructures like quantum wells and dots due to coherent resonant tunneling owing to their potential applications in photo-detection [16, 17], lasing [18, 19], quantum computing and quantum circuitry [20, 21], optical modulator[22]. On one hand quantum coherence effects in quantum optics and atomic physics is a subject of intense theoretical and experimental investigation while on the other hand its effect in human brain has been a topic of debate and discussion[2].

Coherence effects in two-level system was first studied by Mollow[23] who discovered interesting features in the resonance fluorescence spectrum of a two-level atom driven by a strong electromagnetic field. This was later confirmed by a beautiful experiment[24].

This dissertation follows the style of *Physical Review A*

[1] One of the first experiments to demonstrate the role of atomic coherence was done by Hanle[1]

[2] The authors are encourage to read a nice review article by Mavromatos[27]

Recently a counterpart of the Mollow triplet[23] was obtained for the case of incoherent excitation in a cavity by Valle and Laussy[25] where they showed that the strong-coupling between the cavity and the emitter generates the necessary coherence required. For multi-level system the coherence can be easily generated by coupling the upper-level to an adjacent level by a coherent electromagnetic field which has led to intriguing coherence effects in three-level systems. Recently Scully[12] extended the idea of coherence effects to solar photovoltaic cells and showed that the quantum interference can enhance the photovoltaic thermodynamic power beyond the limit of a system, which does not posses quantum coherence. Infact this coherence can be generated by an external source like microwave radiation source or by noise-induced quantum interference which is essentially different from the former which costs energy.

Although numerous theoretical and experimental studies of coherence effects have been performed, there are still open areas to be explored. For example, quantum coherence and interference which plays a key role in LWI as shown extensively in the literature, can it be used as a tool for enhancing the gain in the X-Ray/XUV regimes for e.g recombination lasers. A realistic approach in this area will open the door for the development of powerful lasers in the wavelength down to “water window” . Generation of XUV radiation has been a focus of intensive research in the past decade. One approach was proposed by Scully[26] in which it was shown that intense short pulses XUV radiations can be produced by cooperative spontaneous emission from visible or IR pulses. Here we have proposed one approach to accomplish the gain enhancement by applying a strong driving field on the adjacent transition to the lasing (XUV) transition and showed that gain can be substantially enhanced. We also investigated a unique way to accomplish effective unidirectional excitation using bi-directional source in four-level model.

Another area in which we want to study interference effects is in the regime of excitation by ultra-short few and multi-cycle pulse. We want to address and investigate its role in

carrier-envelope phase(CEP) effects on atomic excitation thus shining light on a fundamental question: "How many oscillations of the field within the pulse is sufficient to neglect the CEP effect?" Till date most of the research in the CEP effects has been performed in the ionization regime. Here we present an experiment in which we observed CEP effect by multi-cycle pulses. To the best of our knowledge this is the first demonstration of CEP effects by multi-cycle pulses on atomic exception between bound-bound states.

The research in my dissertation will also cover coherent Raman Umklappscattering, quantum interference controlled resonance profiles, using laser induced atomic desorption(LIAD) technique to optically control the alkali-metal vapors and picosecond ultraviolet Yoked superfluorescent (YSF) emission from optically pumped rubidium vapor.

B. Outline

The outline of the present dissertation is summarized here.

Chapter II. In this chapter, we have discussed briefly the mathematical framework used to study the interaction of matter with radiation in semiclassical approximation. We discuss the absorption and dispersion profile of two and three-level (Lambda) system explicitly. To understand the concept of atomic coherence we have addressed two examples namely electromagnetically induced transparency and lasing without inversion.

Chapter III. In this chapter, we have discussed an efficient way of generation coherence in two-level system excited by far off-resonant strong laser pulses. Exact analytical solution for two-level system interacting with a class of pulses (chirped and unchirped) is presented and the solutions are given in terms of Heun Function Hl, which is a generalization of Hypergeometric functions, and Confluent Heun Function H$l^{(c)}$. We also present a unique way of enhancing the excitation by introducing a phase jump in the pulse and the enhancement factor can be as large as 10^6 for a judicious choice of parameters. Using the

results obtained here we estimated a possibility for generating $10nJ - 1\mu J$ of energy in XUV regime.

Chapter IV. In this chapter we have discussed a quantum interference mediated control of the resonance profiles in a generic three-level system and investigate its effect on key quantum interference (QI) phenomena. Namely in a three level configuration with doublets in the ground or excited states, we show a precise control over enhancement and suppression of the emission (absorption) profiles by manipulating the strength of QI and the energy spacing of the doublets. We analyze the application of such QI induced control of the resonance profile in the framework of lasing without inversion and photo-detection.

Chapter V. In this chapter, we have focused on lasing in He and He-like ions that utilizes advantages of the recombination XUV/soft X-ray lasers and the effects of quantum coherence. The latter, for example, is the key for LWI, wherein quantum coherence created in the medium by means of strong driving field helps to partially eliminate resonant absorption on the transition of interest and to achieve gain without population inversion. Such an effect holds promise for obtaining short wavelength lasers in the XUV and X-ray spectral domains, where inverted medium is difficult to prepare due to fast spontaneous decay. We have performed numerical simulations on neutral Helium as our gain medium and showed that a respectable pulse of 10^9 photons at 58.4nm of radiation can be generated. We also explored the connection between gain swept superradiance and transient Raman LWI.

Chapter VI. In this chapter, we have proposed how to integrate the basic idea of recombination lasers with quantum coherence effects. We have discussed a possibility of enhancing the gain in XUV/X-Ray regime of electromagnetic radiation assisted by an external, longer wavelength (in optical domain), coherent source readily available in labs. We estimated at least an order of magnitude enhancement in the output energy in the presence of the coherent drive field. To envision the proof of principle experiment, we applied this technique of coherence enhanced lasing in Rubidium and theoretically estimated similar

enhancement factor at D_1 transition thus showing promise of the approach.

Chapter VII. In this chapter, we have experimentally and theoretically shine light on a "fundamental question" related to CEP effects. It is well know that CEP effect is pronounced for few cycle excitation and this has been thoroughly studied theoretical and experimentally. Infact the number of oscillations/cycles of electric field in the pulse which are sufficient to neglect the CEP effect is still an intriguing question. Here we present an experiment in which we observed CEP effects on bound-bound atomic excitation (Zeeman sub-levels) in the radio-frequency(RF) domain by multi-cycle pulses (~ 13 cycles). Our experiment is the first step in the field of CEP effects by multi-cycle pulses.

Chapter VIII. In this chapter, we identify the conditions for coherent Raman scattering to enable the generation of phase-matched, highly directional, nearly-backward-propagating light beams. Our analysis indicates a unique possibility for standoff detection of trace gases using their rotational and vibrational spectroscopic signals. We demonstrate spatial selectivity of Raman transitions and variability of possible Umklappscattering implementation schemes and laser sources.

Chapter IX. In this chapter, we have extended the idea of LIAD to control the alkali-metal vapors. Earlier work in this field has been mainly focused on control of concentration of atoms. Here we performed the proof of principle experiment on cesium and demonstrated that LIAD can be used a powerful tool to optically control and monitor the cesium dimers. We also combined LIAD and with resonance Raman technique to explore a possibility for remote sensing.

Chapter X. In this chapter, we have discussed an experiment on triggered YSF emission from optically pumped rubidium vapors. We have experimental observed the effect of injected pulse on the delay and thus quantifying the spontaneous emission noise intensity in YSF scheme. We also studied the effect of weak drive pulse of power 10nW-100nW on the directionality of the generated YSF signal. The effect of pulse shape and the angle be-

tween the pump and injected pulse on direction of the YSF signal generated and the noise intensity is under progress.

Chapter XI. In this chapter, we have summarized the key results presented in this dissertation.

CHAPTER II

ATOM-FIELD INTERACTION: SEMICLASSICAL THEORY

In this chapter, we will discuss the frame work frequently used in quantum optics to study the interaction of matter with radiation. We will treat the atom as a quantum mechanical system and the field is treated classically. The readers are encouraged to read[2, 28, 29] for detailed analysis.

A. Two-Level Atom

Let us consider a two-level atom (TLA), located at $\vec{r} = \vec{r}_0$, with lower level b and an upper level a [see Fig. 1], interacting with a linearly polarized monochromatic classical field $\vec{E}(\vec{r}, t)$. In dipole approximation, the Hamiltonian for the interaction between a TLA and the radiation field is given as[1]

$$\mathscr{H} = \mathscr{H}_0 + \mathscr{H}_1, \tag{2.1}$$

with

$$\mathscr{H}_1 = -e\vec{r} \cdot \vec{E}(\vec{r}_0, t), \tag{2.2}$$

where $\vec{r}$ is the position of the electron from the nucleus. Here $\mathscr{H}_0$ and $\mathscr{H}_1$ represent the unperturbed (free) and interaction Hamiltonian. The free Hamiltonian of the TLA $\mathscr{H}_0$ is given as

$$\mathscr{H}_0 = \hbar\omega_a \left|a\right\rangle\left\langle a\right| + \hbar\omega_b \left|b\right\rangle\left\langle b\right|. \tag{2.3}$$

[1] Recently we also analyzed the symmetry between two problems (a) interaction of a two-level atom with a classical field and (b) position dependent mass Schrodinger equation (PDMSE). Analytical solution to PDMSE in one- and later generalized to three-dimension is discussed extensively in[30, 31]

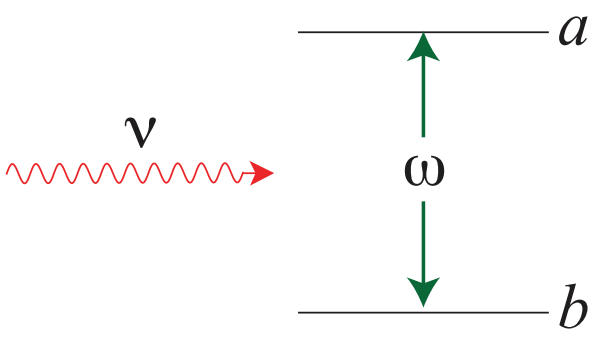

Fig. 1. Interaction of a two-level atom with a single mode radiation field of frequency ν. The atomic transition frequency is ω.

The lower level b and the upper level a are the eigenstates of the free Hamiltonian $\mathscr{H}_0$ with eigenvalues $\hbar\omega_b$ and $\hbar\omega_a$ respectively. Let us consider that the wavefunction corresponding to the levels a and b have definite parity i.e $\langle a|\vec{r}|a\rangle = \langle b|\vec{r}|b\rangle = 0$. Using the completeness relation $|a\rangle\langle a| + |b\rangle\langle b| = 1$, the interaction Hamiltonian $\mathscr{H}_1$ is given as

$$\mathscr{H}_1 = -e(\langle a|\vec{r}|b\rangle|a\rangle\langle b| + \langle b|\vec{r}|a\rangle|b\rangle\langle a|) \cdot \vec{E}(t). \tag{2.4}$$

Let us define dipole moment as

$$\vec{\wp}_{ab} = e\langle a|\vec{r}|b\rangle. \tag{2.5}$$

Substituting Eq.(2.5) in Eq.(2.4) and assume ($\vec{r_0} = 0$) yields,

$$\mathscr{H}_1 = -(\vec{\wp}_{ab}|a\rangle\langle b| + \vec{\wp}_{ba}|b\rangle\langle a|) \cdot \left[\frac{\hat{\epsilon}}{2}\mathscr{E}_b\left(e^{-i\nu t} + e^{i\nu t}\right)\right]. \tag{2.6}$$

Without the loss of generality we shall consider that the field is polarized along the x-direction i.e. $\vec{r} \cdot \hat{\epsilon} = x$. Now from Eq.(2.6) we get

$$\mathscr{H}_1 = -\left[\frac{\wp_{ab}\mathscr{E}_b}{2}|a\rangle\langle b| + \frac{\wp_{ba}\mathscr{E}_b}{2}|b\rangle\langle a|\right]\left(e^{-i\nu t} + e^{i\nu t}\right). \tag{2.7}$$

The total Hamiltonian is now given as

$$\mathscr{H} = \hbar\omega_a\,|a\rangle\langle a| + \hbar\omega_b\,|b\rangle\langle b| - \hbar\Omega|a\rangle\langle b|\left(e^{-i\nu t} + e^{i\nu t}\right) - \hbar\Omega^*|b\rangle\langle a|\left(e^{-i\nu t} + e^{i\nu t}\right). \tag{2.8}$$

where $\Omega_b = \wp_{ab}\mathscr{E}_b/2\hbar$.

1. Probability Amplitude Method

The wave function of a two-level atom can be written in the form

$$|\psi(t)\rangle = C_a(t)|a\rangle + C_b(t)|b\rangle. \tag{2.9}$$

where C_a and C_b are the probability amplitudes of finding the atom in levels a and b respectively. The wave function obeys the Schrödinger equation

$$i\hbar|\dot{\Psi}\rangle = \mathscr{H}\,|\Psi\rangle\,, \tag{2.10}$$

and the equation of motion for the amplitudes C_a and C_b may be written as

$$\dot{C}_a = -i\omega_a + i\Omega_b\left(e^{-i\nu t} + e^{i\nu t}\right)C_b, \tag{2.11}$$

$$\dot{C}_b = -i\omega_b + i\Omega_b^*\left(e^{-i\nu t} + e^{i\nu t}\right)C_a. \tag{2.12}$$

In order to solve for C_a and C_b, we first write the equations of motion for the slowly varying amplitudes

$$C_a = c_a e^{-i[\omega_a t + \phi_a(t)]}, \tag{2.13}$$

$$C_b = c_b e^{-i[\omega_b t + \phi_b(t)]}. \tag{2.14}$$

From Eq.(2.11-2.14), we obtain

$$\dot{c}_a - i\dot{\phi}_a c_a = i\Omega_b c_b\left\{e^{-i[\nu t + \omega_b t + \phi_b - \omega_a t - \phi_a]} + e^{i[\nu t - \omega_b t - \phi_b + \omega_a t + \phi_a]}\right\}, \tag{2.15}$$

$$\dot{c}_b - i\dot{\phi}_b C_b = i\Omega_b^* c_a\left\{e^{-i[\nu t + \omega_a t + \phi_a - \omega_b t - \phi_b]} + e^{i[\nu t - \omega_a t - \phi_a + \omega_b t + \phi_b]}\right\}. \tag{2.16}$$

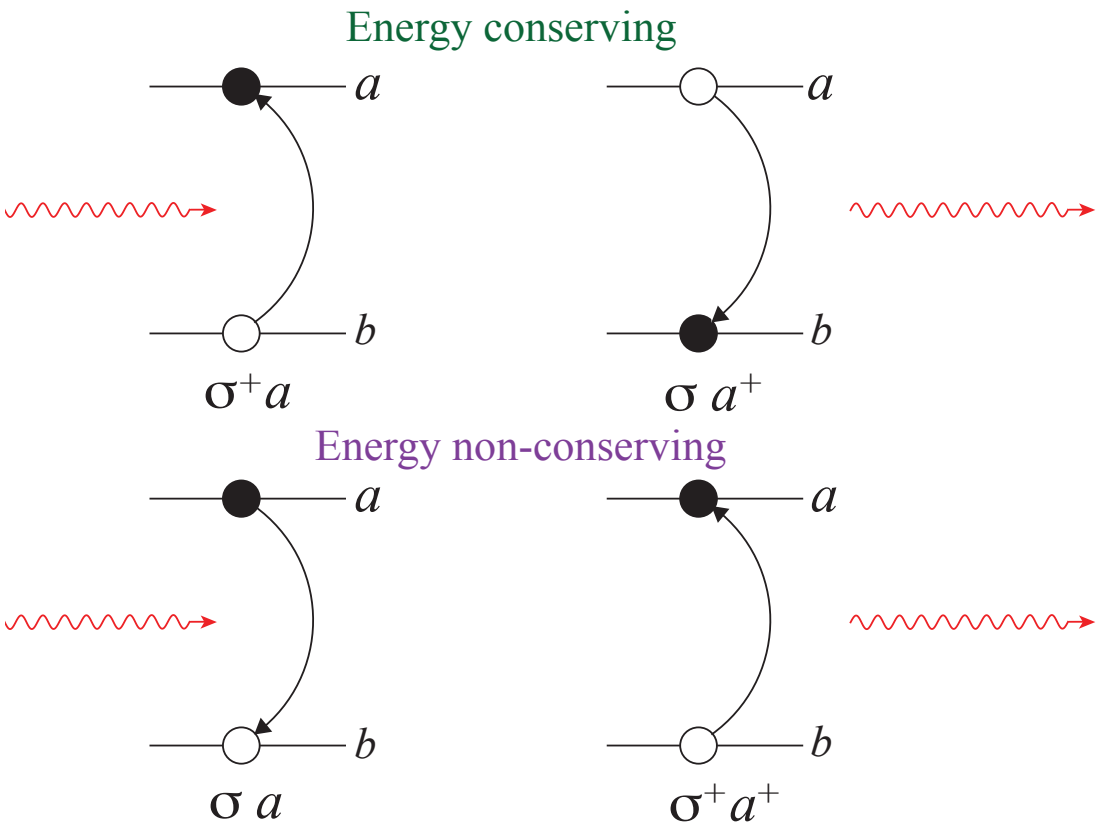

Fig. 2. Pictorial representation of matter-field interaction frequently used in quantum optics and atomic physics where the energy non-conserving terms are dropped while making rotating wave approximation(RWA).

From Eqs.(2.15-2.16), we see that proper choice of ϕ_a and ϕ_b can eliminate the fast oscillating exponentials. For example, we consider

$$\nu t + \omega_b t + \phi_b - \omega_a t - \phi_a = 0. \tag{2.17}$$

Substituting Eq.(2.17) in Eqs.(2.15-2.16) yields

$$\dot{c}_a - i\dot{\phi}_a c_a = i\Omega_b \left[1 + e^{2i\nu t}\right] c_b, \tag{2.18}$$

$$\dot{c}_b - i\dot{\phi}_b c_b = i\Omega_b^* \left[e^{-2i\nu t} + 1\right] c_a. \tag{2.19}$$

In Fig. 2 we have shown a pictorial representation of matter-field interaction which includes both energy conserving and non-conservation process. Now $e^{\pm 2i\nu t}$ is a rapidly oscillating term, so in rotating wave approximation(RWA), we neglect such terms[2]. Thus we get

$$\dot{c}_a - i\dot{\phi}_a c_a = i\Omega_b c_b, \tag{2.20}$$

$$\dot{c}_b - i\dot{\phi}_b c_b = i\Omega_b^* c_a. \tag{2.21}$$

Before we move further let us draw some conclusions based on some simple scenarios. If the single mode radiation field of frequency ν is resonant with the atomic transition frequency i.e. $\omega_a - \omega_b = \nu$ then from Eq.(2.17) we get $\phi_b - \phi_a = 0$[3].

(1) For off-resonant interaction, let us start with $\phi_a = 0$. From Eq.(2.17) we get $\dot{\phi}_b = \Delta_b$, where the detuning $\Delta_b = \omega_a - \omega_b - \nu$. Thus Eqs.(2.20, 2.21) yields,

$$\dot{c}_a = i\Omega_b c_b, \tag{2.22}$$

$$\dot{c}_b = i\Delta_b c_b + i\Omega_b^* c_a. \tag{2.23}$$

The equivalent Hamiltonian can be written as

$$\mathscr{H} = -\Delta_b |b\rangle\langle b| - \Omega_b |a\rangle\langle b| - \Omega_b^* |b\rangle\langle a|. \tag{2.24}$$

(2) Let us consider another choice $\phi_b = 0$. From Eq.(2.18, 2.19) we get $\dot{\phi}_a = -\Delta_b$. Thus Eqs.(2.20, 2.21) yields,

$$\dot{c}_a = -i\Delta_b c_a + i\Omega_b c_b, \tag{2.25}$$

$$\dot{c}_b = i\Omega_b^* c_a. \tag{2.26}$$

[2]It is worth mentioning here that when we are working with strong few cycle pulses then RWA is not a good approximation. Details of few and multi-cycle pulse excitation is presented extensively in chapter III section D and chapter VII

[3]Here the simplest choice would be to take $\phi_a = \phi_b = 0$

The equivalent Hamiltonian can be written as

$$\mathscr{H} = \Delta_b|a\rangle\langle a| - \Omega_b|a\rangle\langle b| - \Omega_b^*|b\rangle\langle a|. \tag{2.27}$$

(3) At last we assume $\dot{\phi}_b = \Delta_b/2$ and $\dot{\phi}_a = -\Delta_b/2$. Now Eqs.(2.20, 2.21) yields,

$$\dot{c}_a = -i(\Delta_b/2)c_a + i\Omega_b c_b, \tag{2.28}$$

$$\dot{c}_b = i(\Delta_b/2)c_b + i\Omega_b^* c_a. \tag{2.29}$$

The equivalent Hamiltonian can be written as

$$\mathscr{H} = (\Delta_b/2)|a\rangle\langle a| - (\Delta_b/2)|b\rangle\langle b| - \Omega_b|a\rangle\langle b| - \Omega_b^*|b\rangle\langle a|. \tag{2.30}$$

2. Density Matrix Approach

We now consider the two-level atomic system again where the state of the system is a linear combination of levels a and b as given by Eq.(2.9). Then the density matrix operator can be written as

$$\rho = |C_a|^2|a\rangle\langle a| + C_aC_b^*|a\rangle\langle b| + C_bC_a^*|b\rangle\langle a| + |C_b|^2|b\rangle\langle b|. \tag{2.31}$$

Taking the matrix elements, we get,

$$\rho_{aa} = \langle a|\rho|a\rangle = C_aC_a^*, \tag{2.32}$$

$$\rho_{ab} = \langle a|\rho|b\rangle = C_aC_b^*, \tag{2.33}$$

$$\rho_{ba} = \langle b|\rho|a\rangle = C_bC_a^* = \rho_{ab}^*, \tag{2.34}$$

$$\rho_{bb} = \langle b|\rho|b\rangle = C_bC_b^*. \tag{2.35}$$

The evolution of the density matrix elements $\rho_{\alpha\beta}$ is governed by the Liouville or Von Neumann equation of motion for the density matrix

$$i\hbar\dot{\rho} = [\mathscr{H}, \rho]. \tag{2.36}$$

In Eq.(2.36) we have not included the decay of the levels due to spontaneous emission, collisions and other phenomena. These terms are added to Eq.(2.36) phenomenologically. To illustrate this let us consider the Hamiltonian Eq.(2.8).The equation of the motion for the density matrix elements are now given as

$$\dot{\rho}_{aa} = -\gamma_b \rho_{aa} - i\left[\Omega_b^* \left(e^{-i\nu t} + e^{i\nu t}\right) \rho_{ab} - \Omega_b \left(e^{-i\nu t} + e^{i\nu t}\right) \rho_{ab}^*\right], \tag{2.37}$$

$$\dot{\rho}_{bb} = \gamma_b \rho_{aa} + i\left[\Omega_b^* \left(e^{-i\nu t} + e^{i\nu t}\right) \rho_{ab} - \Omega_b \left(e^{-i\nu t} + e^{i\nu t}\right) \rho_{ab}^*\right], \tag{2.38}$$

$$\dot{\rho}_{ab} = -\left(\gamma_{ab} + i\omega\right) \rho_{ab} - i\Omega_b \left(e^{-i\nu t} + e^{i\nu t}\right) \left(\rho_{aa} - \rho_{bb}\right), \tag{2.39}$$

where γ_b is the spontaneous decay rate from $a \to b$ and γ_{ab} is the decay rate of the coherence ρ_{ab}. Similar to the probability amplitude method, we will write ρ_{ab} in terms of a slowly varying envelope as

$$\rho_{ab} = \varrho_{ab} e^{-i\nu t}. \tag{2.40}$$

Using Eq.(2.40) in Eqs.(2.37-2.39) and invoking the RWA yields,

$$\dot{\rho}_{aa} = -\gamma_b \rho_{aa} - i\left[\Omega_b^* \varrho_{ab} - \Omega_b \varrho_{ab}^*\right], \tag{2.41}$$

$$\dot{\rho}_{bb} = \gamma_b \rho_{aa} + i\left[\Omega_b^* \varrho_{ab} - \Omega_b \varrho_{ab}^*\right], \tag{2.42}$$

$$\dot{\varrho}_{ab} = -\left(\gamma_{ab} + i\Delta_b\right) \varrho_{ab} - i\Omega_b \left(\rho_{aa} - \rho_{bb}\right). \tag{2.43}$$

Let us solve Eqs.(2.41-2.43) in steady state, which gives the coherence term as

$$\bar{\varrho}_{ab} = \frac{\gamma_b \Omega_b \left(\Delta_b + i\gamma_{ab}\right)}{4\gamma_{ab}\Omega_b + \gamma_b \Delta_b^2 + \gamma_b \gamma_{ab}^2}, \tag{2.44}$$

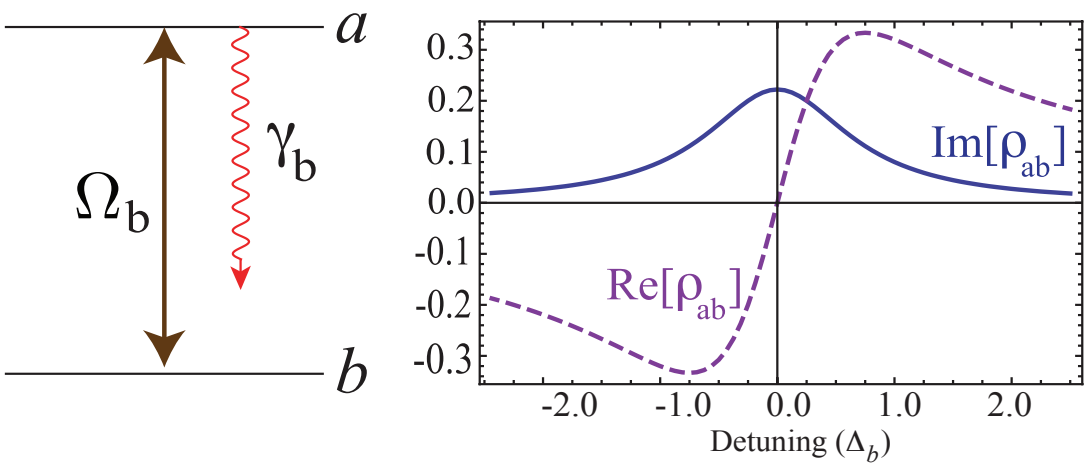

Fig. 3. (a) Interaction of a two-level atom with a off-resonant single mode radiation field of frequency ν. (b) Steady-state real and imaginary part of ϱ_{ab} as a function of normalized detuning Δ_b/γ_b. For numerical simulation we took, $\gamma_b = 1, \Omega_b = 1$ and $\gamma_{ab} = \gamma_b/2 = 0.5$

and the population of the upper level is

$$\bar{\varrho}_{aa} = \frac{2\gamma_{ab}\Omega_b^2}{4\gamma_{ab}\Omega_b^2 + \gamma_b\Delta_b^2 + \gamma_b\gamma_{ab}^2}. \tag{2.45}$$

In Fig. 3, we shown the plot of real and imaginary part of $\bar{\varrho}_{ab}$ which governs the dispersion and absorption of the field Ω_b. We see that in steady-state the two-level system will exhibit absorption ($\Im[\bar{\varrho}_{ab}] > 0$) which is maximum at resonance and dies off $\propto 1/\Delta_b^2$ for far detuned excitation i.e $\Delta_b \gg \Omega_b, \gamma_b$. Later this chapter we will show that in the presence of a third level (Lambda configuration), the system exhibits zero absorption on the probe transition at resonance.

B. Maxwell-Schrödinger Equation

Till now we have considered an interaction of a single mode field with one TLA. However in many problems in quantum optics, we are interested in the interaction of the electromagnetic field with a medium of large numbers of atoms. In this section we will derive

the equations to describe the propagation of a field through a medium in semi-classical approximation. Classical electromagnetic radiation is governed by Maxwell's Equations [2]:

$$\nabla \cdot \mathbf{D} = 0, \quad \nabla \times \mathbf{E} = -\frac{\partial \mathbf{B}}{\partial t}, \tag{2.46}$$

$$\nabla \cdot \mathbf{B} = 0, \quad \nabla \times \mathbf{H} = \mathbf{J} + \frac{\partial \mathbf{D}}{\partial t}, \tag{2.47}$$

where,

$$\mathbf{D} = \epsilon_0 \mathbf{E} + \mathbf{P}, \quad \mathbf{B} = \mu_0 \mathbf{H}, \quad \mathbf{J} = \sigma \mathbf{E}. \tag{2.48}$$

Here $\mathbf{P}$ is the macroscopic polarization of the medium. Combining Eqs.(2.46, 2.47) and using simple vector algebra, we obtain the wave equation,

$$\nabla \times (\nabla \times \mathbf{E}) + \mu_0 \sigma \frac{\partial \mathbf{E}}{\partial t} + \frac{1}{c^2} \frac{\partial^2 \mathbf{E}}{\partial t^2} = -\mu_0 \frac{\partial^2 \mathbf{P}}{\partial t^2}, \tag{2.49}$$

where $\epsilon_0 \mu_0 c^2 = 1$. Now the polarization $\mathbf{P}$ can be regarded as the source term for the radiation $\mathbf{E}$. To simplify the mathematical structure let us consider that the field is propagating along the $z-$axis and polarized along the $x-$axis,

$$\mathbf{E} = \mathcal{E}(z,t)\hat{x}. \tag{2.50}$$

If the variation of the laser field intensity transverse to the laser axis is slow on the length scale of the optical wavelength, we can neglect the $x-$ and $y-$contribution. Eq.(2.49) reduces to

$$-\frac{\partial^2 \mathcal{E}}{\partial z^2} + \mu_0 \sigma \frac{\partial \mathcal{E}}{\partial t} + \frac{1}{c^2} \frac{\partial^2 \mathcal{E}}{\partial t^2} = -\mu_0 \frac{\partial^2 P}{\partial t^2}. \tag{2.51}$$

The field of frequency ν is given by

$$\mathcal{E}(z,t) = \frac{1}{2} \mathscr{E}(z,t) \exp[i(kz - \nu t)] + \text{c.c}, \tag{2.52}$$

where $\mathscr{E}(z,t)$ is slowly varying function of position and time. Neglecting the higher harmonics, the polarization is given by,

$$P(z,t) = \frac{1}{2}\mathscr{P}(z,t)\exp[i(kz-\nu t)] + \text{c.c}, \tag{2.53}$$

where $\mathscr{P}(z,t)$ are slowly varying functions of position and time. Here we can write

$$\mathscr{P}(z,t) = 2\wp_{ba}\rho_{ab}\exp[-i(kz-\nu t)] + \text{c.c}. \tag{2.54}$$

Substituting Eq.(2.53, 2.54) in Eq.(2.51), and applying the following approximations

$$\frac{\partial\mathscr{E}}{\partial t} \ll \nu\mathscr{E}, \quad \frac{\partial\mathscr{E}}{\partial z} \ll k\mathscr{E}, \quad \frac{\partial\mathscr{P}}{\partial t} \ll \nu\mathscr{P}, \quad \frac{\partial\mathscr{P}}{\partial z} \ll k\mathscr{P}, \tag{2.55}$$

we obtained the field amplitude equations to be,

$$\frac{\partial\mathscr{E}}{\partial z} + \frac{1}{c}\frac{\partial\mathscr{E}}{\partial t} = -\kappa\mathscr{E} + i\left(\frac{N\wp_{ba}\nu}{\epsilon_0 c}\right)\varrho_{ab}, \tag{2.56}$$

where $\kappa = \sigma/2\epsilon_0 c$ is the linear loss coefficient and

$$\rho_{ab} = \varrho_{ab}\exp[i(kz-\nu t)]. \tag{2.57}$$

Let us rewrite Eq.(2.56) in the form which is has been most commonly used here[4]. We transform Eq.(2.56) in terms of the Rabi frequency $\Omega = \wp_{ab}\mathscr{E}/2\hbar$ as

$$\frac{\partial\Omega}{\partial z} + \frac{1}{c}\frac{\partial\Omega}{\partial t} = i\left(\frac{N|\wp_{ab}|^2\nu}{2\epsilon_0 c\hbar}\right)\varrho_{ab}. \tag{2.58}$$

The spontaneous decay rate from $a \to b$ is given as

$$\gamma_b = \frac{1}{4\pi\epsilon_0}\frac{4\omega_{ab}^3|\wp_{ab}|^2}{3\hbar c^3}. \tag{2.59}$$

[4]In the most part of this dissertation we have neglected the linear loss term

Here γ_b is the radiative decay rate of the atom in free space[5]. Combining Eq.(2.58), Eq.(2.59) and using the definition $2\pi c = \lambda\nu$ and assuming $\omega = \nu$ we obtain

$$\frac{\partial\Omega}{\partial z} + \frac{1}{c}\frac{\partial\Omega}{\partial t} = i\eta\varrho_{ab}, \tag{2.60}$$

where the coupling constant $\eta = (3/8\pi)N\lambda^2\gamma_b$. Here λ_b is the wavelength corresponding to the transition $a \to b$. When the field is off-resonance then η is given as

$$\eta = \frac{3}{8\pi}N\lambda^2\gamma_b(1 - \Delta/\omega). \tag{2.61}$$

To study the evolution of a field, propagating through a medium of two-level atoms, we numerically solve Eqs.(2.41, 2.42, 2.43, 2.60) with proper initial conditions. One example could be the evolution of a weak probe field through a highly inverted medium of two-levels atoms. In chapter VI, we have considered this problem extensively.

C. Three-Level Atom

In the previous section we observed that in steady state two level system always exhibit absorption. Here we will show that in the presence of a third level which is coupled to the upper level a drastically changes the absorption and dispersion profile of the transition $a \leftrightarrow b$. Let us consider a three-level atom as shown in Fig. 4 in Lambda and Cascade configurations. In this section of the chapter we will in detail discuss the Lambda configuration where the transition $a \leftrightarrow c$ is coupled to a strong drive field Ω_a and the transition $a \leftrightarrow b$ is coupled to weak probe field Ω_b. The off-diagonal decay rates for ρ_{ab}, ρ_{ac} and ρ_{cb} are denoted by γ_{ab}, γ_{ac}, and γ_{cb} respectively.

[5]Recently Vladimirova $et.al.$ presented a detailed analysis of the modification of resonance fluorescence spectra of a TLA placed near a metal sphere[32]

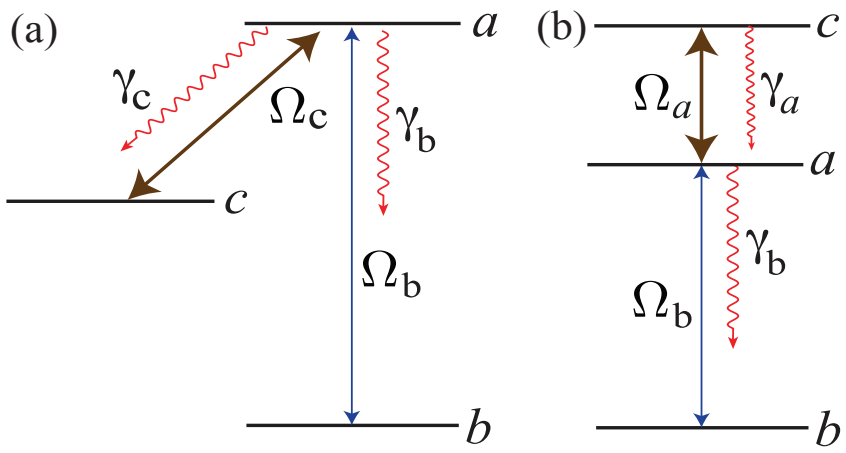

Fig. 4. Three level system in (a) Lambda and (b) Cascade configuration.

1. Electromagnetically Induced Transparency

The interaction Hamiltonian for the system in the RWA can be written as [2]

$$\mathscr{H} = -\hbar\Omega_c e^{i\Delta_c t}|a\rangle\langle c| - \hbar\Omega_b e^{i\Delta_b t}|a\rangle\langle b| + \text{c.c}, \tag{2.62}$$

where $\Delta_c = \omega_{ac} - \nu_c$ and $\Delta_b = \omega_{ab} - \nu_b$. Using the evolution equation for the density matrix elements i.e Eq.(2.36), we obtain for the coherence terms ρ_{ij} as

$$\dot{\rho}_{ab} = -\gamma_{ab}\rho_{ab} - i\Omega_b e^{i\Delta_b t}(\rho_{aa} - \rho_{bb}) + i\Omega_c e^{i\Delta_c t}\rho_{cb}, \tag{2.63}$$

$$\dot{\rho}_{ac} = -\gamma_{ac}\rho_{ac} - i\Omega_c e^{i\Delta_c t}(\rho_{aa} - \rho_{cc}) + i\Omega_b e^{i\Delta_b t}\rho^*_{cb}, \tag{2.64}$$

$$\dot{\rho}_{cb} = -\gamma_{cb}\rho_{cb} + i\Omega^*_c e^{-i\Delta_c t}\rho_{ab} - i\Omega_b e^{i\Delta_b t}\rho^*_{ac}. \tag{2.65}$$

Let us now make a transformation defined as

$$\rho_{ab} = \varrho_{ab} e^{i\Delta_b t}, \tag{2.66}$$

$$\rho_{ac} = \varrho_{ac} e^{i\Delta_c t}, \tag{2.67}$$

$$\rho_{cb} = \varrho_{cb} e^{i(\Delta_b - \Delta_c)t}, \tag{2.68}$$

and $\varrho_{ii} = \rho_{ii}$. Substituting inEqs.(2.63-2.65) we obtain,

$$\dot{\varrho}_{ab} = -\Gamma_{ab}\varrho_{ab} - i\Omega_b(\varrho_{aa} - \varrho_{bb}) + i\Omega_c\varrho_{cb}, \tag{2.69}$$

$$\dot{\varrho}_{ac} = -\Gamma_{ac}\varrho_{ac} - i\Omega_c(\varrho_{aa} - \varrho_{cc}) + i\Omega_b\varrho^*_{cb}, \tag{2.70}$$

$$\dot{\varrho}_{cb} = -\Gamma_{cb}\varrho_{cb} + i\Omega^*_c\varrho_{ab} - i\Omega_b\varrho^*_{ac}. \tag{2.71}$$

Solving for $\varrho^{(1)}_{ab}$ where we keep the probe field term Ω_b to its lowest order but keeping Ω_c to all orders we obtain

$$\varrho^{(1)}_{ab} = -i\Omega_b\left[\frac{\Gamma_{ca}\Gamma_{cb}(\varrho^{(0)}_{aa} - \varrho^{(0)}_{bb}) + (\varrho^{(0)}_{cc} - \varrho^{(0)}_{aa})|\Omega_c|^2}{\Gamma_{ac}(\Gamma_{ab}\Gamma_{cb} + |\Omega_c|^2)}\right]. \tag{2.72}$$

To make the analytical approach simple, let us assume $\Delta_c = 0$ i.e we drive the transition $a \leftrightarrow c$ at resonance. As the atoms are initially in the ground level b,

$$\varrho^{(0)}_{bb} = 1, \quad \varrho^{(0)}_{aa} = \varrho^{(0)}_{cc} = 0. \tag{2.73}$$

Substituting Eq.(2.73) in Eq.(2.72) we obtain,

$$\varrho^{(1)}_{ab} = i\Omega_b\left[\frac{\gamma_{cb} + i\Delta_b}{(\gamma_{ab} + i\Delta_b)(\gamma_{cb} + i\Delta_b) + |\Omega_c|^2}\right]. \tag{2.74}$$

Using the relation $\mathscr{P} = \epsilon_0\chi\mathscr{E}$ and the definition Eq.(2.54), we obtain the complex susceptibility as

$$\chi = i\frac{N|\wp_{ab}|^2}{\epsilon_0\hbar}\left[\frac{\gamma_{cb} + i\Delta_b}{(\gamma_{ab} + i\Delta_b)(\gamma_{cb} + i\Delta_b) + |\Omega_c|^2}\right], \tag{2.75}$$

where N is the number density of atoms. We know that the real and imaginary part of the complex susceptibility are related to the dispersion and absorption, respectively. Thus we obtain

$$\chi' = \Re(\chi) = \frac{N|\wp_{ab}|^2\Delta_b}{\epsilon_0\hbar}\left[\frac{\gamma_{cb}(\gamma_{ab} + \gamma_{cb}) + (\Delta_b^2 - \gamma_{cb}\gamma_{ab} - |\Omega_c|^2)}{(\Delta_b^2 - \gamma_{cb}\gamma_{ab} - |\Omega_c|^2)^2 + \Delta^2(\gamma_{cb} + \gamma_{ab})^2}\right], \tag{2.76}$$

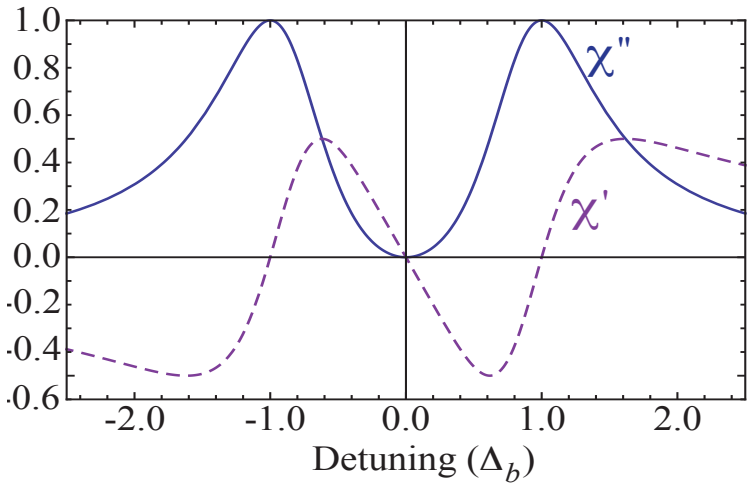

Fig. 5. Real (solid line) and imaginary (dashed line) parts of the complex susceptibility as a function of the normalized detuning Δ_b/γ_b.

$$\chi'' = \Im(\chi) = \frac{N|\wp_{ab}|^2}{\epsilon_0\hbar}\left[\frac{\Delta_b^2(\gamma_{ab}+\gamma_{cb}) - \gamma_{cb}(\Delta_b^2 - \gamma_{cb}\gamma_{ab} - |\Omega_c|^2)}{(\Delta_b^2 - \gamma_{cb}\gamma_{ab} - |\Omega_c|^2)^2 + \Delta^2(\gamma_{cb}+\gamma_{ab})^2}\right], \tag{2.77}$$

where $\chi = \chi' + i\chi''$. In Fig. (5) we have plotted the real and complex part of the susceptibility χ versus the detuning Δ_b in the units of γ_{ab}. For numerical simulation we took $\Omega = \gamma_b, \gamma_{cb} = 10^{-4}\gamma_{ab}$. We see that when the probe field is resonant with the transition $a \leftrightarrow b$ i.e $\Delta_b = 0$, $\chi' = 0$ and $\chi'' \sim 0$. Thus the medium becomes transparent under the action of the drive field Ω_c. It is important to mention that this transparency is sensitive to γ_{cb} which is the decay of the coherence of the dipole forbidden transition $c \leftrightarrow b$.

2. Lasing Without Inversion

In the closed $\Lambda-$system [as shown in Fig. 6] the lasing and the driving fields couple the upper level a and two lower levels b and c respectively. The spontaneous decay rates from $a \to b$ is γ_b, and from $a \to c$ is γ_c, and $\gamma = \gamma_b + \gamma_c$. Pumping rates from $b \to a$ is r_b, from $c \to a$ is r_c. Population exchange rate (for e.g. collisions) are γ_1 from $c \to b$, and γ_2 from

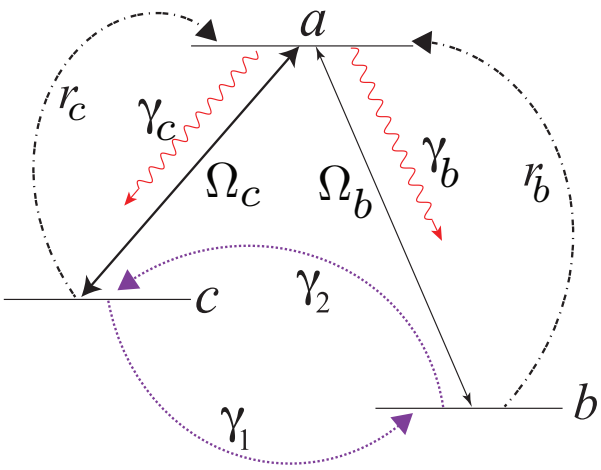

Fig. 6. Three-level system in lambda configuration. The lasing and the driving fields couple the upper level a and two lower levels b and c respectively. The spontaneous decay rates from $a \to b$ is γ_b, and from $a \to c$ is γ_c, and $\gamma = \gamma_b + \gamma_c$. Pumping rates from $b \to a$ is r_b, from $c \to a$ is r_c. Population exchange rate (for e.g. collisions) are γ_1 from $c \to b$, and γ_2 from $b \to c$.

$b \to c$. The interaction Hamiltonian is given as

$$\mathscr{H} = -\left(\Omega_b|a\rangle\langle b| + \Omega_c|a\rangle\langle c| + \text{c.c}\right). \tag{2.78}$$

The density matrix equations can be written as

$$\dot{\rho}_{bb} = -(\gamma_2 + r_b)\rho_{bb} + \gamma_1\rho_{cc} + \gamma_b\rho_{aa} + i\left(\Omega_b^*\rho_{ab} - \Omega_b\rho_{ab}^*\right), \tag{2.79}$$

$$\dot{\rho}_{cc} = -(\gamma_1 + r_c)\rho_{cc} + \gamma_2\rho_{bb} + \gamma_c\rho_{aa} + i\left(\Omega_c^*\rho_{ac} - \Omega_c\rho_{ac}^*\right), \tag{2.80}$$

$$\dot{\rho}_{ab} = -\Gamma_{ab}\rho_{ab} - i\Omega_b(\rho_{aa} - \rho_{bb}) + i\Omega_c\rho_{cb}, \tag{2.81}$$

$$\dot{\rho}_{ca} = -\Gamma_{ca}\rho_{ca} + i\Omega_c^*(\rho_{aa} - \rho_{cc}) - i\Omega_b^*\rho_{cb}, \tag{2.82}$$

$$\dot{\rho}_{cb} = -\Gamma_{cb}\rho_{cb} + i\Omega_c^*\rho_{ab} - i\Omega_b\rho_{ca}, \tag{2.83}$$

$$1 = \rho_{aa} + \rho_{bb} + \rho_{cc}. \tag{2.84}$$

where,

$$\gamma_{ab} = \frac{\gamma + r_b + \gamma_2}{2}, \quad \gamma_{ac} = \frac{\gamma + r_c + \gamma_1}{2}, \quad \gamma_{cb} = \frac{r_c + r_b + \gamma_1 + \gamma_2}{2}. \tag{2.85}$$

We solve Eqs.(2.79-2.84) in the steady state by setting all the time time derivative equal to zero. We obtained the steady-state coherences in terms of the populations as

$$\bar{\rho}_{ab} = -i\Omega_b \left[\frac{(\bar{\rho}_{aa} - \bar{\rho}_{bb})(\Gamma_{ca}\Gamma_{cb} + |\Omega_b|^2) + (\bar{\rho}_{cc} - \bar{\rho}_{aa})|\Omega_c|^2}{\mathcal{D}} \right], \tag{2.86}$$

$$\bar{\rho}_{ca} = i\Omega_c^* \left[\frac{(\bar{\rho}_{aa} - \bar{\rho}_{cc})(|\Omega_c|^2 + \Gamma_{ca}\Gamma_{ab}) + (\bar{\rho}_{bb} - \bar{\rho}_{aa})|\Omega_b|^2}{\mathcal{D}} \right], \tag{2.87}$$

$$\bar{\rho}_{cb} = \Omega_b\Omega_c^* \left[\frac{(\bar{\rho}_{aa} - \bar{\rho}_{bb})\Gamma_{ca} + (\bar{\rho}_{aa} - \bar{\rho}_{cc})\Gamma_{ab}}{\mathcal{D}} \right], \tag{2.88}$$

where,

$$\mathcal{D} = \Gamma_{ab}\Gamma_{ca}\Gamma_{cb} + \Gamma_{ab}|\Omega_b|^2 + \Gamma_{ca}|\Omega_c|^2. \tag{2.89}$$

In the limit of weak probe field, we will keep Ω_b to its lowest term but all the terms for Ω_c then Eq.(2.86, 2.87) takes the form,

$$\rho_{ab}^{(1)} = -i\Omega_b \left[\frac{(\rho_{aa}^{(0)} - \rho_{bb}^{(0)})\Gamma_{ca}\Gamma_{cb} + (\rho_{cc}^{(0)} - \rho_{aa}^{(0)})|\Omega_c|^2}{\Gamma_{ca}\left(\Gamma_{ab}\Gamma_{cb} + |\Omega_c|^2\right)} \right]. \tag{2.90}$$

$$\rho_{ca}^{(1)} = i\Omega_c^* \left[\frac{\rho_{aa}^{(0)} - \rho_{cc}^{(0)}}{\Gamma_{ca}} \right]. \tag{2.91}$$

Next we solve for the population terms $\rho_{ll}^{(0)}$ by solving Eqs.(2.79, 2.80) supplemented by Eqs.(2.84, 2.90, 2.91). Further we assume that the Rabi frequencies corresponding to the probe and the drive fields are real. The populations are given as

$$\rho_{aa}^{(0)} = \frac{Br_b + r_br_c + \gamma_1 r_b + \gamma_2(B + r_c)}{\mathcal{M}'}, \tag{2.92}$$

$$\rho_{bb}^{(0)} = \frac{B\gamma_b + \gamma_b r_c + \gamma_1(B + \gamma_b + \gamma_c)}{\mathcal{M}'}, \tag{2.93}$$

$$\rho_{cc}^{(0)} = \frac{Br_b + \gamma_c r_b + \gamma_2(B + \gamma_b + \gamma_c)}{\mathcal{M}'}, \tag{2.94}$$

where $\mathcal{M}'$ is the sum of the numerators in the above expressions. From these expressions we obtain the condition for population inversion on the lasing transition $\rho_{aa}^{(0)} > \rho_{bb}^{(0)}$ as,

$$r_c(r_b + \gamma_2 - \gamma_b) + \gamma_1(r_b - \gamma_b - \gamma_c) + (r_b - \gamma_1 + \gamma_2 - \gamma_b)B > 0. \tag{2.95}$$

If we use the definition of population inversion as $\bar{\rho}_{aa} + \bar{\rho}_{cc} > \bar{\rho}_{bb}$, we obtain the condition as

$$B(2r_b - \gamma_1 + 2\gamma_2 - \gamma_b) + r_c(\gamma_2 - \gamma_b + r_b) + r_b(\gamma_1 + \gamma_c) - (\gamma_1 - \gamma_2)(\gamma_b + \gamma_c) > 0. \tag{2.96}$$

In the absence of any incoherent pump on the drive transition $a \leftrightarrow c$ i.e. $r_c = 0$, Eqs.(2.95, 2.96) gives,

$$B(r_b - \gamma_1 + \gamma_2 - \gamma_b) + \gamma_1(r_b - \gamma_b - \gamma_c) > 0, \tag{2.97}$$

$$B(2r_b - \gamma_1 + 2\gamma_2 - \gamma_b) + r_b(\gamma_1 + \gamma_c) - (\gamma_1 - \gamma_2)(\gamma_b + \gamma_c) > 0. \tag{2.98}$$

The condition for gain can be obtained by using the expression for populations in Eq.(2.90) which gives,

$$\begin{aligned} B\left[r_b(r_b - \gamma_1 + 2\gamma_2 - \gamma_b + \gamma_c) - \gamma_1(\gamma_1 + \gamma_b) + \gamma_2(\gamma_2 + \gamma_c)\right] \\ +\gamma_1(r_b + \gamma_1 + \gamma_2)(r_b - \gamma_b - \gamma_c) > 0. \end{aligned} \tag{2.99}$$

Interestingly for symmetric bidirectional pumping i.e $\gamma_1 = \gamma_2$, strong drive and $r_b = 0$, we never observe inversion on the lasing transition but the system is inverted $\rho_{aa}^{(0)} + \rho_{cc}^{(0)} > \rho_{bb}^{(0)}$ if $\gamma_2 > \gamma_b$. The condition for gain from Eq.(2.99) gives

$$\gamma_c > \gamma_b. \tag{2.100}$$

Thus to observed lasing without inversion the spontaneous decay rate on the decay transition should be greater that the decay rate on the lasing transition[6]. Further more if we

[6]In the case of three-level atom in the cascade configuration the condition is reverse i.e $\gamma_b > \gamma_a$

assume that purely phase decay $\gamma_{cb}^{p} = (\gamma_1 + \gamma_2)/2$, we obtain the condition for gain as

$$B\left[r_b(r_b + \gamma_c - \gamma_b + 3\gamma_2) + 2\gamma_2^2 - 2\gamma_1^2 + \gamma_2(\gamma_b + \gamma_c) - 2\gamma_b(\gamma_1 + \gamma_2)\right] \\ +\gamma_1(r_b - \gamma_b - \gamma_c)(r_b + 2\gamma_1 + 2\gamma_2) > 0. \tag{2.101}$$

If we consider pumping in both the directions $\gamma_1 = \gamma_2$, strong drive and $r_b = 0$, we obtain the necessary condition for gain as[7]

$$\gamma_c > 3\gamma_b. \tag{2.102}$$

Thus we can see from Eq.(2.99-2.102) that even when small amount of population is in the excited state still we can observe gain on the probe transition. Physically in the lasing without inversion the essential idea is the cancellation of absorption on the probe transition via atomic coherence and interference[8]. In fact this is also the essence of electromagnetic induced transparency.

To conclude, in this introductory chapter we laid the foundation for the mathematical analysis used in the dissertation. We used semiclassical approach to quantify the interaction of radiation with matter. We extensively derived the Hamiltonian for two-level atom with a single mode field[9]. We also discussed two simple examples which are the manifestation of quantum interference phenomena namely electromagnetic induced transparency and lasing without inversion.

[7]For detailed analysis on V scheme also, read the conference paper by Nikonov[33]

[8]For simple and rigorous analysis of lasing without inversion and electromagnetic induced transparency readers are suggested to go through sections 7.3 and 7.4 of Scully and Zubairy[2]

[9]The extension to three-level system is derived in appendix A. In Appendix B, we present a brief discussion of the symmetry of the evolution of identical seed pulse at the boundary $z = 0$ and $z = L$ in the forward and backward direction respectively

CHAPTER III

EFFICIENT EXCITATION OF UV AND XUV COHERENCE BY FAR OFF-RESONANCE STRONG PULSES*

A. Introduction

The two-level system (TLS)[2, 28, 29] is a very rich and useful model that helps to understand physics of many problems ranging from interaction with electromagnetic fields to level-crossing[34, 35, 36]. For example, interaction of a beam of atoms in Stern-Gerlach apparatus[37] and Bloch-Siegert shift[38] can be understood using TLS. Recently TLS has been extensively studied as a quantum bit (qubit) for quantum information theory[39]. Two-level atom (TLA) description is valid if the two atomic levels involved are resonant or nearly resonant with the driving field, while all other levels are highly detuned. TLS can be realized exactly for a spin-1/2 system, and, approximately, for a multi-level system in a magnetic field when all other magnetic sub-levels are detuned far-off resonance.

When the frequency of the driving field is in resonance with the atomic transition frequency, the Schrödinger equation for the time evolution of state amplitudes is exactly solvable for any time dependence of the field $\Omega(t)$. For off-resonance excitation several exactly solvable models for the TLS have been proposed in the past[40, 41] where solutions to the Schrödinger equation are expressed in terms of known functions like Hypergeomteric functions. Several approximate solutions have also been proposed based on perturbation

*Part of this chapter is reprinted with permission from "Coherent excitation of a two-level atom driven by a far-off-resonant classical field: Analytical solutions" by P. K. Jha and Y. V. Rostovtsev, 2010. *Phys. Rev. A* 81, 033827(1)-033837(8); "Analytical solutions for a two-level system driven by a class of chirped pulses" by P. K. Jha and Y. V. Rostovtsev, 2010. *Phys. Rev. A* 82, 015801(1)-015801(4); "Coherent control of atomic excitation using off-resonant strong few-cycle pulses" by P. K. Jha, H. Eleuch and Y. V. Rostovtsev, 2010. *Phys. Rev. A* 84, 045805(1)-045805(4), Copyright [2010] by American Physical Society

theory and the adiabatic approximation[42, 43].

Recently, the topic has been in a focus of research related to generation of short wavelength radiation[26, 44]. A two-level atomic system under the action of a far-off resonance strong pulse of laser radiation has been considered and it has been shown that such pulses can excite remarkable coherence on high frequency far-detuned transitions; and this coherence can be used for efficient generation of UV and soft X-ray (XUV) radiation[44].

To describe excited coherence, we are interested to understand the mechanism of breaking adiabaticity that leads to excited coherence in the system when the laser pulse has already passed. Thus we are interested going beyond classical electrodynamics[45]. Indeed, an electric field causes polarization of dielectrics is given by

$$P(t,r) = \int_{-\infty}^{t} dt' \chi(t-t') \mathcal{E}(t',r), \tag{3.1}$$

where $\chi(\tau)$ is the dielectric response function. It is important to note that once the field is removed, the polarization adiabatically returns to practically zero. Breaking of adiabaticity is especially difficult when the frequency of the applied field is far from the atomic resonance. Finding exact analytical solutions for such a problem will not only supplement numerical simulations but will also be useful in understanding the underlying physics.

In this chapter, using a proper variable transformation, we find a class of pulse $\Omega(t)$ for which the Schr$\ddot{o}$dinger equation for the time evolution of the state amplitudes can be transformed into the well known Heun equation[46, 47]. The solutions are given in terms of the Heun function which is a generalization of the Hypergeometric function. Using the degeneracy of Heun to Hypergeometric equation, Bambini-Berman model can be generalized to this model. Later we introduce a phase jump in the pulse and study its effect on the population transfer and coherence generated in TLS system.

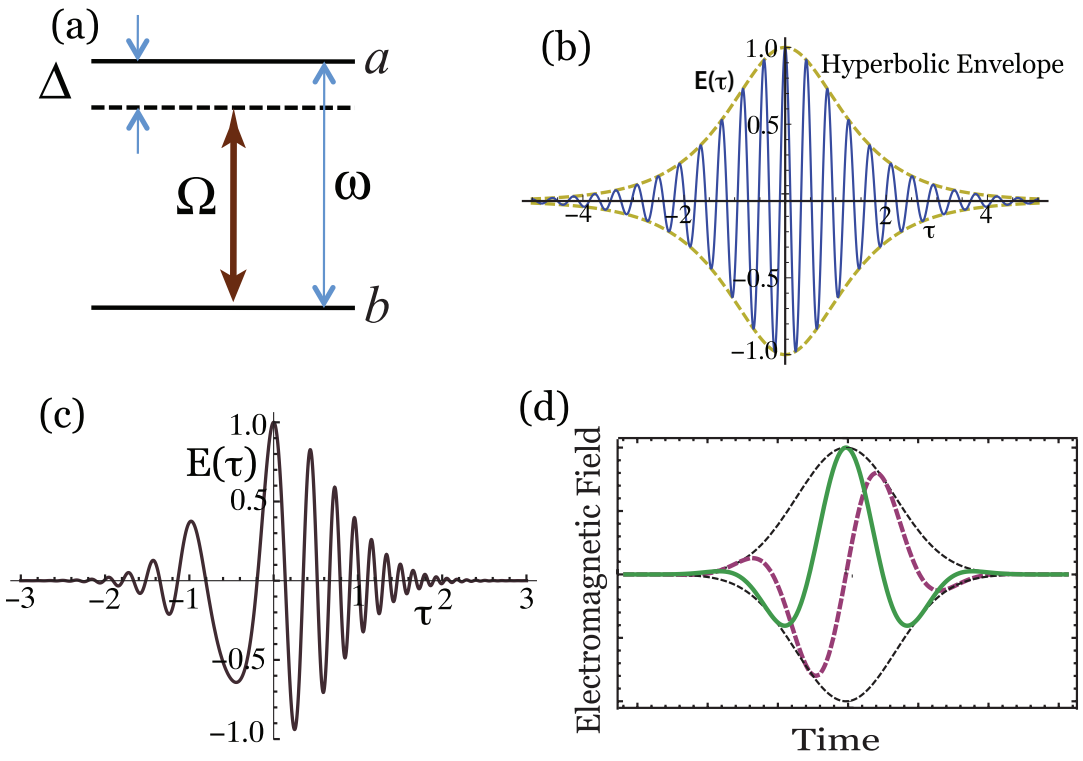

Fig. 7. (a) Two-level atomic system, atomic transition frequency $\omega = \omega_a - \omega_b$, detuning $\Delta = \omega - \nu$ and Rabi frequency $\Omega(t) = \wp\mathcal{E}(t)/2\hbar$. (b) Unchirped classical electromagnetic field E(t)= sech(αt)cos(νt). (c) Quadratic chirped electric field E(t)=$\exp(-\alpha^2 t^2)\cos(\nu t + \kappa t^2)$. (d) Few-cycle sine (dashed line) and cosine (solid line) pulse with Gaussian envelope.

B. Multi-Pulse Excitation

The equation of motion for the probability amplitudes for the states a and b [see Fig. 7(a)] of a Two Level Atom (TLA) interacting with a classical field is given as

$$\dot{C}_a = i\frac{\wp\mathcal{E}(t)}{\hbar}\cos(\nu t)e^{i\omega t}C_b, \tag{3.2a}$$

$$\dot{C}_b = i\frac{\wp^*\mathcal{E}(t)}{\hbar}\cos(\nu t)e^{-i\omega t}C_a, \tag{3.2b}$$

where $\hbar\omega$ is the energy difference between two levels, $\wp$ is the atomic dipole moment; $E(t) = \mathcal{E}(t)\cos\nu t$ [see Fig. 7(b)]. In the Rotating Wave Approximation (RWA) we replace

$\cos(\nu t)e^{\pm i\omega t} \rightarrow e^{\pm i\Delta}/2$ where $\Delta = \omega - \nu$[1], is detuning from resonance. Introducing $\Omega(t) = \wp\mathcal{E}(t)/2\hbar^2$, Eq.(3.2) reduces to

$$\dot{C}_a = i\Omega(t)e^{i\Delta t}C_b, \tag{3.3a}$$

$$\dot{C}_b = i\Omega^*(t)e^{-i\Delta t}C_a, \tag{3.3b}$$

which have an integral of motion $|C_a|^2 + |C_b|^2 = 1$[3]. There are a variety of ways to approach the problem of solving for $C_a(t)$. One method is to define $f(t) = C_a(t)/C_b(t)$. For the function $f(t)$, Eq.(3.3) yields the following Riccati Equation[44]

$$\dot{f} + i\Omega^*(t)e^{-i\Delta t}f^2 - i\Omega(t)e^{i\Delta t} = 0. \tag{3.4}$$

Then $|C_a(t| = |f(t)|/\sqrt{1 + |f(t)|^2}$. Alternatively, we can get a second order linear differential equation for $C_a(t)$, from Eq.(3.3)

$$\ddot{C}_a(t) - \left[i\Delta + \frac{\dot{\Omega}}{\Omega}\right]\dot{C}_a(t) + |\Omega|^2 C_a(t) = 0. \tag{3.5}$$

The general solution for Eq(3.5) has not been found yet, however there are solutions for several cases in terms of special functions. To find a solution for Eq.(3.5) we introduce a new variable

$$\varphi = \varphi(\tau), \tag{3.6}$$

---

[1]Here we use the convention that all frequencies are circular frequencies so that $\hbar\nu$ (not $h\nu$) is the photon energy.

[2]In this section we have defined the Rabi frequency $\Omega(t) = \wp\mathcal{E}(t)/2\hbar$ rather than the usual definition $\Omega(t) = \wp\mathcal{E}(t)/\hbar$.

[3]Here we consider a two-level atom with stable levels (or neglect any kinds of decay due to spontaneous emission, collision etc on the time scale of the pulse) interacting with a classical external electromagnetic field

subject to the condition that $\varphi(\tau)$ is real, positive and monotonic function of τ and $\varphi_0 \leq \varphi \leq \varphi_1$. In terms of the variable φ and the dimensionless parameters

$$\tau = \alpha t, \quad \beta = \frac{\Delta}{\alpha}, \quad \gamma = \frac{\Omega_0}{\alpha}, \tag{3.7}$$

one may write Eq.(3.5), for real $\xi(\tau)$ in the form

$$C_a^{''} + \left[\frac{\ddot{\varphi}/\dot{\varphi} - i\beta - \dot{\xi}/\xi}{\dot{\varphi}}\right] C_a^{'} + \frac{\gamma^2\xi^2}{\dot{\varphi}^2} C_a = 0, \tag{3.8}$$

where a prime indicates differentiation with respect to φ and $\Omega(\tau) = \gamma\xi(\tau)$. Let us determine the condition under which Eq.(3.8) has the form

$$C_a^{''}(\varphi) + P(\varphi)C_a^{'}(\varphi) + Q(\varphi)C_a(\varphi) = 0. \tag{3.9}$$

Using Eq.(3.8,3.9) and some trivial algebra we get,

$$\tau = -\frac{1}{i\beta}\int \left(P + \frac{Q^{'}}{2Q}\right) d\varphi. \tag{3.10}$$

1. Heun Equation

Bambini-Berman studied the case in which Eq.(3.9) has the form of a Gauss Hypergeometric equation which includes Rosen-Zener Model as a special case. Now let us consider when Eq.(3.9) is of the form of Heun equation[4][46, 47] with the independent variable φ.

$$\frac{d^2C_a}{d\varphi^2} + \left(\frac{u}{\varphi} + \frac{v}{\varphi - 1} + \frac{w}{\varphi - c}\right)\frac{dC_a}{d\varphi} + \frac{(ab\varphi - q)C_a}{\varphi(\varphi - 1)(\varphi - c)} = 0, \tag{3.11}$$

[4]Heun Equation: For real $\Omega(\tau)$, we get an additional constraint for our asymmetric parameters $q < 0, ab/q < 1$, if $q \neq 0$, or $ab > 0$, if $q = 0$. Confluent Heun Equation: $q < 0, p/q > -1$, if $q \neq 0$, or $p < 0$, if $q = 0$.

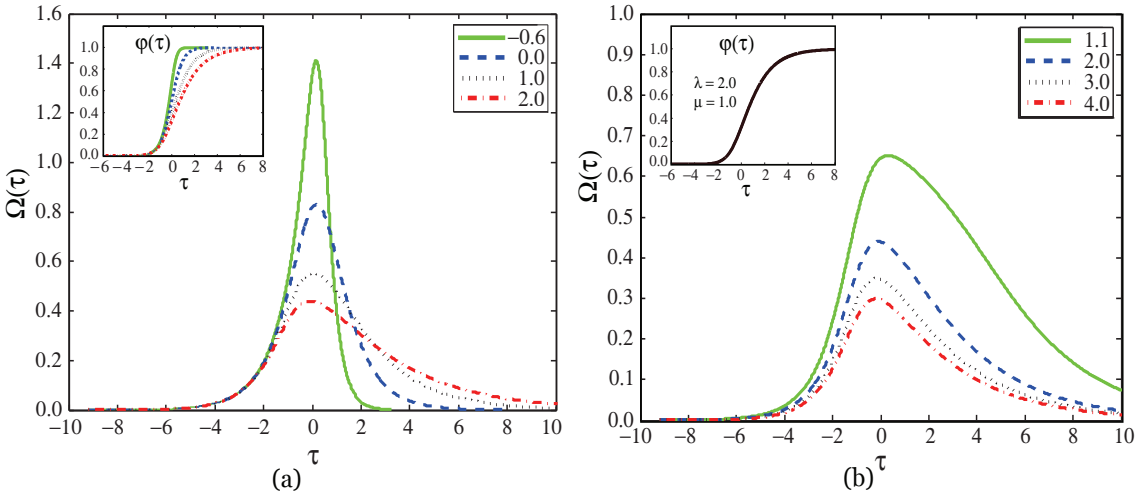

Fig. 8. Pulse shapes given by Eq.(3.17). (a) Pulse shapes with varying λ and $c = 2, q = -1, ab = 0$. (b) Pulse shapes with varying c and $\lambda = 2, q = -1, ab = 0$.

where *a,b,c,q,u,v,w* are parameters with $c \neq 0, 1.(c > 1)$. The parameters are constrained, by the general theory of Fuchsian equations, as

$$u + v + w = a + b + 1. \tag{3.12}$$

From Eq.(3.11) and Eq.(3.9) and some algebra we get

$$\dot{\varphi} = 2\varphi(1 - \varphi)/(\mu + \lambda\varphi). \tag{3.13}$$

Equivalently the parameters of the Heun Equation Eq.(3.11) are given as

$$u = \frac{1}{2} - \frac{i\beta\mu}{2}, \quad v = \frac{1}{2} + \frac{i\beta(\lambda + \mu)}{2}, \quad w = \frac{1}{2}, \quad a = 0, \quad b = \frac{1}{2} - \frac{i\beta\lambda}{2}. \tag{3.14}$$

For $\varphi(\tau)$ to be a monotonically increasing function of τ, $\dot{\varphi}$ must be real and positive i.e $\mu > 0, \lambda/\mu > -1$. The time variable τ as a function of φ is obtained by integrating Eq.(3.13) which gives,

$$2\tau = \ln[\varphi^{\mu}/(1 - \varphi)^{\mu+\lambda}]. \tag{3.15}$$

The general solution for Eq.(3.11), which has regular singularity at $\varphi = 0$ is given in terms

of the Heun local solutions, H$l(\varphi)$ as,

$$C_a = \mathrm{P}_1\varphi^{1-u}\mathrm{H}l[c, q+(1-u)((c-1)v+a+b-u+1); \\ a-u+1, b-u+1, 2-u, v; \varphi] + \mathrm{P}_2\mathrm{H}l\left[c, q; a, b, u, v; \varphi\right], \tag{3.16}$$

where the constants, $\mathrm{P}_1, \mathrm{P}_2$ can be found using the initial conditions of the system. In the limit $\tau \to \infty$, the population left in the level a can be obtained by substituting $\varphi \to 1$ in Eq.(3.16). The form of the pulse can be obtained by equating Eq.(3.8) and Eq.(3.11) which gives

$$\Omega(\tau) = \left[\frac{4\varphi(1-\varphi)(ab\varphi - q)}{(c-\varphi)}\right]^{1/2}\left(\frac{1}{\mu+\lambda\varphi}\right), \tag{3.17}$$

where $\varphi(\tau)$ is given by Eq.(3.15). In Fig. 8 we have plotted the pulse envelopes' of the classical field, given by Eq.(3.17), for which the two-level atom problem can be exactly solved. They also show the effect of the asymmetric parameters λ and ab respectively, for $\mu = 1$, on the symmetry of the shapes. Pulse shapes showing the effects of other parameters can also be plotted easily from Eq(3.17).

There are three kinds of solutions to the Heun equation Eq.(3.11). Local Solutions Hl, Heun functions Hf and Heun Polynomials Hp[48, 49, 50]. The series solution Eq.(3.16) is written as[47]

$$\mathrm{H}l\left[c, q; a, b, u, v; \varphi\right] = \sum_{j=0}^{\infty} s_j\varphi^j = 1 + \frac{q}{uc}\varphi + \sum_{j=2}^{\infty} s_j\varphi^j, \tag{3.18}$$

where s_j obeys the three term recursion relation

$$(j-1+a)(j-1+b)s_{j-1} - \{j[(j-1+u)(1+c)+vc \\ +a+b+1-u-v]+q\}s_j + (j+1)(j+u)s_{j+1} = 0, \tag{3.19}$$

with the initial conditions

$$s_0 = 1, \quad s_1 = \frac{q}{uc}, \quad \text{and} \quad s_j = 0, \quad \text{if} \quad j < 0. \tag{3.20}$$

The solution Eq.(3.18) is valid only within a circle centered at the origin $\varphi = 0$ whose radius is the distance from the origin to the nearest singularity $\varphi = 1$ or $\varphi = c$. For $c > 1$, the radius of convergence is 1[47]. From Eq.(3.19), we can say that Heun function remains the same with the exchange of the parameters a and b. It can be easily verified that the Heun equation Eq.(3.11) can be reduced to the Hypergeometric equation in several ways[47]. They are

$$c = 1, \quad q = ab, \tag{3.21a}$$

$$w = 0, \quad q = cab, \tag{3.21b}$$

$$c = 0, \quad q = 0. \tag{3.21c}$$

Let us now consider the simplest case of $c = 0, q = 0$. Then for $a + b = 0$ and $1/2 - v = -i\beta/2$, Eq.(3.11) reduces to standard form of the Gauss Hypergeometric equation

$$\frac{d^2C_a}{d\varphi^2} + \left[\frac{r - (1 + a + b)\varphi}{\varphi(1 - \varphi)}\right]\frac{dC_a}{d\varphi} - \frac{abC_a}{\varphi(1 - \varphi)} = 0. \tag{3.22}$$

where $r = 1/2 - i\beta/2$. The general solution for Eq.(3.22) is

$$C_a(\varphi) = \mathrm{P}_1\varphi^{1-r}\mathrm{F}[b - r + 1, a - r + 1; 2 - r; \varphi] + \mathrm{P}_2\mathrm{F}[a, b; r; \varphi], \tag{3.23}$$

where the constants, $\mathrm{P}_1, \mathrm{P}_2$ can be found using the initial conditions of the problem. We write the hypergeometric series $\mathrm{F}_{(2,1)}[a, b; c; \varphi]$ as $\mathrm{F}[a, b; c; \varphi]$. The population left in the state a is given as

$$C_{af} = \mathrm{P}_1\mathrm{F}[b - r + 1, a - r + 1; 2 - r; 1] + \mathrm{P}_2\mathrm{F}[a, b; r; 1]. \tag{3.24}$$

Subsequently if $(a+b) = \lambda i\beta$ and $v - 1/2 - (a+b) = \mu i\beta$, we have the generalized Rosen-Zener Model as discussed by Bambini and Berman. One can summarize the degeneracy of

the Heun to Hypergeometric model as follows

$$\mathrm{H}l\,[1, ab; a, b, u, v; \varphi] = \mathrm{F}[a, b; u; \varphi], \tag{3.25a}$$

$$\mathrm{H}l\,[c, cab; a, b, u, a + b - u + 1; \varphi] = \mathrm{F}[a, b; u; \varphi], \tag{3.25b}$$

$$\mathrm{H}l\,[0, 0; a, b, u, v; \varphi] = \mathrm{F}[a, b; a + b - v + 1; \varphi]. \tag{3.25c}$$

2. Confluent Heun Equation

The Confluent Heun Equation is one of the four confluent forms of Heun's equation which is obtained by merging the singularity at $\varphi = c$ that at $\varphi = \infty$. Now we have a regular singularity at $\varphi = 0, 1$ and an irregular singularity at $\varphi = \infty$. In this paper we will consider the following non-symmetrical form of the Confluent Heun equation:

$$\frac{d^2C_a}{d\varphi^2} + \left(\frac{u}{\varphi} + \frac{v}{\varphi - 1}\right)\frac{dC_a}{d\varphi} + \frac{p\varphi + q}{\varphi(\varphi - 1)}C_a = 0. \tag{3.26}$$

Similar to the Heun case, we have the same differential equation for $\dot{\varphi}$ i.e Eq(3.13). For the Confluent Heun Equation, the possible values of the asymmetric parameters are

$$u = \frac{1}{2} - \frac{i\beta\mu}{2}, \quad v = \frac{i\beta(\lambda + \mu)}{2}, \quad p = -q, \tag{3.27a}$$

$$u = \frac{1}{2} - \frac{i\beta\mu}{2}, \quad v = \frac{1}{2} + \frac{i\beta(\lambda + \mu)}{2}, \quad p = 0. \tag{3.27b}$$

The general solution of the Confluent Heun Equation Eq.(3.26) is given as

$$\begin{aligned} C_a(\varphi) =& \mathrm{P}_1\mathrm{H}l^{(c)}[0, u - 1, v - 1, p, q + (1 - uv)/2, \varphi] + \\ & \mathrm{P}_2\varphi^{1-u}\mathrm{H}l^{(c)}[0, 1 - u, v - 1, p, q + (1 - uv)/2, \varphi], \end{aligned} \tag{3.28}$$

where P_1, P_2 can be found using the initial condition of the system. It is worth mentioning here that, the general solution to the Gauss Hypergeometric differential equation Eq.(3.22)

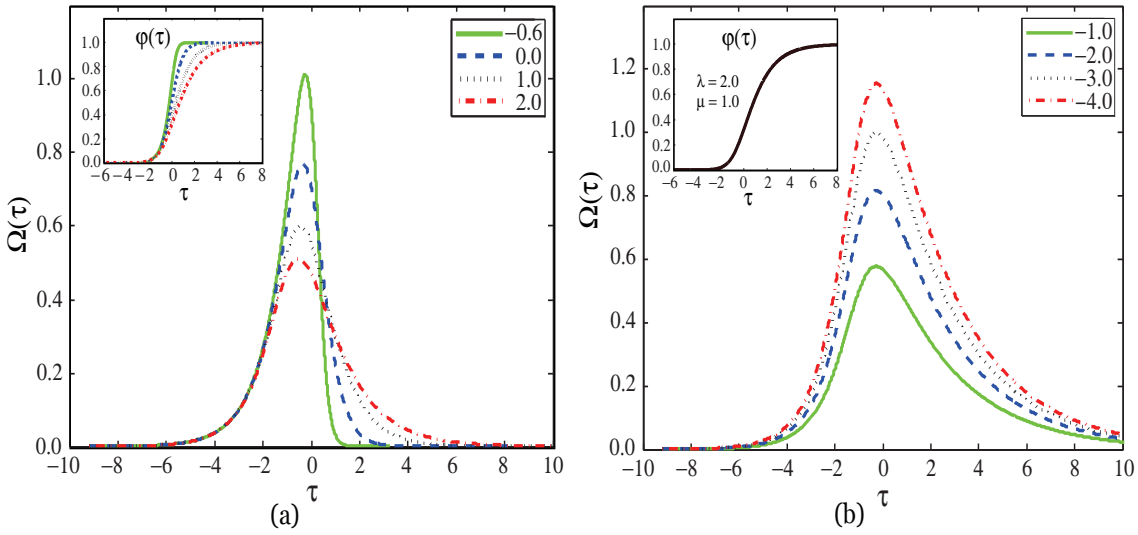

Fig. 9. Pulse shapes given by Eq.(3.30). (a) Pulse shapes with varying λ and $p = -q = 1$. (b) Pulse shapes with varying q and $\lambda = 2, p = 0$.

can be expressed in terms of the Heun functions $\mathrm{H}l^{(c)}$ as

$$C_a(\varphi) = \mathrm{P}_1(\varphi-1)^{-a}\mathrm{H}l^{(c)}[0, a-b, -1+r, 0, ((r-2a)b - r + ra + 1)/2, 1/(1-\varphi)] + \mathrm{P}_2(\varphi-1)^{-b}\mathrm{H}l^{(c)}[0, b-a, -1+r, 0, ((r-2a)b - r + ra + 1)/2, 1/(1-\varphi)]. \tag{3.29}$$

The form of the pulse can be obtained by equating Eq.(3.8) and Eq.(3.26) which gives,

$$\Omega(\varphi) = \frac{[4\varphi(\varphi-1)(p\varphi+q)]^{1/2}}{\mu + \lambda\varphi}, \tag{3.30}$$

where $\varphi(\tau)$ is given by Eq.(3.15). The constraint of λ and μ is also the same as for the Heun case discussed earlier. Fig. 9 shows the pulse shapes for which the two-level atom can be reduced to the Confluent Heun equation. It also qualitatively shows the effect of the asymmetric parameters p and q on the symmetry of the pulse shapes. $\lambda = 0$ corresponds to the symmetric pulse.

3. Exactly Solvable Pulse Shapes

In this section we will consider some specific examples of pulses corresponding to Heun and Confluent Heun equations. Interestingly we will also find a better approximation for a box pulse by introducing a parameter δ which takes care of non-analyticity of the pulse at the edges.

$$\Omega_\delta(t) = \Omega_0 \text{sech}(\alpha t)/\sqrt{\delta - \tanh(\alpha t)}, \quad \delta > 1$$

For this pulse, using the scaling parameters Eq.(3.7), Eq.(3.5) gives

$$\ddot{C}_a(\tau) - \left[i\beta + \frac{1}{2}\left(\frac{1 - 2\delta\tanh\tau + \tanh^2\tau}{\delta - \tanh\tau}\right)\right]\dot{C}_a(\tau) + \frac{\gamma^2 \text{sech}^2\tau}{\delta - \tanh\tau} C_a(\tau) = 0. \tag{3.31}$$

Let us now define a new variable as

$$\varphi(\tau) = \frac{1 + \tanh\tau}{2}. \tag{3.32}$$

In terms of the variable φ, Eq.(3.31) reduces to the Heun equation

$$C_a'' + \left[\frac{u}{\varphi} + \frac{v}{\varphi - 1} + \frac{w}{\varphi - c}\right] C_a' + \frac{ab\varphi - q}{\varphi(\varphi - 1)(\varphi - c)} C_a = 0, \tag{3.33}$$

where,

$$u = \frac{1}{2} - \frac{i\beta}{2}, \quad v = \frac{1}{2} + \frac{i\beta}{2}, \quad w = \frac{1}{2}, \tag{3.34a}$$

$$q = -\frac{\gamma^2}{2}, \quad a = 0, \quad b = \frac{1}{2} \quad c = \frac{\delta + 1}{2}. \tag{3.34b}$$

From Eq.(3.31) we see as $\tau \to -\infty$, $\varphi \to 0$ and $\tau \to \infty$, $\varphi \to 1$. The initial conditions for our system are

$$C_a(\tau \to -\infty) = 0, \quad |C_b(\tau \to -\infty)| = 1. \tag{3.35}$$

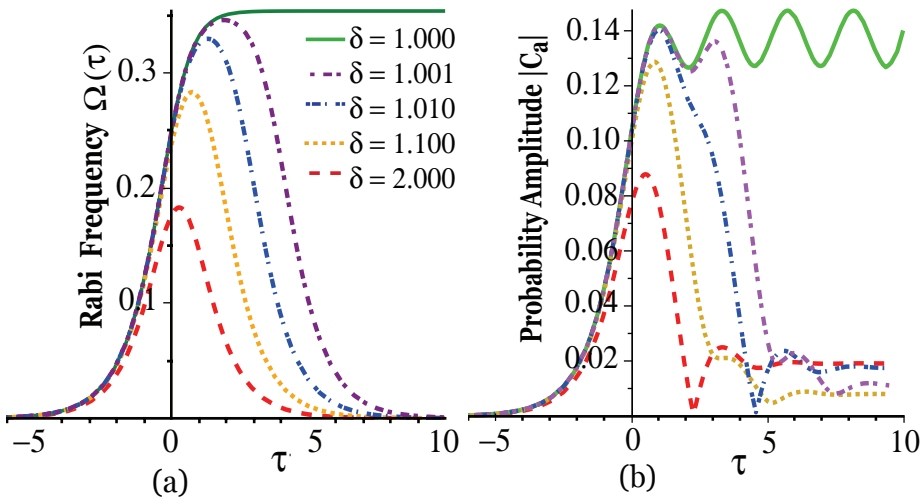

Fig. 10. (a) Pulse shapes for different value of δ. (b) The time dependence of the population in the state a for $\Omega_\delta(\tau)$ pulse for different values of $\delta > 1$. For calculation we take $\alpha = 0.08\omega_c$, varying δ.

The complete solution to Eq.(3.33), satisfying the initial conditions Eq(3.35), is

$$C_a(\varphi) = \frac{\gamma\sqrt{2}}{(i-b)\sqrt{c}}\varphi^{1-u}\mathrm{H}l[c, q+(1-u)((c-1)v + a + b - u + 1); b-u+1, a-u+1, 2-u, v, \varphi]. \tag{3.36}$$

where a, b, c, q, u, v, w are given be Eq.(3.34). Let now consider a case in which $\delta = 1$. So the pulse has the form

$$\Omega_1(t) = \Omega_0\sqrt{1+\tanh\alpha t}. \tag{3.37}$$

Now for this pulse, using the scaling parameters Eq.(3.7), Eq.(3.5) gives

$$\ddot{C}_a(\tau) - \left[i\beta + \frac{1}{2}(1-\tanh\tau)\right]\dot{C}_a(\tau) + \gamma^2(1+\tanh\tau)C_a(\tau) = 0. \tag{3.38}$$

In terms of the variable φ, Eq.(3.38) reduces to

$$C_a'' + \left[\frac{u}{\varphi} + \frac{v}{\varphi-1}\right]C_a' + \frac{q}{\varphi(\varphi-1)^2}C_a = 0, \tag{3.39}$$

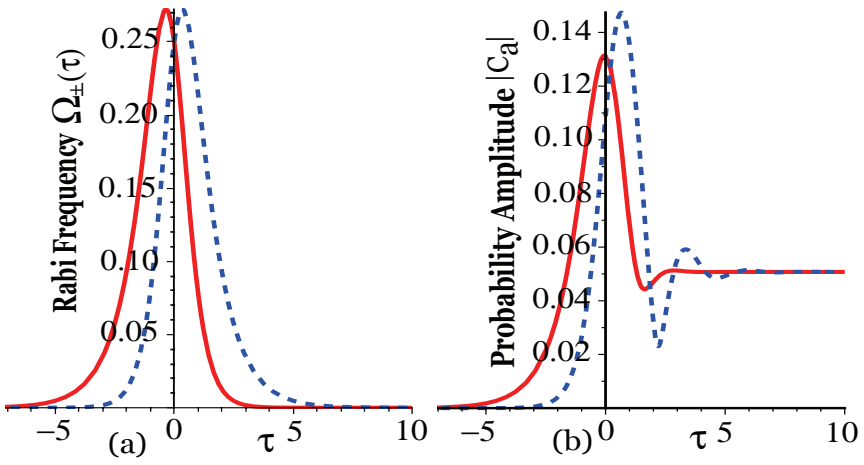

Fig. 11. (a) Pulse shapes for $\Omega_{\pm}(t) = \Omega_0 \text{sech}\alpha t(\sqrt{1 \pm \tanh\alpha t})$. (b) Time dependence of population in the state a for the Pulse shapes in (a). In calculation we take $\Omega_0 = 0.02\omega_c, \alpha = 0.08\omega_c, \Delta = 0.2\omega_c$

where,

$$u = \frac{1}{2} - \frac{i\beta}{2}, \quad v = 1 + \frac{i\beta}{2}, \quad q = \frac{\gamma^2}{2}. \tag{3.40}$$

The general solution to Eq.(3.39) is

$$\begin{aligned} C_a(\varphi) =& \mathrm{P}_1(\varphi - 1)^{\xi}\mathrm{F}[\xi, \xi - 1 + u + v; u; \varphi] + \\ & \mathrm{P}_2\varphi^{1-u}(\varphi - 1)^{\xi}\mathrm{F}[\xi + v, \xi + 1 - u; 2 - u; \varphi], \end{aligned} \tag{3.41}$$

where,

$$\xi = \frac{1 - v}{2} + \sqrt{\left(\frac{1 - v}{2}\right)^2 - q}, \tag{3.42}$$

and q, u, v are given be Eq.(3.40). Using the initial conditions Eq.(3.35) we get $P_1 = 0$ and

$$\mathrm{P}_2 = \frac{\gamma}{\sqrt{2}(u - 1)(-1)^{(\xi+1/2)}}. \tag{3.43}$$

Figure 10 shows the plot of population in the state a corresponding to the pulse Ω_δ satisfying the initial condition.

$$\Omega_+(t) = \Omega_0 \text{sech}\alpha t(\sqrt{1 + \tanh\alpha t})$$

For this pulse, using the scaling parameters Eq.(3.7), Eq.(3.5) gives

$$\ddot{C}_a(\tau) - \left[i\beta + \frac{1}{2}(1 - 3\text{tanh}\tau)\right]\dot{C}_a(\tau) + \gamma^2\text{sech}^2\tau(1 + \text{tanh}\tau)C_a(\tau) = 0. \tag{3.44}$$

In terms of the new variable φ, Eq.(3.44) reduces to the Confluent Heun equation.

$$C_a'' + \left[\frac{u}{\varphi} + \frac{v}{\varphi - 1}\right]C_a' + \frac{\sigma}{\varphi - 1}C_a = 0, \tag{3.45}$$

where,

$$u = -\frac{i\beta}{2}, \quad v = \frac{1}{2} + \frac{i\beta}{2}, \quad \sigma = -2\gamma^2. \tag{3.46}$$

The complete solution to Eq.(3.45) satisfying the initial conditions Eq.(3.35) is

$$C_a(\varphi) = \left(\frac{2\sqrt{2}\gamma}{2i - \beta}\right)\varphi^{1+\frac{i\beta}{2}}\text{H}l^{(c)}[0, 1 + i\beta/2, -1/2 + i\beta/2, -2\gamma^2, 1/2 - \beta^2/8 - i\beta/8, \varphi]. \tag{3.47}$$

$$\Omega_-(t) = \Omega_0\text{sech}\alpha t(\sqrt{1 - \text{tanh}\alpha t})$$

For this pulse, using the scaling transformation Eq.(3.7), Eq.(3.5) gives

$$\ddot{C}_a(\tau) - \left[i\beta - \frac{1}{2}(1 + 3\text{tanh}\tau)\right]\dot{C}_a(\tau) + \gamma^2\text{sech}^2\tau(1 - \text{tanh}\tau)C_a(\tau) = 0. \tag{3.48}$$

In terms of the new variable φ, Eq.(3.48) reduces to the Confluent Heun equation.

$$C_a'' + \left[\frac{u}{\varphi} + \frac{v}{\varphi - 1}\right]C_a' + \frac{\eta}{\varphi}C_a = 0, \tag{3.49}$$

where,

$$u = \frac{1}{2} - \frac{i\beta}{2}, \quad v = \frac{i\beta}{2}, \quad \eta = 2\gamma^2. \tag{3.50}$$

The complete solution to Eq.(3.49), satisfying the initial conditions Eq.(3.35), is

$$C_a(\varphi) = \left(\frac{2\sqrt{2}\gamma}{\beta - i}\right)\varphi^{\frac{1}{2}+\frac{i\beta}{2}}\text{H}l^{(c)}[0, 1/2 + i\beta/2, -1 + i\beta/2, 2\gamma^2, 1/2 - 2\gamma^2 - \beta^2/8 - i\beta/8, \varphi]. \tag{3.51}$$

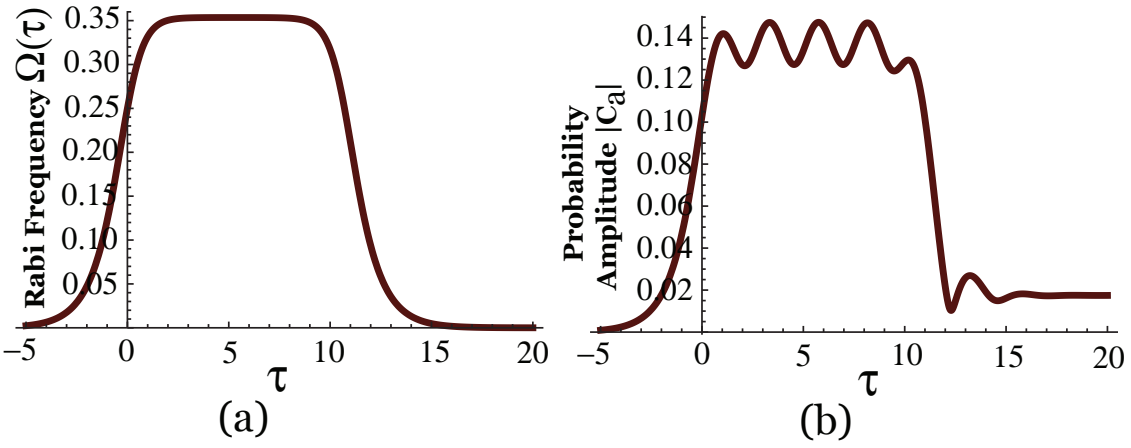

Fig. 12. (a) Box Pulse for $\delta - 1 = 10^{-9}$. (b) Time dependence of population in the state a for the Box Pulse $\Omega_\delta(\tau)$. In calculation we take $\Omega_0 = 0.02\omega_c, \alpha = 0.08\omega_c, \Delta = 0.2\omega_c$

In Fig. 11 we have plotted the pulse shapes $\Omega_\pm(\tau)$ and the corresponding time evolution of the probability amplitude for state a. One of the simplest and exactly solvable pulse shapes is a Box Pulse. Indeed it is a non-analytical pulse but it gives information about the basic oscillatory nature of solution (probability amplitude). Let us define our pulse as

$$\Omega(t) = \Omega_0 \Theta(t)\Theta(t_0 - t), \quad t_0 > 0, \tag{3.52}$$

where, $\Theta(t)$ is a unit step function. The solution for Eq.(3.5) corresponding to the box pulse is

$$C_a(t) = \frac{i\Omega_0}{\sqrt{\Delta^2/4 + \Omega_0^2}} e^{i(\Delta/2)t} \text{sin}(\sqrt{\Delta^2/4 + \Omega_0^2})t, \quad t < t_0. \tag{3.53}$$

The oscillatory nature of the solution $|C(t)|$ is evident from the sine function. Let us consider the pulse shape of the form

$$\Omega_\delta(t) = \frac{\Omega_0 \text{sech}\alpha t}{\sqrt{\delta - \text{tanh}\alpha t}}, \quad \delta = 2c - 1. \tag{3.54}$$

where c is one of the singularities of the Heun Equation. Assuming $c > 1$ gives $\delta > 1$. A pulse shape of the form Eq.(3.54) is positive definite and it vanishes at $\tau = \pm\infty$. Let us see

what happens when δ approaches but never reaches to 1. We see from Figs. 10(a) and 12(a), that as δ approaches to 1, the pulse become more and more broad there by making it a better approximation for a box pulse (taking care of non-analyticity at the edges). The general solution for the pulse of the form Eq.(3.54), is given by Eq.(3.16) where the asymmetric parameters are given by Eq.(3.34).

C. Multi-Cycle Chirped Pulse Excitation

It is well know that the chirped pulses [51, 52] are used to produce maximal coherence in atomic and molecular systems. Maximal coherence can be used for generation of short-wavelength of radiation molecular spectroscopy, for example, time-resolved coherent Raman spectroscopy, to obtain molecule-specific signals from molecules, which can serve as a marker molecule for bacterial spores [51].

In this section we will present two class of chirped pulses for which the problem can be solved exactly in analytical form. Using the appropriate chirping parameters, the population transfer, after the the pulse is gone, can be optimized and for the pulse considered here, four-order of magnitudes enhancement was obtained. Unchirped pulse corresponding to Heun and Confluent Heun equation has been recently investigated extensively [53] where we have included an estimate of energy of emission of soft x-ray and ultraviolet radiation via excited quantum coherence in the atomic system. The estimate shows good potential for a source of coherent radiation based on the discussed mechanism.

The equation of motion for the probability amplitudes for the states a and b of a TLA interacting with a classical field (under rotating-wave approximation RWA) with non-zero

chirping [54]. is given as

$$\dot{C}_a = i\Omega(t)e^{i\vartheta(t)}C_b, \tag{3.55a}$$

$$\dot{C}_b = i\Omega^*(t)e^{-i\vartheta(t)}C_a, \tag{3.55b}$$

where $\vartheta(t) = \Delta t + \phi(t)$. Here $\Delta = \omega - \nu$ and $\Omega(t) = \wp\mathcal{E}(t)/2\hbar$. To solve for C_a, we can get a second order linear differential equation for $C_a(t)$ from Eq.(3.55), which in terms of the dimensionless parameters Eq.(3.8) is given as

$$\ddot{C}_a - \left[i\beta + \frac{\dot{\Omega}(\tau)}{\Omega(\tau)} + i\dot{\phi}(\tau)\right]\dot{C}_a + \Omega^2(\tau)C_a = 0. \tag{3.56}$$

In order to find analytical solution for Eq.(3.56), We introduce a new variable $\varphi = \varphi(\tau)$ defined by

$$\tau = (1/2)\ln[\varphi^{\mu}/(1-\varphi)^{\mu+\lambda}], \tag{3.57}$$

and make an ansatz for the pulse envelope $\Omega(\tau)$ and the chirping function $\phi(\tau)$ as

$$\Omega(\tau) = \left[\frac{2\varphi(1-\varphi)}{(c-\varphi)}\right]^{1/2}\left(\frac{\gamma}{\mu+\lambda\varphi}\right), \tag{3.58a}$$

$$\dot{\phi}(\tau) = \left\{\frac{-2c\,\zeta + 2[(\zeta+\xi) + c(\zeta+\eta)]\varphi}{(\varphi-c)(\mu+\lambda\varphi)}\right\}. \tag{3.58b}$$

In terms of the variable $\varphi(\tau)$ and the definition of $\Omega(\tau), \dot{\phi}(\tau)$ from Eq.(3.58), Eq.(3.56) takes the form

$$C_a'' + \left[\frac{\rho}{\varphi} + \frac{\sigma}{\varphi-1} + \frac{\upsilon}{\varphi-c}\right]C_a' + \frac{ab\varphi - q}{\varphi(\varphi-1)(\varphi-c)}C_a = 0, \tag{3.59}$$

where $(c > 1)$ and

$$\begin{aligned} &\rho = \frac{1}{2} - i\left(\zeta + \frac{\beta\mu}{2}\right),\ \sigma = \frac{1}{2} + i\left[\frac{\beta(\mu+\lambda)}{2} - \eta\right], \\ &\upsilon = \frac{1}{2} - i\xi,\ q = -\frac{\gamma^2}{2},\ a = 0,\ b = \frac{1}{2} + \frac{i\beta\lambda}{2},\ c = \frac{\delta+1}{2}. \end{aligned} \tag{3.60}$$

The parameters of a Heun Equation[46, 47] are constrained, by the general theory of

Fuschsian equations as, $\rho + \sigma + \upsilon = a + b + 1$ which provides us a the first constraint relation for the chirping parameters ζ, η, ξ as

$$\zeta + \eta + \xi = 0. \tag{3.61}$$

The quantity $\nu + \dot{\phi}$ is the instantaneous pulse frequency; thus $\dot{\phi}$ should vanish for maximum of $\Omega(\tau)$. From Eq.(3.58a), we get the corresponding φ_0 which satisfy the equation

$$\lambda\varphi^3 - (2\lambda + \mu)\varphi^2 + c(\lambda + 2\mu)\varphi - c\mu = 0. \tag{3.62}$$

Thus the second constraint relation for the chirping parameters is given as

$$\frac{-2c\,\zeta + 2[(\zeta + \xi) + c(\zeta + \eta)]\varphi_0}{(\varphi_0 - c)(\mu + \lambda\varphi_0)} = 0. \tag{3.63}$$

The general solution for Eq.(3.59), which has regular singularity at $\varphi = 0$ is given in terms of Heun local solutions, H$l(\varphi)$ as,

$$\begin{aligned} C_a(\varphi) = \mathrm{P}_1\varphi^{1-\rho}\mathrm{H}l[c, q + (1-\rho)((c-1)\sigma + a + b - \rho + 1); \\ a - \rho + 1, b - \rho + 1, 2 - \rho, \sigma; \varphi] + \mathrm{P}_2\,\mathrm{H}l\,[c, q; a, b, \rho, \sigma; \varphi]\,, \end{aligned} \tag{3.64}$$

where the constants, $\mathcal{P}_1, \mathcal{P}_2$ can be found using the initial conditions of the system. In the limit $\tau \to \infty$, the population left in the level a can be obtained by substituting $\varphi \to 1$ in Eq.(3.64). Let us consider a simple case of $\mu = 1, \lambda = 0$ in Eq.(3.57) and Eq.(3.58a) gives

$$\varphi(\tau) = \frac{1 + \tanh(\tau)}{2}, \tag{3.65a}$$

$$\Omega(\tau) = \gamma\left[\frac{2\varphi(1-\varphi)}{(c-\varphi)}\right]^{1/2}. \tag{3.65b}$$

From Eq(3.65) the pulse takes the form

$$\Omega(\tau) = \frac{\gamma\,\mathrm{sech}(\tau)}{\sqrt{\delta - \tanh(\tau)}}, \quad \delta = 2c - 1. \tag{3.66}$$

This pulse shape serves as an excellent model for a smooth box pulse, by taking care of

non-analyticity at its edges with the help of the pulse parameter δ. Using Eq.(3.62) we get $\varphi_0 = c \pm \sqrt{c^2 - c}$. From one of our earlier assumptions $c > 1$ only one of the possible values is allowed for φ_0 as $0 \leq \varphi_0 \leq 1$. Subsequently using $\varphi_0 = c - \sqrt{c^2 - c}$ in Eq.(3.63), we get the constraint equation as

$$\frac{\zeta - \eta}{\xi} = \delta - \sqrt{\delta^2 - 1}. \tag{3.67}$$

The defining equation for the chirping function takes the form

$$\phi(\tau) = \xi \left\{ \left(\delta - \sqrt{\delta^2 - 1} \right) \tau + \ln[\delta \cosh(\tau) - \sinh(\tau)] \right\}. \tag{3.68}$$

For the pulse defined by Eq.(3.66), using the scaling parameters Eq.(3.7) and the chirping function Eq.(3.68), Eq.(3.56) gives

$$\begin{aligned} \ddot{C}_a(\tau) - \Bigg[\frac{1}{2} \left(\frac{1 - 2\delta \tanh\tau + \tanh^2\tau}{\delta - \tanh\tau} \right) - i\xi \Big(\sqrt{\delta^2 - 1} \\ - \frac{\delta^2 - 1}{\delta - \tanh(\tau)} \Big) + i\beta \Bigg] \dot{C}_a(\tau) + \frac{\gamma^2 \operatorname{sech}^2\tau}{\delta - \tanh\tau} C_a(\tau) = 0. \end{aligned} \tag{3.69}$$

Let us define the initial conditions for our system as

$$C_a(\tau \to -\infty) = 0, \quad |C_b(\tau \to -\infty)| = 1. \tag{3.70}$$

Solution for Eq.(3.69), satisfying the initial conditions is give as

$$\begin{aligned} C_a(\varphi) = \mathrm{P}\varphi^{1-\rho} \mathrm{H}l[c, q + (1-\rho)((c-1)\sigma + a + \\ b - \rho + 1); a - \rho + 1, b - \rho + 1, 2 - \rho, \sigma; \varphi], \end{aligned} \tag{3.71}$$

where $\varphi(\tau)$ is given by Eq.(3.65a) and the Heun parameters as .

$$\begin{aligned} \rho = \frac{1}{2} - i \left(\zeta + \frac{\beta}{2} \right), \; \sigma = \frac{1}{2} + i \left[\frac{\beta}{2} - \eta \right], \\ \upsilon = \frac{1}{2} - i\xi, \; q = -\frac{\gamma^2}{2}, \; a = 0, \; b = \frac{1}{2}, \; c = \frac{\delta + 1}{2}. \end{aligned} \tag{3.72}$$

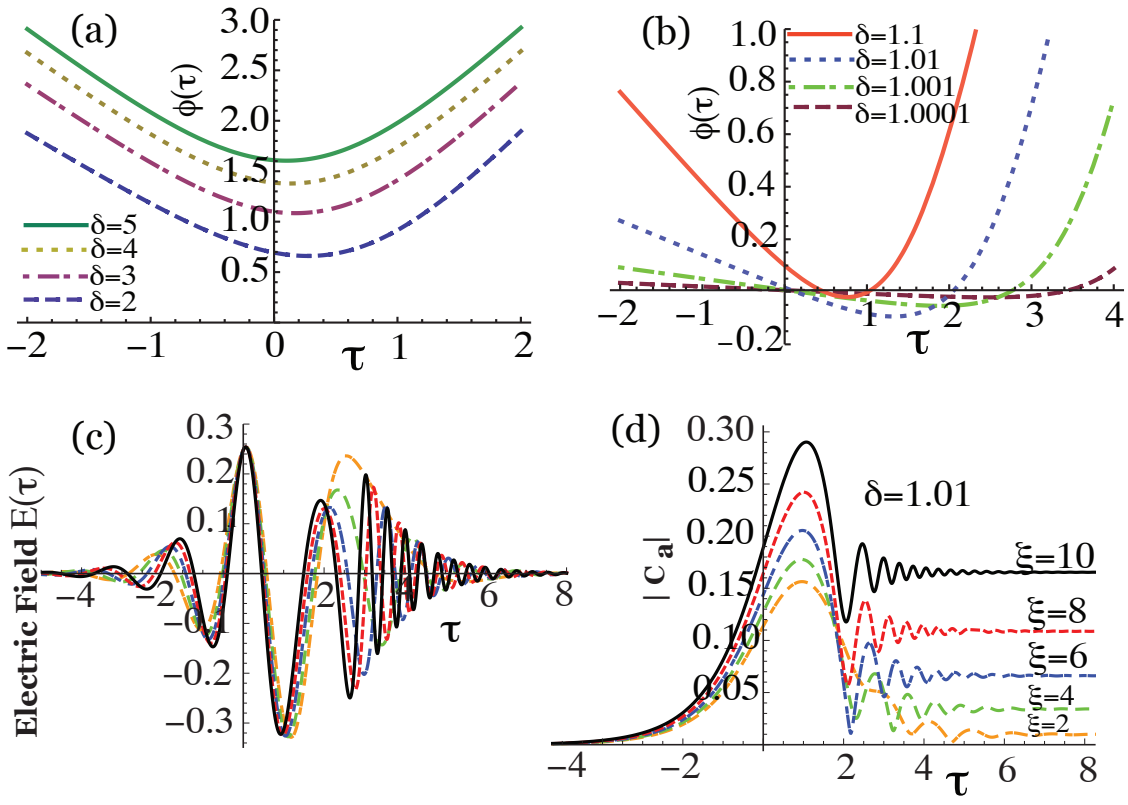

Fig. 13. (I) Heun Equation case: Chirping function $\phi(\tau)$ given by Eq.(3.68) for $\xi = 10$ and (a) $\delta > 1$, (b) $\delta \approx 1$ (c) The Electric field $\mathrm{E}(\tau)$ for varying ξ and $\delta = 1.01$. (d) Probability amplitudes for the upper level $|a\rangle$ for the corresponding fields in (c). $|C_a(\tau)|$ is given by Eq.(3.71).

The chirping parameters ζ, η and the constant P are given as

$$\zeta = -\frac{\xi}{2}\left(1 - \delta + \sqrt{\delta^2 - 1}\right), \tag{3.73a}$$

$$\eta = -\frac{\xi}{2}\left(1 + \delta - \sqrt{\delta^2 - 1}\right), \tag{3.73b}$$

$$\mathrm{P} = i\gamma\left[\frac{2^{(1-i\xi)}(1+\delta)^{i\xi-1/2}}{1 + i(2\zeta + \beta)}\right]. \tag{3.73c}$$

Here we have kept ξ as a free parameter for the chirping function $\phi(t)$. In Fig. 13, we have considered some forms of the chirping function $\phi(\tau)$ [see Figs. 13(a,b)] for $\delta > 1$ and $\delta \approx 1$ respectively, given by Eq.(3.68). Influence of chirping on the evolution of the

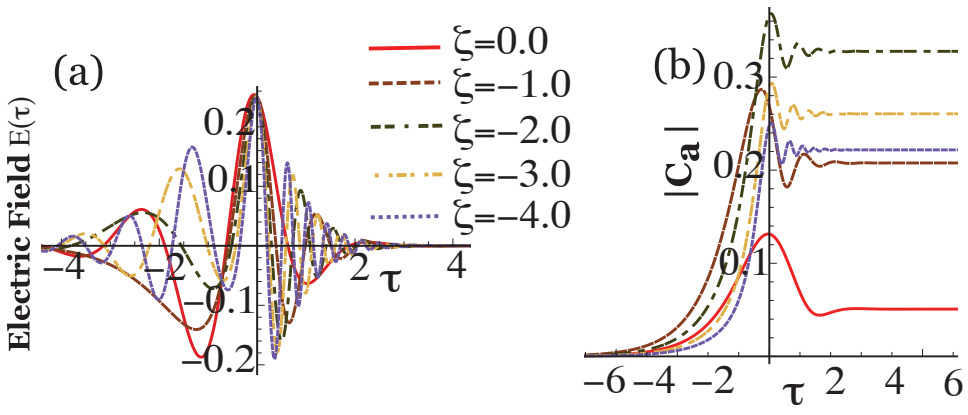

Fig. 14. (II) Confluent Heun Equation case: (a) Profile of the Electric field $\mathrm{E}(\tau)$ for varying ζ. (b) Probability amplitudes for the upper level a for the corresponding fields in (a). The pulse envelope $\Omega(\tau)$ and $\dot{\phi}(\tau)$ is given by Eq.(3.80).

probability amplitude for the upper level a in shown in Fig. 13(d) for the corresponding pulses in Fig. 13(c)

In this section we will discuss another class of pulse and the corresponding chirping function. Let us define the pulse and the chirping function as

$$\Omega(\tau) = \frac{2\sqrt{2}\,\gamma(1-\varphi)\sqrt{\varphi}}{\mu+\lambda\varphi}, \tag{3.74a}$$

$$\dot{\phi}(\tau) = \frac{2\zeta - 2(\zeta+\eta)\varphi}{\mu+\lambda\varphi}. \tag{3.74b}$$

In terms of the variable $\varphi(\tau)$ and the definition of $\Omega(\tau), \dot{\phi}(\tau)$ from Eq.(3.58), Eq.(3.56) takes the form

$$\frac{d^2C_a}{d\varphi^2} + \left(\frac{u}{\varphi} + \frac{v}{\varphi-1}\right)\frac{dC_a}{d\varphi} + \frac{(p\varphi+q)C_a}{\varphi(\varphi-1)} = 0. \tag{3.75}$$

where

$$u = \frac{1}{2} - i\left[\zeta + \frac{\beta\mu}{2}\right],\ v = i\left[\frac{\beta(\lambda+\mu)}{2} - \eta\right],\ p = -q = 2\gamma^2. \tag{3.76}$$

The critical point which corresponds to the peak of $\Omega(\tau)$ is given by

$$\varphi_0 = -\left[\frac{\lambda+3\mu-\sqrt{(\lambda+\mu)(\lambda+9\mu)}}{2\lambda}\right], \tag{3.77}$$

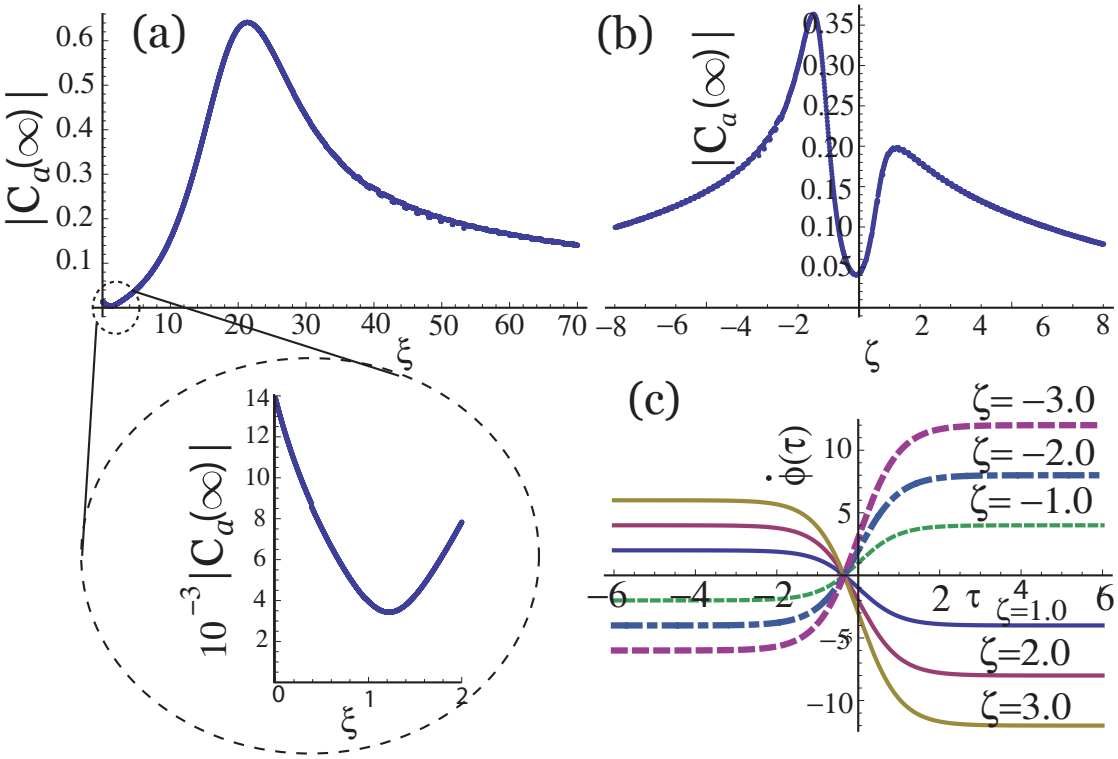

Fig. 15. Effect of chirping on the population left in the excited states a. (a) Heun Equation and (b) Confluent Heun Equation. The inset shows the dip (minima) in the population left for the Heun case. For calculations $\beta = 2.5, \gamma = 0.25, \delta = 1.01$ (c) Chirping function for the Confluent Heun case $\dot{\phi}(\tau)$.

and the corresponding τ_0 can be found using Eq.(3.57). At this point $\dot{\phi} = 0$ which gives a constraint relation as

$$3\zeta(\lambda+\mu) - \zeta\sqrt{(\lambda+\mu)(\lambda+9\mu)} + \eta\left(\lambda + 3\mu - \sqrt{(\lambda+\mu)(\lambda+9\mu)}\right) = 0. \tag{3.78}$$

The general solution of the Confluent Heun Equation Eq.(3.75) is given as

$$\begin{aligned} C_a(\varphi) =& \mathrm{P}_1 \mathrm{H}l^{(c)}[0, u-1, v-1, p, q+(1-uv)/2, \varphi] + \\ & \mathrm{P}_2 \varphi^{1-u} \mathrm{H}l^{(c)}[0, 1-u, v-1, p, q+(1-uv)/2, \varphi], \end{aligned} \tag{3.79}$$

where P_1, P_2 can be found using the initial condition of the system. In the limit $\tau \to \infty$, the population left in the level a can be obtained by substituting $\varphi \to 1$ in Eq.(3.79).

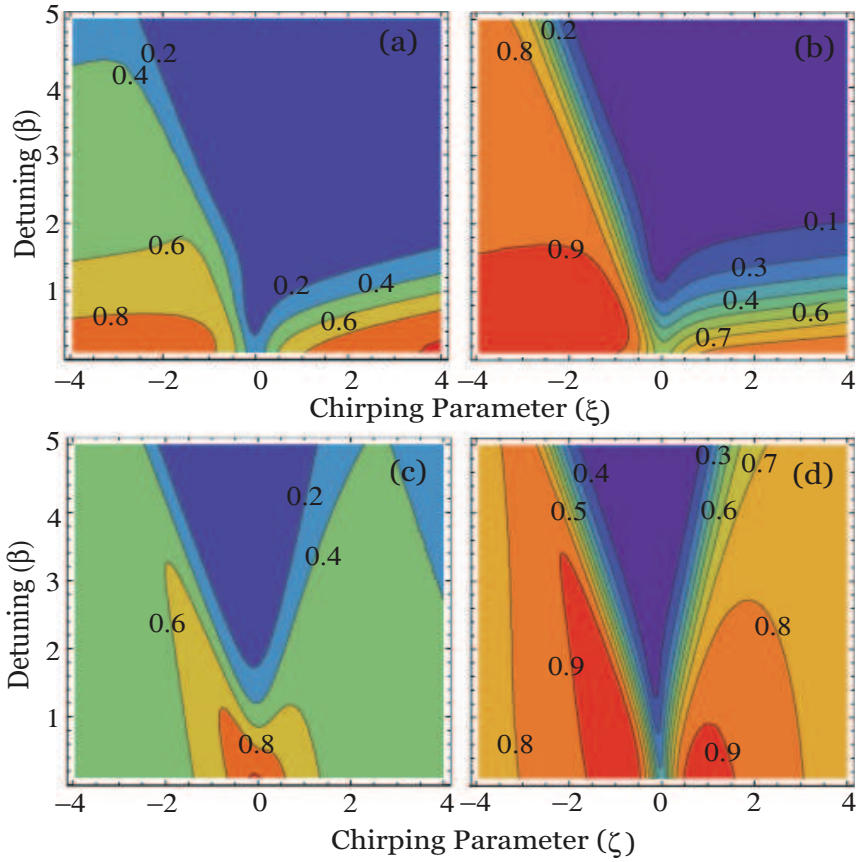

Fig. 16. Contour plot sowing the effect of the pulse parameters such as t_0, τ, ν, and Ω_0 on the population left in the excited state a in (a), (b), (c), and (d) respectively. The influence of the phase jump time t_0 is symmetric as shown in (a). The parameters used are $\Omega_0 = 0.875\omega, \nu = 0.75\omega, \gamma = 1.25\omega, t_0 = 0$, and $\alpha = 0.331\omega$ as required appropriately. For (c) we used $\alpha = 0.110\omega$.

Let us consider a simple case of $\mu = 1, \lambda = 0$. Thus the new variable is given by Eq.(3.65a). From Eqs.(3.77, 3.78) we get $\varphi_0 = 1/3$ and $\eta = 2\zeta$. Pulse shape $\Omega(\tau)$ and the chirping function can be written as

$$\Omega(\tau) = \gamma\,\mathrm{sech}(\tau)\left[1 - \tanh(\tau)\right]^{1/2}, \tag{3.80a}$$

$$\dot{\phi}(\tau) = -\zeta\left[1 + 3\tanh(\tau)\right]. \tag{3.80b}$$

For the pulse defined by Eq.(3.80a), using the scaling parameters Eq.(3.7) and the chirping

function Eq.(3.80b), Eq.(3.56) gives

$$\ddot{C}_a(\tau) - \left\{ i\beta - \frac{1}{2}\left[1 + 3\text{tanh}(\tau)\right] - i\zeta\left[1 + 3\text{tanh}(\tau)\right] \right\} \dot{C}_a(\tau) + \gamma^2 \text{sech}^2(\tau)\left[1 - \tanh(\tau)\right] C_a(\tau) = 0. \tag{3.81}$$

Let us define the initial conditions for our system as Eq.(3.70). Solution for Eq.(3.81), satisfying the initial conditions is give as

$$C_a = \mathcal{P}\varphi^{1-u}\text{H}l^{(c)}[0, 1-u, v-1, p, q + (1-uv)/2, \varphi], \tag{3.82}$$

where $\varphi(\tau)$ is given by Eq.(3.65a) and the Heun parameters as .

$$u = \frac{1}{2} - i\left[\zeta + \frac{\beta}{2}\right],\ v = i\left[\frac{\beta}{2} - \eta\right],\ p = -q = 2\gamma^2. \tag{3.83}$$

The constant P is given as

$$\text{P} = \gamma\left[\frac{2^{(3/2+3i\zeta)}}{(2\zeta + \beta) - i}\right]. \tag{3.84}$$

Here we have kept ζ as a free parameter for the chirping function $\phi(\tau)$ given by Eq.(3.80). Influence of chirping on the evolution of the probability amplitude for the upper level $|a\rangle$ in shown in Fig. 14(b) for the corresponding pulses in Fig. 14(a). To see the effect of chirping on the population left in the upper level a, we have plotted in Fig. 15, $|C_a(\infty)|$ as a function of the free chirping parameter for the Heun and the Confluent Heun case for a particular choice of the detuning β and the peak Rabi frequency γ. We see that $|C_a(\infty)|$ ranges from $4 \cdot 10^{-3} \backsim 6 \cdot 10^{-1}$. In Fig. 16 we have plotted population a contour plot of the population left in the upper level a as a function of detuning β and the free chirping parameters ξ, ζ for the Heun and the Confluent Heun case respectively.

D. Few-Cycle Pulse Excitation

Modern pulsed lasers produce bursts of light that are both ultra-short and ultra-strong, exhibiting durations comparable to those of molecular vibrations, and electric fields rivaling those near an atomic nucleus [55]. Attosecond lasers, emitting pulses with only a few optical cycles per pulse [56], hold the promise of controlling the phase difference between the carrier wave and its envelope[57]. Interaction of such ultrashort pulses with a two-level atom under rotating-wave approximation does not give us the complete picture since the variation of the atomic polarization and population within the optical cycle is not slow. Thus we should not neglect the contribution of the counter-rotating terms in the Hamiltonian while studying few cycle pulses interaction with atomic systems [58, 59, 60, 61, 62, 63, 64, 65]. On the other hand if the fields are not too strong and the variation of the atomic polarization and population within the optical cycle is slow, RWA appears to be a good approximation.

In this section we study the interaction of few-cycle pulses, in contrast to many cycle pulses [66, 67, 68], with two-level system. These pulse have a phase jump ϕ at $t = t_0$. Thus they can be characterized by the parameters peak Rabi frequency Ω_0, pulse width τ, carrier frequency ν, phase jump ϕ and jump moment t_0 along with the pulse envelope (which we have considered gaussian for the numerical simulation). We present an analytical solution for this problem. Using the appropriate characterizing parameters, the population transfer, can be optimized and for the pulse considered here, enhancement of $10^6 - 10^8$ factor was obtained.

The equation of motion for the probability amplitudes for the states a and b of a two-level atom (TLA) interacting with a classical field is given by Eq.3.2. In this section we will work without RWA, hence the Riccati Eq.(3.4) takes the new form as

$$\dot{f} + i\Omega^*(t)\cos(\nu t)e^{-i\omega t}f^2 - i\Omega(t)\cos(\nu t)e^{i\omega t} = 0. \tag{3.85}$$

The approximate solution for Eq.(3.7), in terms of the tip angle θ is given as[44]

$$f(t) = i\int_{-\infty}^{t} dt' \left\{ \left[\frac{d\theta(t')}{dt'} - \theta^2(t') \frac{d\theta^*(t')}{dt'} \right] \exp\left[2\int_{t'}^{t} \theta(t'')\dot{\theta}^*(t'')dt'' \right] \right\}, \tag{3.86}$$

where the tip angle $\theta(t)$ has been defined as

$$\theta(t) = \int_{-\infty}^{t} \Omega(t')\text{cos}(\nu t')e^{i\omega t'}dt'. \tag{3.87}$$

To see how well the approximate solution works, we have plotted the probability amplitude $|C_a(\infty)|$ for a complex pulse shape given by $\Omega(t) = \Omega_0[\text{sech}(\alpha t) + \text{sech}(\alpha t - 3)]$ [see Fig. 17]. Numerical simulation (dashed) and analytical solution (solid) shown in Figs.17(a) and 17(b) are nearly identical.

1. Pulses With Arbitrary Phase Jump

In this section we will investigate the dynamics of a two-level atom subjected to few-cycle pulse with a phase jump at an arbitrary time $t = t_0$. Let us define the Rabi frequency $\Omega(t)$ for our model as

$$\Omega(t) = \begin{cases} \Omega_-(t) & \text{if } t < t_0, \\ \Omega_+(t) & \text{if } t \geq t_0, \end{cases} \tag{3.88}$$

where $\Omega_+(t) = e^{i\phi}\Omega_-(t)$ and ϕ is the phase jump introduced to the electromagnetic field at $t = t_0$. Equivalently the tip angle define by Eq.(3.87) takes the form

$$\theta(t) = \begin{cases} \theta_-(t) & \text{if } t < t_0, \\ \theta_+(t) & \text{if } t \geq t_0. \end{cases} \tag{3.89}$$

From the definition of the Rabi frequency Eq.(3.88), we can easily see that $\theta_+ = e^{i\phi}\theta_-$.The time evolution of our system is divided into two regimes $(-\infty, t_0)$ and (t_0, ∞). In both

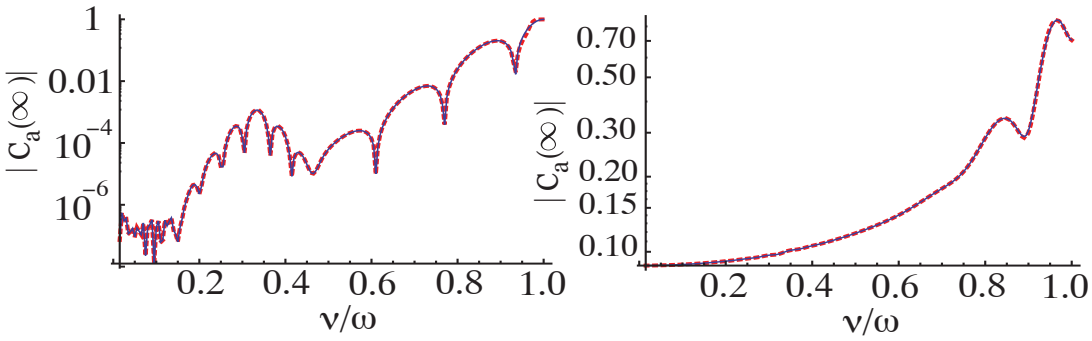

Fig. 17. Population left in the upper level a after applying $\Omega(t) = \Omega_0[\text{sech}(\alpha t)$ +sech$(\alpha t - 3)]$ pulse as a function of the frequency ν/ω obtained by numerical solution of Eq.(3.2) (dots) and using our approximate analytical result Eq.(3.86) (solid line). In calculations we take $\Omega_0 = 0.04\omega$ and $\alpha = 0.075\omega$. In (a) $\phi = 0$ while in (b) $\phi = \pi, t_0 = 0$.

these regimes, the functional form of the solutions remains the same. We can write

$$f_\phi(t) = \begin{cases} f_-(t) & \text{if } t < t_0, \\ f_+(t) & \text{if } t \geq t_0. \end{cases} \tag{3.90}$$

Eq.(3.86) is the solution for $\phi = 0$ for the initial condition $f(-\infty) = 0$. Using the same initial condition we can safely write

$$f_-(t) = i \int_{-\infty}^{t} dt' \Phi_-(t') \text{exp} \left[2 \int_{t'}^{t} \zeta_-(t'') dt'' \right], \tag{3.91}$$

where

$$\Phi_-(t') = \left[\frac{d\theta_-(t')}{dt'} - \theta_-^2(t') \frac{d\theta_-^*(t')}{dt'} \right], \tag{3.92a}$$

$$\zeta_-(t'') = \theta_-(t'') \dot{\theta}_-^*(t''). \tag{3.92b}$$

As the functional form of $f_+(t)$ and $f_-(t)$ are the same, we can write

$$f_+(t) = i \int_{t_0}^{t} dt' \Phi_+(t') \text{exp} \left[2 \int_{t'}^{t} \zeta_+(t'') dt'' \right] + c, \tag{3.93}$$

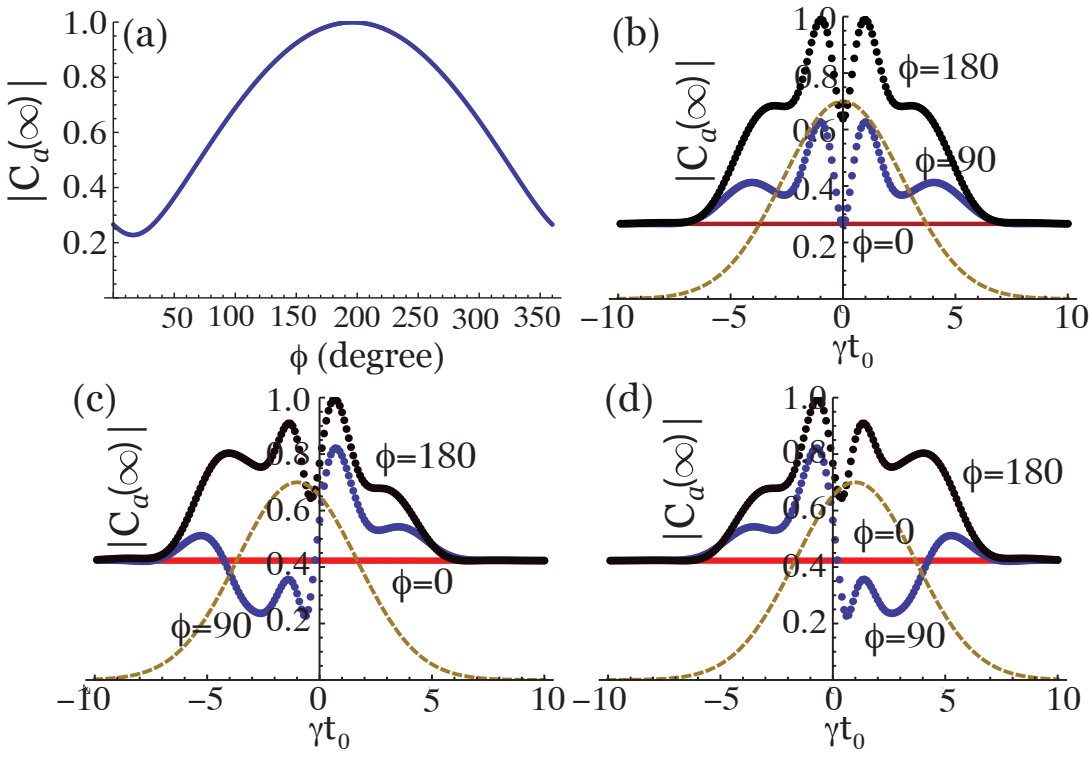

Fig. 18. Effect of jump time t_0. (a) Here we have plotted the probability amplitude $|C_a(\infty)|$ against the phase jump ϕ. Phase jump is introduced at the peak of the gaussian envelope. (b) The symmetric influence on the degree of excitation with respect to the position of t_0. The symmetric response is lost for shifted gaussian input pulse (c) and (d). For numerical calculations we chose $\Omega_0 = 0.875\omega$, $\nu = 0.75\omega$, $\alpha = 0.331\omega$ and $\gamma = 1.25\omega$.

where $\Phi_+(t') = e^{i\phi}\Phi_-(t')$ and $\zeta_+(t') = \zeta_-(t')$ The constant c can be obtained by demanding the continuity of $f_\phi(t)$ at $t = t_0$ which gives

$$c = i\int_{-\infty}^{t_0} dt'\Phi_-(t')\exp\left[2\int_{t'}^{t_0}\zeta_-(t'')dt''\right]. \tag{3.94}$$

Population transferred to the level a during the interaction is given as $|C_a(\infty)|^2 = |f_\phi(\infty)|^2/(1+|f_\phi(\infty)|^2)$. In order to study the effect of the phase jump ϕ let us define a relative change in the amplitude

$$r_\phi(t) = \left|\frac{f_\phi(t) - f(t)}{f(t)}\right|. \tag{3.95}$$

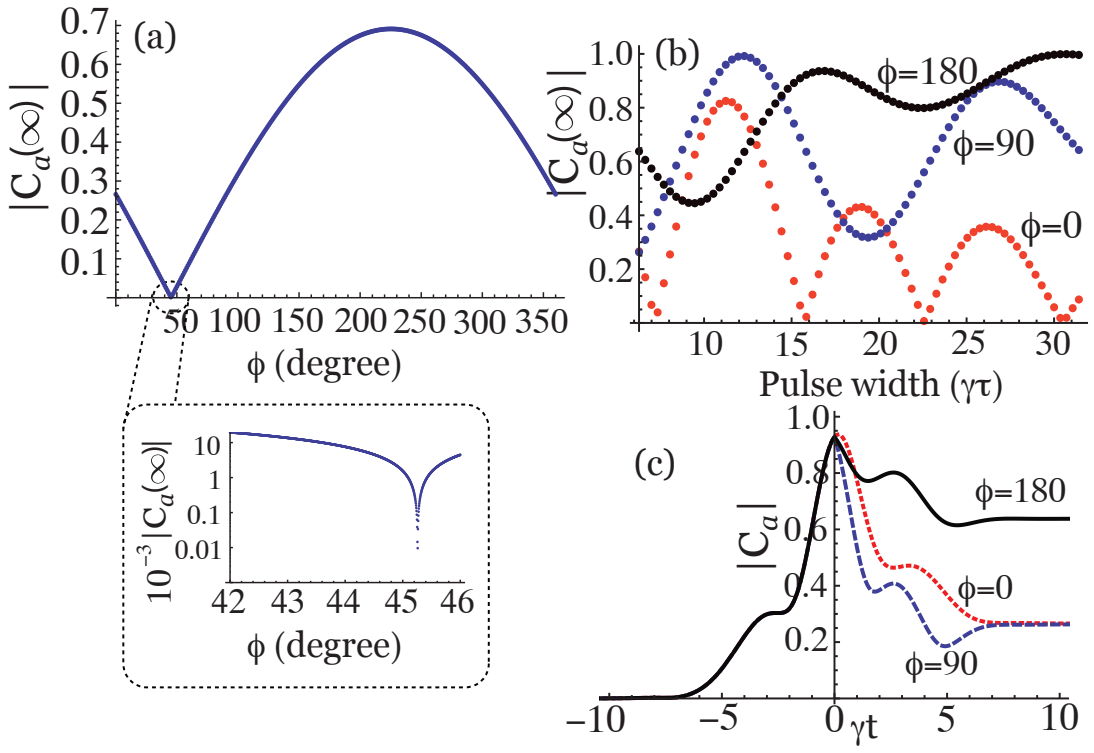

Fig. 19. Effect of α. (a) Probability amplitude $|C_a(\infty)|$ varies in the range from $10^{-5} \backsim 0.7$. (b) We have plotted $|C_a(\infty)|$ against normalized pulse width $\gamma\tau$ for fixed ω, ν, Ω_0 and three combinations of the phase jump $\phi = 0, \pi/2, \pi$. (c) Shows the temporal evolution for the three combinations used in (b). For numerical simulation we chose $\Omega_0 = 0.875\omega$, $\nu = 0.75\omega$, $\gamma = 1.25\omega$ and $\alpha = 0.331\omega$.

Using Eq.(3.91), Eq.(3.93) and Eq.(3.86) we get,

$$r_\phi(t) = \left| \frac{(e^{i\phi} - 1)\int_{t_0}^{t} dt' \Phi_-(t') \text{exp}\left[2\int_{t'}^{t} \zeta_-(t'')dt''\right]}{\int_{-\infty}^{t} dt' \Phi_-(t') \text{exp}\left[2\int_{t'}^{t} \zeta_-(t'')dt''\right]} \right|. \tag{3.96}$$

The asymptotic value $r_\phi(\infty)$ can be obtained by $t \to \infty$ in Eq.(3.96). We can easily see from the Eq.(3.96), that $r_\phi(\infty)$ attains its maximum value for $\phi = \pi$.

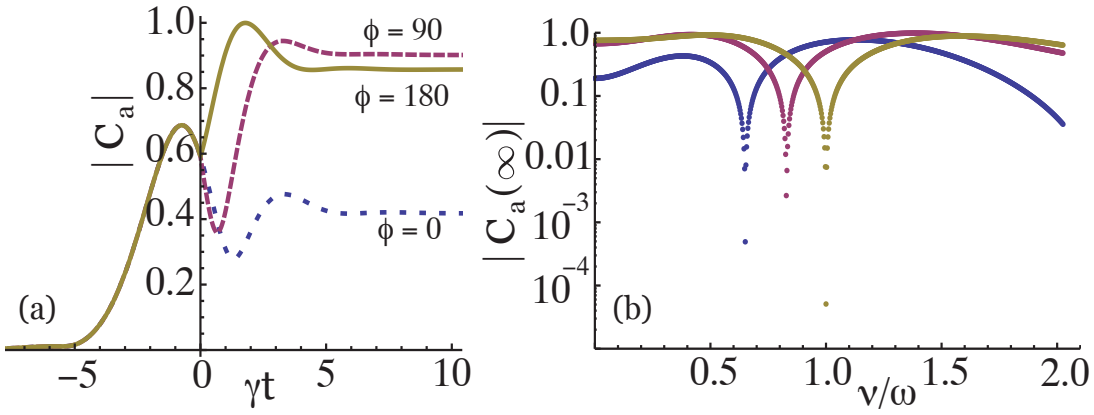

Fig. 20. (a) Temporal behavior of $|C_a|$ for difference combination of ϕ. (b) Plot of $|C_a(\infty)|$ against ν/ω. For numerical simulation we chose $\Omega_0 = 0.875\omega$, $t_0 = 0, \gamma = 1.25\omega$ and $\alpha = 0.331\omega$.

2. Effect of Pulse Parameters

In this section we will discuss the effect of the pulse parameters like phase jump time t_0, pulse witdth τ, detuning Δ and peak Rabi frequency Ω_0 on the degree of excitation of the upper level a. For the computational purpose we have considered a Gaussian pulse of the form $\Omega(t) = \Omega_0 e^{-\alpha^2 t^2}$ where $\alpha = 2\sqrt{\ln 2}/\tau$ (τ is the FWHM of the pulse). The main result showing the effect of relative position of t_0, with respect to the peak of the pulse, on the atomic excitation is shown in Figs. 18 and 22(a) where we have shown the dynamics of the two-level atom interacting with few-cycle pulse with a phase jump. In Fig. 18(a) we have one such scenario of $\phi = \pi/2$. Here the phase jump is introduced in the field at the peak of the gaussian envelope i.e $t_0 = 0$ and plotted the probability amplitude $|C_a(\infty)|$ against the phase jump ϕ. Interestingly the difference in the maximum and the minimum value corresponds to $\Delta\phi = \pi$. The symmetric nature of the atomic excitation is observed in Fig. 18(b) and in the contour plot Fig. 22(a). With the shifted Gaussian pulse $\Omega = \Omega_0 e^{-\alpha^2(t \pm t_s)^2}$ [see Figs. 18(c) and 18(d)] the symmetry is lost. Also the effect of the phase jump becomes significant for t_0 within the FWHM of the pulse and gradually

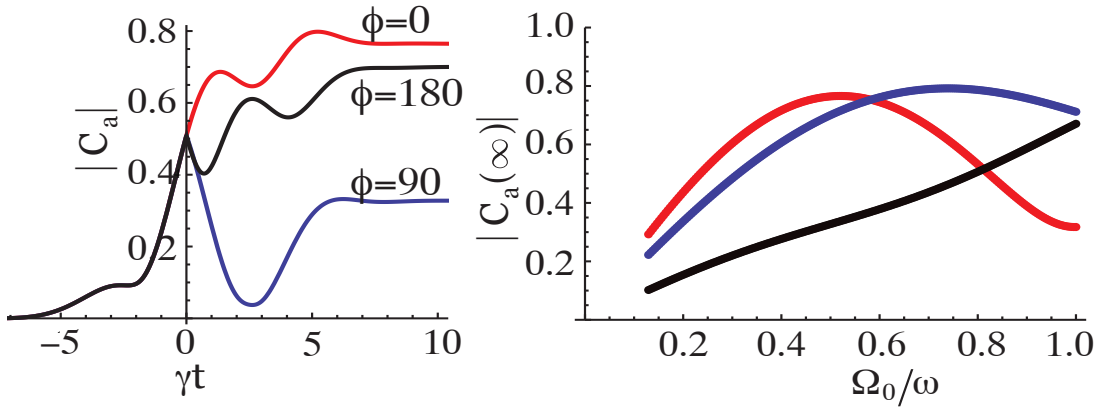

Fig. 21. (a) Temporal behavior of $|C_a|$ for difference combination of ϕ. (b) Plot of $|C_a(\infty)|$ against Ω_0. For numerical simulation in (b), we chose a shifted gaussian pulse with $t_s = 1$, $\nu = 0.75\omega$, $t_0 = 0, \gamma = 1.25\omega$ and $\alpha = 0.331\omega$. $\Omega_0 = 0.875\omega$ for Fig. (a).

decreases when t_0 is close to the tail of the pulse. Identical response of the system, for $\gamma t_0 \approx 10$, is observed for three combinations of the phase jump $\phi = 0, \pi/2, \pi$.

While investigating the effect of few-cycle pulses on atomic systems, the parameter α plays an important role for a given value of the carrier frequency ν. It determines the number of cycles of the field in the pulse. The main results showing the effect of α or the pulse width τ is given in Fig. 19 and in the contour plot in Fig. 22(b). If we look at the inset of Fig. 19(a) we see that the probability amplitude $|C_a(\infty)|$ varies in the range from $10^{-5} \backsim 0.7$. In Fig. 19(b) we have used three combination of phase jump ϕ ($\phi = 0, \pi/2, \pi$) to study the effect of α on the degree of excitation. For lower pulse width ($2 \leq \gamma\tau \leq 15$)$\phi = \pi/2$ creates more excitation than $\phi = 0$ or π.

In order to study the effect of detuning Δ we have plotted the response of the system in terms of $|C_a(\infty)|$ for the three combination of ϕ. Fig. 20(a) shows the temporal behavior while Fig. 21(b) gives the information about steady-state population. The probability amplitude $|C_a(\infty)|$ varies in the range from $4.4 \times 10^{-4} \backsim 0.4$ for $\phi = 0$ and $5 \times 10^{-5} \backsim 0.9$ for $\phi = \pi$. When $|C_a(\infty)|$ is $\backsim 4.4 \times 10^{-4}$ for $\phi = 0$ we have $|C_a(\infty)| \backsim 1$ for $\phi = \pi$,

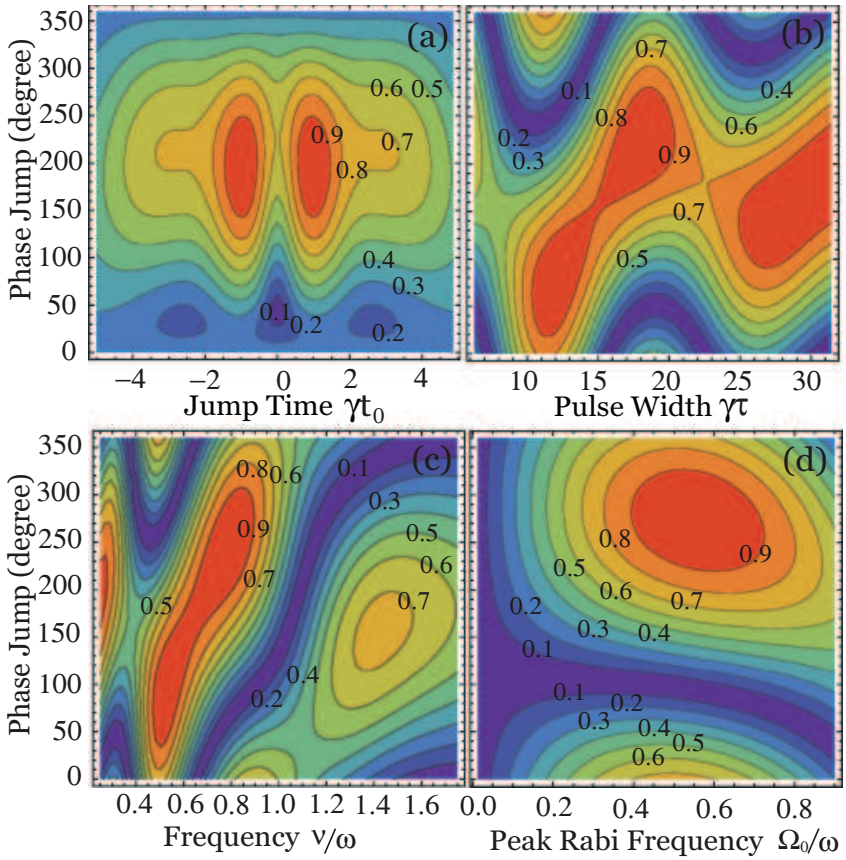

Fig. 22. Contour plot sowing the effect of the pulse parameters such as t_0, τ, ν, and Ω_0 on the population left in the excited state a in (a), (b), (c), and (d) respectively. The influence of the phase jump time t_0 is symmetric as shown in (a). The parameters used are $\Omega_0 = 0.875\omega, \nu = 0.75\omega, \gamma = 1.25\omega, t_0 = 0$, and $\alpha = 0.331\omega$ as required appropriately. For (c) we used $\alpha = 0.110\omega$.

thus we have an enhancement of $10^6 - 10^8$ factor in the population transfer by introducing a phase jump of π at the peak of the envelope function.

The effect of the peak Rabi frequency Ω_0 on the degree of excitation of the upper level in shown in Fig. 21 and in the contour plot Fig. 22(d). While Fig. 21(a) shows the temporal behavior of $|C_a|$ on the other hand Fig. 21(b) gives the information about the population left in the upper level after the pulse is gone. We see that for some choice of Ω_0 $\phi = 0$ has the maximum effect while for some $\phi = \pi/2$ is dominant.

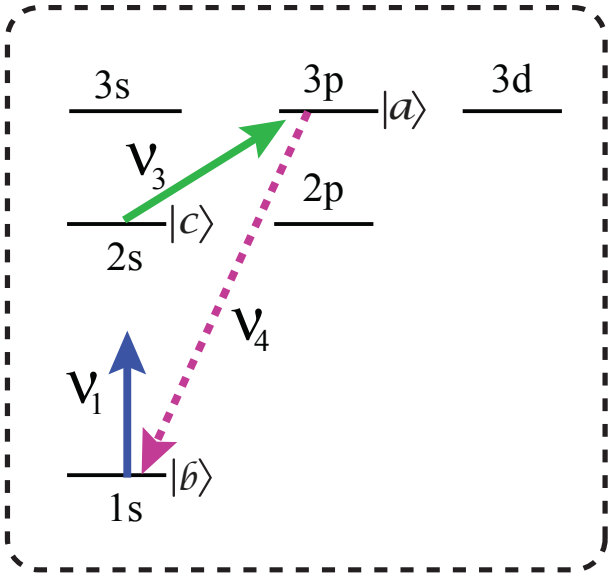

Fig. 23. Field configuration and level structure of H or He^+. All population is initially in the ground state b. First, the strong short far-off resonant pulse with frequency ν_1 is applied to the system to excite coherence between levels $b = 1s$ and $c = 2s$, and then the second pulse with the frequency ν_3, which is close to the transition between levels $2s$ and $2p$, is applied to generate XUV pulse with higher frequency ν_4.

E. Generation of X-ray and UV(XUV) Radiation

The obtained results can be applied to the generation of X-ray and UV (XUV) radiation, which is one of the main topics in modern optoelectronics and photonics [69]. Recent progress in ultrashort, e.g. attosecond, laser technology allows searchers to obtain ultra-strong fields [70]. Interaction of such strong and broadband fields with a two-level atomic system, even under the action of a far-off resonance laser radiation is of current interest [71, 26, 72, 73, 44]. Strong short laser pulses can excite remarkable coherence on high frequency transitions; and this coherence can be used for surprisingly efficient generation of XUV radiation [26, 72, 73, 44]. In the first step we excite the atoms (e.g., from the $1s$ to $2s$ states of or He^+, etc.) via a short pulse of femto- or attosecond radiation e.g., from a

conventional Ti-sapphire laser system). The excitation occurs due to the coherent coupling between $1s$ and 2p and then 2p and 2s. In the second step, we apply another pulse which scatters off the Raman coherence (prepared in the first step), generating short wavelength anti-Stoke radiation as depicted in Fig. 23. The generation of radiation is a coherent process that (contrary to conventional superfluorescence) does not require population inversion (see Appendix C). The higher efficiency of coherent process has been demonstrated in various spectral regions[74, 75, 76, 77, 78, 79, 80, 81].

We have analytically calculated above that the level of excited coherence when a two level atom is driven by a ultra-short intense pulse. The coherence is sufficiently large that this can be used for nonlinear generation of XUV radiation, i.e, see Figs.10(b),11(b) and 12(b), coherence can be of the order of 0.1. It is instructive to estimate the level of XUV field that can be generated by using this coherence. After an ultra-strong and short pulse, we apply a strong resonant and relatively long pulse. The applied probe pulse Ω_3 and generated signal Ω_4 are coupled to each other via coherence excited in the medium (Rabi frequencies are defined as $\Omega_{3,4} = \wp_{3,4}E_{3,4}/\hbar$). Hence, the propagation equation for Ω_4 is given by

$$\frac{\partial \Omega_4}{\partial z} = -i\eta_4 \rho_{ab}, \tag{3.97}$$

where ρ_{ab} is the appropriate atomic coherence (see Fig. 24), and $\eta_4 = k_4 \wp_4^2 N/2\hbar$, where $\wp_4$ is the dipole moment at the transition between. The corresponding equation for the density matrix coherence ρ_{ab} is

$$\dot{\rho}_{ab} = -\Gamma_{ab}\rho_{ab} + i\Omega_4(\rho_{aa} - \rho_{bb}) - i\Omega_3\rho_{cb}, \tag{3.98}$$

and, for short pulses, $\rho_{ab} \simeq -i\Omega_3\tau\rho_{cb}$. Then, we can estimate the intensity of the signal field, by

$$\Omega_4 = \frac{k_4 L \wp_{ab}^2 N}{2\hbar}\rho_{cb}\Omega_3\tau, \tag{3.99}$$

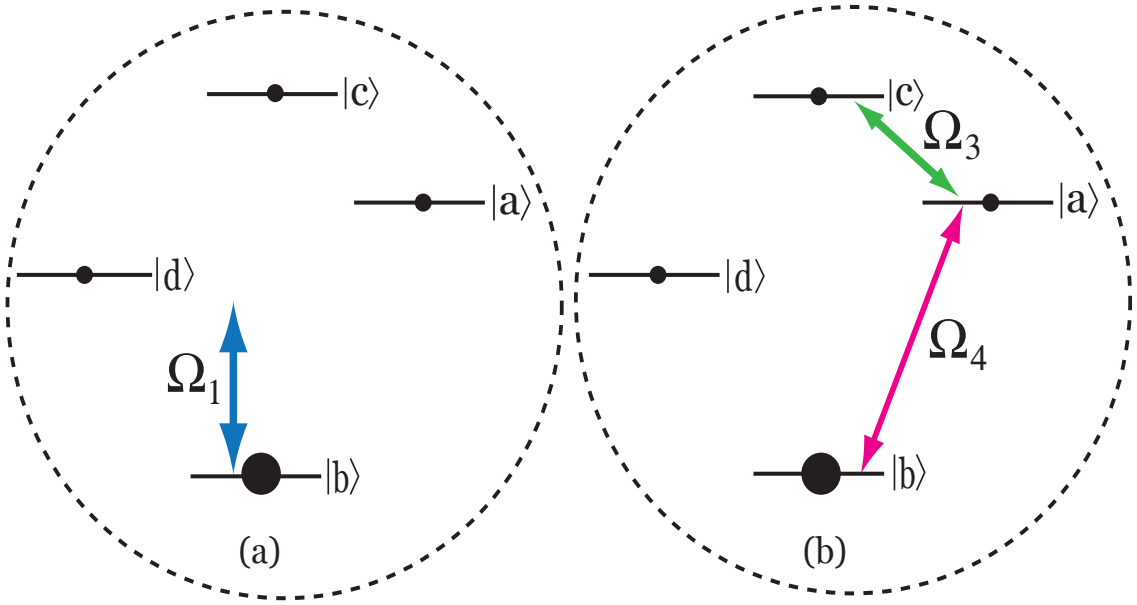

Fig. 24. Two-stage generation scheme for X-ray generation. (a) Applying a strong pulse allows one to excite an atomic system by transferring population to electronic excited states. (b) Coherence is then induced by applying a resonant field.

where k_4 is the wavenumber for signal radiation, L is the length of the active medium, $\wp_{ab}$ is the dipole moment at the transition between a and b levels, τ is the time duration of the pump laser pulse. Using the parameters $N \simeq 10^{16-19}$ cm^{-3}, $\wp_{ab} \simeq 1D$, $L = 100$ μm, $\rho_{cb} = 10^{-1}$, $\Omega_3\tau = 1 - 10^3$, $\tau = 1$ ps, $\lambda = 10$ nm, we obtain energy $\simeq 10$ $nJ - 1$ μJ. This estimate shows the promise of the approach. This estimate is valid on the time scale when the collisions in the plasma destroy the coherence. It occurs at the times of order $\delta t = 1/\sigma c N \simeq 1$ ps, where σ is the atomic cross-section for atomic collisions that destroy the excited coherence.

F. Conclusion

In this chapter we have found several analytical solutions for a two-level atomic system under the action of a far-off- resonant strong pulse (chirped, unchirped and few-cycle) of laser

radiation. The solutions are given in terms of the Heun function, which is a generalization of the hypergeometric function. The Rosen-Zener and Bambini- Berman models belong to this class of pulses as special cases. A better approximation for the box pulse is also obtained here, which takes care of nonanalyticity at the edges by introducing a parameter δ. We also analyzed pulse shapes with phase jump at an instant of time t_0 and showed a unique way of enhancing the excitation. The enhancement factor can be as large as 10^6 for a judicious choice of parameters. The results obtained here have applications to the generation of XUV radiation and the estimate reported here shows good potential as a source of coherent radiation.

CHAPTER IV

QUANTUM INTERFERENCE CONTROLLED RESONANCE PROFILES*

A. Introduction

Study of quantum interference (QI) had led to the discovery of numerous fascinating phenomena in various type of systems ranging from atoms to biomolecules [2, 83, 84]. In atomic systems for example, one of the earliest known effect of QI is the modification of the absorption profiles that comes about due to interference among the bound-bound and bound-continuum transitions, a phenomenon now called Fano interference [85]. Agarwal [86] later showed how QI among decay pathways can lead to generation of coherence and population trapping in a multi-level atomic configuration. A counter-intuitive application of such *Agarwal-Fano QI* was discovered by Harris in the form of inversion-less lasing (LWI) [87]. This non-energy conserving phenomena had thereof lead to several theoretical investigations [88, 89, 90] and experimental demonstration [5, 6, 7]. Furthermore, during the past decade study of QI effects has been extended to tailored semiconductor nanostructures like quantum wells and dots due to coherent resonant tunneling owing to their potential applications in photo-detection [16, 17], lasing [18, 19], quantum computing and quantum circuitry [20, 21].

In the seminal work of Scully [12] it was shown that coherence induced by external source can break the detailed balance between emission and absorption and enhance, in principle, the quantum efficiency of a photovoltaic cell. Ref [12] demonstrated the role of quantum coherence in a simple way. In a recent work we showed that coherence induced by QI can enhance the power of the Photocell and Laser Quantum Heat Engines [91, 92]

---

*Reprinted with permission from "Quantum-interference-controlled resonance profiles from lasing without inversion to photodetection" by K. E. Dorfman, P. K. Jha and S. Das, 2011. *Phys. Rev. A* 84, 053803(1)-053803(8), Copyright [2011] by American Physical Society

following the earlier work on Photo-Carnot Engine enhanced by quantum coherence [93]. The main idea is that the quantum coherence induced by either an external drive or QI among the decay paths alters the detailed balance between emission and absorption and can enhance the efficiency of the system compared to that without quantum coherence. In the case of photovoltaic cells quantum coherence leads to suppression of radiative recombination [12] or enhancement of absorption [92] and thus, increase of the efficiency. Furthermore, the results of the Ref. [12] have initiated debates about the principle issues. In his article [94] Kirk attempts to investigate the limits of Ref. [12] and, in particular, argues that Fano interference does not break detailed balance of the photocell. Note, that noise induced coherence via Fano interference was later shown to indeed enhance the balance breaking in photovoltaics where it leads to increase in power [95, 96, 91, 92].

These investigations have hence generated renewed interest in the fundamental question of noise induced interference effects on the emission and absorption profile of an atom or atom like system (excitons in quantum wells or dots) [97]. As such, we in this paper undertake a thorough theoretical investigation of the vacuum induced interference effects on the resonance line profiles of a three level system with doublets in ground (excited) state configuration (see Fig. 25). Our analysis is quite general and applies to atoms, molecules as well as quantum wells and dots. We study the time profile of absorption and emission probabilities and derive its close form expression in the steady state regime. In the present work we use a simple probability amplitude method to calculate the resonance profiles since the states involved in calculation have zero photon occupation number. The latter is equivalent to the density matrix formalism usually used in this type of problems [91, 92].

The probabilities of emission and absorption are found to have strong functional dependence on the the energy spacing between the doublets (2Δ) and interaction strength p. In the case of atomic system p is governed by a mutual orientation of dipole moments. In semiconductor systems p has a meaning of the phase shift acquired by the wave function

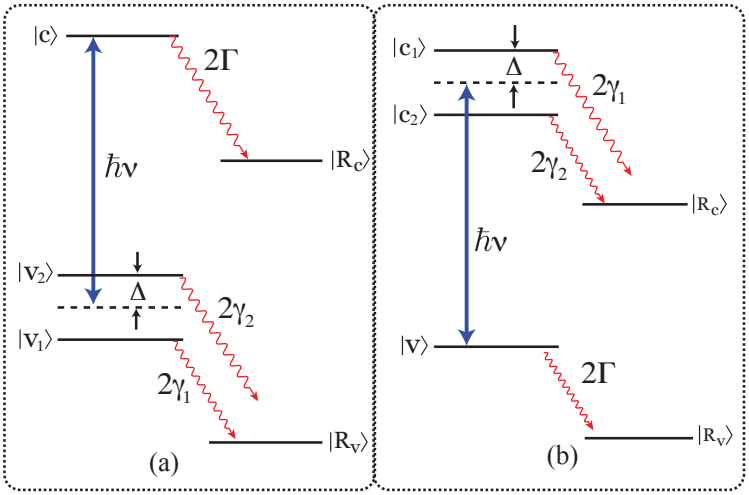

Fig. 25. The scheme of the three level system with the doublet in the ground state (a) and in the excited state (b). Radiative decay from the doublet states to the reservoir is 2γ while the excited (ground) state to the reservoir is 2Γ.

between two interfering pathways. This thus provides us with two different parameter by which we can regulate the QI in the system. For example, we show that depending on the choice of energy spacing between the doublets compared to spontaneous decay rate we can use destructive interference to achieve either LWI by enhancing the emission or photodetectors and interferometers by reducing emission and enhancing absorption. Moreover depending on the p we can manipulate the interference type from destructive to constructive which can significantly alter the resonance profiles [see Fig. 27]

B. Theoretical Model

In order to investigate the effect of QI on the emission and absorption profile of an atomic, molecular or semiconductor system we consider a three level configuration with a ground state doublet $\upsilon_{1,2}$ and excited state c [see Fig. 25(a)]. The three level system is excited by coherent field with the central frequency ν so that the energies of state $\upsilon_{1,2}$ are related to c as $\nu \pm \Delta$, where Δ half of the energy spacing between the ground state doublet. The ground

state doublet $v_{1,2}$ decays to the reservoir state R_v with the rate $2\gamma_{1,2}$ respectively and the excited state decays to the reservoir state R_c with the decay rate 2Γ. Furthermore, states $v_{1,2}$ can represent either Zeeman sub-levels in atoms, vibrational levels within electronic band in molecules or intrasubband in semiconductor. Since the typical relaxation rate of electronic (intersubband) transition is much smaller than that of vibrational (intrasubband), we neglect direct decay process between level c and $v_{1,2}$. Note that the decay of ground state doublets $v_{1,2}$ to the same state R_v leads to a vacuum induced coherence among them. The physics of this coherence is attributed to the *Agarwal-Fano QI* of the transition amplitudes among the decay pathways. Note that analysis presented below is valid for the system with excited state doublet $c_{1,2}$ and single ground state v (as per Fig. 25b, see discussion). We will show later that such QI plays a major role in the line profiles of an atomic system [87, 98]. The time dependent amplitudes of the states $v_{1,2}$ and c essentially exhibits the effect of coherence on the dynamics of the system. The probability amplitude method can be applied in the present system since states $v_{1,2}$ and c have zero photon occupation number. Solving the time dependent Schrödinger equation, the dynamical evolution of the probability amplitudes $v_{1,2}$ and c of finding system in corresponding states $v_{1,2}$ and c (i.e. states with zero photons) in Weisskopf-Wigner approximation is given by

$$\dot{v}_2(t) = -(\gamma_2 + i\Delta)v_2(t) - p\sqrt{\gamma_1\gamma_2}v_1(t) - i\Omega_2 c(t), \tag{4.1}$$

$$\dot{v}_1(t) = -(\gamma_1 - i\Delta)v_1(t) - p\sqrt{\gamma_1\gamma_2}v_2(t) - i\Omega_1 c(t), \tag{4.2}$$

$$\dot{c}(t) = -i\Omega_2 v_2(t) - i\Omega_1 v_1(t) - \Gamma c(t), \tag{4.3}$$

where $\Omega_{1,2} = \wp_{1,2}\mathcal{E}_0/2\hbar$ and $\wp_{1,2}$ are the respective Rabi frequencies and dipole moments of the corresponding transitions $v_{1,2} \leftrightarrow c$ with $\mathcal{E}_0$ being the amplitude of the applied electric field. The term $p\sqrt{\gamma_1\gamma_2}$ arises due to QI of the decay pathways of the ground state doublet. It is clearly seen from the above set of equations that this term for $p \neq 0$ couples the

amplitudes of the states v_1 and v_2. Such a coupling is known as *Agarwal-Fano coupling* in the literature [99] and have several implications ranging from superradiance [100, 101] and entanglement [101] to quantum solar cells [12, 91, 92]. The interference strength is typically determined in terms of the relative orientation of the dipole moments of the decay transitions and is given by coefficient a p as,

$$p = \frac{\vec{\wp}_{v_1 R_v} \cdot \vec{\wp}_{v_2 R_v}}{|\vec{\wp}_{v_1 R_v}||\vec{\wp}_{v_2 R_v}|} \tag{4.4}$$

where $\vec{\wp}_{v_1 R_v}$ and $\vec{\wp}_{v_2 R_v}$ are the dipole moment corresponding to the transition $v_1 \leftrightarrow R_v$ and $v_2 \leftrightarrow R_v$ respectively with $p = \pm 1$ exhibiting the maximal interference among the decay paths. Here $p = 1$ corresponds to the two dipole moment vectors parallel to each other on the other hand when they are anti-parallel $p = -1$. Non-orthogonal dipole moments in optical transition have been generated using superposition of singlet and triplet states due to spin-orbit coupling in sodium dimers [102]. More generally, interference strength p is a phase shift acquired by wavefunction between initial and final states. Equations (4.1)-(4.3) can be written and solved in the dressed basis using the approach developed by Scully [103] as discussed in Appendix E for general p and in the presence of additional decay rates Γ, γ. The probability of emission P_{emiss} defined as a sum of population of the doublet v_1, v_2 and of the reservoir state R_v due to conservation of probability, can be written in terms of populations of states c and R_c as

$$P_{\text{emiss}}(\tau|c) = 1 - |c(\tau)|^2 - 2\tilde{\Gamma} \int_0^\tau |c(\tau')|^2 d\tau'. \tag{4.5}$$

In the long time limit, $\tau \gg 1, 1/\tilde{\Gamma}$ and assuming $\gamma_1 = \gamma_2 = \gamma$ for simplicity, the probability of emission defined in Eq.(4.5) (derived in Appendix E) yields

$$P_{\text{emiss}}(\infty|c) = \frac{(\tilde{\Gamma}+1)(\tilde{\Omega}_1^2 + \tilde{\Omega}_2^2) - 2p\tilde{\Omega}_1\tilde{\Omega}_2}{\tilde{\Gamma}\left[(\tilde{\Gamma}+1)^2 + \tilde{\Delta}^2 - p^2\right]}. \tag{4.6}$$

where the tilde signifies that all the parameters are now dimensionless as they are normalized by γ. The probability of absorption from level v_1 can be evaluated in a similar manner. For the initial conditions $v_1(0) = 1$,$v_2(0) = 0$ and $c(0) = 0$ the probability of absorption P_{abs} is given by the sum of population on states c and R_c:

$$P_{\text{abs}}(\tau|v_1) = |c(\tau)|^2 + 2\tilde{\Gamma}\int_0^{\tau} |c(\tau')|^2 d\tau' \tag{4.7}$$

that yields the following expression in the long time limit, $\tau \gg 1, 1/\tilde{\Gamma}$ (see Appendix E)

$$P_{\text{abs}}(\infty|v_1) = \frac{1}{\mathcal{D}}\left\{\left[2(1+\tilde{\Delta}^2)(1+\tilde{\Gamma}) - \tilde{\Gamma}p^2\right]\tilde{\Omega}_1^2 - 2(\tilde{\Gamma}+2)p\tilde{\Omega}_1\tilde{\Omega}_2 + (\tilde{\Gamma}+2)p^2\tilde{\Omega}_2^2\right\} \tag{4.8}$$

where $\mathcal{D} = 2(1+\tilde{\Delta}^2 - p^2)\left[(\tilde{\Gamma}+1)^2 + \tilde{\Delta}^2 - p^2\right]$. The probability of absorption from level v_2 can be derived in the same way as for the level v_1 by interchanging $v_1 \leftrightarrow v_2$ in Eq. (4.7) and $\tilde{\Omega}_1 \leftrightarrow \tilde{\Omega}_2$ in Eq. (4.8). Comparison of Eq. (4.6) with Eq. (4.8) yields that probability of emission and absorption can vary substantially in the presence ($p \neq 0$) or absence ($p = 0$) of interference.

So far we have discussed a model with doublet in the ground state. Let us now consider doublet in the excited state [as shown in Fig. 25(b)]. In practice this configuration is commonly used in semiconductor systems like quantum wells and dots. The expression for the probability of emission and absorption in case of excited state doublet can be obtained as follows. If we start with $|c_1\rangle$, the probability of emission is given by

$$P_{\text{emiss}}(\tau|c_1) = |v(\tau)|^2 + 2\tilde{\Gamma}\int_0^{\tau} |v(\tau')|^2 d\tau' \tag{4.9}$$

Similarly the probability of absorption from $|v\rangle$ yields

$$P_{\text{abs}}(\tau|v) = 1 - |v(\tau)|^2 - 2\tilde{\Gamma}\int_0^{\tau} |v(\tau')|^2 d\tau'. \tag{4.10}$$

The expression for the emission and absorption probability can be calculated by following

a procedure similar to that outlined in appendix E for the ground state doublet. In the long time limit $t \gg \gamma^{-1}, \Gamma^{-1}$, we find that the expression for emission and absorption probabilities obtained from Eqs.(4.9)-(4.10) reduces to Eqs.(4.8) and (4.6) respectively.

C. Discussion

1. Lasing without Inversion and Photodetectors

The model discussed in the previous section is relevant for the design of the systems with nonrecpirocal relation between emission and absorption. For instance, suppressed absorption or/and enhanced emission in the laser systems allows for operating without population inversion. On the other hand enhanced absorption with suppressed emission can results in the photodetector or photovoltaic/solar cell system with enhanced power output[91, 92]. Both LWI and photodetector schemes can be realized in atomic molecular and semiconductor systems. In atoms Agarwal-Fano type QI can arise between decay channels from magnetic sub-levels. In molecular systems on the other hand, decay pathways of different vibrational/rotational levels lead to asymmetric absorption/emission profiles due to interference. In the case of semiconductors, Agarwal-Fano interference comes about quite naturally in a system of two quantum wells or dots grown at nanometer separations [18, 19]. The tunneling/Förster interactions among the wells/dots renormalizes the bare energies and bare states of the system thereby creating new eigenstates which then reveals the interference in decay channels through tunneling to the same continuum [104, 103]. Note that QI and coherence effects in semiconductors are strongly effected by the presence of dephasing environment and hence experiments in these systems are carried out at very low temperatures (10 K). This thereby restrict their practical feasibility for various applications involving QI. However, recently quantum dot photodetector enhanced by Fano-type interference assisted with metallic hole array was reported operating at 77 K [17]. Hence in

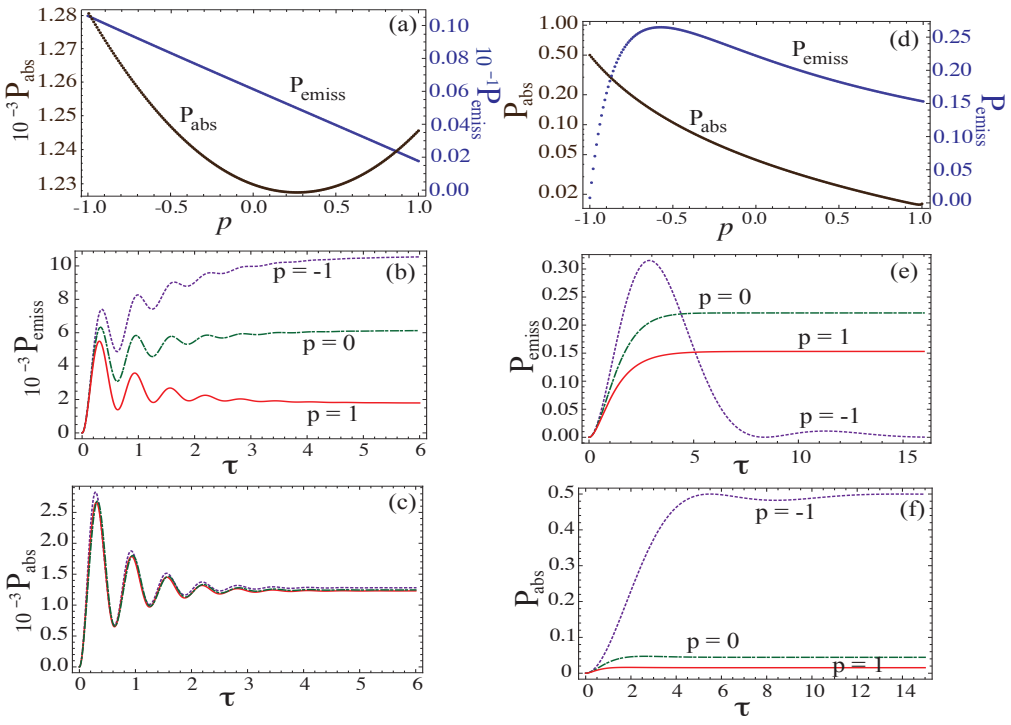

Fig. 26. Steady state (a,d) and temporal evolution (b,c,e,f) of the emission and absorption probability for the three level model with the doublet in the ground state. (a,d) shows the effect of the parameter 'p' on the steady state values of the probability of emission and absorption. (b,e) shows the temporal behavior of the probaility of emisison for three choices of 'p'. (c,f) shows the temporal behavior of the probability of absorption for the same choices of p as in (b,e). For numerical simulation we took, $\gamma = 1$, $\Omega_1 = \Omega_2 = 0.3\gamma$, $\Gamma = 0.4\gamma$ and $\Delta = 10\gamma$ for (a,b,c) and $\Delta = 0.01\gamma$ for (d,e,f).

near future realization of Fano like QI effects in nanostructure and its various applications might be achievable even at room temperatures.

To put the above ideas to prospective, we discuss the functional dependence of the of emission and absorption probabilities on the interference strength p and the level spacing Δ in the steady state and transient regime. We show in Fig. 26 the steady state behavior and temporal evolution of emission and absorption probabilities for different values of p and Δ. Figures in the upper panel 26(a, b, c) correspond to large level spacing compare to

spontaneous decay rate $\Delta \gg \gamma$ ($\tilde{\Delta} \gg 1$). The steady state emission profile is seen to be strongly influenced by the strength of QI. It varies from its minimum at $p = 1$ to maximum at $p = -1$ (see Fig. 26a). The enhancement in emission is found to be almost 10 fold. However for absorption the effect of interference is not significant as p varies from -1 to 1. Therefore, for $p = -1$ one can achieve regime with largest emission, which can be useful in inversionless lasing schemes. On the other hand at $p = 1$, as emission reaches its minimum, it is attractive in realization of photo-detectors and photovoltaic devices. Note, that in semiconductor double quantum well system, control over p can be achieved by manipulating of the width of the shallow well [19]. The time evolution of the resonance profiles shown in Figs. 26b and 26c exhibits oscillatory behavior in the emission and absorption probabilities. Period of oscillations is determined by the frequency $\sqrt{\Delta^2 - \gamma^2}$ and thus strongly depend on the level spacing. We see further that the oscillations gets damped with time and the probabilities eventually reaches the steady state.

For small level spacing $\Delta \ll \gamma$ ($\tilde{\Delta} \ll 1$), the situation becomes less trivial. In this case the behavior of emission and absorption profiles is depicted in the lower panel of Fig. 26(d, e, f). In the steady state the both the probabilities varies significantly with the interference strength p [see Fig. 26(d)]. We find that while absorption probability increases monotonically from $p = 1$ to $p = -1$, emission is seen to first increase until about $p = -0.5$ beyond which it rapidly decreases to reach the minimum value at $p = -1$. This is in sharp contrast to the behavior of the emission probability for large Δ. In the time dependent profiles [Fig. 26(e), 26(f)] we find that in comparison to the case of large splitting both emission and absorption probabilities show no oscillations and reach their steady state values that depend strongly on the interference strength. Furthermore, interesting case arise at $p = -1$ where emission profile first reaches its maximum and then drops down to the steady state that has the smallest value compare to other $p \neq -1$. In the same time absorption profile at $p = -1$ reaches its maximum value at steady state. Note that in

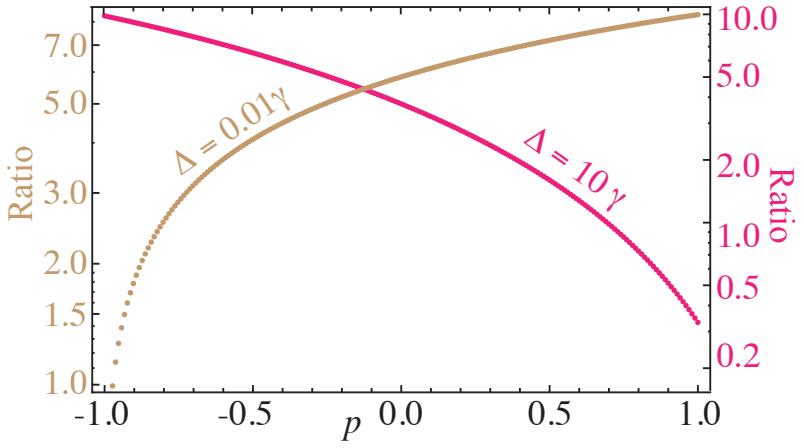

Fig. 27. Ratio of the probability of emission to absorption for two combinations of coupling Δ as a function of the parameter p. For numerical simulation we took, $\Omega_1 = \Omega_2 = 0.3\gamma$, $\Gamma = 0.4\gamma$.

contrast to that, for large splitting at $p = -1$ emission has its maximum [see Fig. 26(b)]. Therefore, not only interference strength determines the emission and absorption profile, but the level spacing itself has strong impact. Namely, for fixed value of p, for example $p = -1$, large level spacing Δ yields the strongest emission [see Fig. 26(b)] which is in favor of lasing process. In the same time for small level spacing the emission is strongly suppressed while absorption reaches its maximum [see Figs. 26(e,f)], which is perfect situation for photo-detection and photocell operation. Furthermore, it is worth noting, that despite the asymmetry between curves for $p = \pm 1$ in Fig. 26, result for $p = 1$ can be derived from $p = -1$ case by changing the sign of the Rabi frequency, for instance: $\Omega_1 \to -\Omega_1$.

To study further the effects of p and Δ and to understand the special case of antiparallel alignment $p = -1$ consider the ratio of emission and absorption given by Eq. (4.6) and (4.8):

$$\frac{P_{\text{emiss}}}{P_{\text{abs}}} = \frac{2(1+\tilde{\Gamma}-p)(1+\tilde{\Delta}^2-p^2)}{\tilde{\Gamma}[\tilde{\Delta}^2(1+\tilde{\Gamma})+\tilde{\Gamma}(1-p)+(1-p)^2]}, \tag{4.11}$$

where for simplicity we assume $\Omega_1 = \Omega_2$. Fig. 3 shows the ratio in Eq. (4.11) as a function of interference strength p for the case of small and large level spacing. If the spacing is

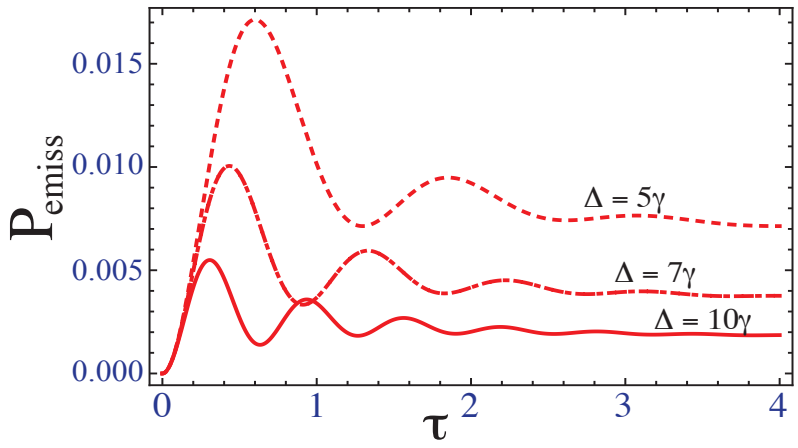

Fig. 28. Probability of emission in the three level model lower doublet for different choices of Δ. For numerical simulation we took, $\Omega_1 = \Omega_2 = 0.3\gamma$, $\Gamma = 0.4\gamma, \gamma = 1, \tau = \gamma t, p = 1$.

small, $\Delta \ll \gamma$, then the ratio in Eq. (4.11) monotonically increasing from $p = -1$ to $p = 1$, while for large spacing $\Delta \gg \gamma$, the behavior is essentially the opposite, i.e. it is monotonically decreasing function as we mention above. Furthermore, in the limit of weak field $\Omega_1 = \Omega_2 = \Omega \ll 1$ Eq. (4.11) yields for $p = 0, 1$ result that is independent of Δ. Namely for no interference, i.e. $p = 0$ Eq. (4.11) yields $2/\tilde{\Gamma}$, while for parallel alignment $p = 1$ it yields $2/(1 + \tilde{\Gamma})$. On the other hand the case of antiparallel alignment ($p = -1$) is special. In particular, for small spacing $\Delta \ll \Gamma \ll \gamma$ Eq. (4.11) gives $\tilde{\Delta}^2/\tilde{\Gamma} \ll 1$, while for $\Delta \gg \gamma$ and $\Gamma \ll \gamma$ the result is $4/\tilde{\Gamma} \gg 1$. Therefore, the present analysis not only confirms that destructive interference can alter the detailed balance but also exhibits that by controlling two parameters. Namely by adjusting the interference strength p and energy spacing Δ, one can regulate the ratio between emission and absorption probabilities in the system. This possible manipulation of p and Δ hence also suggest that in the same system with two lower (upper) levels one can induce either suppression of emission [91, 92] or absorption [18, 19], respectively. The later choice governed by level spacing Δ can be also controlled externally either by adjusting the current through the junction, or by

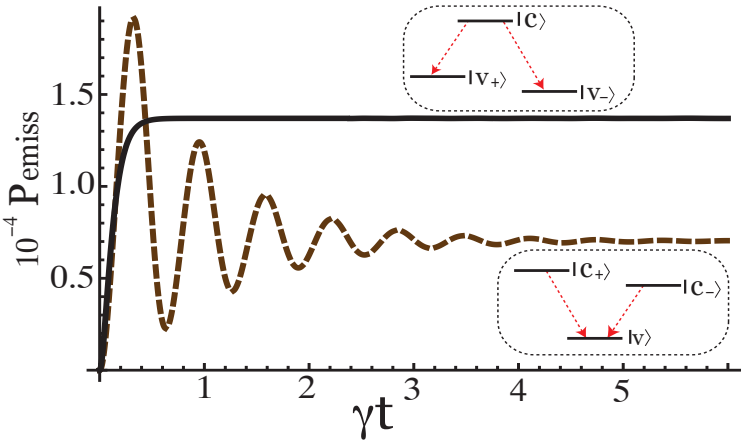

Fig. 29. Probability of emission P_{emis} as a function of dimensionless time τ for three-level system with doublet in excited state - (dashed line) and for three level system with doublet in ground state - (solid line) calculated numerically according to Eqs. (4.5) and (4.7) based on the solution of Eqs. (4.1)- (4.3). For numerical simulations we took $\Omega_1 = 0.1\gamma, \Omega_2 = 0.08\gamma, \Gamma = 10\gamma, \Delta = 0.1\gamma$.

manipulating the magnetic field in hyperfine splitting [105, 106]. In Fig. 28 we have plotted the effect of Δ on the temporal evolution of the probability of emission. The results show that the oscillations in the probability varies with the increase of Δ. Furthermore, for fixed Δ and γ the number of oscillations is governed by rate Γ since probability decays as $\exp(-\Gamma t)$. For interference strength p, control can be achieved by a tailored variation of the quantum well widths [19]. Summarizing the proposed scheme with lower doublet can be applied to the system that requires emission (absorption) suppression or enhancement and thus is very attractive for both: light emitting devices, such as LWI and light absorbing photodetector systems.

2. Quantum Beats in Semiclassical Picture

Besides broad range of applications, interference effects and in particular its sensitivity to the level spacing discussed in the present work are related to fundamental question about

the applicability of semiclassical theory in quantum problems. Semiclassical description (SCT) can predict self-consistent and physically acceptable behavior of many physical systems and explain almost all quantum phenomena. However It is not always correct. For instance, the phenomena of quantum beats has substantially different result if considered in the framework of quantum electrodynamics (QED)[2]. Namely, for different configurations of three-level systems: for instance $V$and Λ schemes [see Fig. 29] that are initially prepared in a coherent superposition of all three states SCT description predicts the existence of quantum beats for both schemes, whereas QED theory predicts no quantum beats in the case of Λ scheme. The explanation of the phenomenon is quite straightforward and based on quantum theory of measurements. In the case of V scheme the coherently excited atom decays to the same final state v starting from c_+ and c_- and one cannot determine which decay channel was used. Therefore this interference that is similar to the double-slit problem leads to the existence of quantum beats. However in the case of Λ scheme that has also two decay channels: $c \rightarrow v_+$ and $c \rightarrow v_-$, after a long time the observation of the atom's final state (v_+ or v_-) will determine which decay channel was used. In this case we do not expect quantum beats. Three-level systems with doublet in the ground state or excited state is in a way similar to the Λ and V types of atom respectively. Therefore we can also study the quantum beats effect in those systems. Note that in the model of Fig. 25 we have additional radiative decays of states which guarantees that system can reach a steady state within finite amount of time.

Figure 29 illustrates that in the case of doublet in excited state (V scheme) with large spacing between levels c_+ and c_- $\tilde{\Delta} >> 1$, the probability of emission oscillates as a function of time and reaches the steady state at the time scale determined by radiative decay $1/\tilde{\Gamma} >> 1$. However, for the case of doublet in the ground state (Λ scheme) with small spacing $\tilde{\Delta} << 1$ the probability of emission does not process any quantum beats and smoothly reach the steady state. Therefore, phenomenon of Fano interference has a

potential to resolve the fundamental question about an applicability of the semiclassical description to the problem of quantum beats.

D. Conclusion

To conclude, in this chapter we investigated the effect vacuum induced QI on the emission(absorption) profile of a three-level system with a doublet in the ground or excited state [see Fig. 25(a)]. We show that QI can enhance the balance breaking between emission and absorption. We use probability amplitude method, since the states involved in calculation have zero photon occupation number. Furthermore, our findings are in full agreement with the results obtained by density matrix formalism. We observed that the interference strength p governed by the phase shift between the decay pathways play a crucial role on the emission(absorption) dynamics of the system. For the closely spaced doublet $(\Delta \ll \gamma)$, for which the vacuum induced QI becomes important, the behavior of the emission(absorption) profile of our model appears counterintuitive. For $p \sim -1$, the ratio of probability of emission to probability of absorption is very small, a condition favorable for applications like photovoltaics. On the other hand for $p \sim 1$, the ratio is large thus favorable for amplification without population inversion in steady-state [see Fig. 26(b,e)]. In addition to these applications we found that Agarwal-Fano QI can also predicts the occurrence of fundamental phenomena like quantum beats in the semi-classical framework, that fully agrees with the QED description.

CHAPTER V

USING QUANTUM COHERENCE TO GENERATE GAIN IN THE XUV AND X-RAY*

A. Introduction

Gain-swept superradiance (GSS) in an ensemble of two- level atoms was extensively studied in the 1970s in connection with laser lethargy and coherence brightening in the X-ray laser[107, 108, 109]. In GSS, the inversion is created by injecting a short excitation pulse that produces a gain-swept medium. Among other things, it was found that GSS can yield intense pulses without population inversion. This is closely related to Dicke superradiance[1][110] in which the maximum emission rate occurs when there are equal number of atoms in the excited and ground states, i.e., when the population inversion is zero [see Fig. 30(a)].

Lasing without inversion (LWI) in an ensemble of three- level atoms, with a coupling laser driving two of the levels was demonstrated in the 1990s [see Fig. 30(b) and (c)][2]. Those studies involved continuous pumping and were largely in the visible and IR spectral regimes. Most recently, we have been investigating lasing in the extreme ultraviolet (XUV) using gain-swept excitation together with transient LWI[121]. In this paper, we have ex-

---

* Part of this chapter reprinted with permission from "Using Quantum Coherence to Generate Gain in the XUV and X-Ray: Gain-Swept Superradiance and Lasing Without Inversion" by E. A. Sete, A. A. Svidzinsky, Y. V. Rostovtsev, H. Eleuch, P. K. Jha, S. Suckewer, and M. O. Scully, 2012. *IEEE J. Sel. Topics Quantum Electron.* 18, 541-553, Copyright [2012] by The Institute of Electrical and Electronics Engineers, Inc.

[1] Recently, the GSS has been applied to the stand-off detection of trace impurities[111]

[2] The first suggestion of LWI in a three-level system was given in[112]. For more recent LWI theoretical work, see[113, 114, 115]. For the first LWI oscillator demonstration, see[116, 117]. The first clear explanation of transient behavior in LWI was given by Harris and Macklin[118]; see also[119]. The papers of Braunstein and R. Shuker on X-ray LWI in a ladder system also include time-dependent effects (see, e.g.,[120])

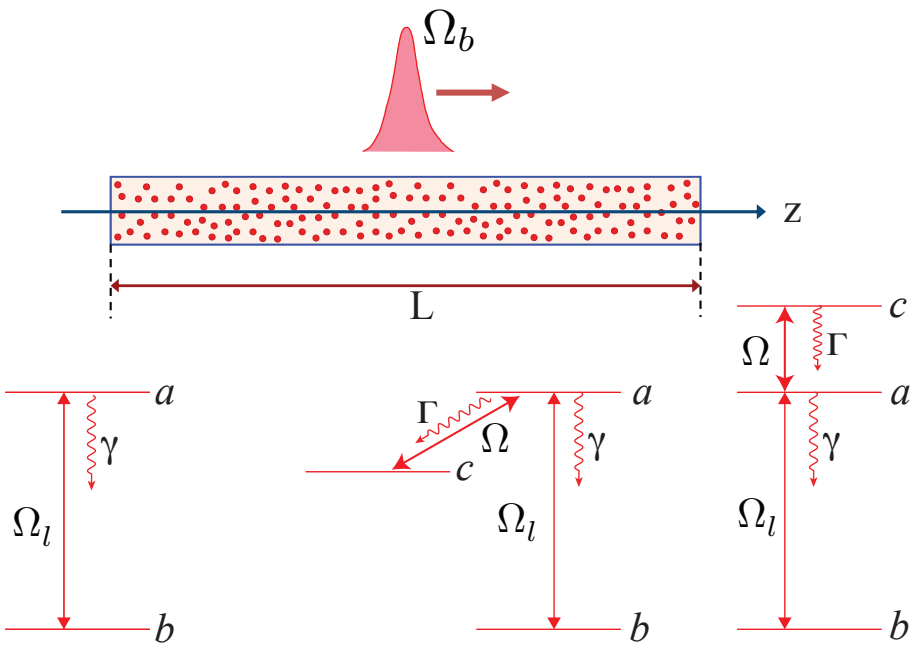

Fig. 30. Excitation pulse traveling at the speed of light prepares atoms in an excited state, so that the spontaneous emission from atoms excited earlier can be simultaneous with excitation by the pump pulse. (a) For the case of two-level atoms, this can yield GSS. (b), (c) Three-level atoms in Λ or Ξ schemes can yield transient LWI under swept gain conditions.

plored connections between GSS and transient Raman LWI in He atom (ladder scheme), where we have initial Raman inversion yet the system operates without inversion in the lasing transition. Moreover, we have shown a pure transient LWI using He-like ion B3+ operating at 6.1nm.

Typical results are shown in Fig. 31(a) for the case of ladder Raman lasing in He as sketched in Fig. 31(b). Here, we see that there is no population inversion on the lasing ($a \rightarrow b$) transition if we start with a little bit of Raman inversion, $\rho_{cc}(0) = 0.56, \rho_{aa}(0) = 0$, and $\rho_{bb}(0) = 0.44$. However, as per the analysis sketched in Section II, a respectable laser pulse of $\sim 10^9$ photons at 58 nm is emitted. As illustrated in Fig. 31(b), the initial population $\rho_{cc}(0)$ derives from the transfer of population from 2^3S to 3^1D. This is discussed in some

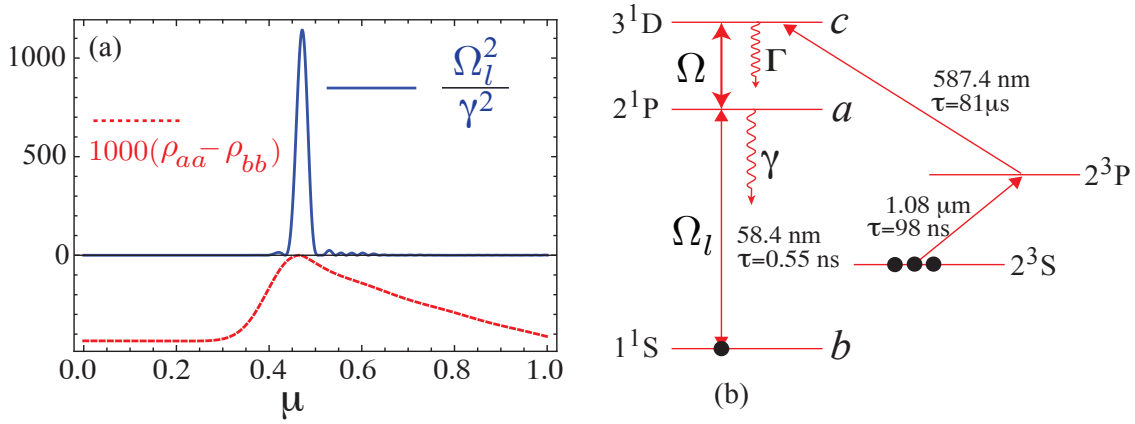

Fig. 31. (a) Plots of the square of output field Ω_l (solid curve) and scaled inversion between a to b transition (dashed curve) versus retarded time $\mu = t - z/c$ for initial condition $\rho_{cc}(0) = 0.56, \rho_{aa}(0) = 0$, and $\rho_{bb}(0) = 0.44$. The dashed curve shows that the inversion is always negative. The unit of time is $\tau_1 = 0.55$ns which is the $|a\rangle \rightarrow |b\rangle$ spontaneous transition lifetime. The energy output is a respectable few nanojoules compared to the input energy ∼0.01 pJ, other parameters are given in Table I. (b) XUV lasing scheme in He. Initial population in 2^3S is driven to level 3^1D via a counter intuitive pair of pulses in which the 587nm pulse is followed by the 1.08μm pulse. Once the atom (or ion) is in the 3^1D state, it is driven by a strong pulse at 668 nm to the state 2^1P. This results in Raman lasing action yielding short pulses at 58 nm. Energy levels of $He^4$and transition rates are taken from [124].

detail in Section III. The experimental discussion of Section III focuses on XUV generation via transient Raman lasing in He (at 58 nm) using well-developed technology of population excitation via cold laser plasmas and transfer of population via dark state stimulated Raman adiabatic passage (STIRAP). The use of an RF Paul trap to confine an extended cloud of charged He-like ions and produce transient LWI in, e.g., Li^+ and B^{3+} (at 6.1 nm) naturally follows the He example. Such traps could store more than 10^8 ions in a small diameter[122, 123]

B. Theoretical

In order to clarify the physics and establish the connection with GSS, we next briefly summarize the analysis behind ladder Raman lasing as in Fig. 30(c). The laser field Ω_l and the atomic density matrix ρ are determined from the coupled Maxwell-Schrödinger equations. Maxwells equations yield

$$\frac{\partial}{\partial z}\Omega_l(z,t) + \frac{1}{c}\frac{\partial}{\partial t}\Omega_l(z,t) = i\eta\rho_{ab}(z,t) \tag{5.1}$$

where $\Omega_l = \wp_{ab}\mathcal{E}_l/\hbar$ is the Rabi frequency of the laser $\wp_{ab}$ and $\mathcal{E}_l$ being, respectively, the dipole matrix element for $a \rightarrow b$ transition and the coupling field strength. The atomic polarization is governed by the off-diagonal element of the density matrix ρ_{ab} times N, where N is the density of the atoms, $\eta = 3N\lambda^2\gamma/4\pi$ with λ being the wavelength of the radiation on the $a \rightarrow b$ transition and γ the radiation decay rate between these levels.

Turning to the dynamics of the atom, we note that the transitions from c to a and from a to b are dipole allowed, while the transition from c to b is dipole forbidden making our system a cascade scheme. The transition $c \rightarrow a$ is driven by a strong coherent field of Rabi frequency Ω, while a weak probe field Ω_l is applied to the $a \rightarrow b$ transition. The Hamiltonian describing the interaction between a three level atom and the two classical fields in the rotating wave approximation and at resonance is given by

$$\mathscr{H} = -\hbar\Omega|c\rangle\langle a| - \hbar\Omega_l|a\rangle\langle b| + h.c. \tag{5.2}$$

and the master equation for the atom density matrix can be written as

$$\begin{aligned}\frac{d}{dt}\rho = -\frac{i}{\hbar}[\mathscr{H},\rho] - \frac{\Gamma}{2}\left(\sigma_1^\dagger\sigma_1\rho + \rho\sigma_1^\dagger\sigma_1 - 2\sigma_1\rho\sigma_1^\dagger\right) \\ - \frac{\gamma}{2}\left(\sigma_2^\dagger\sigma_2\rho + \rho\sigma_2^\dagger\sigma_2 - 2\sigma_2\rho\sigma_2^\dagger\right)\end{aligned} \tag{5.3}$$

in which $\sigma_1 = |a\rangle\langle c|, \sigma_1^\dagger = |c\rangle\langle a|, \sigma_2 = |b\rangle\langle a|, \sigma_2^\dagger = |a\rangle\langle b|$. Without obtaining explicit

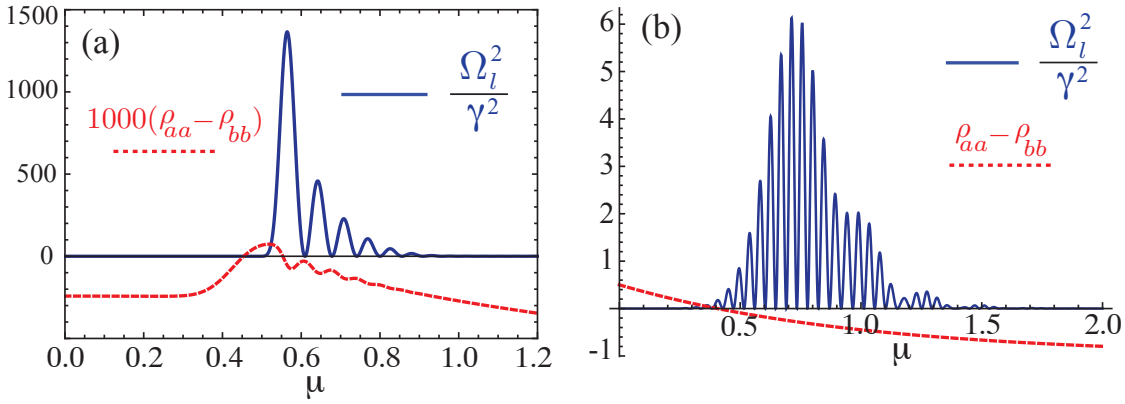

Fig. 32. Plot of the square field Ω_l/γ, where γ is the $a \rightarrow b$ decay rate, versus retarded time $\mu = t - z/c$ for $z = 13$ and initial conditions (a)$\rho_{cc}(0) = 0.75, \rho_{aa}(0) = 0.00$, and $\rho_{bb}(0) = 0.25$ and (b) $\rho_{cc}(0) = 0.00, \rho_{aa}(0) = 0.75$, and $\rho_{bb}(0) = 0.25$. The dashed curves in both figures represent the population inversion between $|a\rangle$ and $|b\rangle$.

steady-state solutions, some general conclusions can be drawn from the equations of motion of the density matrix elements on the condition of gain without inversion. For instance, the steady-state solution of ρ_{ab} yields

$$\Im(\rho_{ab}) = \frac{2\Omega_l}{\gamma}(\rho_{bb} - \rho_{aa}) + \frac{2\Omega}{\gamma}\Re(\rho_{cb}) \tag{5.4}$$

It follows from (5.4) that for sufficiently large negative values of $\Re(\rho_{cb})$, amplification $(\Im(\rho_{ab}) < 0)$ can be obtained without population inversion. The problem with such a steady-state operation is that it requires continuous pumping from b to c. This can be achieved by incoherent optical driving when flash-lamp sources are available. For XUV transition, this is a problem, and the most common pumping is via electronatom collisions in plasma. However, the quantum coherence ρ_{bc} is wiped out by electron impact. Hence, we prefer transient lasing that does not require continuous pumping. To introduce transient lasing, we note that one can write a condition for amplification of the lasing field in terms

Table I. Numerical values of parameter used in Figs. 31(a) and 32

Fig.	$\frac{c}{\gamma L}$	N(cm^{-3})	Size	Input Lasing field	Input drive field	Energy(J)
31(a)	16.5	10^{15}	13	$0.01\frac{t^2}{t^2+0.01}$	$9.9e^{-[(t-0.4)/0.1]^2}$	4.16×10^{-9}
32(a)	16.5	10^{14}	13	$0.01\frac{t^2}{t^2+1}$	$5.0e^{-[(t-0.4)/0.1]^2}$	1.18×10^{-8}
32(b)	16.5	10^{14}	13	$0.01\frac{t^2}{t^2+1}$	0	1.28×10^{-10}

of the populations only. From the equation for $\dot{\rho}_{bb}$ we have

$$\Im(\rho_{ab}) = (\gamma\rho_{aa} - \dot{\rho}_{bb})/2\Omega_l \tag{5.5}$$

Then, the amplification condition $\Im(\rho_{ab}) < 0$ implies $\dot{\rho}_{bb} > \gamma\rho_{aa}$. This shows that there is no amplification in the steady state yet it is possible to realize a transient lasing gain. This is the basis for this paper, which combines several unconventional aspects of laser and atomic physics in order to produce transient Raman LWI in various regimes. To demonstrate the feasibility of transient lasing, we focus on He and He-like ions as indicated in Fig. 31(b). Numerical solutions to the coupled MaxwellSchrodinger equations with initial pumping to the c ladder state, together with the Ω coupling to a and lasing to b are shown in Figs. 31(a) and 32. In numerical simulations, we have normalized time and distance such that the equations become dimensionless. We choose the unit of time to be $\tau_1 = 0.55$ ns and the unit of length is $L = 1$ cm. For our system, $\Gamma = \tau_2^{-1} = 6.4 \times 10^7 s^{-1}, \gamma = \tau_1^{-1} = 1.8 \times 10^9 s^{-1}$, and $\lambda = 58.4$nm. A summary of parameters used in each figure is given in Table I.

We send in a very weak lasing field Ω_l and let it propagate through the medium along the z-axis. We plot the output lasing field square Ω_l^2 versus retarded time $\mu = t - z/c$in Fig. 31(a); please note that $\rho_{aa} - \rho_{bb} < 0$ for all time. Fig. 32(a) shows output Ω_l^2 as a function of μ for a 13cm long sample. The inset shows population inversion as a function of μ in the lasing transition $a \rightarrow b$. The system starts to lase with inversion; however, after a short

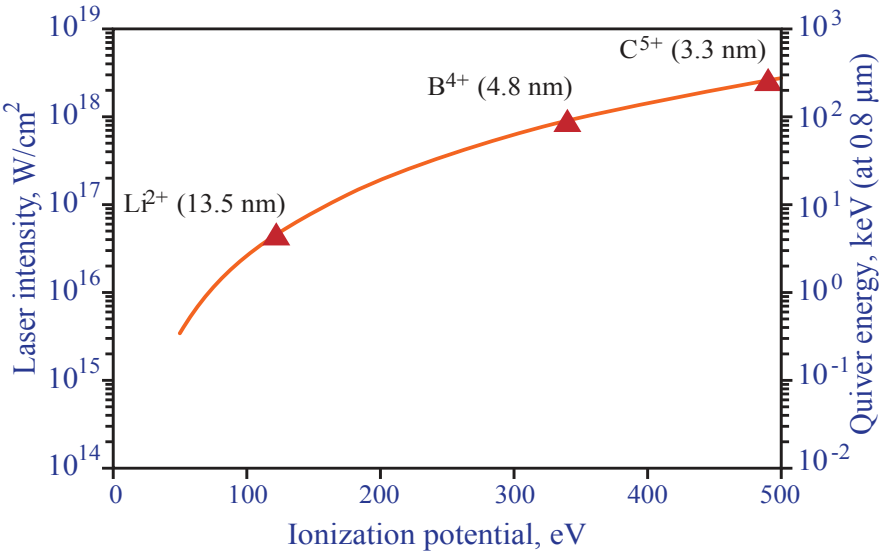

Fig. 33. Laser intensities required for an ionization rate of $10^{12}s^{-1}$ versus ionization potential of H-like ions (from[126]); solid line: Keldysh theory [125]. Corresponding quiver energy $\epsilon_q = e^2E^2/4m_e\omega^2$ is shown on the right for laser wavelength $\lambda = 0.8\mu$m.

time, it operates without inversion on the $a \to b$ transition. This is due to a combination of build up of the coherence ρ_{bc} between levels b and c and the macroscopic dipole going as ρ_{ab}. Note that the latter has much in common with the effect of laser lethargy[107] and the build up of superradiance.

One can demonstrate the connection with superradiance by pumping directly into the a state, so that the problem is essentially the two-level atom problem of Fig. 30(a). Most of the emission takes place well after time when $\rho_{aa} = \rho_{bb}$ which is the earmark of GSS. This is further discussed. Note, however, that the output energy associated with Fig. 32(b) is now decreased by two orders of magnitude compared to the transient LWI case of Fig. 32(a).

C. Experimental Details

In order to make clear the experimental viability of the present scheme, we next discuss the two key points of excitation of 2^3S and subsequent transfer to 3^1D in He, specifically

1) we first inject an ultrashort high-power laser pulse to ionize the He gas. We then turn off the laser and rapid recombination and de-excitation follow such that the lowest states of He atoms are prepared according to their statistical weights. Hence, for the sake of simplicity, we take the relative population of the 2^3S and 1^1S states to be 3 to 1, as in Fig. 31(b);

2) the population in the 2^3S state is then transferred to the 3^1D state via the 2^3P levels by a combination of optical pumping and dark state adiabatic transfer.

Let us first consider the physics of the laser plasma as produced in our Princeton X-ray laser facility. We envision a laser plasma created by Keldysh tunneling with a non-Boltzmann distribution of neutral excited atoms. This involves $He^+ \rightarrow He$ electron capture via three-body recombination. Three-body recombination for H-like ions is approximately proportional to the fourth power of the principal quantum number n^4 and to the square of the electron density as Ne_2. Hence, for sufficiently high initial electron density, three-body non-radiative recombination will dominate two-body radiative recombination and radiative decay.

However, the collisional ionization from highly excited states is also fast; thus, in order for three-body recombination rates to dominate ionization rates, the recombining plasma should have a low electron temperature T_e, if its electrons have Maxwellian energy distribution; otherwise, average electron energy should be low. In order to create a fully ionized He^+ plasma at low temperature, we consider the example of a plasma capillary $10 - 100\mu$m in diameter and a few centimeters long. The tunneling ionization can be used to generate the plasma[125, 126, 127, 128]. In this way, we can strip one electron from He

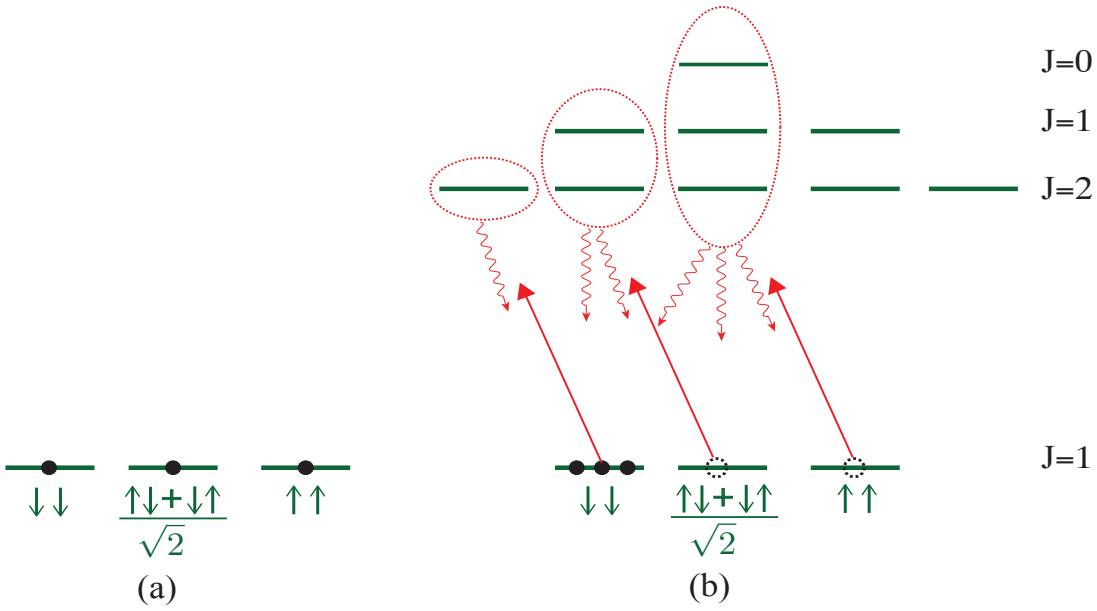

Fig. 34. (a) Atoms geing uniformly distributed in all the three magnetic sub levels of the 2^3S_1 state. (b) Optical pumping by broadband left circularly polarized light to the $2^3P_{2,1,0}$ states result in the transfer of all the population of the spin state $\downarrow\downarrow$

atoms without significantly heating the plasma, especially for ultrashort laser pulses. The laser intensity needs to be in the order of 10^{15}W/cm^2 for efficient tunneling ionization of He to He^+ according to Keldysh theory[125] (see [[126], Fig. 33]). For needle like plasma column, such intensities can easily be obtained from a Ti/Sapphire laser at wavelength $\lambda = 0.8\mu$m and $\sim$ 1m J energy per pulse in pulses of 50-100 fs duration with ionization pulse propagating in plasma channel. Use of such short pulses is crucial to minimize plasma heating. In the right-hand side of Fig. 33, the vertical axis shows the quiver energy ϵ_q (in keV), which electrons are gaining in a laser electric field E. If electrons do not collide, then their quiver energy disappears with termination of the laser pulse. Therefore, it is important to use laser pulses shorter than collision times of electrons in order to minimize plasma heating during the ionization process.

It should also be noted that quiver energy, ϵ_q goes as λ^2; hence, shorter wavelength

laser beams are advantageous for creating cooler plasma as heating is proportional to quiver energy ϵ_q[125, 126]. Therefore, it is often beneficial to use the second or even third harmonic of Ti/Sapphire laser even at a cost of several times less pulse energy than fundamental pulse energy. Additional plasma cooling is provided by its rapid radial expansion, for which the use of a small plasma column diameter is very important, as well as beneficial from the point of view of required laser pulse energy.

The bottom line is that we can create a cold laser plasma that recombines to produce an excited neutral gas. In particular, the metastable 2^3S (8000-s radiative life time) state will be formed with a statistical weight of around 3 compared to the 1^1S state.

D. Robust Population Transfer And Level Degeneracy Problem

Let us proceed to consider the transfer of population from the three 2^3S spin states to one particular magnetic sublevel of the 3^1D manifold. At time $t = 0$, the population resides in the three spin sublevels $\chi_{1,-1}, \chi_{1,0}, \chi_{1,1}$ as per Fig. 34(a). We first optically pump the atoms into one of the 2^3S spin states, say the $\chi_{1,-1}$ state as indicated in Fig. 34(b). Robust population transfer from the triplet 2^3S to singlet 3^1D is then made possible by STIRAP[129]. In this technique, one subjects the system, whose state is 2^3S at $t = 0$, to a so so called counter intuitive pulse sequence with Rabi frequencies Ω_2 and Ω_1 in which the $\Omega_2(2^3P \rightarrow 3^1D$ pulse precedes the $\Omega_1(2^3S \rightarrow 2^3P$ pulse [see Fig. 31(b)]. This pulse sequence ideally results in a complete transfer of population to the desired state 3^1D without necessarily populating the 2^3P state in the process. The mechanism of STIRAP is best understood in the dressed state basis in which we introduce bright and dark states. Beginning with the dark state

$$|0\rangle = \frac{\Omega_2|2^3S\rangle - \Omega_1|3^1D\rangle}{\sqrt{\Omega_1^2 + \Omega_2^2}} \tag{5.6}$$

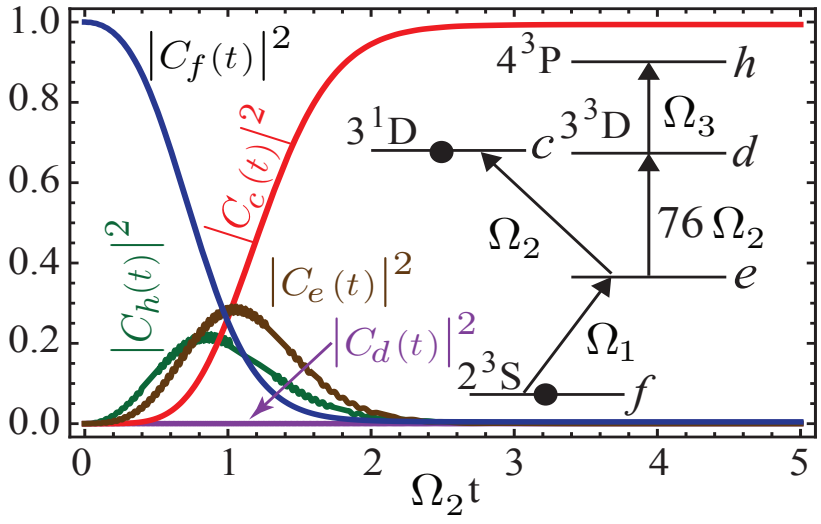

Fig. 35. Plots of probabilities for finding the system in different levels versus scaled time $\Omega_2 t$. With the help of a third laser field, the population is transferred to the desired state c. The inset shows the level scheme used for the STIRAP process, which in this involves three Gaussian pulses $\Omega_1(t) = 2\exp[-(t-0.3)^2/2]$, $\Omega_2(t) = 2\exp[-(t-0.4)^2/2]$ and $\Omega_3(t) = 150\exp[-(t-1)^2]$.

we apply Ω_2 before Ω_1 so that $|0\rangle \sim |2^3S\rangle$ during the early stages of transfer. Then, we adiabatically turn on Ω_1 while turning off Ω_2, such that $|0\rangle \sim |3^1D\rangle$ for large times. The condition of adiabaticity implies the following estimate of the required pulse energy:

$$W > 1000\frac{\hbar c S}{\lambda^3 \gamma \tau_{pulse}} \tag{5.7}$$

where S is the cross-section area of the pulse, τ_{pulse} is the pulse duration, λ and γ are the wavelength and the rate of the transition. For the weakest $3^1D \rightarrow 2^3P$ transition, $\lambda = 587$nm and $\gamma = 1.23 \times 10^4 s^{-1}$. Then, for a plasma capillary of radius ~ 0.1 mm and pulse duration $\tau_{pulse} = 1ps$, (7) yields $W > 0.4$mJ. Currently, compact picosecond lasers are commercially available with much greater energy, i.e., a few millijoule per pulse just from oscillator-regen amplifier (front-end) is well within the state of the art.

We next proceed to calculate the population transfer from 2^3S to 3^1D via STIRAP

technique. First, we send in a strong resonant pulsed laser Ω_2 to couple the 2^3P to 3^1D transition. It is worth to note that 3^1D and 3^3D are essentially degenerate states (only 0.2-nm splitting), and thus, the applied laser inevitably couples the 2^3P to 3^3D which is 1000 times stronger than the 2^3P to 3^1D transition. The Rabi frequencies of the two transitions are related by $\tilde{\Omega}_2 = \sqrt{\lambda_{de}^3 \tau_{ce} / \lambda_{ce}^3 \tau_{de}} \Omega_2 \sim 76\Omega_2$. If one uses input pulses shorter than the spontaneous decay time of these transitions, the population will be transferred to the undesired state 3^3D. To overcome this problem, it is necessary to apply pulses that are wider than the spontaneous decay times. For an optimum delay between the probe and driving pulses, it is indeed possible to transfer all the initial population in 2^3S to 3^1D. However, in plasmas, due to collision of electrons with atoms, the collisional decay time can be shorter than the duration of laser pulses, and thus, STIRAP may not work.

To overcome this difficulty, we suggest to use an additional laser pulse that couples the 3^3D to the higher energy state 4^3P. This essentially cancels absorption by the 3^3D and enhances the transition to 3^1D. The equivalent scheme is sketched in the inset of Fig. 35. For sufficiently strong driving field Ω_3 the population in 2^3S can be transferred completely to the desired state 3^1D (see Fig. 35). The optimum population transfer is exhibited when the Rabi frequency Ω_3 is approximately twice stronger than $\tilde{\Omega}_2$.

Results shown in Fig.35 are obtained by numerically solving equations for C_h, C_d , C_c, C_e and C_f which are probability amplitudes to find the system in the states h, d, c, e and f respectively, and for initial conditions $C_h(0) = C_d(0) = C_c(0) = C_e = 0$ and

$C_f = 1$. For resonant driving field, the evolution equation read

$$\dot{C}_h(t) = i\Omega_3(t)C_d(t), \tag{5.8a}$$

$$\dot{C}_c(t) = i\Omega_2(t)C_e(t), \tag{5.8b}$$

$$\dot{C}_d(t) = i\tilde{\Omega}_2(t)C_e(t) + i\Omega_3(t)C_h(t), \tag{5.8c}$$

$$\dot{C}_e(t) = i\Omega_2(t)C_c(t) + i\tilde{\Omega}_2(t)C_d(t) + i\Omega_1(t)C_f(t), \tag{5.8d}$$

$$\dot{C}_f(t) = i\Omega_1(t)C_e(t), \tag{5.8e}$$

where $\tilde{\Omega}_2 \sim 76\Omega_2$ Rabi frequencies $\Omega_i (j = 1, 2, 3)$ given in the figures are dimensionless, so that the unit of time is the inverse of the amplitude of Ω_2.

Once the population is transferred to the singlet 3^1D state, a strong driving field is applied on the 3^1D to 2^1P transition. This generates coherence between 3^1D and 2^1P which in turn makes possible transient gain between 2^1P to 1^1S [see Figs. 31(a) and 32]

E. Discussion

In order to better understand the key results of Section II, we next consider the old problem of swept gain in short-wavelength (two-level atom) laser systems. For example, the following quote from[108] adopted for the present purposes, summarizes the physics.

"In considerations involving short-wavelength lasers, it is clear that in view of the very short spontaneous lifetimes, one would like to sweep the excitation in the direction of lasing in order that the atoms be prepared in an excited state just as the radiation from previously excited atoms reaches them.... We find that the small-signal regime of the amplifier is highly anomalous, and that superradiance plays an important role in the non-linear regime."

A coherent evolution of an ultra short pulse can be described by the coupled Maxwell

-Schrödinger equations. For a pulse whose electric field is given by

$$E(z,t) = \mathcal{E}_l(z,t)e^{i(kz-\omega t)} \tag{5.9}$$

with $\mathcal{E}_l(z,t)$ being its amplitude, and an atomic polarization having an amplitude $\mathcal{P}$ and population inversion $\Delta\mathcal{N} = \rho_{aa} - \rho_{bb}$ Maxwell-Schrodinger equation read

$$\frac{\partial}{\partial z}\Omega_l = \alpha\mathcal{P} \tag{5.10}$$

$$\frac{\partial}{\partial z}\mathcal{P} = \Omega_l\Delta\mathcal{N} \tag{5.11}$$

$$\frac{\partial}{\partial z}\Delta\mathcal{N} = -\Omega_l\mathcal{P} \tag{5.12}$$

In the above, the Rabi frequency is $\Omega_l = \wp\mathcal{E}_l/\hbar$ with $\wp$ being the atomic dipole matrix element, $\mu = t - z/c$ is the retarded time. The solutions for (23) and (24) are given by

$$\mathcal{P} = \sin\left[\int_{-\infty}^{\mu}\Omega_l(\mu')d\mu'\right] \tag{5.13}$$

$$\Delta\mathcal{N} = \cos\left[\int_{-\infty}^{\mu}\Omega_l(\mu')d\mu'\right] \tag{5.14}$$

and therefore

$$\frac{\partial}{\partial z}\Omega_l = \alpha\sin\left[\int_{-\infty}^{\mu}\Omega_l(\mu')d\mu'\right] \tag{5.15}$$

In particular, for a thin region of thickness Δz and a step function input pulse, we have

$$\Omega_l(z+\Delta z,\mu) = \Omega_l(z,\mu) + \alpha\Delta z\sin[\Omega_l(z)\mu]. \tag{5.16}$$

Thus, the output pulse is given by the input step function with an additional emitted field whose envelope oscillates at a frequency Ω_l. It should be noted that this emitted field is not governed by the population inversion $\Delta\mathcal{N}$. We have here a simple example of laser gain without inversion. The pulse is gaining energy at a maximal rate when $\Omega_l\mu = \pi/2$ at which point the population inversion $\Delta\mathcal{N} = \cos(\Omega_l\mu)$ vanishes.

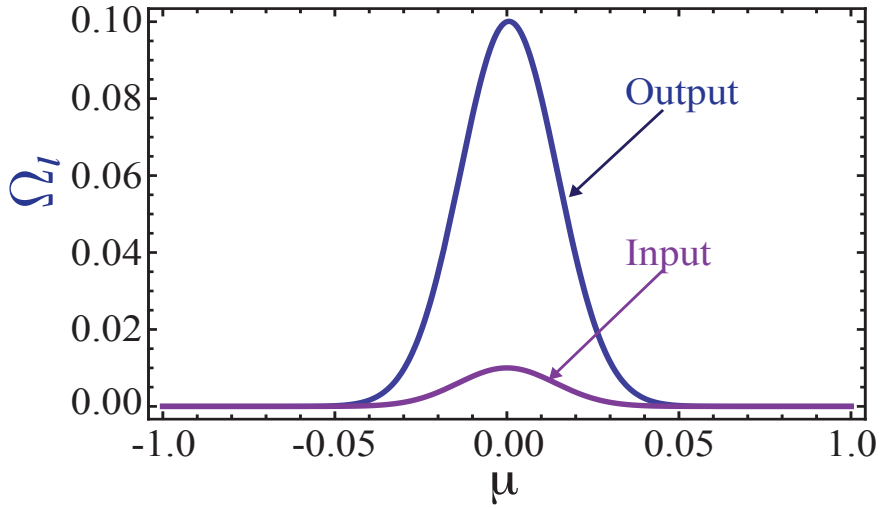

Fig. 36. Plot of $\Omega_l(\mu, z)$ versus μ for α =0.06 and $z = 5$cm and for an initial input pulse $\Omega_l(\mu, 0) = 0.1\exp(-t^2/0.4)$

If we consider the case where Ω_l is slowly varying in μ, one can write5.16 as

$$\frac{d}{dz}\Omega_l = \alpha \sin\left[\mu\Omega_l(\mu, z)\right] \tag{5.17}$$

which can be written in the form

$$\int_{\Omega_l(\mu,0)}^{\Omega_l(\mu,z)} \frac{d\Omega_l}{\sin(\mu\Omega_l)} = \int_0^z \alpha dz \tag{5.18}$$

Performing the integration, we obtain

$$\ln\left[\tan\left(\frac{\mu\Omega_l(\mu, z)}{2}\right)\right] - \ln\left[\tan\left(\frac{\mu\Omega_l(\mu, 0)}{2}\right)\right] = \alpha\mu z \tag{5.19}$$

This yields,

$$\Omega_l(\mu, z) = \frac{2}{\mu}\arctan\left[\tan(\mu\Omega_l(\mu, 0)/2)e^{\alpha\mu z}\right] \tag{5.20}$$

As an example, if we take $\alpha = 0.06$, $z = 5$cm, and input pulse $\Omega_l(\mu, 0) = 0.1\exp[-(t/0.2)^2]$, the output pulse is amplified approximately by a factor of one order of magnitude as shown in Fig. 36.

F. Conclusion

To put the present XUV scheme in context, we note that there are several methods for producing extreme ultraviolet and soft X-ray lasing: for example, using a capillary discharge [130], a free-electron laser [131], optical field ionization of a gas cell [132], or plasma-based recombination lasers [133]. Coherent XUV and soft X-ray radiation can also be produced by the generation of harmonics of an optical laser in a gas or plasma medium. Our goal here is to investigate the extent to which (transient) LWI might be useful in this problem.

Electron excitation has been the mechanism of choice for the pumping of a wide variety of XUV lasers. Alternatively, high-intensity ultrashort (with pulse duration less then 100 fs) optical pulses can be used to pump recombination lasers[126]. In this method, intense circularly polarized light ionizes atoms via tunneling process. Then, atoms recombine yielding species in excited electron states.

The three-body recombination scheme is attractive due to its potential of achieving lasing at XUV- soft X-ray wavelengths with relatively moderate pumping requirements. Several experiments have demonstrated gain and lasing in such scheme[134, 135, 136]. Recombination mechanism relies on obtaining ions in a relatively cold plasma which is possible due to short duration of the pump pulse. Then, rapid recombination and de-excitation processes follow during which transient population inversion can be created.

In this chapter, we focused on lasing in He and He-like ions that utilizes advantages of the recombination XUV soft X-ray lasers and the effects of quantum coherence. The latter, for example, is the key for LWI, wherein quantum coherence created in the medium by means of strong driving field helps to partially eliminate resonant absorption on the transition of interest and to achieve gain without population inversion. Such an effect holds promise for obtaining short wavelength lasers in the XUV and X-ray spectral domains.

CHAPTER VI

COHERENCE ENHANCED LASING*

A. Introduction

In 1905 Einstein showed that the entropy of light displayed both wave and particle aspects which led him to introduce the concept of a photon [137]. Later in 1917 he discovered stimulated emission by using detailed balance [138] and considering a beam of two-level atoms with ground state b and excited state a ($E_a - E_b = \hbar\omega$) interacting with electromagnetic field. Assuming that atomic populations in the excited N_a and the ground N_b states satisfy the rate equations [139]

$$\dot{N}_a = -AN_a - BU(\omega)(N_a - N_b), \tag{6.1}$$

$$\dot{N}_b = AN_a + BU(\omega)(N_a - N_b), \tag{6.2}$$

where AN_a is the rate of spontaneous emission and $BU(\omega)(N_a - N_b)$ is the corresponding rate of stimulated process, we obtain that in equilibrium

$$[A + BU(\omega)]N_a = BU(\omega)N_b. \tag{6.3}$$

This condition is referred to as detailed balancing. In equilibrium at temperature T relation between atomic populations is given by the Boltzmann distribution

$$\frac{N_a}{N_b} = \exp(-\hbar\omega/k_B T). \tag{6.4}$$

*Part of this chapter reprinted with permission from "Coherence Enhanced Transient Lasing in XUV Regime" by P. K. Jha, A. A. Svidzinsky and M. O. Scully, 2012. *Laser Phys. Lett* 9, 368-376 Copyright [2012] by Astro Ltd.

Combining Eqs. (6.3) and (6.4) and using the Planck formula for the photon energy density per unit frequency

$$U(\omega) = \frac{\hbar\omega^3}{\pi^2 c^3} \frac{1}{\exp(\hbar\omega/k_B T) - 1} \tag{6.5}$$

yield the ratio of the spontaneous and stimulated emission coefficients

$$\frac{A}{B} = \frac{\hbar\omega^3}{\pi^2 c^3}. \tag{6.6}$$

When we deal with transitions in the XUV or X-ray regimes, the fast spontaneous decay rates, which are given by Einstein's A coefficient, make it difficult to create population inversion. In the late 80's it was proposed and demonstrated experimentally that lasing can be achieved without population inversion if more than two levels are involved. This technique allows lasing even when a small fraction of population is in the excited state.

Recently there is much interest in developing XUV and X-ray coherent sources [140, 141, 142] which are useful tool for high resolution microscopy of biological elements [143], crystallography and condense matter in general. There are several methods for producing extreme ultra-violet lasing: for example, using a capillary discharge [144], a free-electron laser [145], optical field ionization of a gas cell [146] or plasma-based recombination lasers[147, 148]. Coherent XUV radiation can also be produced by the generation of harmonics of an optical laser in a gas or plasma medium [149, 150, 151].

The quest for compact "table-top" XUV and X-ray laser sources that can be used in individual research laboratories has motivated exploration of various excitation mechanisms, e.g., collisional [152, 153], recombinational [147, 148], etc. Ionization-recombination excitation technique holds promise for making efficient lasers at shorter wavelengths and has been successfully implemented [154]. In particular, a portable X-ray laser utilizing such excitation mechanism and operating in transient regime at 13.5 nm has been demonstrated by Princeton group [155, 156, 157]. The laser uses H-like Li ions [see Fig. 37(b)] as an

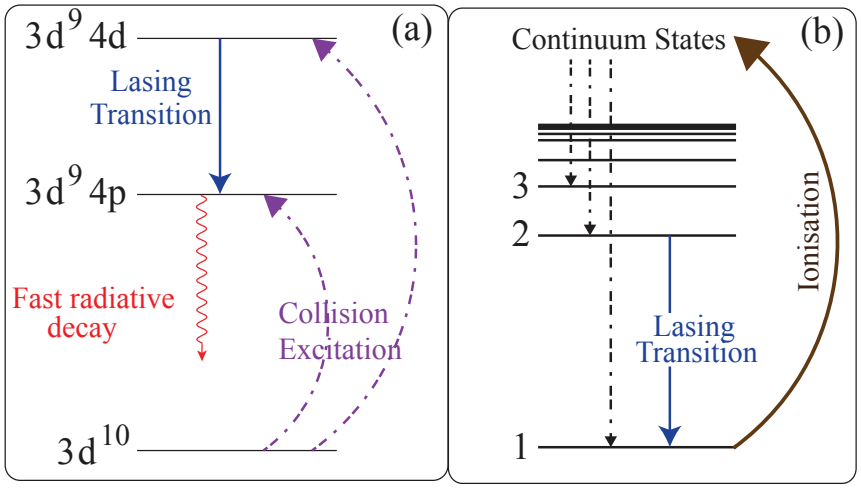

Fig. 37. (a) Lasing in Ni-like ions. (b) Lasing in H-like ions

active medium which are excited by ionization-recombination process. The basic idea of recombination lasers is that atoms are stripped off electrons in the initial step and then ions recombine by a three-body non-radiative recombination process which requires high density of electrons and prepares atoms or ions in highly excited states. By collisional de-excitation the population is transferred to lower excited states on a time scale of a few pico-seconds. For proper density, population inversion can be achieved on the probe-transition on a time scale of $10 - 100$ ps. We call this "Inversion-Window".

Other than collisional recombination, schemes involving electron impact collisions were also proposed to create inversion in Ne-like ions [158, 159, 160, 161]. Such schemes were later used for Ni-like ions as well [see Fig. 37(a)]. Here the lasing transition is $3d^9 4d \rightarrow 3d^9 4p$. The two lasing levels are populated by electron collisions. While the radiative decay from the upper lasing level ($3d^9 4d$) to the ground state ($3d^{10}$) is dipole forbidden, the fast radiative decay from the lower lasing level to the ground state makes it possible to achieve population inversion on the lasing transition and yield lasing in the "Inversion-Window".

Our goal is to investigate the extent to which coherence effects can help to make

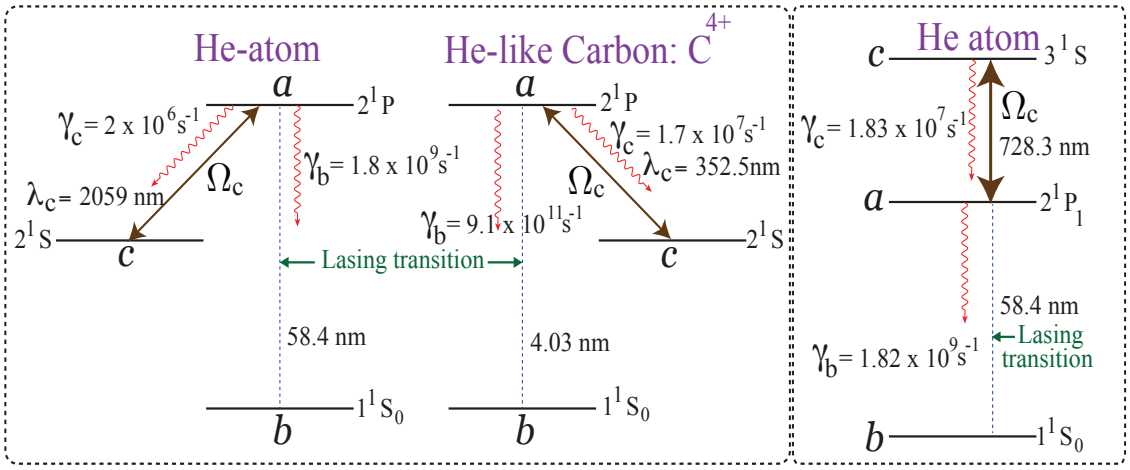

Fig. 38. Energy level diagram of He atom and He-like Carbon in Λ configuration (left box) and in He atom cascade configuration (right box).

shorter wavelength lasers. Here we study how presence of a coherent drive at optical frequency, during the inversion window, can enhance radiation generated in the adjacent XUV or X-ray lasing transition and, thus, utilize the advantages of the recombination excitation technique and the quantum coherence effects. We consider a three-level scheme and, as an example, will have in mind gas of He atoms or He-like Carbon ions as an active medium. The corresponding energy levels of He and C^{4+} and their decay rates are shown in Fig. 38. We assume that $a \leftrightarrow c$ optical transition is driven by a coherent resonant field with Rabi frequency Ω_c while short wavelength transition $a \leftrightarrow b$ is coupled to a weak probe laser field Ω_b. We disregard contributions to decoherence caused by T_2 processes.

B. Gain Enhancement by Coherent Drive

We consider three-level atomic system in Lambda (Λ) configuration where the transitions $a \leftrightarrow c$ and $a \leftrightarrow b$ are dipole allowed but the transition $c \leftrightarrow b$ is forbidden [see Fig. 39]. We assume that at the initial moment of time the population is distributed between all three levels which can be achieved, e.g., by the ionization-recombination excitation. Transition

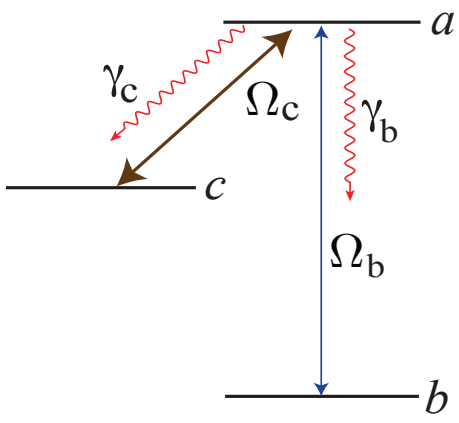

Fig. 39. Three-level atomic system in $\Lambda-$configuration.

$a \leftrightarrow c$ is driven in resonance with the Rabi frequency Ω_c. We investigate how a weak laser seed pulse at the $a \leftrightarrow b$ transition evolves during its propagation through the medium. Evolution of the atomic density matrix ϱ_{ij} is described by the set of coupled equations [2]

$$\dot{\varrho}_{ab} = -\Gamma_{ab}\varrho_{ab} + i\Omega_b(\varrho_{bb} - \varrho_{aa}) + i\Omega_c\varrho_{cb}, \tag{6.7}$$

$$\dot{\varrho}_{cb} = i(\Omega_c^*\varrho_{ab} - \Omega_b\varrho_{ac}^*), \tag{6.8}$$

$$\dot{\varrho}_{ac} = -\Gamma_{ac}\varrho_{ac} - i\Omega_c(\varrho_{aa} - \varrho_{cc}) + i\Omega_b\varrho_{cb}^*, \tag{6.9}$$

$$\dot{\varrho}_{aa} = -(\gamma_c + \gamma_b)\varrho_{aa} - i\left(\Omega_c^*\varrho_{ac} - \text{c.c}\right) - i\left(\Omega_b^*\varrho_{ab} - \text{c.c}\right), \tag{6.10}$$

$$\dot{\varrho}_{cc} = \gamma_c\varrho_{aa} + i(\Omega_c^*\varrho_{ac} - \text{c.c}), \tag{6.11}$$

$$\varrho_{aa} + \varrho_{bb} + \varrho_{cc} = 1, \tag{6.12}$$

where $\Gamma_{ab} = \Gamma_{ac} = (\gamma_c + \gamma_b)/2$ are the relaxation rates of the off-diagonal elements of the atomic density matrix, γ_c and γ_b are the spontaneous decay rates into the levels c and b, Ω_c is the Rabi frequency of the laser field.

Next we discuss two regimes, namely $\gamma_c \gg \gamma_b$ which can be treated analytically and $\gamma_c \lesssim \gamma_b$ which we investigate numerically.

1. Steady-State Approximation

Here we assume that $\gamma_c \gg \gamma_b$ and populations in the levels a and c reach approximate steady state (that is $1/\gamma_b \gg t \gg 1/\gamma_c$). To find analytical solution we assume that Ω_c =const (a real number) and Ω_b is very small. Under these assumptions equations describing evolution of levels c and a decouple and become

$$\dot{\varrho}_{cc} = \gamma_c \varrho_{aa} + i\Omega_c(\varrho_{ac} - \text{c.c}), \tag{6.13}$$

$$\dot{\varrho}_{aa} = -(\gamma_c + \gamma_b)\varrho_{aa} - i\Omega_c(\varrho_{ac} - \text{c.c}), \tag{6.14}$$

$$\dot{\varrho}_{ac} = -\Gamma_{ac}\varrho_{ac} - i\Omega_c(\varrho_{aa} - \varrho_{cc}). \tag{6.15}$$

The steady state solution ($\bar{\varrho}_{ij}$) of these equations is (we put $\gamma_b = 0$)

$$\bar{\varrho}_{aa} = \frac{4\Omega_c^2}{\gamma_c^2 + 8\Omega_c^2}[\varrho_{cc}(0) + \varrho_{aa}(0)], \tag{6.16}$$

$$\bar{\varrho}_{cc} = \frac{\gamma_c^2 + 4\Omega_c^2}{\gamma_c^2 + 8\Omega_c^2}[\varrho_{cc}(0) + \varrho_{aa}(0)], \tag{6.17}$$

$$\bar{\varrho}_{ac} = \frac{2i\gamma_c\Omega_c}{\gamma_c^2 + 8\Omega_c^2}[\varrho_{cc}(0) + \varrho_{aa}(0)], \tag{6.18}$$

where $\varrho_{cc}(0) + \varrho_{aa}(0)$ is the net population of the levels c and a. Evolution of the weak laser pulse Ω_b is described by the Maxwell equations which in the slowly varying amplitude approximation can be written as

$$\frac{\partial\Omega_b}{\partial z} + \frac{1}{c}\frac{\partial\Omega_b}{\partial t} = i\eta_{ab}\varrho_{ab}, \tag{6.19}$$

where $\eta_{ab} = (3/8\pi)N\lambda_{ab}^2\gamma_b$ is the coupling constant, N is the atomic density and λ_{ab} is the wavelength of the $a \leftrightarrow b$ transition. This equation must be supplemented by the equation for ϱ_{ab}

$$\dot{\varrho}_{ab} = -\Gamma_{ab}\varrho_{ab} + i\Omega_b(\bar{\varrho}_{bb} - \bar{\varrho}_{aa}) + i\Omega_c\varrho_{cb} \tag{6.20}$$

which couples to the equation for ρ_{cb}

$$\dot{\varrho}_{cb} = i(\Omega_c \varrho_{ab} - \Omega_b \varrho^*_{ac}). \tag{6.21}$$

Here we took into account that ϱ_{bb}, ϱ_{aa} and ϱ_{ac} are approximately constant. Let us look for solution of Eqs. (6.19-6.21) in the form of a plain wave

$$\Omega_b(t,z) \sim e^{i\omega t - ikz} \tag{6.22}$$

$$\varrho_{ab}(t,z) \sim e^{i\omega t - ikz} \tag{6.23}$$

$$\varrho_{cb}(t,z) \sim e^{i\omega t - ikz} \tag{6.24}$$

which yields the following dispersion relation

$$\left(\omega^2 - \Omega_c^2 - \frac{i\gamma_c\omega}{2}\right)(ck - \omega) + c\omega\eta_{ab}(\bar{\varrho}_{bb} - \bar{\varrho}_{aa}) + c\eta_{ab}\Omega_c\bar{\varrho}_{ac} = 0, \tag{6.25}$$

here ω is the detuning of the laser pulse frequency from the $a \leftrightarrow b$ transition frequency. If in Eq. (6.25) we treat ω as real then imaginary part of k gives gain (absorption) per unit length as a function of ω

$$\mathrm{Im}(k) = \eta_{ab}\frac{\gamma_c\omega^2(\bar{\varrho}_{aa} - \bar{\varrho}_{bb})/2 + \Omega_c\left(\Omega_c^2 - \omega^2\right)\mathrm{Im}(\bar{\varrho}_{ac})}{\left(\omega^2 - \Omega_c^2\right)^2 + \gamma_c^2\omega^2/4}. \tag{6.26}$$

In particular, for the mode resonant with the $a \leftrightarrow b$ transition $\omega = 0$ and we obtain

$$G = \mathrm{Im}(k) = \frac{\eta_{ab}}{\Omega_c}\mathrm{Im}(\bar{\varrho}_{ac}). \tag{6.27}$$

Eq. (6.27) shows that if $\mathrm{Im}(\bar{\varrho}_{ac}) > 0$ there is positive gain no matter what are the populations of the levels a and b. Thus, one can have gain without population inversion. This is the case for the $\Lambda-$ scheme in the approximate steady state for which, according to Eq. (6.18), $\mathrm{Im}(\bar{\varrho}_{ac}) > 0$. However, in the transient regime the steady state approximation is valid only for $\gamma_c \gg \gamma_b$. If $\gamma_c \lesssim \gamma_b$ the time evolution of atomic populations must be taken

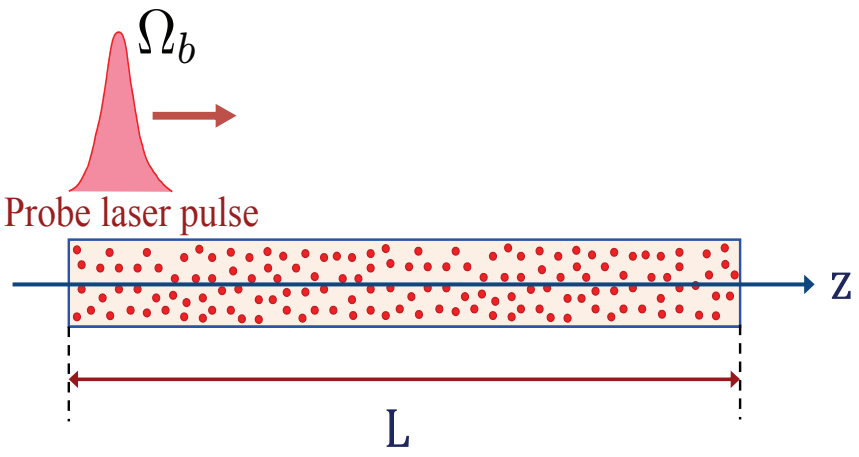

Fig. 40. Weak laser probe pulse Ω_b propagates through the atomic medium of length L gaining or losing its energy.

into account. In this regime we found no gain without population inversion. However, presence of the coherent drive field Ω_c can enhance lasing with inversion. We discuss this next.

2. Transient Lasing with Population Inversion

As before, we consider a three-level scheme having in mind gas of He atoms or He-like Carbon ions as an active medium. The corresponding energy levels and their decay rates are shown in Fig. 38. We are interested in evolution of a weak laser pulse $\Omega_b(t, z)$ propagating along the $z-$axis through the atomic medium [see Fig. 40]. First we discuss the Λ-scheme shown in Fig. 39. We assume that driving field Ω_c =const, however, populations of the levels a, b and c depend on time (transient regime). We use semiclassical approach in which evolution of $\Omega_b(t, z)$ is described by the Maxwell's equation (6.19) which is supplemented by the quantum mechanical equations (6.7)-(6.12) for the atomic density matrix.

For a weak probe field Ω_b one can put $\Omega_b = 0$ in Eqs. (6.9)-(6.11). Then Eqs. (6.9)-(6.11) for the density matrix elements ϱ_{ac}, ϱ_{aa} and ϱ_{cc} decouple from the other equations.

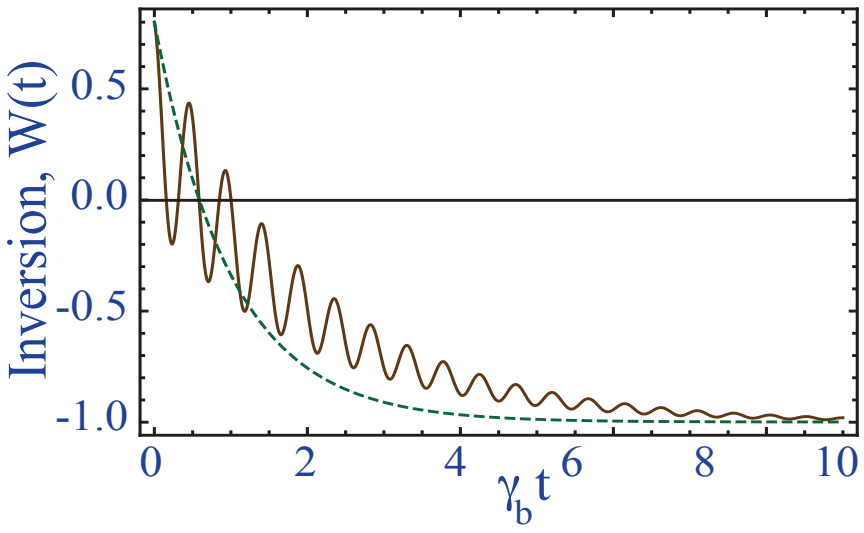

Fig. 41. Inversion $W(t)$ in the probe transition ($a \leftrightarrow b$) vs dimensionless time $\gamma_b t$. Solid curve shows the result for $\Omega_c = 6.625\gamma_b$ while dashed line is obtained with no drive. In calculations we take $\gamma_c = 1.83 \times 10^{-5}\gamma_b$ and the initial condition $\varrho_{aa}(0) = 0.9$, $\varrho_{bb}(0) = 0.1$, $\varrho_{cc}(0) = \varrho_{ac}(0) = \varrho_{ab}(0) = 0$

In particular, for $\Omega_c, \gamma_b \gg \gamma_c$ and $\varrho_{ac}(0) = 0$ we obtain (assuming Ω_c is real)

$$\varrho_{aa} = e^{-\gamma_b t/2}\varrho_{aa}(0)\left\{\left(1+\frac{\varrho_{cc}(0)}{\varrho_{aa}(0)}\right)\sin^2(\Omega_c t) + \cos(2\Omega_c t) - \frac{\gamma_b}{4\Omega_c}\sin(2\Omega_c t)\right\}, \tag{6.28}$$

$$\varrho_{cc} = e^{-\gamma_b t/2}\varrho_{aa}(0)\left\{\left(1+\frac{\varrho_{cc}(0)}{\varrho_{aa}(0)}\right)\sin^2(\Omega_c t) + \frac{\varrho_{cc}(0)}{\varrho_{aa}(0)}\cos(2\Omega_c t) + \frac{\gamma_b}{4\Omega_c}\frac{\varrho_{cc}(0)}{\varrho_{aa}(0)}\sin(2\Omega_c t)\right\}, \tag{6.29}$$

$$\varrho_{ac} = ie^{-\gamma_b t/2}\varrho_{aa}(0)\sin(\Omega_c t)\left\{\left(\frac{\varrho_{cc}(0)}{\varrho_{aa}(0)}-1\right)\cos(\Omega_c t) + \frac{\gamma_b}{4\Omega_c}\left(1+\frac{\varrho_{cc}(0)}{\varrho_{aa}(0)}\right)\sin(\Omega_c t)\right\}. \tag{6.30}$$

Using Eq. (6.12) for conservation of the net population we find that population difference

between levels a and b, defined as $W(t) = \varrho_{aa}(t) - \varrho_{bb}(t)$, is given by

$$W(t) = \frac{\varrho_{aa}(0)}{2} e^{-\gamma_b t/2} \left[3\left(1 + \frac{\varrho_{cc}(0)}{\varrho_{aa}(0)}\right) + \left(1 - \frac{\varrho_{cc}(0)}{\varrho_{aa}(0)}\right) \cos(2\Omega_c t) - \frac{\gamma_b}{2\Omega_c}\left(2 - \frac{\varrho_{cc}(0)}{\varrho_{aa}(0)}\right) \sin(2\Omega_c t) \right] - 1. \tag{6.31}$$

In Fig. 41 we plot the population difference $W(t)$ as a function of time for initial conditions $\varrho_{aa}(0) = 0.9$, $\varrho_{bb}(0) = 0.1$ and $\varrho_{cc}(0) = 0$. Solid line is obtained for $\Omega_c = 6.625\gamma_b$ while for dashed line $\Omega_c = 0$. Driving the $a \leftrightarrow c$ transition yields oscillations in the population difference between a and b levels.

a. Helium-Like Carbon

Next we solve Eqs. (6.7)-(6.12) and (6.19) numerically and obtain evolution of the probe laser pulse $\Omega_b(t, z)$ when the $a \leftrightarrow c$ transition is driven by a constant coherent field Ω_c or by a constant incoherent pump Φ. We perform simulations for the initial condition $\varrho_{aa}(0) = 0.9$, $\varrho_{bb}(0) = 0.1$, $\varrho_{cc}(0) = 0$ and take $\eta/\gamma_b = 19353$ cm^{-1} and $\gamma_c = 1.83 \times 10^{-5}\gamma_b$. As an example, we consider He-like Carbon ions for which states 2^1S_0 ($c-$ level), 2^1P_1 ($a-$level) and the ground state 1^1S_0 ($b-$level) form $\Lambda-$scheme [see Fig. 38]. For C^{4+} ions the model parameters are $\lambda_{ab} = 4.027$ nm, $\lambda_{ac} = 352.5$ nm, $\gamma_c = 1.67 \times 10^7$ s^{-1} and $\gamma_b = 9.09 \times 10^{11}$ s^{-1}. Then for ion density $N = 10^{18}$ cm^{-3} we obtain $\eta/\gamma_b = 19353$ cm^{-1}. We assume that input probe laser pulse has a Gaussian shape

$$\Omega_b(t, z = 0) = 0.01 \exp\left[-\left(\frac{\gamma_b t - 0.15}{0.05}\right)^2 \right] \gamma_b. \tag{6.32}$$

During propagation of the weak laser pulse through the medium the atomic population spontaneously decays into the ground state. After a certain time the medium is no longer inverted and the laser pulse begins to attenuate. Thus, there is an optimum length of the atomic sample which yields maximum enhancement of the pulse energy. For the optimum

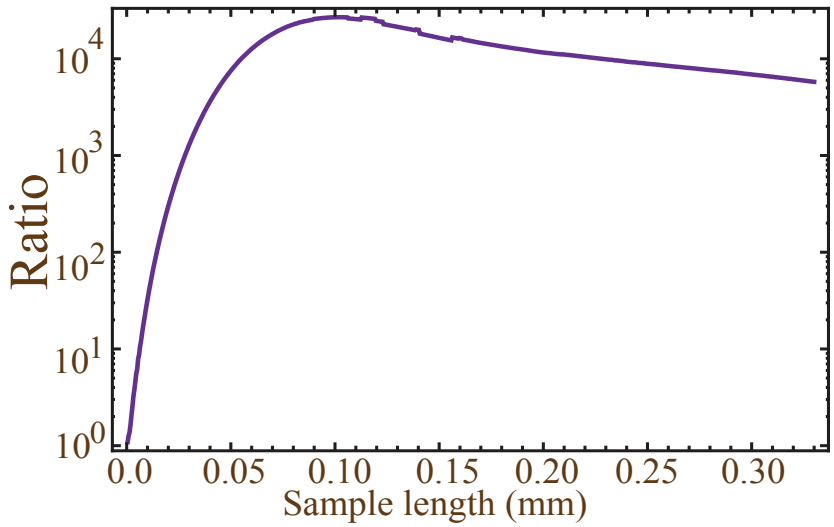

Fig. 42. Ratio of the output energy to the input energy of the probe laser pulse as a function of sample length L with no external drive. In numerical simulations we take $\gamma_c = 1.83 \times 10^{-5}\gamma_b$, $\eta/\gamma_b = 19353$ cm^{-1} and assume Gaussian initial probe pulse shape given by Eq. (6.32). Initial populations are $\varrho_{aa}(0) = 0.9$, $\varrho_{bb}(0) = 0.1$ and $\varrho_{cc}(0) = 0$, while initial coherences are equal to zero.

length the pulse leaves the medium at the onset of absorption. In Fig. 42 we plot the ratio of the output pulse energy to the input energy as a function of the sample length assuming there is no external drive. We find that optimum length corresponding to maximum output energy without any drive is $L = 0.102$ mm. At this optimum length the ratio of the output to the input probe field energy is $\sim 2.7 \times 10^4$.

Next we turn on the coherent driving field Ω_c, but keep the sample length to be $L = 0.102$ mm. This length does not corresponds to the maximum gain for three-level system and chosen as a demonstration that coherent drive can enhance the gain for a fixed sample size. In Fig. 43(a) we plot the ratio of the output laser pulse energy (at $z = L$) to the input energy (at $z = 0$) as a function of strength of the driving field Ω_c. One can see that in the presence of coherent drive the output pulse energy oscillates as a function of Ω_c. Such oscillations appear because coherence ϱ_{ac} averaged over the pulse propagation time

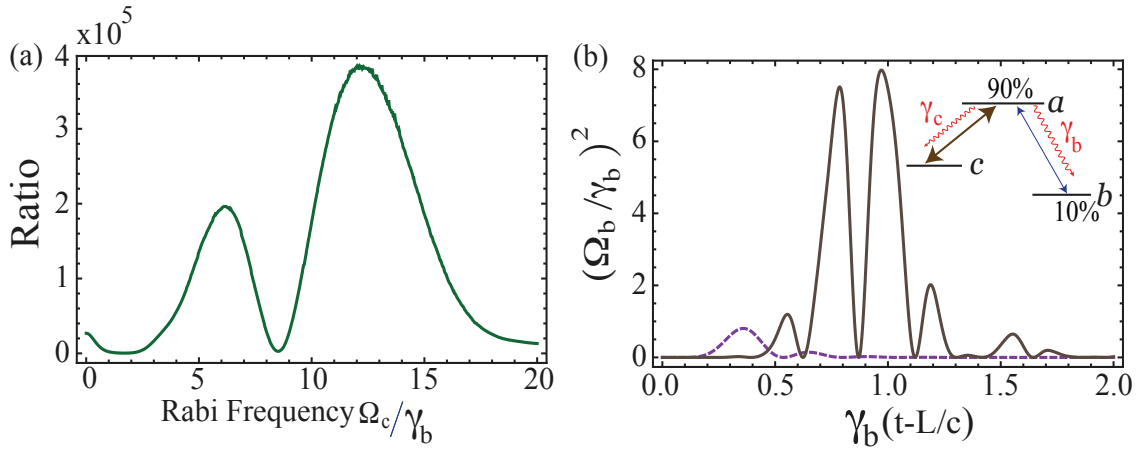

Fig. 43. (a) Ratio of the output energy to the input energy of the probe laser pulse as a function of the driving field Rabi frequency Ω_c. The ratio is $\sim 2.7 \times 10^4$ at $\Omega_c = 0$. (b) Square of the output probe pulse Ω_b/γ_b as a function of time for optimal sample length $L = 0.102$ mm with (solid line) and without (dashed) coherent drive field Ω_c. In numerical simulations we take $\gamma_c = 1.83 \times 10^{-5}\gamma_b$, $\eta/\gamma_b = 19353$ cm^{-1} and assume Gaussian initial probe pulse shape given by Eq. (6.32). The length of the sample is $L = 0.102$ mm, while the initial populations are $\varrho_{aa}(0) = 0.9$, $\varrho_{bb}(0) = 0.1$, $\varrho_{cc}(0) = 0$ and $\varrho_{ac}(0) = \varrho_{ab}(0) = 0$.

depends on Ω_c. At $\Omega_c \sim 6\gamma_b$ the enhancement factor is 7 as compared to the case with no drive field. The enhancement factor increases upto 14 for $\Omega_c \sim 12\gamma_b$. Thus, coherent drive can increase the laser pulse output energy more than an order of magnitude as compared to the pulse energy with no drive. Fig. 43(b) shows the shape of the output pulse $\Omega_b(t, z = L)$ for the optimum length in the absence of the external drive (dashed line) and optimum coherent drive $\Omega_c = 12\gamma_b$ (solid line).

If we replace the coherent drive by an incoherent pump Φ, which does not induce coherence, the gain becomes smaller when Φ increases [see Fig. 44]. The enhancement due to coherence can also be obtained for He gas as an active medium at much lower density $N = 10^{13}$ cm^{-3} with lasing at 58.4 nm. Now the model parameters are given in the left side of Fig. 38 which yields $\eta/\gamma_b = 40.75$ cm^{-1}.

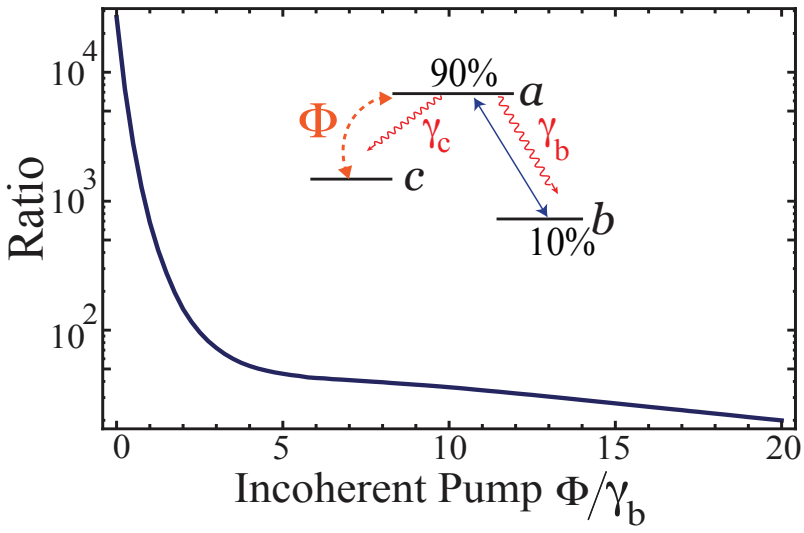

Fig. 44. Ratio of the output energy to the input energy of the probe laser pulse as a function of the incoherent pump rate Φ. The ratio is $\sim 2.7 \times 10^4$ at $\Phi = 0$

b. Neutral He as Active Medium

Next we consider $\Xi-$scheme formed by the 3^1S_0 ($c-$ level), 2^1P_1 ($a-$level) and the ground state 1^1S_0 ($b-$level) of the Helium atom (see Fig. 38 right side). For this scheme the model parameters are $\lambda_{ab} = 58.4$ nm, $\lambda_{ca} = 728.3$ nm, $\gamma_c = 1.83 \times 10^7$ s^{-1} and $\gamma_b = 1.82 \times 10^9$ s^{-1}. Then for atomic density $N = 2 \times 10^{13}$ cm^{-3} we obtain $\eta/\gamma_b = 81.50$ cm^{-1}. We assume that the input probe laser pulse has a Gaussian shape

$$\Omega_b(t, z = 0) = 0.01 \exp\left[-\left(\frac{\gamma_b t - 0.28}{0.10}\right)^2\right] \gamma_b, \tag{6.33}$$

while the drive pulse is also Gaussian with a broader width

$$\Omega_c(t, z = 0) = \Omega_{c0} \exp\left[-\left(\frac{\gamma_b t - 0.28}{0.40}\right)^2\right]. \tag{6.34}$$

Similar to the Λ-scheme we first optimize the length of the sample for the given initial population distribution and obtain that the optimum length corresponding to maximum output energy without drive is $L = 5.19$ cm. Then we turn on the driving field Ω_c, but keep

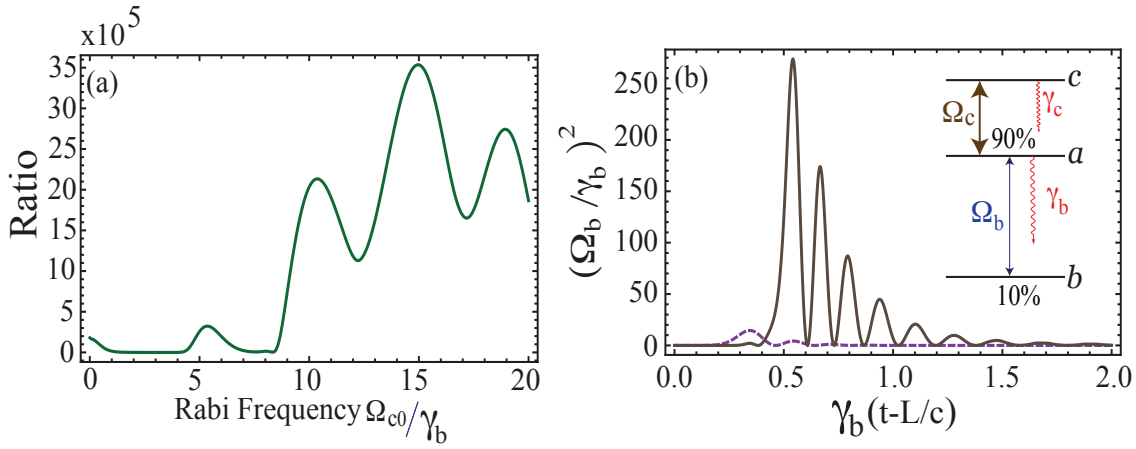

Fig. 45. (a) Ratio of the output energy to the input energy of the probe laser pulse as a function of the driving field Rabi frequency Ω_{c0}. (c) Square of the output probe pulse Ω_b/γ_b as a function of time with $\Omega_{c0} = 15\gamma_b$ (solid line) and $\Omega_c = 0$ (dashed line). In numerical simulations we take $\gamma_c = 0.01\gamma_b$, $\eta/\gamma_b = 81.50$ cm^{-1} and assume Gaussian initial probe laser pulse (Eq. (6.33)) and Gaussian driving field (Eq. (6.34)). The length of the sample is $L = 5.19$ cm, while the initial populations are $\rho_{aa}(0) = 0.9$, $\rho_{bb}(0) = 0.1$, $\rho_{cc}(0) = 0$ and $\rho_{ca}(0) = \rho_{ab}(0) = 0$.

the sample length to be the same. Fig. 45(a) shows the ratio of the output laser pulse energy (at $z = L$) to the input energy (at $z = 0$) as a function of strength of the coherent drive. One can see that, similar to the Λ configuration, the output pulse energy oscillates as a function of Ω_c and the laser pulse output energy can be increased more than an order of magnitude as compared to the pulse energy with no drive. Thus, coherence can help to extract more energy from the inverted medium and convert it into coherent laser radiation for both Λ and cascade configurations. Fig. 45(b) shows the shape of the output pulse $\Omega_b(t, z = L)$ for $\Omega_{c0} = 0$ (dashed line) and optimum coherent drive of $\Omega_{c0} = 15\gamma_b$ (solid line).

C. Backward Vs Forward Gain

Till now we have considered the evolution of the injected seed pulse at $z = 0$ in the forward direction. In this section we will briefly discuss the evolution of an identical see pulse

injected at the end of the sample i.e $z = L$. We will consider the three-level system in Lambda configuration in the limit $\gamma_b \gg \gamma_c$ as shown in Fig. 39 and we drive the transition $a \leftrightarrow b$ in the forward direction. We write the electric field as,

$$\vec{E}_c(z,t) = \frac{\epsilon_c^+}{2}\left[\mathcal{E}_c^+(z,t)e^{i\theta_c^+} + \text{c.c}\right], \tag{6.35}$$

$$\vec{E}_b^{\pm}(z,t) = \frac{\epsilon_b^{\pm}}{2}\left[\mathcal{E}_c^{\pm}(z,t)e^{i\theta_c^{\pm}} + \text{c.c}\right], \tag{6.36}$$

where

$$\theta^+ = kz - \nu t, \quad \theta^- = -kz - \nu t \tag{6.37}$$

Here (+) and (-) sign as the superscript means forward and backward direction respectively. We can write the off-diagonal term as

$$\dot{\rho}_{ab} = -\omega_{ab}\rho_{ab} - i\vec{\wp}_{ab}\cdot\vec{E}_b(\rho_{aa} - \rho_{bb}) + i\vec{\wp}_{ac}\cdot\vec{E}_c\rho_{cb} \tag{6.38}$$

$$\dot{\rho}_{ac} = -\omega_{ac}\rho_{ac} - i\vec{\wp}_{ac}\cdot\vec{E}_c(\rho_{aa} - \rho_{cc}) + i\vec{\wp}_{ab}\cdot\vec{E}_b\rho_{cb}^* \tag{6.39}$$

$$\dot{\rho}_{cb} = -\omega_{cb}\rho_{cb} - i\vec{\wp}_{ab}\cdot\vec{E}_b\rho_{ac}^* + i\vec{\wp}_{ca}\cdot\vec{E}_c\rho_{ab} \tag{6.40}$$

Let us make the following transformation

$$\rho_{ab} = \varrho_{ab}^+ e^{i\theta_1^+} + \varrho_{ab}^- e^{i\theta_1^-}, \tag{6.41}$$

$$\rho_{ac} = \varrho_{ac}^+ e^{i\theta_c^+}, \tag{6.42}$$

$$\rho_{cb} = \varrho_{cb}^+ e^{i\theta_3^+} + \varrho_{cb}^- e^{i\theta_3^-}, \tag{6.43}$$

where

$$\theta_1^{\pm} = \theta_b^{\pm};\ \theta_2^+ = \theta_c^+;\ \theta_3^+ = \theta_b^+ - \theta_c^+;\ \theta_3^- = \theta_b^- - \theta_c^+ \tag{6.44}$$

Using the transformation Eqs. (6.41-6.44) in Eqs. (6.38-6.40) we obtain for the backward direction:

$$\dot{\rho}_{ab}^- = -\Gamma_{ab}\rho_{ab}^- - i\Omega_b^-(\rho_{aa} - \rho_{bb}) + i\Omega_c\rho_{cb}^- \tag{6.45}$$

$$\dot{\rho}_{cb}^{-} = -\Gamma_{cb}\rho_{cb}^{-} - i\Omega_b^{-}\rho_{ac}^{+*} + i\Omega_c^{*}\rho_{ab}^{-} \tag{6.46}$$

and for the forward direction we obtain

$$\dot{\rho}_{ab}^{+} = -\Gamma_{ab}\rho_{ab}^{+} - i\Omega_b^{+}(\rho_{aa} - \rho_{bb}) + i\Omega_c\rho_{cb}^{+} \tag{6.47}$$

$$\dot{\rho}_{cb}^{+} = -\Gamma_{cb}\rho_{cb}^{+} - i\Omega_b^{+}\rho_{ac}^{+*} + i\Omega_c^{*}\rho_{ab}^{+} \tag{6.48}$$

$$\dot{\rho}_{ac}^{+} = -\Gamma_{ac}\rho_{ac}^{+} - i\Omega_c(\rho_{aa} - \rho_{cc}) + i\Omega_b^{+}\rho_{cb}^{+*} \tag{6.49}$$

The evolution of the population is given as

$$\dot{\varrho}_{aa} = -(\gamma_b + \gamma_c)\varrho_{aa} - i(\Omega_b^{+*}\varrho_{ab}^{+} - \Omega_b^{+}\varrho_{ab}^{+*}) - i(\Omega_b^{-*}\varrho_{ab}^{-} - \Omega_b^{-}\varrho_{ab}^{-*}) - i(\Omega_c^{+*}\varrho_{ac}^{+} - \Omega_c^{+}\varrho_{ac}^{+*}) \tag{6.50}$$

$$\dot{\varrho}_{bb} = \gamma_b\varrho_{aa} + i(\Omega_b^{+*}\varrho_{ab}^{+} - \Omega_b^{+}\varrho_{ab}^{+*}) + i(\Omega_b^{-*}\varrho_{ab}^{-} - \Omega_b^{-}\varrho_{ab}^{-*}) \tag{6.51}$$

$$\dot{\varrho}_{cc} = \gamma_c\varrho_{aa} + i(\Omega_c^{+*}\varrho_{ac}^{+} - \Omega_c^{+}\varrho_{ac}^{+*}) \tag{6.52}$$

From Eqs. (6.50-6.52) we see that the population equations are symmetric under the transformation $+ \leftrightarrow -$, hence the evolution of the injected (identical) seed pulse at the respective ends of the sample will be the same.

D. Rubidium Laser

In this section we will briefly review coherence enhanced Rubidium laser[1]. The level structure for the Rubidium laser (D_1line) is shown in Fig. 46. Contrary to last section where we discussed coherence enhanced lasing in Helium and Helium-like Carbon in the transient regime, here we will show that in the presence of the drive field Ω_a gain on the lasing transition (D_1) transition can be enhanced substantially.

[1]For detailed analysis of Rubidium laser, and the conditions under which lasing action can be achieved on (D_1) transition, please read[162]

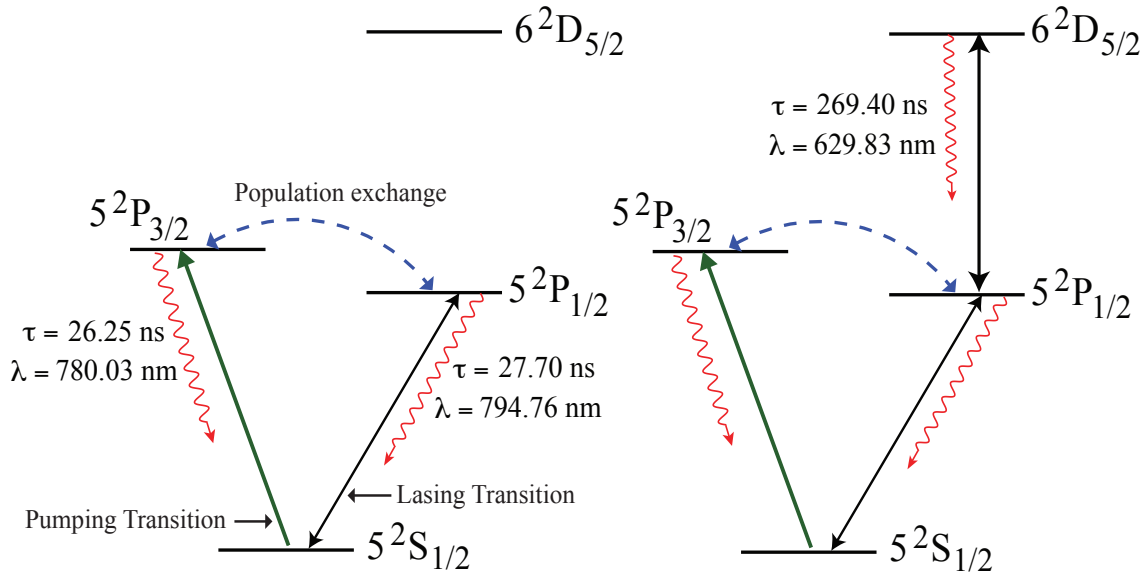

Fig. 46. Energy level diagram of atomic Rubidium. Here we have the dipole allowed transitions $5^2S_{1/2} \leftrightarrow 5^2P_{1/2}$ (D_1)line and $5^2S_{1/2} \leftrightarrow 5^2P_{3/2}$ (D_2)line. The population between the levels $P_{1/2}$ and $P_{3/2}$ are exchanged due to collisions by buffering the alkali vapor with other gasses like helium, ethane etc.

One important condition to achieve population inversion on the lasing transition is that the rate of population exchange between $5^2P_{3/2}$ and $5^2P_{1/2}$ should be much faster than the rate of spontaneous decay from the level $5P \rightarrow 5S$. Here in this section we have assumed He as the buffer gas. The excitation transfer cross-section for Rb induced by collisions with rare gas atoms and alkali metals can be found in[163].

1. Steady State Gain

The equation of motion for the density matrix elements ϱ_{ij} are given as,

$$\dot{\varrho}_{ab} = -\Gamma_{ab}\varrho_{ab} - i\Omega_b(\varrho_{aa} - \varrho_{bb}) + i\Omega_a^*\varrho_{cb} - i\Omega_e\varrho_{ea}^*, \tag{6.53}$$

$$\dot{\varrho}_{ca} = -\Gamma_{ca}\varrho_{ca} - i\Omega_a(\varrho_{cc} - \varrho_{aa}) - i\Omega_b^*\varrho_{cb}, \tag{6.54}$$

$$\dot{\varrho}_{eb} = -\Gamma_{eb}\varrho_{eb} - i\Omega_e(\varrho_{ee} - \varrho_{bb}) - i\Omega_b\varrho_{ea}, \tag{6.55}$$

$$\dot{\varrho}_{cb} = -\Gamma_{cb}\varrho_{cb} + i\Omega_a\varrho_{ab} - i\Omega_b\varrho_{ca} - i\Omega_e\varrho_{ce}, \tag{6.56}$$

$$\dot{\varrho}_{ce} = -\Gamma_{ce}\varrho_{ce} + i\Omega_a\varrho^*_{ea} - i\Omega^*_e\varrho_{cb}, \tag{6.57}$$

$$\dot{\varrho}_{ea} = -\Gamma_{ea}\varrho_{ea} + i\Omega_e\varrho^*_{ab} - i\Omega^*_b\varrho_{eb} - i\Omega_a\varrho^*_{ce}. \tag{6.58}$$

The population terms is given as

$$\dot{\varrho}_{aa} = -(\gamma_b + R_{ae})\varrho_{aa} + R_{ea}\varrho_{ee} + \gamma_a\varrho_{cc} + i(\Omega^*_a\varrho_{ca} - \Omega_a\varrho^*_{ca}) - i(\Omega^*_b\varrho_{ab} - \Omega_b\varrho^*_{ab}), \tag{6.59}$$

$$\dot{\varrho}_{bb} = \gamma_b\varrho_{aa} + \gamma_e\varrho_{ee} + i(\Omega^*_b\varrho_{ab} - \Omega_b\varrho^*_{ab}) + i(\Omega^*_e\varrho_{eb} - \Omega_e\varrho^*_{eb}), \tag{6.60}$$

$$\dot{\varrho}_{cc} = -\gamma_a\varrho_{cc} - i(\Omega^*_a\varrho_{ca} - \Omega_a\varrho^*_{ca}), \tag{6.61}$$

$$\dot{\varrho}_{ee} = -(\gamma_e + R_{ea})\varrho_{ee} + R_{ae}\varrho_{aa} - i(\Omega^*_e\varrho_{eb} - \Omega_e\varrho^*_{eb}), \tag{6.62}$$

where,

$$\begin{aligned}
\Gamma_{ca} &= \frac{\gamma_a + \gamma_b + R_{ae}}{2}, \quad \Gamma_{cb} = \frac{\gamma_a}{2}, \quad \Gamma_{ce} = \frac{\gamma_a + \gamma_e + R_{ea}}{2} \\
\Gamma_{ea} &= \frac{\gamma_e + \gamma_b + R_{ae} + R_{ea}}{2}, \quad \Gamma_{eb} = \frac{\gamma_e + R_{ea}}{2}, \quad \Gamma_{ab} = \frac{\gamma_b + R_{ea}}{2}
\end{aligned} \tag{6.63}$$

Let us assume that all the fields are real and we keep the probe field Ω_b to the lowest order while we consider all orders for the drive fields Ω_e and Ω_a [see Fig. 47(a)]. In this limit, we obtain the coherence $\varrho^{(1)}_{ab}$ as

$$\varrho^{(1)}_{ab} = -i\Omega_b\left[\frac{(\varrho^{(0)}_{aa} - \varrho^{(0)}_{bb})\mathcal{A} + (\varrho^{(0)}_{cc} - \varrho^{(0)}_{aa})\mathcal{B} - (\varrho^{(0)}_{ee} - \varrho^{(0)}_{bb})\mathcal{C}}{\mathcal{D}}\right], \tag{6.64}$$

where,

$$\mathcal{A} = \Gamma_{ca}\Gamma_{eb}\left[\Gamma_{cb}(\Gamma_{ce}\Gamma_{ea} + \Omega^2_a) + \Gamma_{ea}\Omega^2_e\right] \tag{6.65}$$

$$\mathcal{B} = \Gamma_{eb}\left[\Gamma_{ce}\Gamma_{ea} + \Omega^2_a - \Omega^2_e\right]\Omega^2_a \tag{6.66}$$

$$\mathcal{C} = \Gamma_{ca}\left[\Gamma_{cb}\Gamma_{ce} + \Omega^2_e - \Omega^2_a\right]\Omega^2_e \tag{6.67}$$

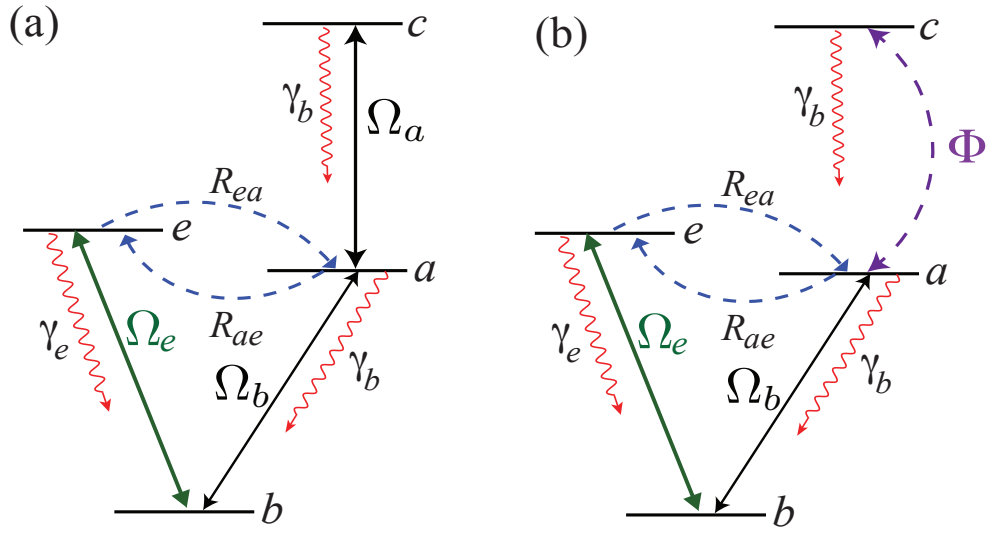

Fig. 47. Four-level model for coherence enhanced rubidium laser. Here couple the drive transition with a coherent field of Rabi frequency Ω_e. The bidirectional population exchange between the upper levels e and a is denoted by R. In (a) we have shown a drive field of Rabi frequency Ω_a while in (b) we substitute the coherent drive field with an incoherent pump Φ

$$\mathcal{D} = \Gamma_{ca}\Gamma_{eb}\left[(\Gamma_{ab}\Gamma_{cb}+\Omega_a^2)(\Gamma_{ce}\Gamma_{ea}+\Omega_a^2)+(\Gamma_{cb}\Gamma_{ce}+\Gamma_{ab}\Gamma_{ea}-2\Omega_a^2)\Omega_e^2+\Omega_e^4\right] \tag{6.68}$$

It can be easily verified that we can obtain the know results $\varrho_{ab}^{(1)}$ for cascade and Vee scheme. The zeroth order population obtained from Eqs. (6.59-6.62) as

$$\varrho_{aa}^{(0)} = \frac{2R_{ea}(\Gamma_a\Gamma_{ca}+2\Omega_a^2)\Omega_e^2}{\mathcal{M}} \tag{6.69}$$

$$\varrho_{bb}^{(0)} = \frac{(\gamma_a\Gamma_{ca}+2\Omega_a^2)[R_{ea}\gamma_b\Gamma_{eb}+(R_{ae}+\gamma_b)(\gamma_e\Gamma_{eb}+2\Omega_e^2)]}{\mathcal{M}} \tag{6.70}$$

$$\varrho_{cc}^{(0)} = \frac{2R_{ea}\Omega_a^2\Omega_e^2}{\mathcal{M}} \tag{6.71}$$

$$\varrho_{ee}^{(0)} = \frac{2(R_{ae}+\gamma_b)\Omega_e^2}{\mathcal{M}} \tag{6.72}$$

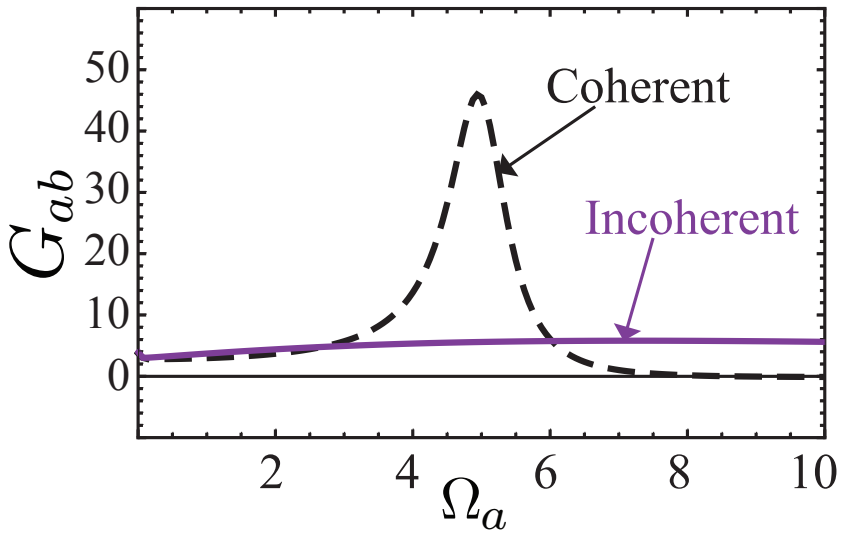

Fig. 48. Plot of the gain G_{ab} in the presence of a coherent drive Ω_a(dashed Black) and incoherent pump Φ(solid purple). For numerical simulation we used $R_{ea} = 1, R_{ae} = 0.74, \gamma_b = 0.085, \gamma_e = 0.087, \gamma_a = 0.0084, \Omega_b = 0.001, \Omega_e = 5.$

where, $\mathcal{M} = \gamma_a \Gamma_{ca} \left[R_{ea}(\gamma_b \Gamma_{eb} + 2\Omega_e^2) + (R_{ae} + \gamma_b)(\gamma_e \Gamma_{eb} + 4\Omega_e^2) \right]$. In the absence of the drive field Ω_a, and strong pump field $\Omega_e \gg \gamma_e, \gamma_b, R_{ea}, R_{ae}$ we obtain

$$\varrho_{aa}^{(0)} = \frac{R_{ea}}{R_{ea} + 2(R_{ae} + \gamma_b)}, \tag{6.73}$$

$$\varrho_{bb}^{(0)} = \frac{R_{ae} + \gamma_b}{R_{ea} + 2(R_{ae} + \gamma_b)}, \tag{6.74}$$

$$\varrho_{ee}^{(0)} = \frac{R_{ae} + \gamma_b}{R_{ea} + 2(R_{ae} + \gamma_b)}, \tag{6.75}$$

The steady-state inversion ($\varrho_{aa}^{(0)} + \varrho_{ee}^{(0)} - \varrho_{bb}^{(0)}$) is given as,

$$\frac{R_{ae}}{R_{ea} + 2(R_{ae} + \gamma_b)} > 0 \tag{6.76}$$

and also on the lasing transition $(a \leftrightarrow b)$ we obtain,

$$\varrho_{aa}^{(0)} - \varrho_{bb}^{(0)} = \frac{R_{ea} - R_{ae} - \gamma_b}{R_{ea} + 2(R_{ae} + \gamma_b)}, \tag{6.77}$$

For inversion on the lasing transition we require

$$R_{ea} > R_{ae} + \gamma_b \tag{6.78}$$

Let us now study the effect of drive field Ω_a on the gain G_{ab} defined as

$$G_{ab} = \frac{3}{8\pi} N \lambda_b^2 \gamma_b \frac{\varrho_{ab}}{-i\Omega_b} \tag{6.79}$$

The result of the numerical simulation of Eqs. (6.53-6.62) is shown in Fig. 48 in which we have shown the effect of the drive field on the gain G_{ab}. We see that in the presence of the drive field we can enhance the gain by an order of magnitude for $\Omega_a \sim 5$. To emphasize the role of the coherence we simulated Eqs. (6.53-6.62) in the presence of the incoherent pump and we do not see any substantial enhancement.

E. Conclusion

In this chapter we study the effect of coherence on the transient lasing. First we illustrated a possibility of having transient lasing without population inversion in $\Lambda-$scheme when spontaneous decay rate of the driving transition γ_c is greater than those of the lasing transition γ_b. However, such condition is usually not satisfied for lasing at shorter wavelength as the spontaneous decay rate is proportional of the third power of the frequency. Having in mind improving performance of XUV and X-ray lasers with inversion by driving a longer wavelength optical transition, we consider Λ and Cascade schemes with $\gamma_b \gg \gamma_c$.

To show the effect of coherence we first optimize parameters of the model in the absence of the driving field, i.e., find the sample length for the fixed initial populations which yields the maximum output energy of the laser pulse. Then we drive the $a \leftrightarrow c$ transition with a coherent source Ω_c or an incoherent pump Φ. We demonstrate that coherent drive can yield substantial enhancement of the laser pulse energy for highly inverted medium than in

the absence of the coherent drive, while incoherent pump results in energy decrease. We applied this coherence enhanced lasing scheme for Rubidium laser in steady-state regime and demonstrated that an enhancement of an order of magnitude can be achieved. Thus, implementation of a coherent drive at optical frequency could be a useful tool for improving performance of lasers in XUV and X-ray regions.

CHAPTER VII

CARRIER-ENVELOPE PHASE EFFECTS ON ATOMIC EXCITATION BY MULTI-CYCLE PULSES*

A. Introduction

As is well-known, the electric field of a laser pulse given by

$$E(t) = \mathcal{E}_0 f(t) \cos(\nu t + \phi) \tag{7.1}$$

can be characterized by its amplitude $\mathcal{E}_0$, its carrier envelope $f(t)$, its frequency ν, and its carrier-envelope phase (CEP) ϕ. The CEP is the most difficult parameter to control and even to measure. Recently, a lot of research has been devoted to the CEP. Namely, the CEP strongly affects many processes involving ultrashort few-cycle pulses [164]. In particular, CEP effects on high-harmonic generation [165], strong-field photoionization [166], the dissociation of HD^+ and H_2^+ [167], the electron dynamics in a strong magnetic field [168], the population inversion during a quantum transition [169], and the external- and internal-photo-effect currents [170, 171] have been demonstrated by few-cycle pulses.

For longer laser pulses, the influence of the CEP becomes smaller (very often it is beyond the experimental abilities to be measured). So the important question is what is the maximal duration of laser pulses that can still have the CEP effects? It is a fundamental question, but also it brings new interesting possibilities to measure and control parameters of laser pulses and applications. A stabilized and adjustable CEP is important for applications such as optical frequency combs [172] and quantum control in various me-

*Part of this chapter is reprinted with permission from "Experimental observation of carrier-envelope-phase effects by multicycle pulses" by P. K. Jha, Y. V. Rostovtsev, H. Li, V. A. Sautenkov, and M. O. Scully 2010. *Phys. Rev. A* 81, 033404(1)-033404(6), Copyright [2011] by American Physical Society

dia [173]. Several techniques have been developed to control the CEP of femtosecond pulses [174, 168]. A crucial step in attaining this control is measuring the CEP to provide feedback to the laser system. Promising approaches for short pulses use, for instance, photoionization [175] and quantum interference in semiconductors [171].

For longer pulses, on the other hand, there are no such methods. Recently, a method has been presented for the measurement of the absolute CEP of a high-power, many-cycle driving pulse, by measuring the variation of the XUV spectrum [176] by applying the interferometric polarization gating technique to such pulses [177]. We stress here that extending the CEP control to longer pulses creates interesting possibilities to generate pulses with accuracy that is better than the period of optical oscillation. First, it allows researchers to improve laser systems that generate laser pulses with better reproducibility and accuracy and better controlled. Second, it provides an additional handle to control the process of collisions. Femtosecond pulses are shorter than the time duration of collisions and cannot be used to study collisions under the action of electromagnetic fields; meanwhile the current approach of extending the duration of the pulses with measureable or controllable CEP allows researchers to extend the coherent control to a new level when they are able to study molecular collisions or electron collisions in nanostructures under the action of strong electromagnetic fields with known CEP. Electromagnetically induced magnetochiral anisotropy in a resonant medium demonstrated in [178] can be enhanced by the control of the CEP of optical radiation in the laser induced chemical reactions [179].

In this chapter, we present the CEP effects in the population transfer between two bound atomic states interacting with pulses consisting many cycles in contrast with few-cycle pulses [64]. For our experiment, we use intense radio-frequency (RF) pulses interacting with the magnetic Zeeman sub-levels of Rubidium (Rb) atoms. We have found that, for long pulses consisting two carrier frequencies, the CEP of the pulse strongly affects that transfer. It is worth noting here that our scheme has no limitation on the duration of pulses.

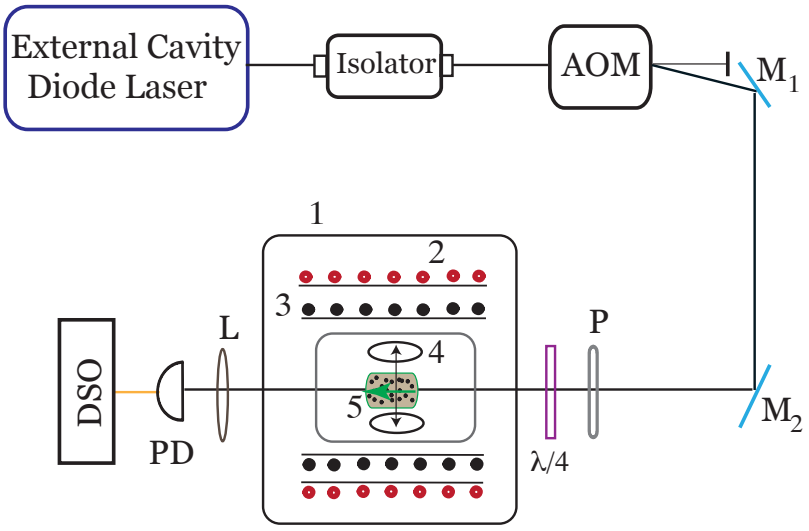

Fig. 49. Experimental setup. ECDL-External cavity diode laser; AOM- Acousto-optic modulator; P- Polarizer, PD-Photodiode; L-Lens, the oven is assembled with 1. copper tube; 2. non-magnetic heater on a magnetic shield; 3. solenoid; 4. pair of Helmholtz coils; 5. Rb cell.

The significance of our experiment is that it provides the insight of CEP effect in a new regime. The experiment is the first, to our knowledge, to observe the CEP effect on a transition between two *bound* atomic states with such *long* pulses. Our experiment provides a unique system serving as an experimental model for studying ultrashort optical pulses. The obtained results may be easily extended to optical experiment.[1]

B. Experiment

In this section we will discuss the experimental aspect of our paper. We discuss the setup and the procedure to measure the population transfer due to RF excitation, taking into account the dephasing factor η. In subsection B, we present our experimental results which includes the non-linear behavior of the multi-photon excitation peak ③ [see Fig. 52(a)].

[1] Zeeman sublevels are well isolated from other states and provide a good approximation to a two-level system.

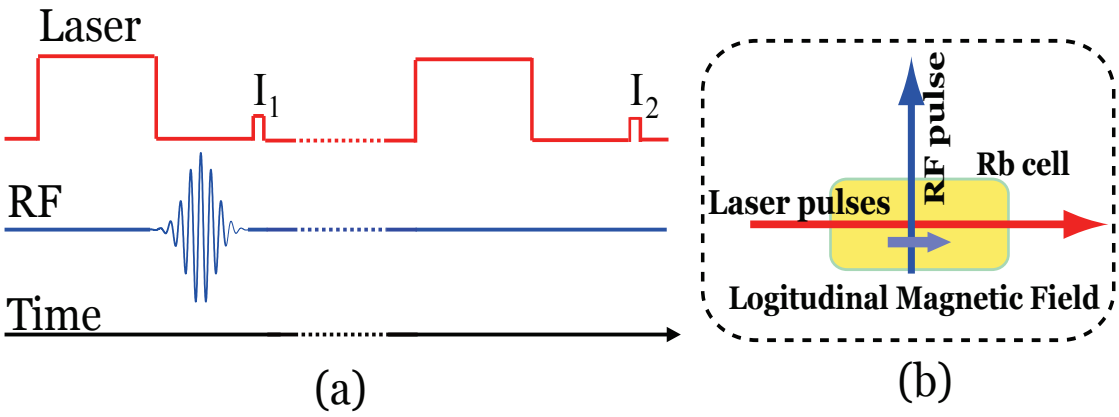

Fig. 50. (a) Time sequence of the laser and the RF pulses to determine the population transfer due to RF excitation. (b) Configuration of the laser and rf pulses along with the longitudinal magnetic field with respect to the Rb cell.

Effect of the CEP of the carrier-frequency components on the population transfer due to multi-photon excitation is shown in Fig. 54.

1. Setup and Population transfer

The experimental setup is shown in Fig. 49. An external cavity diode laser was tuned to the D_1 resonance line of ^{87}Rb atoms at $|5^2S_{1/2}; F = 1\rangle \leftrightarrow |5^2P_{1/2}; F = 1\rangle$ transition. A 2.5 cm long cell containing ^{87}Rb (and 5 torr of Neon) is located in an oven. The cell is heated in order to reach an atomic density of the order of 10^{11} cm^{-3}. A longitudinal static magnetic field is applied along the laser beam to control the splitting of the Zeeman sub-levels of the ground state $|5^2S_{1/2}; F = 1, m_F = -1, 0, 1\rangle$. A pair of Helmholtz coils produces a transverse bichromatic rf field with two central frequencies at ν_1 and ν_2.

In this experiment we tuned the longitudinal magnetic field to control the Zeeman splitting while keeping the carrier frequencies intact. A function generator was programmed to provide multi-cycle bichromatic pulses with controllable parameters, such as the pulse duration, CEPs and the amplitudes of the two carrier frequencies.

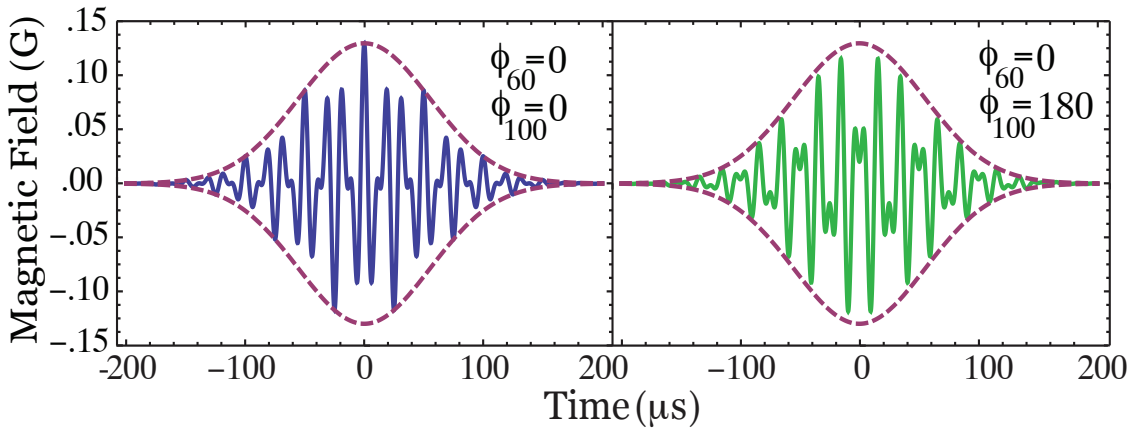

Fig. 51. CEP-shaped bichromatic pulses with spectral components of 60 kHz and 100kHz. FWHM for both the pulse is 130 μs with gaussian envelope. Unit of the magnetic field is Gauss.

To determine the population transfer due to the rf excitation, the experiment is performed with a sequence of laser pulses with a rf pulse followed by a sequence of laser pulses without rf pulse. For the transmitted probe pulse intensity is given by $I_1 = I_0\eta e^{N\sigma LP_a}$, where I_0 is the probe pulse input intensity, η is the factor due to dephasing, N is the atomic density, σ is the absorption cross-section, L is the cell length and P_a is the population of the upper levels due to RF excitation. For the second sequence , in which there is no RF excitation, the transmitted probe pulse intensity is given by $I_2 = I_0\eta$. Therefore, the population due to rf excitation is given by the quantity $-ln(I_1/I_2) = N\sigma LP_a$.

The energy level scheme of ^{87}Rb and the configuration of the optical and RF pulses is shown in Fig. 50. The ground state of ^{87}Rb has three Zeeman sub-levels; a right-circularly polarized (RCP) laser pulse optically pumps the system and drives the atoms to the sub-level $|5^2S_{1/2}; F = 1, m_F = 1\rangle$. This is followed by the bichromatic rf pulse, which excites the atoms to the sub-levels $|5^2S_{1/2}; F = 1, m_F = -1, 0\rangle$ whose population is subsequently determined by measuring the transmission of a following weak RCP optical probe pulse. The rf pulse is delayed by 165 μs with respect to the optical-pumping laser pulse and has a

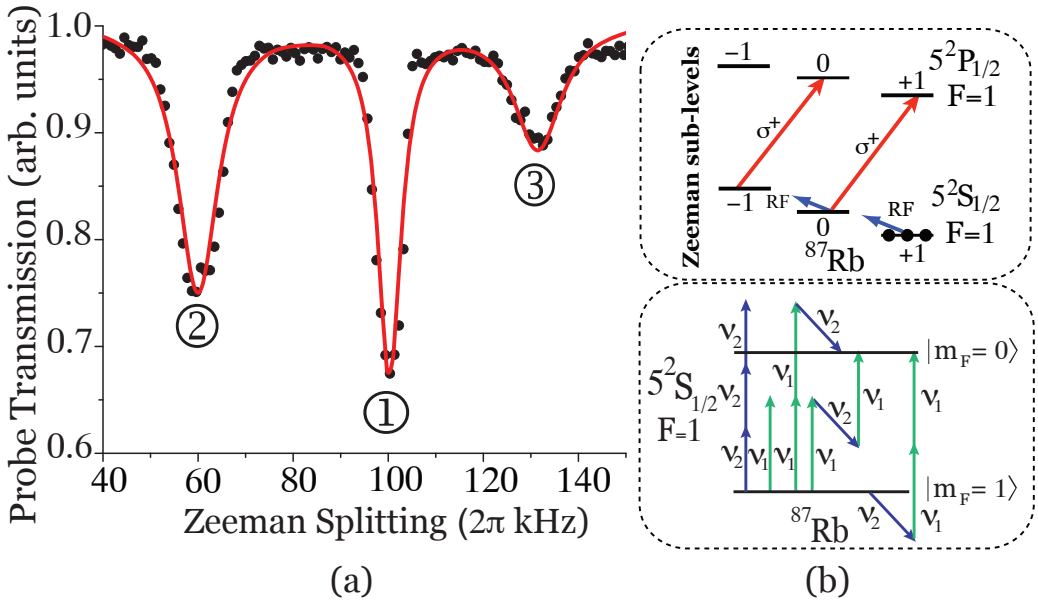

Fig. 52. (a) Optical probe transmission profile for the one-photon [peaks ① and ②] and three-photon [peak ③] transition under the bichromatic rf field excitation. (b) Upper block: Energy level scheme of ^{87}Rb; Lower block: Resonant and non-resonant pathways contributing to three-photon peak.

duration of 130 μs (FWHM). In Fig. 51 we have plotted two such CEP-shaped bichromatic pulses, with spectral components of 60 kHz and 100kHz, used in our experiment. The transmitted intensity of the probe pulse, delayed by 330 μs with respect to the optical-pumping pulse, is monitored by a fast photodiode.

2. Experimental Results

Single and multi-photon (resonant and non-resonant) excitation under bichromatic rf field interaction with ^{87}Rb are shown in Fig. 52. Peaks ① and ② in the probe transmission profile are single photon absorption peaks at frequencies ω_1=100kHz and ω_2=60kHz respectively. Peak ③ emerges due to different possible excitations between the initial and the final states [see Fig. 52 (b) lower block]. Resonant multi-photon excitation which corresponds to peak ③ at ω=140kHz in Fig. 52, is shifted to about ω=130kHz. The rf field is

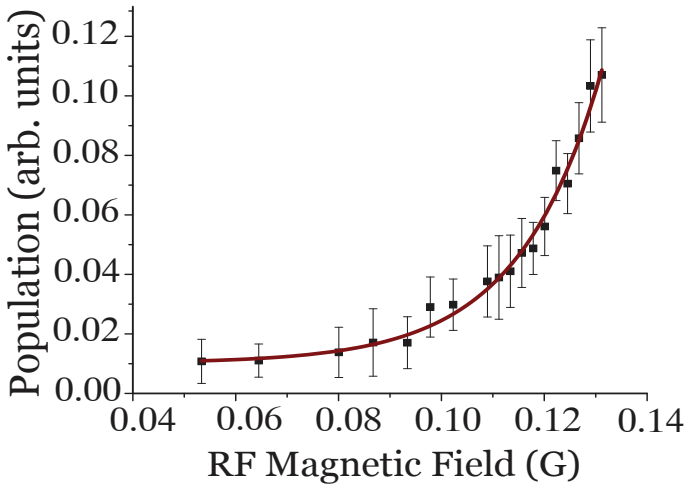

Fig. 53. Non-linear dependence of multi-photon excitation on the traverse magnetic field. Unit of the magnetic field is Gauss.

very strong, so non-resonant one- and three-photon transition should be taken into account [see Appendix G]. These non-resonant contributions interfere with resonant three-photon transitions and the excited population depends on the phases of fields with frequencies ν_1 and ν_2. To study this peak we first investigated the dependence of population transfer as a function of the applied transverse magnetic field strength. Fig. 53 shows the non-linear behavior of the process, in which the multi-photon excitation is negligible for weak transverse magnetic field and starts to grow non-linearly with the increase in the amplitude of the driving RF pulse.

The main results of the experiment are shown in Fig. 54 where we have plotted the population (σNLP_a) as a function of carrier-envelope phase of one of the two spectral components of the bichromatic field while keeping the other phase component at zero. Fig. 54(a)(II) shows the oscillatory behavior when the phase of $\phi_{60\text{kHz}}$ is changed while keeping $\phi_{100\text{kHz}} = 0$. Similar effect is observed vice-versa which is shown in Fig. 54(a)(I). Ratio of the frequency of oscillations for the two cases, when the phase is changed from $0 \rightarrow 2\pi$, is $O_r = 0.578 \pm 0.035$ which is equal to ν_2/ν_1. Fig. 54(b) shows the effect of

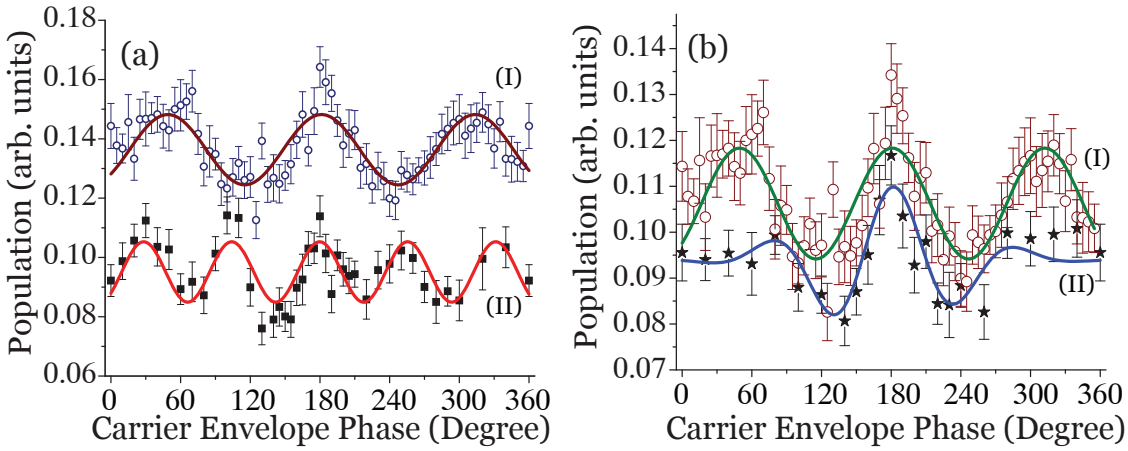

Fig. 54. Oscillatory nature of the population transfer by changing the phase of one carrier frequency while keeping the other at zero for the bichromatic rf Pulse. (a) (I) Changing the phase $\phi_{100\text{kHz}}$ and $\phi_{60\text{kHz}}$=0 (II) Changing the phase $\phi_{60\text{kHz}}$ and $\phi_{100\text{kHz}}$=0. (b) Effect of the pulse duration T (FWHM) on the population transfer. (I) T=130μs, (II) T=100μs. Here we changed the phase $\phi_{100\text{kHz}}$ while keeping $\phi_{60\text{kHz}} = 0$

pulse duration (i.e number of cycles) on the population transfer where we have plotted the population transferred for two set of pulse width T(full width at half maximum, FWHM). Here (I) T=130μs, (II) T=100μs. In either case we changed the phase of $\phi_{100\text{kHz}}$ while keeping $\phi_{60\text{kHz}} = 0$. In Fig. 54 (a) we have shifted the curve (I) vertically, for the sake of clarity and distinguish the variations in the two curve (I) & (II) clearly. We experimentally observed a variation in the population about 25%.

C. Theory

Let us now move to the theoretical aspect of the results obtained here. The goal of theoretical consideration presented here is to gain physical insights that helps to understand the CEP effects for such long pulses that have envelop containing up to fifteen periods of oscillations, as well as the limitations imposed on the length of pulses.

The Hamiltonian for an atomic state with $F = 1$ in a magnetic field $B = (B_x, B_y, B_z)$ is given by

$$\mathscr{H} = -g\mu_0 \begin{pmatrix} B_z & \frac{B_x+iB_y}{\sqrt{2}} & 0 \\ \frac{B_x-iB_y}{\sqrt{2}} & 0 & \frac{B_x+iB_y}{\sqrt{2}} \\ 0 & \frac{B_x-iB_y}{\sqrt{2}} & -B_z \end{pmatrix}, \tag{7.2}$$

where $g = -1/2$ is the Lande factor for this Rb state, μ_0 is the Bohr magneton, $B_z = B_0$ is the static magnetic field that is chosen in the direction of the z-axis; B_x and B_y are the transverse components driven by a function generator. The linearly-polarized bichromatic magnetic field is given as,

$$B_x(t) = e^{-\alpha^2 t^2}\{B_1\text{cos}(\nu_1 t + \phi_1) + B_2\text{cos}(\nu_2 t + \phi_2)\}, \tag{7.3}$$

where $\alpha = (2\sqrt{\text{ln}2})/T$ and T is the FWHM duration of the pulse and $B_y = 0$. For the magnetic dipole transition, the relaxation due to atomic motion is the most important. The density matrix equations is given by

$$\dot{\rho} = -\frac{i}{\hbar}[\mathscr{H}, \rho] - \Gamma(\rho - \rho_0), \tag{7.4}$$

where $\mathscr{H}$ is given by Eq.(7.2), Γ quantifies the relaxation process due to atomic motion and ρ_0 is the thermal equilibrium density matrix of the atoms in the cell without the optical and RF fields. For simple explanation we will consider only two levels coupled by the bichromatic field and neglect any type of relaxation. The Rabi frequency is given by

$$\Omega(t) = e^{-\alpha^2 t^2}\{\Omega_1\text{cos}(\nu_1 t + \phi_1) + \Omega_2\text{cos}(\nu_2 t + \phi_2)\}, \tag{7.5}$$

where $\Omega_{(1,2)} = g\mu_0 B_{(1,2)}/\sqrt{2}\hbar$. The equation of motions for the probability amplitudes C_a

and C_b are given by

$$\dot{C}_a = i\Omega(t)e^{i\omega t}C_b, \tag{7.6a}$$

$$\dot{C}_b = i\Omega^*(t)e^{-i\omega t}C_a. \tag{7.6b}$$

Let us consider the perturbative approach $C_b(t) \cong 1$. We look for a solution of the form $C_a = C_a^{(1)} + C_a^{(3)}$ where

$$C_a^{(1)} = i\int_{-\infty}^{\infty} \Omega(t')e^{i\omega t'}dt' \tag{7.7}$$

and

$$C_a^{(3)} = -i\int_{-\infty}^{\infty}\left\{\Omega(t')e^{i\omega t'}\int_{-\infty}^{t'}\left[\Omega^*(t'')e^{-i\omega t''}\int_{-\infty}^{t''}\Omega(t''')e^{i\omega t'''}dt'''\right]dt''\right\}dt' \tag{7.8}$$

The excited population is the result of interference of resonant three-photon excitation and non-resonant one-photon with frequency ν_1 and three-photon ν_2 where the detunings are 30 kHz and 50 kHz correspondingly [see inset of Fig. 52(a)]. The probability amplitude can be written as

$$C_a = A_1(\nu_1)e^{-i\phi_1} + A_3(\nu_2)e^{-i3\phi_2} + A_3(2\nu_1 - \nu_2)e^{-i(2\phi_1-\phi_2)} \tag{7.9}$$

that gives the same dependences on the phases of bichromatic field as shown in Fig. 54. Here, in a weak field approximation,

$$A_1(\nu_1) = i\left(\frac{\sqrt{\pi}}{2\alpha}\right)\Omega_1 e^{-[(\omega-\nu_1)/2\alpha]^2}, \tag{7.10}$$

is the probability amplitude of non-resonant excitation due to one-photon transition,

$$A_3(\nu_2) = -i\left[\frac{\sqrt{\pi}\Omega_2^3}{16\sqrt{3}\alpha\nu_2(\omega-\nu_2)}\right]e^{-\left[(\omega-3\nu_2)^2/12\alpha^2\right]}, \tag{7.11}$$

is due to non-resonant three-photon excitation, and

$$A_3(2\nu_1-\nu_2) = -i\left(\frac{\sqrt{\pi}\Omega_1^2\Omega_2}{8\sqrt{3}\alpha}\right)\left[\frac{1}{2\nu_1(\omega-\nu_1)}+\frac{1}{(\nu_1-\nu_2)(\omega-\nu_1)} + \frac{1}{(\nu_1-\nu_2)(\omega+\nu_2)}\right] e^{-\left[(\omega-2\nu_1+\nu_2)^2/12\alpha^2\right]} \tag{7.12}$$

is due to resonant three-photon excitation. Here the first terms corresponds to Hyper-Raman type process, the second term corresponds to Doppleron type process as shown in the lower block of Fig. 52 (b).

In Appendix G we have shown the relative strength of the three processes with the experimental parameters. We show that when we excite with strong field i.e large Rabi frequency we should be careful about neglecting the contributions from the off-resonant processes.

As is clearly seen from Eq.(7.9), the CEP effect occurs due to the interference of the terms that have different dependence on the field phases. The condition for the better visibility of the interference is related to the amplitudes and frequencies of fields. It is better to have amplitude be the same to have high visibility, on the other hand, if only one term dominates the CEP effect disappears. It is very interesting to note here that the CEP effects do not depend explicitly on the duration of pulses but only on the field amplitudes and their frequencies.

D. Conclusion

We use intense RF pulses interacting with the magnetic Zeeman sub-levels of Rubidium (Rb) atoms, we have experimentally and theoretically shown the CEP effects in the population transfer between two bound atomic states interacting with pulses consisting of many cycles (up to 15 cycles) of the field. It opens several exciting applications and interesting possibilities that can be easily transfer to optical range and enhance current and create new

set of tools to control CEP of laser pulses.

These tools allow researchers to improve laser systems that generate laser pulses with better reproducibility and accuracy and better controlled. Also the tools provide an additional handle to control the process of collisions, and the current approach of extending the duration of the pulses with measurable or controllable CEP allows researchers to extend the coherent control to a new level where they are able to study molecular collisions or electron collisions in nano-structures under the action of strong electromagnetic fields with known CEP. In particularly, the obtained results can be applied to control of chemical reactions [179].

CHAPTER VIII

COHERENT RAMAN UMKLAPPSCATTERING*

A. Introduction

The universal requirement of momentum conservation in coherent light matter interactions imposes stringent limitations on the range of wave-vector directions allowed for the coherent signals [180, 181, 182]. Specifically, generation of backward-propagating beams in nonlinear wave-mixing processes has been a long-standing problem in optical science, impeding the application of wave-mixing-based techniques to standoff detection [183, 184]. When applied to a generic third-order process generating a field with a frequency ω_4 through the coherent mixing $\omega_1 \pm \omega_2 \pm \omega_3$ of light fields with frequencies ω_1, ω_2, and ω_3, momentum conservation translates into the following requirement for the wave vectors $\mathbf{k_i} = n_i\omega_i/c$ of the optical fields $i = 1, 2, 3$ involved in the wave-mixing process (c is the speed of light in vacuum and $n_i = n(\omega_i)$ is the index of refraction at the frequency ω_i): $\Delta\mathbf{k} = \mathbf{k_4} \pm (\mathbf{k_1} \pm \mathbf{k_2} \pm \mathbf{k_3}) = 0$. With properly designed periodic structures, this phase-matching condition can be satisfied by picking up the momentum deficit from the reciprocal lattice of the structure. This approach has been successfully demonstrated with a variety of photonic structures [185, 186].

In the standoff detection mode, however, creation of subwavelength lattices, needed to phase-match the backward wave, is technically difficult requiring a complex arrangement of auxiliary high-power laser beams [184] or modulating the index of refraction [187]. In the microscopy mode, backward coherent anti-Stokes Raman scattering (CARS) becomes

---

*Reprinted with permission from "Coherent Raman Umklappscattering" by L. Yuan, A.A. Lanin, P.K. Jha, A.J. Traverso, D.V. Voronine, K.E. Dorfman, A.B. Fedotov, G.R. Welch, A.V. Sokolov, A.M. Zheltikov, and M. O. Scully, 2012. *Laser Phys. Lett* 8, 736-741 Copyright [2011] by Astro Ltd. Published exclusively by WILEY-VCH Verlag GmbH & Co. KGaA

possible [188] due to the specific geometry of tightly focused light beams scattered by microinhomogeneities in a biotissue. None of such epi-CARS microscopy beam-interaction geometries, however, seems to suggest a realistic way of scaling to larger beam propagation paths that are needed for optical standoff detection.

Recent experimental demonstrations of backward stimulated emission from atomic oxygen produced by UV laser pulses in the air [189], yielding a highly directional backward-propagating light beam with an excellent quality and an average power well above the microwatt level, offer a powerful tool for standoff spectroscopy. Still, in order to benefit from the chemical selectivity provided by the Raman effect, and to obtain efficient (coherent) signal generation, the $\Delta\mathbf{k} = 0$ momentum conservation (phasematching) needs to be satisfied. The main goal of this paper is to demonstrate that coherent Raman scattering of laser fields can give rise to a highly directional (phase-matched) nearly backpropagating CARS signals, and to use phasematching to resolve individual signal components in space. This regime of the Raman effect, referred to hereinafter as coherent Raman Umklappscattering, by analogy with phonon-phonon and electron-phonon Umklappscattering in solids [190], is shown to be well suited for standoff detection applications, including remote sensing of trace gases in the atmosphere and on the surfaces of distant objects, paving the way for the development of a new class of security and ecological safety monitoring systems.

Coherent anti-Stokes Raman scattering by molecular vibrations [188, 191] and molecular rotations [192, 193] has a broad range of applications. For example, the real-time detection of a low concentration of bacterial endospores ($\approx 10^4$ spores) via CARS was demonstrated [194, 195]. We note that the traditional CARS cannot be used in a standoff mode in scenarios involving perfectly parallel forward and backward propagating laser beams, because of the phasematching constraints. However, we show that under certain conditions, a small angle between laser beams satisfies phasematching. Moreover, the angled geometry provides a convenient spatial separation of the applied laser and generated

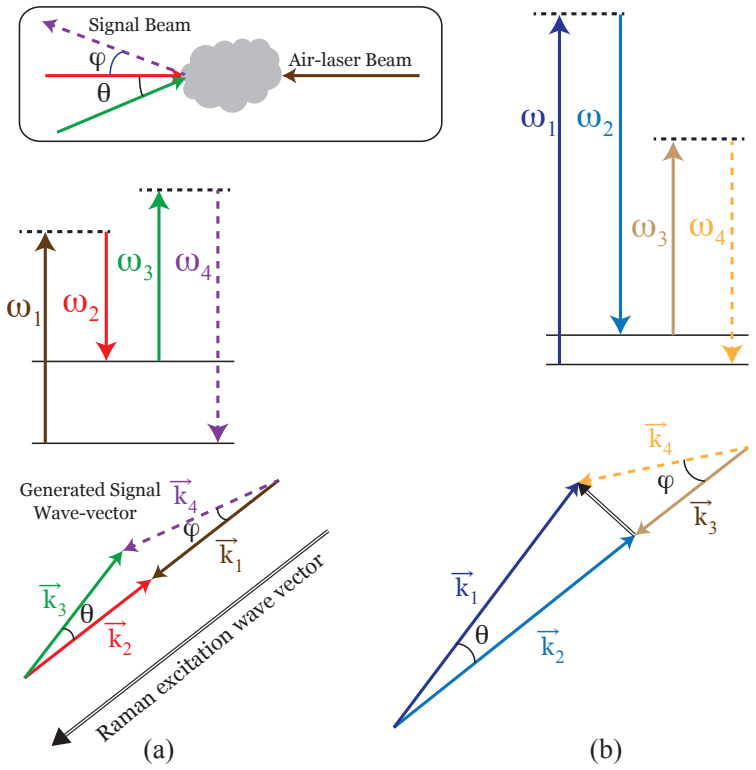

Fig. 55. Energy level and k-vector diagrams for coherent Raman Umklappscattering using angled counter-propagating ground- and air-laser beams. Signal wave is generated in the direction $\mathbf{k_4}$. Coherent Raman scattering is realized by molecular vibrations (a) and molecular rotations (b). On the energy-level diagrams (top), solid horizontal lines denote real molecular energy levels of the species to-be-detected, and dashed lines correspond to virtual states. (Inset: General configuration of the beams in a cloud.)

signal beams [196, 197]. The corresponding spatial separation of various Raman transition lines allows improving detection capabilities which in conventional spectrally separated methods may be limited by detector resolution or by spectral line broadening.

B. Implementation Schemes

We consider a coherent Raman scattering process where optical fields with frequencies ω_1 and ω_2, referred to as the pump and Stokes fields, are used for a coherent selective

excitation of a Raman-active mode with the frequency Ω in a medium. The third field, with frequency ω_3, is used to probe this coherence, giving rise to Stokes and anti-Stokes signal fields with frequencies $\omega_4 = \omega_3 - (\omega_1 - \omega_2) = \omega_3 - \Omega$ and $\omega_4 = \omega_3 + (\omega_1 - \omega_2) = \omega_3 + \Omega$, respectively. Detection of these signals would allow a chemically selective detection of trace gases in the beam interaction region. Throughout the rest of the paper, we focus on anti-Stokes generation, as shown in Fig. 55; Stokes generation can be easily calculated in an analogous way.

To set the framework for our analysis, we consider the application where our pump field ω_1 in Fig. 55(a) [or probe field ω_3 in Fig. 55(b)] is generated in the air at a point beyond the Raman-active region we want to detect or analyze, and that this field is directed back towards the ground where our Stokes and probe (or pump) fields originate. This could be accomplished by creating a backward-propagating oxygen laser as described in Ref [189]. Our analysis shows that the small-angle CARS phasematching requires that two of the three applied laser frequencies are nearly equal. Two possibilities exist, as shown in Fig. 55. In both cases, two laser beams are sent from the ground: one counter-propagating with respect to the air-laser beam, and the other one slightly angled. In the lower part of Fig. 55 [both (a) and (b)] we denote beams by their k-vectors and show how these k-vectors align to satisfy phasematching. We consider two cases [(a) and (b)] that differ in the way how molecular excitation is prepared. In case (a), molecular coherence (in the species to be detected) is excited by the air-laser beam ($\mathbf{k_1}$, pump, frequency ω_1) together with the counter-propagating beam sent from the ground ($\mathbf{k_2}$, Stokes, frequency ω_2), while in case (b) molecular oscillations (whose k-vector is shown in Fig. 55 by a double-line arrow) are driven by two beams sent from the ground, at a small angle with respect to each other ($\mathbf{k_1}$ and $\mathbf{k_2}$, pump and Stokes). The beam at $\mathbf{k_3}$ then scatters off the molecular coherence wave. In both cases, the anti-Stokes signal beam $\mathbf{k_4}$ is then generated in the direction toward the observer. The molecular frequency (equal to $\omega_1 - \omega_2$) is small in case (b). Below, we

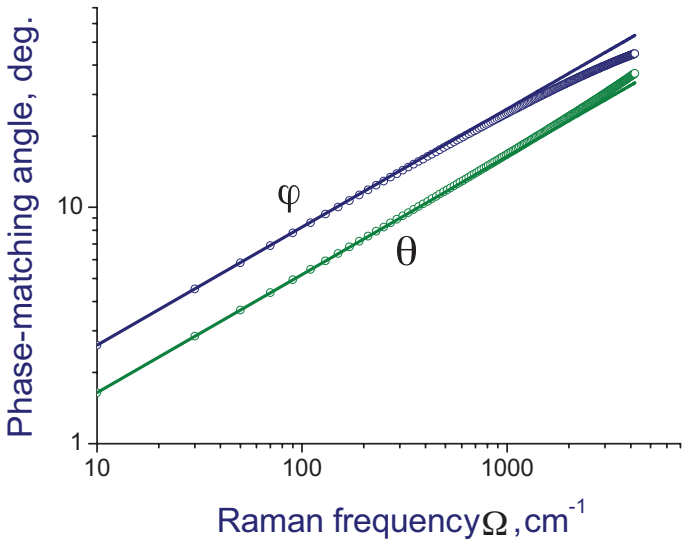

Fig. 56. The angles between the pump and Stokes beams θ and probe and anti-Stokes beams φ providing phasematching for the anti-Stokes field generation in the noncollinear beam geometry shown in Fig. 55 versus the Raman frequency calculations using the exact formula for $|\Delta k|$ with dispersion included (circles) and the approximation of Eqs. (8.1) and (8.2) (solid lines). The pump wavelength is 532 nm.

present detailed calculations for the situation described in Fig. 55(b).

C. Results and Discussion

We examine phasematching options for backward CARS due to molecular rotations induced in a gas medium by forward pump and Stokes fields and probed by a backward field with an arbitrary frequency ω_3. Neglecting the frequency dependence of the refractive index $n_i = 1$, and analyzing the wave-vector arrangement shown in Fig. 55(b), we find in the case of small θ

$$\theta \approx 2 \left(\frac{\omega_3 \Omega}{\omega_1^2 + \omega_1 \omega_3} \right)^{\frac{1}{2}}, \tag{8.1}$$

$$\varphi \approx 2 \frac{\omega_1}{\omega_3} \left(\frac{\omega_3 \Omega}{\omega_1^2 + \omega_1 \omega_3} \right)^{\frac{1}{2}}. \tag{8.2}$$

In Fig. 56, we compare predictions of Eqs. (8.1) and (8.2) with the results of exact calculations performed using the relevant frequency dependence of $n(\omega)$ for the atmospheric air. As can be seen from these calculations, the simplified formulas of Eqs. (8.1) and (8.2) give reasonably accurate predictions within a broad range of Ω, providing useful insights into the limitations of the angled beam-interaction geometry imposed by the momentum conservation.

In the case of molecular vibrations, typically used for the standoff detection of trace gases in the atmosphere, the Raman frequencies $(2\pi c)^{-1}\Omega_v$ are on the order of $1000\ \mathrm{cm}^{-1}$. Specifically, for the central frequency of rovibrational Q-branch transitions in molecular oxygen, $(2\pi c)^{-1}\Omega_v \approx 1556\ \mathrm{cm}^{-1}$ and $\lambda = 2\pi c\omega^{-1}$=845 nm (the central wavelength of stimulated emission by atomic oxygen in the atmosphere), we find $\theta_0 \approx 21^o$. With such big angles between the pump and Stokes beam, practical implementation of standoff detection based on coherent Raman scattering would encounter serious difficulties, as probing the atmosphere would require on-ground laser sources and detectors for the coherent backward signal separated by a prohibitively large distance.

Rotational Raman frequencies Ω_r of molecular systems are much lower than Ω_v, with the Ω_r/Ω_v ratio scaling roughly as $(m/M)^{1/2}$ with the ratio of the electron mass m to the relevant atomic mass M. Purely rotational spontaneous Raman scattering is widely used for a lidar remote sensing of the atmosphere [198, 199, 200]. The coherent regime of Raman scattering would radically enhance the Raman signal return due to a higher directionality and a higher magnitude of the coherent Raman response.

In the rigid-rotor approximation, the frequencies of molecular rotational transitions are given by $\Omega_J = 4\pi Bc(2J+3)$, where J is the rotational quantum number, B is the rotational constant, and c is the speed of light. The amplitudes of rotational Raman lines

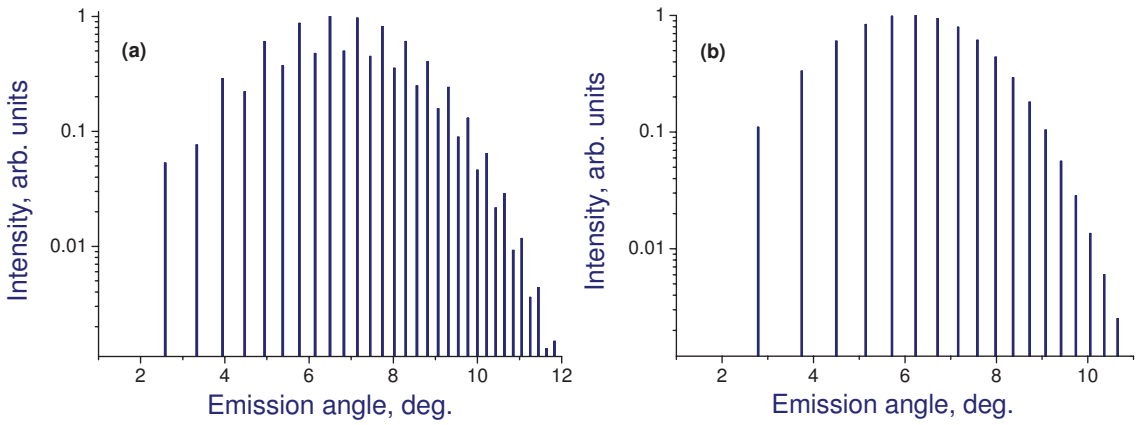

Fig. 57. The amplitudes F_J of rotational Raman lines versus the phasematching angle $\theta_J \approx (2\Omega_J/\omega)^{1/2}$ for N_2 (a) and O_2 (b) with $\omega_3 \approx \omega_1 = \omega$, $\omega_2 = \omega - \Omega_J$, $\omega_4 = \omega + \Omega_J$, and $\lambda = 2\pi c\omega^{-1}$ =845 nm.

centered at ω_J are given by

$$F_J = \frac{(J+2)(J+1)}{(2J+3)} Z_J(\rho_{J+1} - \rho_J), \tag{8.3}$$

where

$$\rho_J = \frac{\exp\left[-\frac{chBJ(J+1)}{kT}\right]}{\sum_J Z_J(2J+1)\exp\left[-chBJ(J+1)/kT\right]}, \tag{8.4}$$

h is the Planck constant, k is the Boltzmann constant, T is the gas temperature, and Z_J is a factor describing the quantum nuclear statistics.

In Fig. 57, we plot the amplitudes F_J of rotational Raman lines versus the phase-matching angle $\theta_J \approx (2\Omega_J/\omega)^{1/2}$ for molecular nitrogen ($B \approx 1.99\mathrm{cm}^{-1}$, $Z_J = 1$ and 2 for odd and even J, respectively [201]) and oxygen ($B \approx 1.44\ \mathrm{cm}^{-1}$, $Z_J = 1$ and 0 for odd and even J, respectively [201]) with $\omega_3 \approx \omega_1 = \omega$, $\omega_2 = \omega - \Omega_J$, $\omega_4 = \omega + \Omega_J$ and $\lambda = 2\pi c\omega^{-1} = 845\mathrm{nm}$. These plots model rotational coherent Raman spectra in the beam geometry as shown in Fig. 55(b). The magnitudes of the Raman lines differ within a range covering two orders of magnitude which provides a suitable dynamic range for the

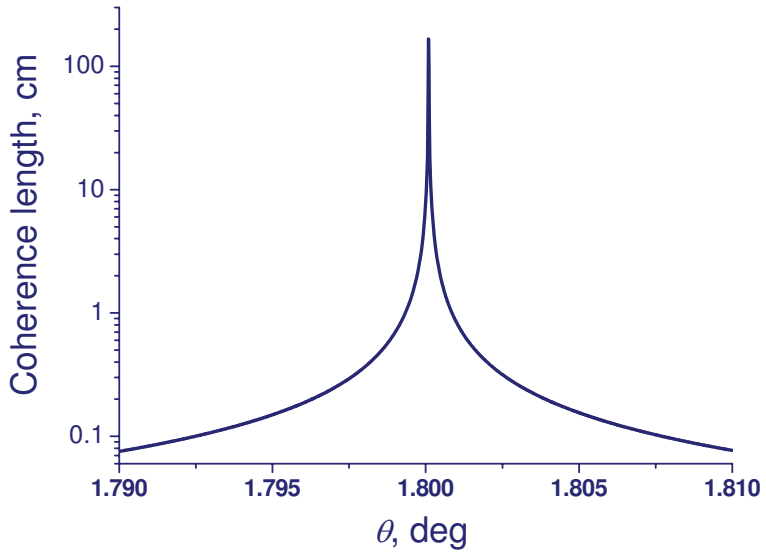

Fig. 58. Coherence length $l = \pi(2|\Delta k|)^{-1}$ calculated as a function of the angle θ between the pump and Stokes beams for the Ω_0 ≈12 cm^{-1} rotational Raman component of molecular nitrogen in the atmospheric air for a pump wavelength of 532 nm and a probe wavelength of 845 nm.

experimental detection of molecular-specific spectroscopic fingerprints.

Fig. 58 displays the coherence length $l = \pi(2|\Delta k|)^{-1}$ calculated as a function of the angle θ between the pump and Stokes beams for the $(2\pi c)^{-1}\Omega_0 \approx 12\ \mathrm{cm}^{-1}$ rotational Raman component of molecular nitrogen in the atmospheric air for a pump wavelength of 532 nm and a probe wavelength of 845 nm. Phasematching is achieved for backward CARS at $\theta_0 \approx 1.8^o$. This small value of θ and a narrow width provide a high directionality and an almost backward propagation of the desired signals.

The scheme in Fig. 55(a) is also phase-matched with a small angle θ between the Stokes and the probe on-ground beams, and with a small angle (φ) between the backwards propagating sky and signal beams. The energy level detuning, Δ, between the Stokes and probe beams is now small compared to all the optical frequencies and does not need to be resonant with the vibrational spacing. These angles are given by equations analogous to

Eqs. (8.1) and (8.2)

$$\theta \approx 2\left(\frac{\omega_1\Delta}{\omega_1^2+\omega_1\omega_2}\right)^{\frac{1}{2}}, \tag{8.5}$$

$$\varphi \approx 2\frac{\omega_2}{\omega_1}\left(\frac{\omega_1\Delta}{\omega_1^2+\omega_1\omega_2}\right)^{\frac{1}{2}}. \tag{8.6}$$

By suitably selecting the Stokes and probe beam frequencies from the ground it may be possible to detect the vibrational coherent Raman spectrum of the target molecules in the sky and realize the standoff spectroscopy.

We now consider a specific example of CO trace molecules to be detected using the backward CARS schemes considered above against the background signal, related to molecular nitrogen and oxygen in the atmospheric air. The pump and Stokes frequencies are tuned to the Raman resonance with transition between rotational or vibrational b and c levels of CO molecules in the electronic ground state (Fig. 59). The pump and Stokes wavelengths are taken to be close to 500 nm and off resonance with an excited electronic state of the molecules [levels a and d in Fig. 59] in order to avoid absorption of these fields over long propagation paths in the atmosphere.

Coherent Raman scattering by rotations and vibrations of molecular oxygen and nitrogen in the atmosphere give rise to a coherent background, which masks the CARS signal from CO molecules. The intensities of both the CARS signal from CO molecules and the nonresonant background are given by

$$I_{CARS,NR} \sim |\chi^{(3)}_{CARS,NR}|^2 I_1 I_2 I_3, \tag{8.7}$$

where I_1, I_2, andI_3 are the intensities of the pump, Stokes, and probe fields, and $\chi^{(3)}_{CARS,NR}$

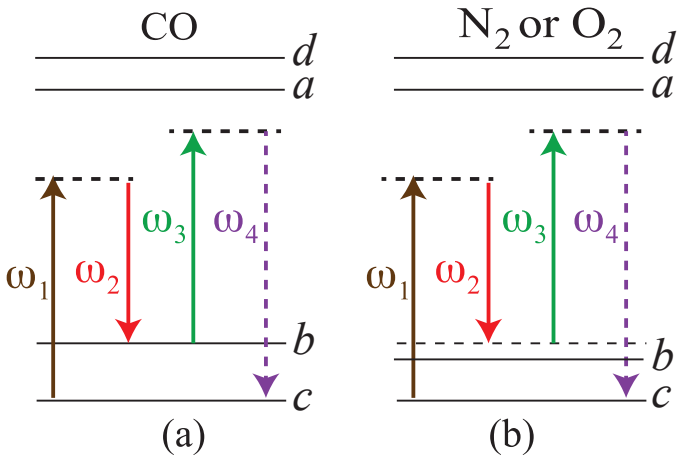

Fig. 59. Diagrams of (a) CARS by CO molecules and (b) coherent nonresonant background generation by nitrogen and oxygen molecules.

is the third-order susceptibility of the form [180, 202]

$$\chi^{(3)}_{\mathrm{CARS,NR}} = \frac{N}{4\pi\varepsilon_0\hbar^3}\left\{\left(\frac{1}{\omega_{bc}-(\omega_1-\omega_2)-i\gamma_{bc}}\right)\right.$$
$$\times\sum_d\left(\frac{\wp_{cd}\wp_{db}}{\omega_{dc}-\omega_4-i\gamma_{dc}}+\frac{\wp_{db}\wp_{cd}}{\omega_{db}+\omega_4+i\gamma_{db}}\right)$$
$$\times\sum_a\left[\rho^{(0)}_{cc}\left(\frac{\wp_{ac}\wp_{ba}}{\omega_{ac}-\omega_1-i\gamma_{ac}}+\frac{\wp_{ba}\wp_{ac}}{\omega_{ac}+\omega_2-i\gamma_{ac}}\right)\right.$$
$$\left.\left.-\rho^{(0)}_{bb}\left(\frac{\wp_{ac}\wp_{ba}}{\omega_{ab}-\omega_2+i\gamma_{ab}}+\frac{\wp_{ba}\wp_{ac}}{\omega_{ab}+\omega_1+i\gamma_{ab}}\right)\right]\right\}. \tag{8.8}$$

Here N is the density of molecules, ω_{ij} is the frequency of transitions between levels i and j, ω_k are the optical frequencies [$k=1,2,3,4$; see Fig. 59], γ_{ij} are the relaxation rates, $\wp_{ij}$ are the dipole moments, and $\rho^{(0)}_{ii}$ is the initial population of the level i. The dipole moments are estimated as $\wp_{ij}\approx ea_0$ for all transitions of different molecules. The sum over a in Eq. (8.8) yields a spontaneous Raman crosssection on the order $10^{-31}\mathrm{cm}^2/\mathrm{sr}$ [202]. The nonresonant frequency denominators in Eq. (8.8) are of the order of $10^{16}\mathrm{rad/s}$ for both CO and nitrogen and of the order of $10^{15}\mathrm{rad/s}$ for oxygen. As the frequencies ω_1 and ω_2 are chosen such that $\omega_{bc}-(\omega_1-\omega_2)=0$ for the bc transition of CO molecules, the frequency

denominator $|\omega_{bc} - (\omega_1 - \omega_2) - i\gamma_{bc}|$ in Eq. (8.8) is estimated as $10^8 \mathrm{s}^{-1}$ in the case of CO molecules. For the coherent background, this denominator is $10^{12} \mathrm{rad/s}$ and $10^{11} \mathrm{rad/s}$ in the case of molecular rotations of O_2 and N_2, and $10^{14} \mathrm{rad/s}$ and $10^{13} \mathrm{rad/s}$ for molecular vibrations of O_2 and N_2 respectively. For these parameters, the ratio of the intensities of the CARS signal from CO molecules to the coherent background intensity is estimated as $1 : 10^{-10}$ for molecular vibrations. The intensity of the CARS signal provided by 1 ppm of CO molecules in the atmospheric air will be thus at the level of 1% of the coherent background intensity, which still allows a reliable detection using appropriate nonresonant background suppression methods [203].

D. Conclusion

The analysis presented in this work shows several realistic schemes for generating backward CARS in a stand-off (remote sensing) configuration. Coherent Raman Umklappscattering of laser fields by molecular rotations and vibrations is shown to enable the generation of phase-matched highly directional, high brightness, nearly backpropagating light beams.

The two proposed angled-beam schemes in Fig. 55 have complimentary capabilities. Scheme (a) allows a flexible selection of the frequency difference $\omega_3 - \omega_2$ such that the angle can be set to any convenient (small) value. Scheme (b) does not give this flexibility (since the difference $\omega_1 - \omega_2$, and therefore the angle θ, are fixed by the Raman frequency), but instead it allows a free choice of the pump wavelength which now does not have to be close to the air-laser wavelength. For example, if the air-laser wavelength turns out to lie in the near IR range (845 nm, from the oxygen laser [189]), the wavelength of the forward-going pump and Stokes beams can still be chosen in the UV range, such as to take advantage of electronic-resonance enhancement.

With each rotational Raman component predominantly emitted in the direction of

phasematching (Fig. 57), the backward CARS beam geometry shown in Fig. 55(b) yields angularly resolved rotational Raman spectra, offering important advantages for spectrum analysis and helping to separate the rotational Raman components from the highly directional backpropagating probe beam. The spatial separation between an on-ground laser source and a detector of the coherent backward signal dictated by phasematching in the considered geometry is a few centimeters per each meter of standoff detection range. Excitation of molecular rotations with properly shaped sequences of ultrashort laser pulses [204, 205] could offer promising options for the enhancement of backward rotational CARS. This coherent Raman Umklapp process is well suited for standoff detection of trace gases in the atmosphere with a sensitivity at the level of 1 ppm.

CHAPTER IX

LASER INDUCED ATOMIC DESORPTION TO CONTROL DIMER DENSITY IN ALKALI-METAL VAPORS*

A. Introduction

Alkali-metal vapor systems are in high demand as time and frequency standards[206], playing an important role in optical metrology [207], and are widely used to test fundamental principles in optical and atomic physics[2]. Together with applications the alkali-metal vapor is one of the most attractive and powerful model systems of laser atom interaction, which has enabled some of the most significant discoveries in natural sciences from pioneering experimental demonstrations of radiation pressure on atoms[208], optical pumping[209, 210], and hyperfine-structure measurements[211] to coherent population trapping[212], magneto-optical trapping[213], and Bose-Einstein condensation[214].

A routine technique for the preparation of alkali-metal vapors for a broad variety of laboratory experiments and applications is based on heated alkali-vapor cells. Alkali vapors in such cells include atomic and molecular components whose overall pressure is controlled by the temperature of the cell. Several elegant techniques have been proposed to control the densities of the atomic and molecular fractions in alkali-metal vapors. In particular, Lintz and Bouchiat[215] have demonstrated the laser induced destruction of cesium dimers in a cesium vapor through a quasiresonant process assisted by collisions of cesium molecules with excited-state cesium atoms and later showed in rubidium vapor by Ban $et. al.$ [216]. Thermal dissociation of cesium dimers in cesium vapor cells have been

* Part of this chapter is reprinted from the manuscript "Ultralow-power local laser control of the dimer density in alkali-metal vapors" by P. K. Jha, K. E. Dorfman, Z. Yi, L. Yuan, Y. V. Rostovtsev, V. A. Sautenkov, G. R. Welch, A. M. Zheltikov and M. O. Scully, (submitted to Applied Physics Letters).

studied by Sarkisyan $et. al.$ [217].

In the past decade, laser induced atom desorption (LIAD)[218, 219] technique has gain much attention for enhancing the vapor density in coated cells where the atoms gets adsorbed on the surface. In a typical LIAD experiment, a desorption laser is turned on and its effect is studied by the analyzing the absorption of a weak probe field resonant to some transition. Work related to this area has been primarily focused on atomic densities for eg. Rb, Cs, K, Na etc. First initiative in the direction of control over dimer concentration using LIAD was studied by the Berkeley group[220].

Here we extend the laser-induced photodesorption technique to ultralow laser powers and use resonant Raman spectroscopy to demonstrate that LIAD[**?**, 221] enables an accurate local control of the density of dimers in alkali-metal vapors. Our experimental strategy is based on studying the optical response from cesium dimers in the presence of a thin metal film of cesium on the window of a closed vapor cell (as shown in Fig. 60) using continuous wave laser at milli-watt power. We use a cylindrical Pyrex cell with a diameter of 3 cm and a length of 75 mm. After desorption from the film the cesium monomers (atoms) can form dimers, trimers and higher order oligomers by colliding with each other. Possibility of dimers adsorption on the surface of the film is beyond the scope of this paper.

B. Experimental Setup

Our experiment setup is shown in Fig. 60. A tunable free-running single-mode diode laser (Sanyo DL7140-201) is used for spectroscopy of cesium molecules. The laser wavelength is set coarsely by adjusting the temperature (+0.04nm/K). Fine frequency tuning is performed by variation of injection current (-0.04cm^{-1}/mA).

The input laser beam is collimated by an aspheric lens, and the prism is used to compress the beam size in horizontal axis. The telescope system expands the beam size by

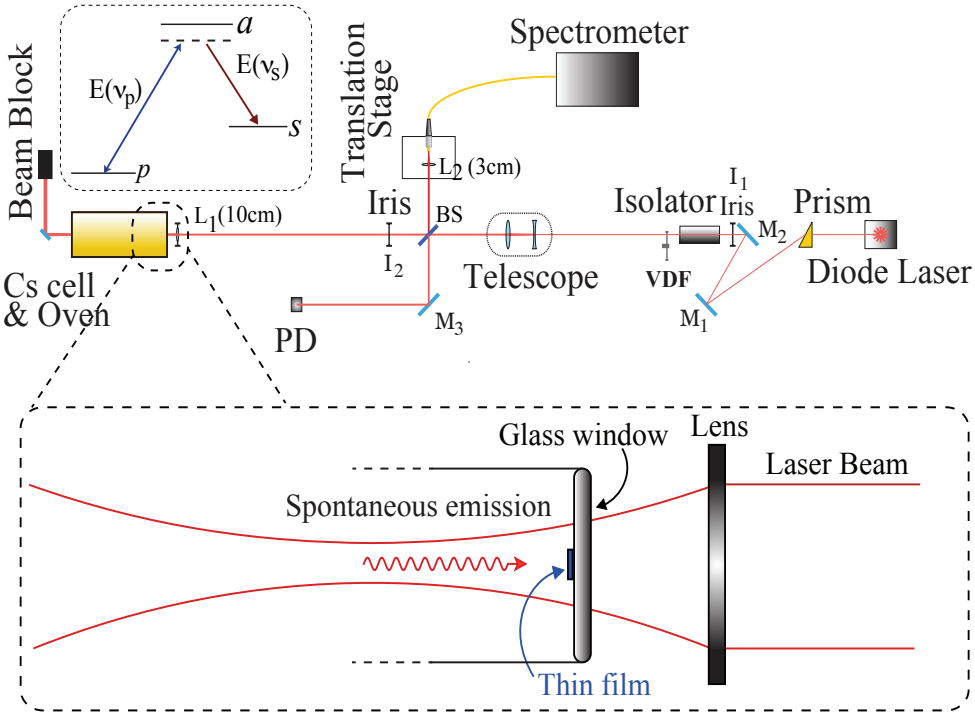

Fig. 60. Experimental setup. The lower inset shows the zoomed part near the window. Here we have a thin film of Cs on one side of the cell inside the oven. The spontaneous emission generated in the backward direction is collected and analyzed using the spectrometer. VDF is variable density filter; L is lens and BS is beam splitter. The upper inset shows a simple three-level model for Raman scattering. Here the lower two levels p and s and upper level a are the vibrational states the ground state $X^1\Sigma_g^+$ and excited state $B^1\Pi_u$ respectively.

a factor of 2. Unfocussed and collimated beam diameter is $\sim$ 3mm. The beam is then focused into the cell through a lens (f=10 cm) designated as L_1; the window of the cell, which has the thin film on the inner surface, is $\sim$ 3cm from the lens. The beam diameter on the window is $\sim$ 4mm which is larger than the film diameter (approximated as circular). The backward light is collimated by the same lens L_1, and after reflected by the beam splitter (BS), it is collected by another lens L_2(f=3 cm) into a multimode fiber which conducts the light into a diffraction spectrometer (Ocean Optics HR2000: spectral resolution 0.065 nm). Irises are used to help collimate the beams and the one close to the cell also helps

block diffuse scattered radiation due to reflections from the windows etc.

C. Experimental Results

The laser wavelength is set resonant to the electronic transition $X^1\Sigma_g^+ \leftrightarrow B^1\Pi_u$ of the dimer. The absorption lines in the absorption cesium molecular band $X^1\Sigma_g^+ \leftrightarrow B^1\Pi_u$ cover wavelength region from 755nm to 810nm[222]. In Fig. 61(a), we have plotted one such spectrum of Raman scattering collected. We tuned the pump laser wavelength, by varying the injection current to the laser, to the resonance by looking at the intensity of one of the Raman peaks (796.16nm). The maximum value of the intensity corresponds to pump wavelength $\lambda_p = 779.9010$ nm (air) [WA-1500 wave meter from Burleigh]. In Fig. 62. we have plotted the resonance enhancement of the peak (796.16nm) against the one photon detuning $\Delta = \omega_{ap} - \nu_p$ which indicates the high sensitivity of the Raman response to the pump wavelength[223]. To simulate the spontaneous Raman spectral response we used [224]

$$S_{RAMAN}(\nu_p, \nu_s) = 2\pi \sum_{p,s} P(p)|\chi_{sp}(\nu_p)|^2 \delta(\omega_{sp} + \nu_s - \nu_p), \tag{9.1}$$

where

$$\chi_{sp}(\nu_p) = \sum_a \frac{\wp_{sa}\wp_{ap}}{-\omega_{ap} + \nu_p + i\Gamma}. \tag{9.2}$$

Here ν_p and ν_s are the pump and Stokes frequency respectively. $P(p)$ is the normalized thermal population distribution given as

$$P(p) = e^{-E_p/kT} / \sum_p e^{-E_p/k_BT}. \tag{9.3}$$

$\hbar\omega_{ij}$ and $\wp_{ij}$ are the energy difference and the electric dipole moment between level i and

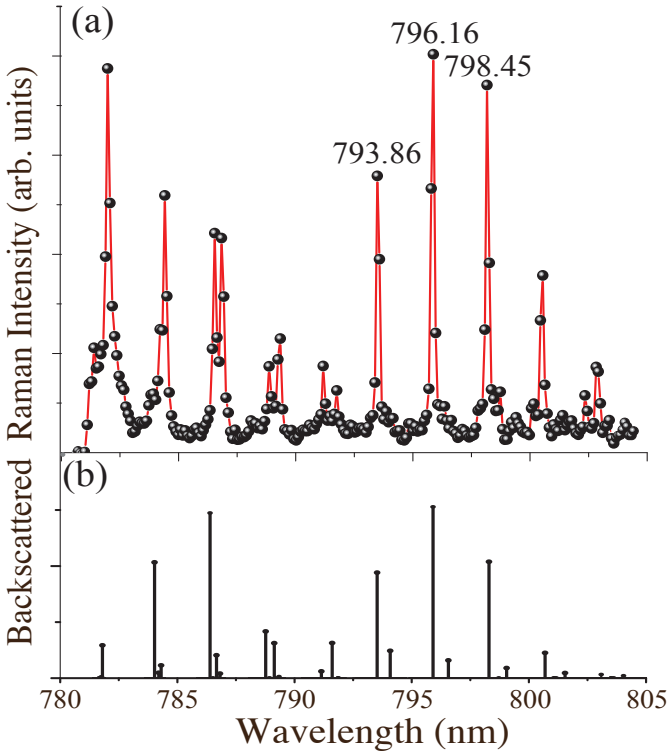

Fig. 61. Plot of intensity of the backscattered radiation (in arbitrary units) (a) experimental and (b) theoretical simulations (discussed in the text).

level j respectively. The square of the dipole moment is proportional to the Franck-Condon factor (FCF). We have approximately calculated FCFs by using the exact eigenfunctions of the Morse Potential [225]. Γ is the transverse relaxation rate.

$$E_v = \hbar\omega(v + \frac{1}{2}) - h\omega\chi(v + \frac{1}{2})^2 \tag{9.4}$$

is the energy of vibrational level v, where ω is the vibrational frequency and $\omega\chi$ is the vibrational anharmonicity [226]. For cesium ground state $X^1\Sigma_g^+$, $\omega_g \sim 42.20(\text{cm}^{-1})$ and $\omega_g\chi_g \sim 0.0819(\text{cm}^{-1})$ while in the excited state $B^1\Pi_u$, $\omega_e \sim 34.33(\text{cm}^{-1})$ and $\omega_e\chi_e \sim 0.08(\text{cm}^{-1})$[227]. Therefore, different amplitudes of the FCFs for different transitions between the vibrational levels in state $X^1\Sigma_g^+$ and $B^1\Pi_u$ indicate that the dipole moment for different transition has different magnitude[228]. Consequently the gain for different tran-

sitions is different. Fig. 61(b) shows the simulated spectrum in the Stokes region using Eq.(9.1) which is an excellent agreement with the experimental data shown in Fig. 61(a). For simulations we took Γ=1 GHz.

The main result of our work is shown in Fig. 63 where we have plotted the intensity of Raman peak (796.16nm) as a function of the pump power for different cell temperatures. Here curves I, II, III corresponds to the cell temperature T_c= 513K, 526K and 543K respectively. In our experiment we monitor the transmission of the film before and after measurements of laser induced fluorescence (LIF) from cesium molecules. The linear dependence between transmitted power and input power is shown in Fig. 63 (inset). It means that under our experimental condition the transmission is independent on the power. Fluorescence signal depends on the input power which indicates that the laser light induce desorption of cesium atoms and molecules from the metal film. Power independence of the film transmission can be explained by moderate evaporation of the film, of the order of several monolayers. The efficiency of the desorption increases with the cell temperature.

To fit our experimental data, we assumed the following fitting function

$$I = \sum_{n=1} \alpha_n P^n \tag{9.5}$$

the coefficients $\alpha_n (n = 1, 2, 3...)$ contains the information about the number density of the dimers, differential cross-section, geometry of the gain medium, contribution due to photodesoprtion etc. In the absence of the film $\alpha_n = 0$ for $n \geq 2$. We further normalize Eq.(9.5) with respect to the linear contribution $(I_1 = \alpha_1 P)$, which yields

$$\frac{I}{I_1} = 1 + \beta_1 P + \beta_2 P^2 + ... \tag{9.6}$$

where $\beta_n = \alpha_{n+1}/\alpha_1$. Next we simplify our analysis by considering$n = 1$ term only. To account for the background noise we added I_0 in Eq.(9.5). In general we know the intensity of the Stokes radiation from a volume of the medium of unit area and a length dz is given

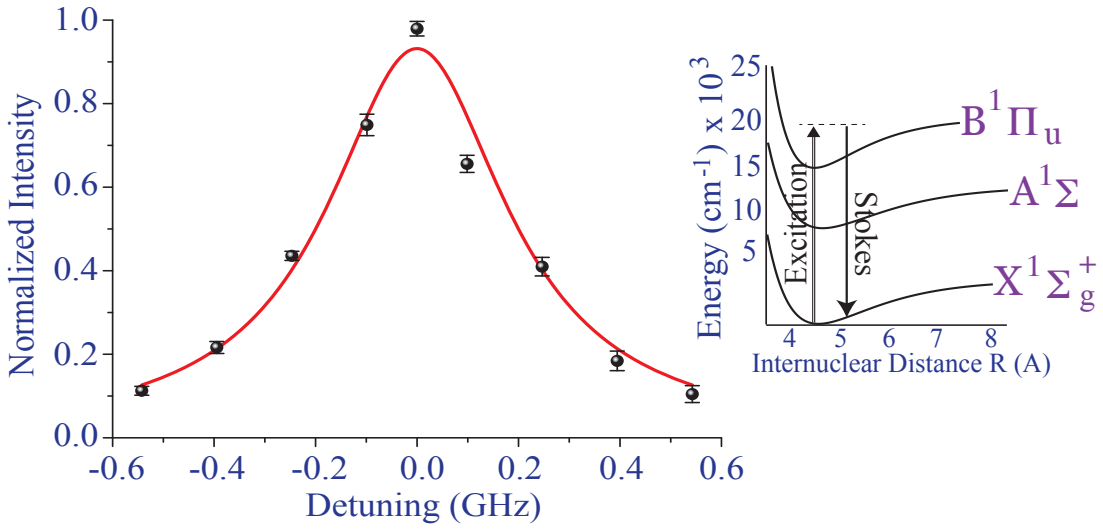

Fig. 62. Plot of the resonance enhancement of the Raman peak at 796.16nm. Full width at half maximum is ~ 0.3 GHz. Insert depicts Relevant energy levels of Cesium dimers.

by [231]

$$dI = N_0(T_c)\frac{d\sigma}{d\Omega}\zeta P dz \tag{9.7}$$

where $N_0(T_c)$ is the density of the scattering molecules, $d\sigma/d\Omega$ is the differential cross section of the spontaneous Raman scattering, ζ is the solid angle in which the scattering is observed, and P is the power of the laser radiation. In table II we have shown the fitting parameter $\beta_1 = \alpha_2/\alpha_1$ and estimated the number density of the cesium dimers. The number in the parentheses is the corresponding fitting error. T_c is the cell temperature and N_1 is the number density of the dimers when the pump power is $P \sim 8.5$mW. In order to estimate for N_1 we use

$$N = N_0\left(1 + \beta_1 P\right) \tag{9.8}$$

From the estimated values at $T_c = 543$K and $P \sim 8.5$mW, the number density of the Cs_2

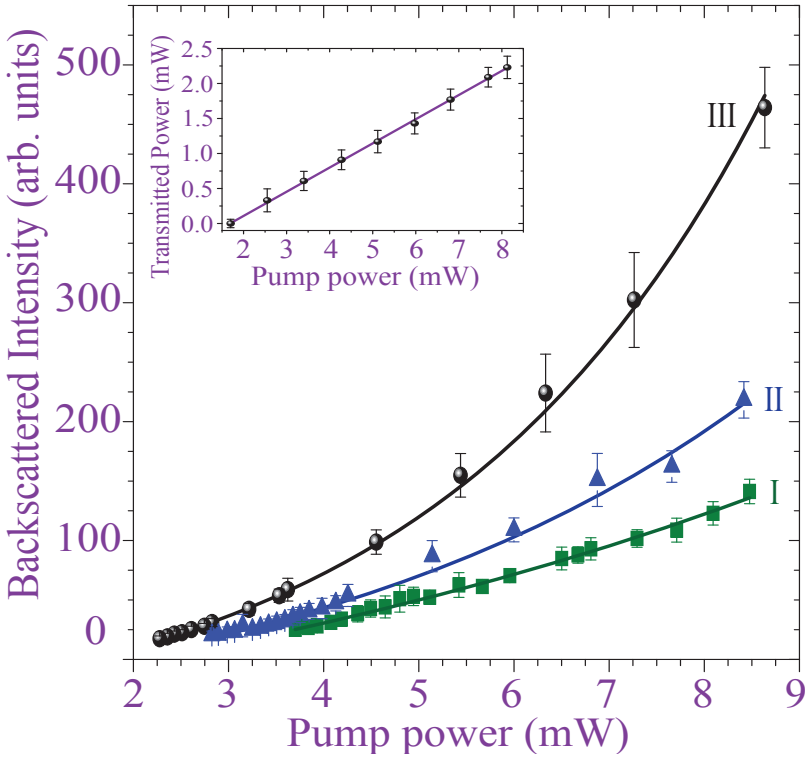

Fig. 63. Plot of the backscattered intensity (arb. units) of the Raman peak at 796.16nm vs the pump power for three different choices of the cell temperature in the presence of the film. Dots illustrate the experimental data and solid lines are fitting using Eq.(9.5).

dimers is ~ 6 times larger than that in the acse when desorption can be neglected. We observed this enhancement in dimer density even at lower cell temperature $T_c = 513$K. Let us introduce an effective temperature T_e which is equivalent to the cell temperature at which the the number density of Cs_2 dimers is $N_e = N_1$. Using the vapor pressure formula [229], we obtained T_e and the result in shown in Table II. We see that the effective temperature can be as high as ~ 54K above the cell temperature.

To verify our assumption that the nonlinear behavior is not attributed to stimulated

Raman scattering(SRS), let us estimate the gain coefficient for SRS under the same experimental condition. For stimulated Raman scattering the stokes intensity in the backward direction under the assumption that pump intensity is not depleted is given by

$$\frac{d}{dz}I_s^b(z) = -gI_s^b(z)I_p \tag{9.9}$$

Here the intensity is $I(z) = 2\epsilon_0 c\hbar^2\Omega(z)|^2/|\wp|^2$ and the gain coefficient

$$g = \left(\frac{N|\wp_{ap}|^2|\wp_{as}|^2\nu_s n_{ps}^{(0)}}{2\epsilon_0^2 c^2\hbar^3\Delta^2\Gamma}\right) \tag{9.10}$$

where $n_{ps}^{(0)} = \varrho_{pp}^{(0)} - \varrho_{ss}^{(0)}$ and Γ is the dephasing of the Raman coherence. In the temperature range from 470 K to 540 K the molecular number density N_m changes from $10^{13} - 10^{14}$ cm^{-3}, the atomic density density N_a changes from $10^{15} - 10^{16}$ cm^{-3}. The ratio of the molecular number density N_m and atomic density N_a is order of 10^{-2}[229]. We have cesium dimers with density 2×10^{14}cm^{-3} at $T \sim 545$K, are pumped by $P \sim 7$mW laser with wavelength tuned to 779.90nm. The diameter of the focused beam at waist is $d = 4\lambda_s f/\pi D \sim 34\mu$m, where the unfocused beam diameter is $D = 0.6$cm, and the focal length of the lens is $f = 10$cm. The depth of the focus $L = 8\lambda_p f^2/\pi D^2 \sim 0.11$cm. The pump intensity is $I_p \sim 300$W/cm^2. The differential spontaneous cross section is $d\sigma/d\Omega \sim 3 \times 10^{-21}$cm^{-2}. For resonance enhanced Raman, the Doppler broadening $\Delta_D = k_p v_{th} \sim 2\times 10^9$s^{-1} for detuning and $\Gamma = 1$GHz. From Eq.(9.9) and the experimental parameters we obtain $g \sim 1.2 \times 10^{-2}$W^{-1}cm. Hence we estimate for $gI_pL \sim 0.4$ which clearly indicates that the stimulated Raman contribution is negligible compared to the LIAD.

D. Conclusion

In this chapter, we discussed a possibility to optically control the density of dimers in alkali-metal vapors using ultra-low power continuous-wave(cw) diode laser. To probe the dimer

Table II. Numerical values of the fitting parameter $\beta = \alpha_2/\alpha_1$ and the number density of the Cs_2 dimers at maximum pump power $P \sim 8.5$mW.

Curve	T_c (K)	β_1	N_1/N_0	T_e (K)
I	513	0.1734(0.009)	2.474(0.108)	567
II	526	0.2972(0.016)	3.526(0.421)	578
III	543	0.6704(0.025)	6.698(0.267)	597

concentration, we used resonant Raman spectroscopy and collected the Raman signal in the backward direction which serves the two-fold purpose

(a) the signal is from the dimers and

(b) envision the idea of remote detection of chemicals using ultra-low power cw lasers. We observed a nonlinear behavior [as shown in Fig. 63] of the intensity vs the pump power contrary to the linear dependence behavior well known from the spontaneous Raman theory. The deviation from the linear behavior is due to the contribution of the Raman signal generated from the cesium dimers produced by photodesorption from the thin film on the window. We estimated the number density of the dimers to be increased by several times in the presence of the film.

The main goal of this experiment to make a significant step in the direction of LIAD which offers a powerful tool to increase number densities of vapor (atoms/dimers) in coated cells which cannot be heated to higher temperatures. An optical control over the dimer density offers an additional tool for numerous applications of the alkali-metal vapors to time and frequency standards[206], optical metrology[207], and to test fundamental principles in optical and atomic physics[2], as well as to be the most attractive and powerful model systems of laser atom interaction.

CHAPTER X

TRIGGERED YOKED-SUPERFLUORESCENT EMISSION*

A. Introduction

In his seminal work Dicke [110] predicted coherence in the spontaneous emission from a system of N excited atoms confined to a region of dimensions smaller than the wavelength. The intensity of the emitted radiation goes as N^2 and this phenomena is knows as Dicke Superradiance(SR). This limitation of volume confinement was later eliminated by Eberly and Rehler [232]. First experimental demonstration was performed by Skribanowitz $et\,al.$[233] using optically pumped hydrogen fluoride(HF) gas. They also gave a theoretical explanation of how and initially inverted two-level system evolves into a superradiant state[234]. A different form of cooperative emission from a system of uncorrelated excited atoms with no initial macroscopic dipole moment, known as superfluorescence(SF) [235] initiates from spontaneous emission[236] and later the system develops macroscopic polarization which give rise to burst of radiation whose maximum intensity is proportional to N^2 and whose time duration is proportional to N^{-1}. Mathematically this process is characterized by the SF time (for a thin cylindrical medium) defined as[237]

$$\tau_{SF} = \frac{8\pi A}{3\lambda^2 N\gamma_b} \tag{10.1}$$

where N is total number of participating atoms, γ_b is the spontaneous emission rate from the upper to the lower level, A is the area of the cross section of the medium. Superfluorescence has been extensively studied both experimentally and theoretically[238, 239, 240, 241]. Recently Nagasono $et\,al.$[242] observed free electron laser induced superfluorescence in

* Part of this chapter is reprinted from the manuscript "Experimental measurement of initial tipping angle for Yoked-Superflourescent emission" by P. K. Jha, Z. Yi, and M. O. Scully, (to be submitted to Physical Review Letters).

Helium where neutral Helium is pumped with ultrafast $\tau_{FWHM} \sim 100$fs pulse at $\lambda_p \sim 53$ nm from the ground state $1^1S_{1/2}$ to the excited state $3^1P_{1/2}$ which decays to the metastable state $2^1S_{1/2}$ emitting a burst of radiation at 503nm.

For three-level systems, the SF emissions can be observed on both the upper leg ($c \rightarrow a$) and the lower leg ($a \rightarrow b$). When both of them occur one by one it is known as Cascade SF[241] on the other hand when the system is prepared in the linear superposition of the lower (b) and the upper level (a) then SF emission on the both the upper and the lower leg occurs simultaneously also known as Yoked-Superfluorescence[243].

More than three-decades ago Vrehen and Schuurmans[244] reported the first direct measurement of the effective initial tipping angle in superfluorescence. The idea was as follows, immediately after the pump pulse creates a complete population inversion a weak pulse of area θ is injected into the SF sample and they measured the delay of the SF pulse generated as a function of $\ln[\theta/2\pi]^2$. They observed that as along as the area of the injected pulse is less than a critical value θ_0 the delay was not effected. When $\theta > \theta_0$ the delay was reduced, then gradually measuring the delay against θ they were able to find the most probable value for the tipping angle $\theta_0 \sim 5 \times 10^{-4}$. This result was closest to the value predicted by Schuurmans, Polder and Vrehen[245]. Later Lee[246] proposed a simple model to incorporate the pumping in the initial evolution of the superfluorescence. The analytical expression for the initial tipping angle was modified to[246].

$$\theta_0 \simeq (2/\langle N \rangle)^{1/2} \exp(\tau_p/4\tau_{SF}) \tag{10.2}$$

and the estimate for the quantum fluctuations was given as

$$\theta^{\pm} \simeq \theta_0 \left\{ 1 \pm [1 - \exp(-\tau_p/2\tau_{SF})]^{1/2} \right\}^{1/2} \tag{10.3}$$

where τ_p is the duration of the pump pulse and τ_{SF} is the collective radiation time given by Eq. (10.1).

Motivated by the experimental work of Vrehen and Schuurmans, we studied the effect of an injected weak but coherent (drive) pulse, resonant with the upper leg of the YSF scheme, on the delay of the super fluorescent signal generated on the lower leg. Inherently there are three fundamental different between our work and the experiment of Vrehen and Schuurmans:

(a) The pump pulse does not create population inversion, rather than it transfer some population from the lower to the upper level using two-photon resonant excitation and also creating a non-zero coherence between these two-levels.

(b) The excitation of the vapor is non-uniform.

(c) The injected and signal pulse are different wavelength.

B. Experimental Details

The schematic of our experiment is shown in Fig. 64. Here we use pump pulse of wavelength 656nm (two-photon resonant with $5S \rightarrow 9S$) and weak drive pulse of wavelength 1491nm (resonant with $9S \rightarrow 6P_{3/2}$) overlapped (temporal and spatial) within the thin rubidium vapor cell. The generated 420 nm signal was filtered by a band-pass filter then analyzed by spectrometer and streak camera. The pump and the drive laser pulses were generated from two optical parametric amplifiers (OPAs). Both OPAs (Coherent) were pumped by a commercial femtosecond laser system (Coherent) with pulses centered at 800nm and the pulse duration was about 30fs. The pump pulses were second harmonics of first OPA signals and polarized in vertical plane, full width at half maximum (FWHM) of pulse duration was about 100fs; while the drive pulses were the direct signals for the second OPA, with a polarization in horizontal plane, the FWHM of pulse duration was about ~ 120fs; both beams had a repetition rate of 1 kHz. The pulse energy of each beam was lowered by a continuous variable metallic neutral density filter respectively, which is not showed on

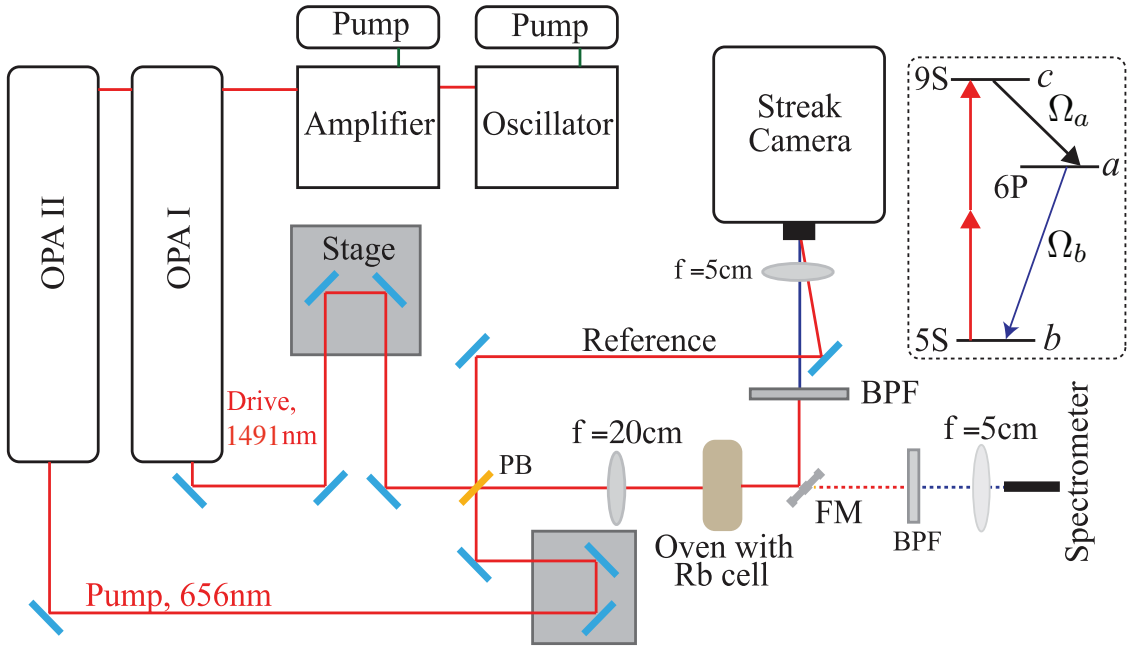

Fig. 64. Experimental schematic. Insert, energy diagram of the transition. HWP, half-wave plate; unnamed parts are mirrors; PB, pellicle beamsplitter; FM, flip mirror; BPF, band-pass filter centered at 420nm, FWHM 10nm; pump and drive pulse energy are adjusted by continuous variable neutral density filters.

the figure. The drive beam went through a pair of 90-degree cornered mirrors mounted on a digital controlled translational stage (Newport), hence the time delay between the pump and drive pulses could be precisely adjusted. Both beam reached a pellicle beamsplitter (PB) and combined collinearly. The PB transmits about 82% of the drive (1491nm) and reflects 44% of the pump (656nm). The combined beam were then focused by a 20cm focal length lens into a Rubidium cell with a Rb vapor thickness of 0.19cm.

The cell is made of sapphire for both wall and windows which allows high temperature operation, it has a cylindrical shape with length of 0.53cm and diameter of 2.54cm. A small tube filled with Rubidium is attached to the wall of the cell, and is connected to cell cavity. Because of this configuration, the tube and the cell body can be heat up to different temperature; in our experiment, the body was at 234°C and the tube was at 214°C, in order

to prevent condensation on the windows. At this set of temperature, the number density of Rb atoms was estimated to be $1.3 \times 10^{15}\text{cm}^{-3}$.

To make sure the two pulses overlap with each other, we putted a piece of thin glass plate (150μm in thickness) into the spatially overlapped focal point of the two beams, and found the four-wave mixing signal by adjusting the delay on the drive beam. After we placed the cell onto the focal point, we also increased the delay of drive to compensate the dispersion induced by the window. 420nm radiation (the signal) was generated from the excited Rb vapor. Together with the pump and drive beam, the signal could be analyzed by the spectrometer after collected by a multimode optical fiber. It was also analyzed by the streak camera (SC) after filtered by a band-pass filter with FWHM of 10nm centered at 420nm.

After filtered and attenuated, the 656nm pump beam transmitted from the pellicle beamsplitter was used as reference for SC. This beam together with the generated signal from the cell were focused into the slid of the SC by a lens with focal length of 5cm. The time resolution of SC is mainly determined by the width of the entrance slid; sufficient mount of light shining into narrow enough slid gives a best resolution with good enough signal-to-noise ratio. In the experiment, we focused the signal onto the slid-plane and set the slid at about 50μm, resulted in a resolution around 2ps.

C. Experimental Results

In this section we will present our experimental results. In Fig. 65 we have plotted the beam profile for the pump beam and signal at the fixed distance from the vapor cell. To obtain the signal (only) we used a narrow bandpass filter center at 420nm and FWHM of 10nm. Fig. 65 indicates that the 420nm signal is not the spontaneous emission from independent excited atoms rather it is cooperative effect which the excited atoms radiate collectively. To

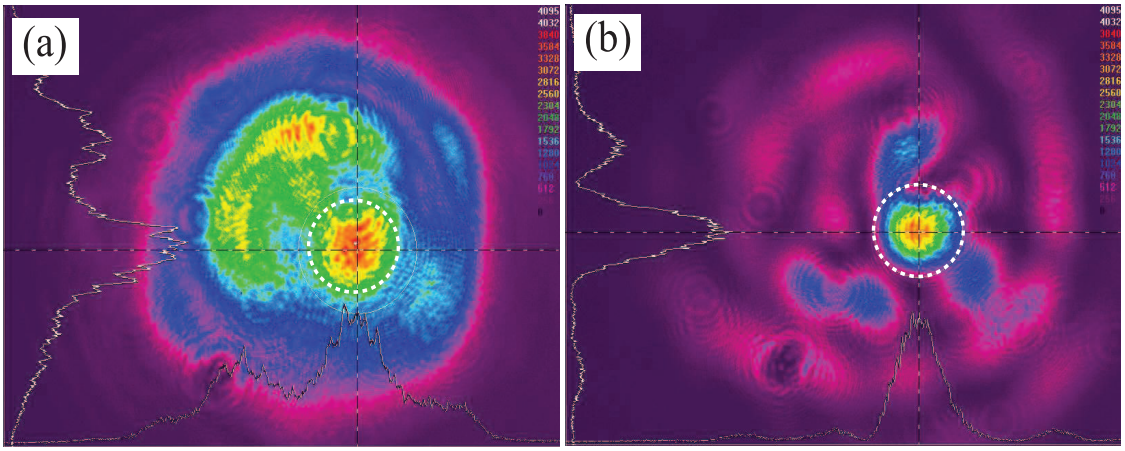

Fig. 65. Beam profiles of the pump (a) and 420nm signal (b)

measure the directionality we did not send any drive pulse rather pumped the atoms from the ground state of Rb (5S) to the excite state (9S) and observed the signal generated at 420nm. Once verifying that we indeed are observing cooperative spontaneous emission, we moved to second phase of the experiment i.e triggered YSF emission.

In the second phase we injected the weak drive field, starting from 1nW, into the sample and measured the delay between the pump and the signal pulse generate. We observed that till ~ 70nW drive power the delay was not affected[1]. When the drive power was further increase the delay in the signal pulse with respect to the pump pulse starts to go down as shown by the solid red circles in Fig. 66. We performed the experiment at constant pump power of 2mW and the effect of the pump power on the tipping angle i.e the threshold pump energy is under progress.

[1]The fluctuation in the delay time could be from the shot to shot variation or averaging over many shot to shot data

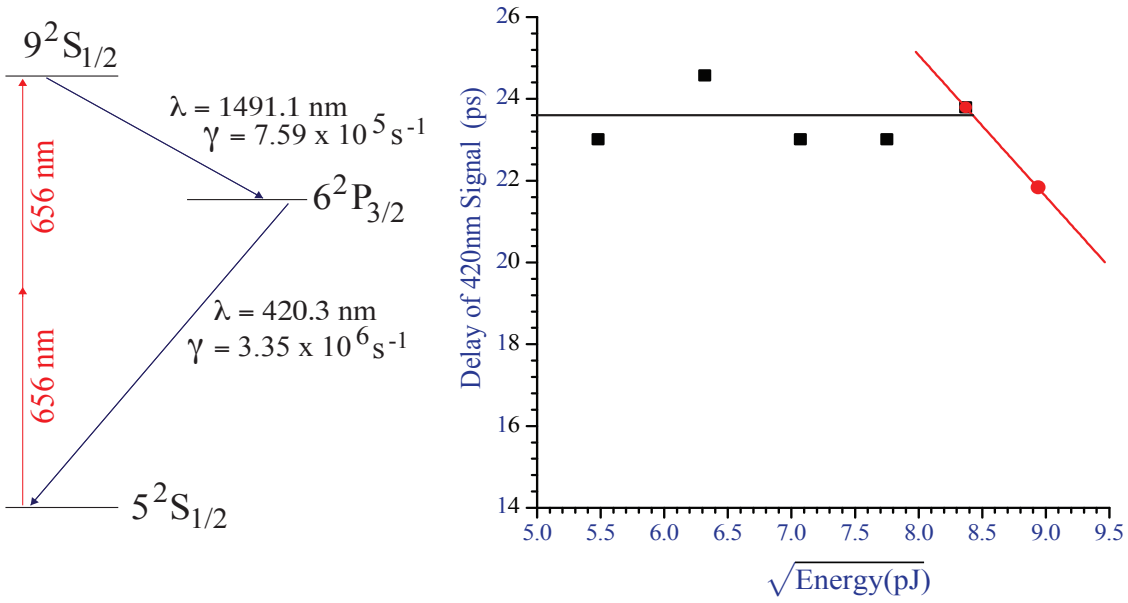

Fig. 66. (a) Energy level diagram for Rb with relevant levels. (b) Delay time τ_D of YSF pulse vs square root of the energy of the injected pulse.

D. Conclusion

In this chapter we have present an experiment, first to the best of our knowledge, in an attempt to quantify the spontaneous emission noise in the YSF scheme for an optically pumped Rubidium vapor. We investigated the effect of weak (1nW-100nW) coherent drive resonant with the upper leg ($9S \rightarrow 6P$) of the YSF scheme($9S \rightarrow 6P \rightarrow 5S$) on the signal generated on the lower leg ($6P \rightarrow 5S$) at $\sim$ 420nm wavelength. Measurement of the tipping angle for as function of the pump power is in progress and it will be reported elsewhere. In the experiment of Vrehen and Schuurmans the cesium vapor was excited (complete population inversion) uniformly and then a weak coherent pulse of area θ was injected.

In our experiment the excitation was non-uniform, non-inversion and the SF pulse is generated even before the pump pulse crosses the sample. Furthermore, this experiment also shows the possibility to generate a forward UV field in the air by adding an extra strong

845 nm drive field to the oxygen experiments, which gives various applications including remote sensing. In the third phase of the experiment we will examine the control of the SF signal for non-collinear pump and drive pulse by measuring the directionality of the 420nm signal against the angle between the pump and drive beams.

CHAPTER XI

CONCLUSION

The primary conclusion of the present dissertation is that quantum coherence plays an active role in modifying the optical properties of matter. The main results are summarized as follows.

(1) An efficient way of exciting coherence in UV and XUV regime by far-off-resonant fields is developed using exact analytical and numerical simulations with and without rotating wave approximations.

(2) A theoretically investigation of the vacuum induced interference effects on the resonance line profiles of a three level system as a model. The result is quite general and applies to atoms, molecules as well as quantum wells and dots.

(3) Using quantum coherence several possibilities for frequency up-conversion and generation of short-wavelength radiation is presented in XUV and X-Ray regime.

(4) A theory predicting a substantial enhancement in the gain in XUV/X-Ray regime of electromagnetic radiation using a external higher wavelength coherent source.

(5) An experiment performed to observe CEP effects on bound-bound atomic excitation (Zeeman sub-levels) in the radio-frequency(RF) domain by multi-cycle pulses (~ 13 cycles). This experiment is an important step forward to shine light on the fundamental question, “How many oscillations/cycles of electric field in a pulse are sufficient to neglect the CEP effect ?”.

(6) A new Raman technique called Coherent Raman Umklappscattering for generating nearly backward coherent anti-stokes Raman scattering(CARS) in a stand-off (remote sensing) configuration. Coherent Raman Umklappscattering of laser fields by molecular rotations and vibrations can generate phase-matched highly directional, high brightness, nearly backward propagating light beams.

(7) A proof of principle experiment on cesium experimentally to demonstrate that LIAD can be used a powerful tool to optically control and monitor the alkali-metal vapors. When this approach is combined with resonance Raman technique it holds a possibility for remote sensing.

(8) Triggered YSF emission is studied experimentally in optically pumped rubidium vapors to quantify the spontaneous emission noise intensity.

REFERENCES

[1] W. Hanle, Z. Phys. 30, 93 (1924).

[2] M. O. Scully and M. S. Zubairy, *Quantum Optics*, (Cambridge University Press, Cambridge, England, 1997).

[3] G. Alzetta, A. Gozzini, L. Moi and G. Orriols, Nuovo Cimento, **36B**, 5 (1976); E. Arimondo and G. Orriols, Nuovo Cimento Lett. **17**, 333 (1976); R.M. Whitley and C.R. Stroud, Jr., Phys. Rev. A **14**, 1498 (1978)

[4] For review articles on LWI theory and concepts see O. Kocharovskaya, Phys. Rep. **219**, 175 (1992); S. Harris, Phys. Today **50**, 36 (1997)

[5] E. S. Fry, X. Li, D. Nikonov, G. G. Padmabandu, M. O. Scully, A. V. Smith, F. K. Tittel, C. Wang, S. R. Wilkinson and S. Y. Zhu, Phys. Rev. Lett. **70**, 3235 (1993).

[6] A. S. Zibrov, M. D. Lukin, D. E. Nikonov, L. Hollberg, M. O. Scully, V. L. Velichansky, and H. G. Robinson, Phys. Rev. Lett. **75**, 1499 (1995).

[7] G. G. Padmabandu, G. R. Welch, I. N. Shubin, E. S. Fry, D. E. Nikonov, M. D. Lukin, and M. O. Scully, Phys. Rev. Lett. **76**, 2053 (1996).

[8] M. M. Kash, V. A. Sautenkov, A. S. Zibrov, L. Hollberg, G. R. Welch, M. D. Lukin, Y. Rostovtsev, E. S. Fry, and M. O. Scully, Phys. Rev. Lett. **82**, 5229 (1999); D. Budker, D. F. Kimball, S. M. Rochester, and V. V. Yashchuk, Phys. Rev. Lett. **83**, 1767 (1999); O. Kocharovskaya, Y. V. Rostovtsev, and M. O. Scully, Phys. Rev. Lett. **86**, 628(2001).

[9] M.O. Scully, Phys. Rev. Lett. **67**, 1855 (1991); U. Rathe, M. Fleischhauer, S. Y. Zhu, T. W. Hansch, M.O. Scully, Phys. Rev. A **47**, 4994 (1993); M. D. Lukin, S. F. Yelin,

A. S. Zibrov, M. O. Scully, Laser Phys. **9**, 759 (1999); J.P. Dowling, C.M. Bowden, Phys. Rev. Lett. **70**, 1421 (1993).

[10] M. Fleischhauer and M. O. Scully, Phys. Rev. A **49**,1973 (1994); H. Lee, M. Fleischhauer and M.O. Scully, Phys. Rev. A **58**, 2587 (1998).

[11] M. Jain, H. Xia, G. Y. Yin, A. J. Merriam, and S. E. Harris, Phys. Rev. Lett. **77**, 4326 (1996); M. Jain, J. E. Field, and G. Y. Yin, Opt. Lett. **18**, 998 (1993).

[12] M. O. Scully, Phys. Rev. Lett. **104**, 207701 (2010).

[13] G. S. Engel, T. R. Calhoun, E. L. Read, T. K. Ahn,T. Mancal, Y.C Cheng, R.E. Blankenship and G.R.Fleming, Nature **446** 782 (2007)

[14] E. Collini, C.Y. Wong, K. E. Wilk, P. M. Curmi, P. Brumer and G. D. Scholes Nature **463** 644(2010).

[15] G. Panitchayangkoon, D. Hayes, K. A. Fransted, J. R. Caram, E. Harel, J. Wen, R. E. Blankenship and G. S. Engel Proc. Nat. Acad. Sci. **107** 12766(2010).

[16] A. K. Wojcik, F. Xie, V. R. Chaganti, A. A. Belyanin, and J. Kono, J. Mod. Opt. **55**, 3305 (2008).

[17] P. Vasinajindakaw, J. Vaillancourt, G. Gu, R. Liu, Y. Ling, and X. Lu, App. Phys. Lett. **98**, 211111 (2011).

[18] J. Faist, F. Capasso, C. Sirtori, K. W. West, and L. N. Pfeiffer, Nature **390**, 589 (1997).

[19] H. Schmidt, K.L. Campman, A. C. Gossard, and A. Imamoglu, Appl. Phys. Lett. **70**, 3455 (1997).

[20] A. E. Miroshnichenko, S. Flach, and Y. S. Kivshar, Rev. Mod. Phys. **82**, 2257 (2010).

[21] H. M. Gibbs, G. Khitrova and S. W. Koch, Nat. Phot **5**, 275 (2011).

[22] S. G. Carter, V. Birkedal, C. S. Wang, L. A. Coldren, A. V. Maslov, D. S. Citrin, and M. S. Sherwin, Science **310**, 651(2005).

[23] B. R. Mollow, Phys. Rev. **188**, 1969 (1969).

[24] F. Y. Wu, S. Ezekiel, M. Ducloy, and B. R. Mollow, Phys. Rev. Lett. **38**, 1077 (1977).

[25] E. del Valle and F. P. Laussy, Phys. Rev. Lett. 105, 233601 (2010).

[26] M.O. Scully, Y. Rostovtsev, A. Svidzinsky, Jun-Tao Chang, J.Mod. Opt. **55**, 3219 (2008).

[27] N. E. Mavromatos, J. Phys.: Conf. Ser. **329** 012026 (2011).

[28] L. Allen and J. H. Eberly, *Optical Resonance and Two-Level Atoms*, (Cambridge University Press, Cambridge, England, 1997).

[29] B. W. Shore, *The Theory of Coherent Atomic Excitation*, (Wiley, 1990).

[30] P. K. Jha, H. Eleuch, Y. V. Rostovtsev, J. Mod. Opt. 58, 652 (2011).

[31] H. Eleuch, P. K. Jha, Y. V. Rostovtsev, Math. Sci. Lett. 1, 1(2012).

[32] Y. V. Vladimirova, V. Y. Klimov, V. M. Pastukhov, and V. N. Zadkov, Phys. Rev. A**85**, 053408 (2012).

[33] D. E. Nikonov, M. O. Scully, M. D. Lukin, E. S. Fry, L. W. Hollberg, G. G. Padmbandu, G. R. Welch, A. S. Zibrov, Proc. SPIE **2798**, 342(1996)

[34] K.-A. Suominen, B.M. Garraway, S. Stenholm, Opt. Commun. **82**, 260 (1991).

[35] K.-A. Suominen, B.M. Garraway, Phys. Rev. A **45**, 374 (1992)

[36] S. Stenholm, Las. Phys. **15**, 1421 (2005).

[37] N. Rosen and C. Zener, Phys. Rev. **40**, 502 (1932).

[38] F. Bloch, A. Siegert, Phys. Rev. **57**, 522 (1940).

[39] M. A. Nielsen and I. L. Chuang, *Quantum Computation and Quantum Information* (Cambridge University Press, Cambridge, England, 1990).

[40] H.C. Torrey, Phys. Rev. **76** 1059 (1949); H. Salwen, Phys. Rev. **99**, 1274 (1955); G.M. Genkin, Phys. Rev. A **58**, 758 (1998); A. Plucinska and R. Parzynski, J. Mod. Optics **54**, 745 (2007); N. Rosen and C. Zener, Phys. Rev. **40**, 502 (1932); M.V. Fedorov, Opt. Commun. **12**, 205 (1974); M.V. Fedorov,Sov. J. Quant. Electron. **5**, 816 (1975).

[41] I. I. Rabi Phys. Rev. **51** 652(1937); L D Landau Physik Z. Sowjetunion **2** 46(1932); Y N Demkov Sov. Phys. JETP **18** 138(1964); F T Hioe Phys. Rev. A **30** 2100(1984); A. Bambini and P. R. Berman Phys. Rev. A **23** 2496(1981); Zakrzewski J Phys. Rev. A **32** 3748(1985); E. E. Nikitin Opt. Spectrosc. **13** 431(1)(1969); N. V. Vitanov J. Phys. B: At. Mol. Opt. Phys. **27** 1791(1994).

[42] A. M. Dykhne Sov. Phys. JETP **11** 411(1960).

[43] J P Davis and P Pechukas J. Chem. Phys. **64** 3129(1976).

[44] Y. Rostovtsev, H. Eleuch, A. Svidzinsky, H. Li, V. Sautenkov, M.O.Scully. Phys. Rev. A **79**, 063833 (2009).

[45] J. D. Jackson, *Classical Electrodynamics* (New York, Wiley, 1962).

[46] K. Heun, Math. Ann. **33**, 161 (1889).

[47] A. Ronveaux, *Heun's Differential Equations*. Oxford University Press, Oxford, 1995.

[48] N. Gurappa and P. K. Panigrahi J. Phys. A. Math. Gen. **37** L605 (2004);

[49] N. Gurappa, P. K. Jha, P. K. Panigrahi, SIGMA **3** 057(2007).

[50] R S Maier Math. Comp. **76** (2007).

[51] M.O. Scully , G.W. Kattawar , R.P. Lucht , et al., Proc. Nat. Acad. Sci. **99**, 10994 (2002).

[52] A. W. Weiner, Rev. Sci. Instrum. **71**, 1929 (2000).

[53] P. K. Jha and Y. V. Rostovtsev, Phys. Rev. A **81**, 033827 (2010).

[54] F. T. Hioe Phys. Rev. A **30**, 2100(1984); F. T. Hioe and C. E. Carroll Phys. Rev. A **32**, 1541 (1985); J. Zakrzewski Phys. Rev. A **32**, 3748 (1985); C. E. Carroll and F. T. Hioe Phys. Rev. A **41**, 2835 (1990); D. Goswami and W S. Warren Phys. Rev. A **50**, 5190 (1994); E J Robinson J. Phys. B **18**, 3687 (1985); P. A. Ivanov and N. V. Vitanov Phys. Rev. A **71**, 063407 (2005); A. Ishkhanyan, K.-A. Suominen, J. Phys. A: Math. Gen. **34** 6301 (2001).

[55] Martin Wegener, Extreme Nonlinear Optics: An Introduction (Berlin, Springer, 2005).

[56] T. Brabec, F. Krausz, Rev. Mod. Phys. **72**, 545 (2000).

[57] A. Baltuska, Th. Udem, M.Uiberacker, M.Hentschel, E.Goulielmakis, Ch. Gohle, R.Holzwarth, V.S.Yakovlev, A.Scrinzi, T.W.Hansch and F.Krausz, Nature, **421**, 611 (2003).

[58] L. W. Casperson, Phys. Rev. A **57**, 609 (1998). See also Phys. Rev. A **46**, 401 (1992)

[59] S. Hughes, Phys. Rev. Lett. **81**, 3363 (1998). See also Phys. Rev. A **62**, 055401 (2000)

[60] N. Doslic, Phys. Rev. A **74**, 013402 (2006)

[61] C. Jirauschek, L. Duan, O. D. Mücke, F. X. KŁrtner, M. Wegener, and U. Morgner, J. Opt. Soc. Am. B **22**, 2065 (2005).

[62] R. Parzyński and M Sobczak, J. Phys. B: At. Mol. Opt. Phys. **37**, 743(2004)

[63] R. Parzyński and M Sobczak, Optics Comm. **228**, 111 (2003).

[64] H. Li, V. A. Sautenkov, Y. V. Rostovtsev, M. M. Kash, P. M. Anisimov, G. R. Welch and M.O. Scully, Phys. Rev. Lett. **104**, 103001 (2010).

[65] P. K. Jha, Y. V. Rostovtsev, H.Li, V. A. Sautenkov and M.O. Scully Phys. Rev. A **83**, 033404 (2011)

[66] N. V. Vitanov, N. J. Phys. **9**, 58 (2007).

[67] B. T. Torosov and N. V. Vitanov, Phys. Rev. A **76**, 053404 (2007).

[68] J. Qian, Y. Qian, M. Ke, Xun-Li Feng, C. H. Oh, and Y. Wang, Phys. Rev. A **80**, 053413 (2009).

[69] P. Jaegle, *Coherent sources of XUV radiation* (Springer, New York, 2005).

[70] P. Gibbon, *Short pulse laser interactions with matter: an introduction* (London : Imperial College Press, 2005).

[71] Y. Rostovtsev, M.O. Scully, J. Mod. Opt. **54**, 1213 (2007).

[72] Y. Rostovtsev, J. Mod. Opt. **55**, 3149 (2008).

[73] Y. Rostovtsev, J. Mod. Opt. **56**, 1949 (2009).

[74] K. H. Hahn, D. A. King, and S. E. Harris,Phys. Rev. Lett. **65**, 2777, (1990);

[75] K. Hakuta, L. Marmet, B. P. Stoicheff, Phys. Rev. Lett. **66**, 596, (1991);

[76] G. Z. Zhang, K. Hakuta, B. P. Stoicheff, Phys. Rev. Lett. **71**, 3099 (1993);

[77] Y. Li and M. Xiao, Opt. Lett. **21**, 1064 (1996).

[78] M. Jain, H. Xia, G. Y. Yin, A. J. Merriam, S. E. Harris, Phys. Rev. Lett. **77**, 4326 (1996).

[79] R. W. Boyd, M. O. Scully, Appl. Phys. Lett. **77**, 3559 (2000).

[80] N. G. Kalugin; Y. V. Rostovtsev, Optics Letters **31**, 969 (2006).

[81] V. A. Sautenkov, C.Y. Ye, Y.V. Rostovtsev, G.W. Welch, M.O. Scully, Phys. Rev. A **70**, 033406 (2004).

[82] See page 958 from A.S.Siegman, *LASERS*, (University Science Books, California, USA, 1986).

[83] Z. Ficek and S. Swain *Quantum Interference and Coherence*, Springer New-York, (2007).

[84] A. Ishizaki, and G . Fleming, PNAS **106**, 17255 (2009).

[85] U. Fano, Phys. Rev. **124**, 1866 (1961).

[86] G. S. Agarwal , Springer Tracts in Modern Physics: Quantum Optics (Springer-Verlag, Berlin, 1974).

[87] S. E. Harris, Phys. Rev. Lett. **62**, 1033 (1989).

[88] M. O. Scully, S. -Y. Zhu, and A. Gavrielides, Phys. Rev. Lett. **62**, 2813 (1989).

[89] O. Kocharovskaya, Phys. Rep. **219**, 175 (1992).

[90] P. Mandel and O. Kocharovskaya, PhysRev. A **45**, 2700 (1992).

[91] M.O. Scully, K.R. Chapin, K.E. Dorfman, M.B. Kim, and A.A. Svidzinsky, Proc. Nat. Acad. Sci. **108**, 15097 (2011).

[92] A.A. Svidzinsky, K.E. Dorfman, and M.O. Scully, to be published Phys. Rev. A **84**, 053818 (2011).

[93] M.O. Scully, M. S. Zubairy, G. S. Agarwal, and H. Walther, Science **299**, 862 (2003).

[94] A.P.Kirk, Phys. Rev. Lett. **106**, 048703 (2011).

[95] M.O.Scully, Phys. Rev. Lett. **106**, 049801 (2011).

[96] K.R.Chapin, K.E.Dorfman, A.A.Svidzinsky, and M.O.Scully, arXiv:1012.5321

[97] Z. Wang, Annals of Physics **326**, 340 (2011).

[98] A. Imamoglu and R. J. Ram, Optics letters **19**, 1744 (1994).

[99] M. O. Scully, Laser Phys. **17**, 635 (2007).

[100] M. O. Scully, E. S. Fry, C. H. R. Ooi, and K. Wodkiewicz, Phys. Rev. Lett. **96**, 010501 (2006).

[101] Sumanta Das, G. S. Agarwal and M. O. Scully, Phys. Rev. Lett. **101**, 153601 (2008)

[102] H. R. Xia, C. Y. Ye, and S. Y. Zhu, Phys. Rev. Lett. 77, 1032 (1996).

[103] M.O.Scully Coherent Control, Fano Interference, and Non-Hermitian Interactions, Workshop held in May, 1999 (Kluwer Academic Publishers, Norwell, MA, 2001).

[104] A. Sitek and P. Machnikowski, Phys. Status. Solidi B **248**, 847 (2011).

[105] P. K. Jha, Y. V. Rostovtsev, H. Li, V. A. Sautenkov, and M. O. Scully, Phys. Rev. A **83**, 033404 (2011)

[106] P. K. Jha, H. Li, V. A. Sautenkov, Y. V. Rostovtsev, and M. O. Scully, Opt. Commun. **284**, 2538 (2011).

[107] F. A. Hopf, P. Meystre, M. O. Scully, and J. F. Seely, Phys. Rev. Lett. **35**, 511, (1975).

[108] R. Bonifacio, F. A. Hopf, P. Meystre, and M. O. Scully, Phys. Rev. A. **12**, 2568, (1975).

[109] F. A. Hopf and M. O. Scully, Phys. Rev. **179**, 399(1969).

[110] R. Dicke, Phys. Rev. **93**, 99, (1954).

[111] V. Kocharovsky, S. Cameron, K. Lehmann, R. Lucht, R. Miles, Y. Rostovtsev, W. Warren, G. R. Welch, and M. O. Scully, PNAS **102**, 7806 (2005)

[112] T. W. Hansch and P. E. Toschek, Z. Phys., **236**, 213 (1970)

[113] O. Kocharovskaya and Ya. I. Khanin, JETP Lett. **48**, 581 (1988).

[114] S. E. Harris, Phys. Rev. Lett., **62**, 1033 (1989).

[115] M. O. Scully, S. Y. Zhu, and A. Gavrielides, Phys. Rev. Lett., **62**, 2813 (1989).

[116] A. S. Zibrov, M. D. Lukin, D. E. Nikonov, L. Hollberg, M. O. Scully, V. L. Velichansky, and H. G. Robinson, Phys. Rev. Lett., **75** 1499 (1995).

[117] G. Padmabandu, G. R. Welch, I. N. Shubin, E. S. Fry, D. E. Nikonov, M. D. Lukin, and M. O. Scully, Phys. Rev. Lett., **76**, 2053 (1996).

[118] S. E. Harris and J. J. Macklin, Phys. Rev. A, **40**, 4135 (1989).

[119] M.O.Scully, Advances in multi-photon processes and spectroscopy, in Proc. US-Japan Workshop Honolulu, USA **14** 126 (1999).

[120] D. Braunstein and R. Shuker, Phys. Rev. A **68**, 013812, 2003.

[121] S.Ya.Kilin,K.T.Kapale,and M.O.Scully, Phys. Rev. Lett. **100**, 173601 (2008).

[122] X. Flechard, E. Linard, A. Mry1, D. Rodrguez, G. Ban, D. Durand, F. Duval, M. Herbane, M. Labalme, F. Mauger, O. Naviliat-Cuncic, J. C. Thomas, and Ph. Velten, Phys. Rev. Lett. **101**, 212504 (2008).

[123] A. M. Ghalambor Dezfuli, R. B. Moore, S. Schwarz, and P. Varfalvy Proceedings of International Nuclear Physics Conference, INPC 2001, E. Norman, G. Wozniak, and L. Schroeder, Eds., p. 932, 2002.

[124] G. W. F. Drake and D. C. Morton, A multiplet table for neutral Helium (4He I) with transition rates, ApJSS **170**, 251(2007).

[125] L.V.Keldysh, Soviet Phys. JETP **20**, 1307 (1965).

[126] N. H. Burnett and P. B. Corkum, J. Opt. Soc. Amer. B **6** 1195 (1989).

[127] Y. Avitzour, S. Suckewer, and E. Valeo, Phys. Rev. E **69**, 046409 (2004).

[128] Y. Avitzour and S. Suckewer, JOSA B, **24** 819 (2007).

[129] K. Bergmann,H. Theuer,and B. W. Shore, Rev. Mod. Phys., **70**, 1003 (1998).

[130] J. J. Rocca,V. Shlyaptsev, F. G.Tomasel, O. D. Cortzar, D. Hartshorn, and J. L. A. Chilla, Phys. Rev. Lett. **73** 2192 (1994).

[131] S. V. Milton,E. Gluskin, N. D. Arnold,C. Benson,W. Berg, S. G. Biedron, M. Borland, Y.-C. Chae, R. J. Dejus, P. K. Den Hartog, B. Deriy, M. Erdmann, Y. I. Eidelman, M. W. Hahne, Z. Huang, K.-J. Kim, J. W. Lewellen, Y. Li, A. H. Lumpkin, O.

Makarov, E. R. Moog, A. Nassiri, V. Sajaev, R. Soliday, B. J. Tieman, E. M. Trakhtenberg, G. Travish, I. B. Vasser- man, N. A. Vinokurov, X. J. Wang, G. Wiemerslage, and B. X. Yang, Science **292** 2037 (2001).

[132] B. E. Lemoff, G. Y. Yin, C. L. Gordon, C. P. J. Barty, and S. E. Harris, Phys. Rev. Lett. **74** 1574 (1995).

[133] S. Suckewer, C. H. Skinner, H. Milchberg, C. Keane, and D. Voorhees, Phys. Rev. Lett. **55** 1753 (1985).

[134] D. V. Korobkin, C. H. Nam, S. Suckewer, and A. Goltsov, Phys. Rev. Lett. **77** 5206 (1996).

[135] Y. Nagata, K. Midorikawa, S. Kubodera, M. Obara, H. Tashiro, and K. Toyoda, Phys. Rev. Lett. **71** 3774 (1993).

[136] K. M. Krushelnick, W. Tighe, and S. Suckewer, J. Opt. Soc. Amer. B **13** 306 (1996).

[137] Einstein A 1905 *Annalen der Physik* **17**, 132

[138] Einstein A 1917 *Physikalische Zeitschrift* **18**, 121

[139] Sargent M, Scully M O and Lamb W Jr 1974 *Laser Physics* (Addison-Wesley, Reading, Mass.)

[140] S. Suckewer and C.H. Skinner, Science **247**, 1553 (1990).

[141] C.H. Skinner, Phys. Fluids B **3**, 2420 (1991)

[142] S. Suckewer and P. Jaeglé, Laser Phys. Lett. **6**, 411 (2009).

[143] C. H. Skinner, D. S. DiCicco, D. Kim, R. J. Rosser, S. Suckewer, A. P. Gupta, and J. G. Hirschberg, J. Microsc. **159**, 51 (1990).

[144] J. J. Rocca, V. Shlyaptsev, F. G. Tomasel, O. D. Cortzar, D. Hartshorn, and J. L. A. Chilla, Phys. Rev. Lett. **73**, 2192 (1994).

[145] S. V. Milton, E. Gluskin, N. D. Arnold, C. Benson, W. Berg, S. G. Biedron, M. Borland, Y.-C. Chae, R. J. Dejus, P. K. Den Hartog, B. Deriy, M. Erdmann, Y. I. Eidelman, M. W. Hahne, Z. Huang, K.-J. Kim, J. W. Lewellen, Y. Li, A. H. Lumpkin, O. Makarov, E. R. Moog, A. Nassiri, V. Sajaev, R. Soliday, B. J. Tieman, E. M. Trakhtenberg, G. Travish, I. B. Vasserman, N. A. Vinokurov, X. J. Wang, G. Wiemerslage and B. X. Yang, Science **292**, 2037 (2001).

[146] B. E. Lemoff, G. Y. Yin, C. L. Gordon, C. P. J. Barty and S. E. Harris, Phys. Rev. Lett. **74**, 1574 (1995).

[147] S. Suckewer, C. H. Skinner, H. Milchberg, C. Keane, and D. Voorhees , Phys. Rev. Lett. **55**, 1753 (1985).

[148] S. Suckewer, C.H. Skinner, D. Kim, E. Valeo, D. Voorhees, and A. Wouters, Phys. Rev. Lett. 57, 1004 (1986).

[149] F. Krausz and M. Ivanov, Rev. Mod. Phys. **81**, 163 (2009).

[150] G. Sansone, E. Benedetti, F. Calegari, C. Vozzi, L. Avaldi, R. Flammini, L. Poletto, P. Villoresi, C. Altucci, R. Velotta, S. Stagira, S. De Silvestri and M. Nisoli, Science **314**, 443 (2006).

[151] M. Schultze, E. Goulielmakis, M. Uiberacker, M. Hofstetter, J. Kim, D. Kim, F. Krausz, and U. Kleineberg, New J. Phys. **9**, 243 (2007).

[152] D.L. Matthews, P.L. Hagelstein, M.D. Rosen, M.J. Eckart, N.M. Ceglio, A.U. Hazi, H. Medecki, B.J. MacGowan, J.E. Trebes, B.L. Whitten, E.M. Campbell,

C.W. Hatcher, A.M. Hawryluk, R.L. Kauffman, L.D. Pleasance, G. Ram- bach, J.H. Scofield, G.Stone, and T.A. Weaver, Phys. Rev. Lett. **54**, 110 (1985)

[153] M.D. Rosen, P.L. Hagelstein, D.L. Matthews, E.M. Campbell, A.U. Hazi, B.L. Whitten, B. MacGowan, R.E. Turner, R.W. Lee, G. Charatis, Gar.E. Busch, C.L. Shepard, and P.D. Rockett, Phys. Rev. Lett. **54**, 106 (1985).

[154] Y. Nagata, K. Midorikawa, S. Kubodera, M. Obara, H. Tashiro and K. Toyoda, Phys. Rev. Lett. **71**, 3774 (1993).

[155] D.V. Korobkin, C.H. Nam, S. Suckewer and A. Goltsov, Phys. Rev. Lett. **77**, 5206 (1996)

[156] K.M. Krushelnick, W. Tighe and S. Suckewer, J. Opt. Soc. Am. B **13**, 306 (1996)

[157] A. Goltsov, A. Morozov, S. Suckewer, R. C. Elton, U. Feldman, K. Krushelnick, T. C. Jones, C. I. Moore, J. F. Seely, P. Sprangle, A. C. Ting, and A. Zigler, Proc. SPIE **3776**, 126 (1999).

[158] A.N. Zherikhin, K.N. Koshelev, and V.S. Letokhov, Sov. J. Quantum Electron. **6**, 82 (1976).

[159] A.V. Vinogradov, I.I. Sobelman, and E.A. Yukov, Sov. J. Quantum Electron. **7**, 32 (1977)

[160] L.A. Vainshtein, A.V. Vinogradov, U.I. Safronova, and I.Yu. Skobelev, Sov. J. Quantum Electron. **8**, 239 (1978).

[161] A.V. Vinogradov and V.N. Shlyaptsev, Sov. J. Quantum Electron. **10**, 754 (1980).

[162] W. F. Krupke, R. J. Beach, V. K. Kanz, and S. A. Payne, Opt. Lett. **28**, 2336 (2003).

[163] M. D. Rotondaro, Ph.D. Thesis, Air Force Institute of Technology, Ohio (1995).

[164] T. Brabec, F. Krausz, Rev. Mod. Phys. **72**, 545 (2000).

[165] A. de Bohan, P. Antoine, D. B. Milosevic, and B. Piraux, Phys. Rev. Lett. **81**, 1837 (1998).

[166] G.G. Paulus, F. Grasbon, H. Walther, P. Villoresi, M. Nisoli, S. Stagira, E. Priori, and S. De Silvestri, Nature **414**, 182 (2001).

[167] V. Roudnev B. D. Esry, and I. Ben-Itzhak, Phys. Rev. Lett. **93**, 163601 (2004).

[168] A. Baltuška,Th. Udem, M. Uiberacker, M. Hentschel, E. Goulielmakis, Ch. Gohle, R. Holzwarth, V. S. Yakovlev, A. Scrinzi, T. W. Hänsch and F. Krausz, Nature **421**, 611 (2003).

[169] C. Jirauschek, et al., J. Opt. Soc. Am. B **22**, 2065 (2005).

[170] A. Apolonski, P. Dombi, G.G. Paulus, M. Kakehata, R. Holzwarth, T. Udem, C. Lemell, K. Torizuka, J. Burgdörfer and T. W. Hänsch, Phys. Rev. Lett. **92**, 073902 (2004)

[171] T. M. Fortier, P. A. Roos, D. J. Jones, S. T. Cundiff, R. D. R. Bhat and J. E. Sipe, Phys. Rev. Lett. **92**, 147403 (2004).

[172] S. A. Diddams, D. J. Jones, Jun Ye, S. T. Cundiff, J. L. Hall, J. K. Ranka, R. S. Windeler, R. Holzwarth, T. Udem, and T. W. Hänsch, Phys. Rev. Lett. **84**, 5102 (2000)

[173] Y.Y. Yin, Ce Chen, D. S. Elliott and A. V. Smith, Phys. Rev. Lett. **69**, 2353 (1992); M. Shapiro and P. Brumer, Adv. At. Mol. Opt. Phys. **42**, 287 (2000); A. Haché, Y. Kostoulas, R. Atanasov, J. L. P. Hughes, J. E. Sipe, and H. M. van Driel, Phys. Rev. Lett. **78**, 306 (1997).

[174] D.J. Jones, S. A. Diddams, J. K. Ranka, A. Stentz, R. S. Windeler, J. L. Hall and S. T. Cundiff, Science **288**, 635 (2000).

[175] A.J. Verhoef et al., Opt. Lett. **31**, 3520 (2006); T. Wittmann, B. Horvath, W. Helml, M. G. Schätzel, X. Gu, A. L. Cavalieri, G. G. Paulus and R. Kienberger, Nature **5**, 357 (2009).

[176] P. Tzallas, E. Skantzakis, and D. Charalambidis, Phys. Rev. A **82**, 061401 (2010).

[177] P. Tzallas, E. Skantzakis, C. Kalpouzos, E. P. Benis, G. D. Tsakiris and D. Charalambidis, Nature Physics **3**, 846 (2007).

[178] V.A. Sautenkov, Y.V.Rostovtsev, H. Chen, P. Hsu, G. S. Agarwal, and M. O. Scully , Phys. Rev. Lett. **94**, 233601 (2005).

[179] H. Rhee, Y-G June, J-S Lee, K-K Lee, J-H Ha, Z. H. Kim, S-J Jeon and M. Cho, Nature **458**, 310 (2009).

[180] N. Bloembergen,J. Opt. Soc. Am. **70**, 1429 (1980).

[181] R.W. Boyd, *Nonlinear Optics* (Academic Press, San Diego, CA 1992).

[182] Y.R. Shen, *The Principles of Nonlinear Optics* (John Wiley & Sons, Inc, Hoboken, NJ 2003).

[183] V. Kocharovsky, S. Cameron, K. Lehmann, R. Lucht, R. Miles, Y. Rostovtsev, W. Warren, G.R. Welch, and M.O. Scully, Proc. Natl. Acad. Sci. **102**, 7806 (2005).

[184] A. M. Zheltikov, M.N. Shneider, and R.B. Miles Appl. Phys. B **83**, 149 (2006).

[185] N. Bloembergen, and A. J. Sievers, Appl. Phys. Lett. **17**, 483 (1970).

[186] C.M. Bowden, and A. M. Zheltikov ed., feature issue of J. Opt. Soc. Am. B **19**, 2042 (2002).

[187] Y.V. Rostovtsev, Z.-E. Sariyanni, and M.O. Scully, Phys. Rev. Lett. **97**, 113001 (2006).

[188] A. Zumbusch, G.R. Holtom, and X.S. Xie, Phys. Rev. Lett. **82**, 4142 (1999).

[189] A. Dogariu, J.B. Michael, M. O. Scully, and R.B. Miles, Science **331**, 442 (2011).

[190] N.W. Ashcroft, and N.D. Mermin, Solid State Physics (Harcourt, Orlando, 1976).

[191] T. Ichimura, N. Hayazawa, M. Hashimoto, Y. Inouye, and S. Kawata, Phys. Rev. Lett. **92**, 220801 (2004).

[192] M. Afzelius, C. Brackmann, F. Vestin, and P. Bengtsson, Applied Optics **43**, 6664 (2004).

[193] T. Seeger, J. Kiefer, A. Leipertz, B.D. Patterson, C.J. Kliewer, and T.B. Settersten, Optics Lett. **34**, 3755 (2009).

[194] D. Pestov, R.K. Murawski, G.O. Ariunbold, X. Wang, M. Zhi, A.V. Sokolov, V.A. Sautenkov, Y.V. Rostovtsev, A. Dogariu, Y. Huang, and M.O. Scully, Science **316**, 265 (2007).

[195] D. Pestov, X. Wang, G.O. Ariunbold, R.K. Murawski, V.A. Sautenkov, A. Dogariu, A.V. Sokolov, and M.O. Scully, Proc. Natl. Acad. Sci. USA **105**, 422 (2008).

[196] A.C. Eckbreth, Appl. Phys. Lett. **32**, 421 (1978).

[197] A. Compaan, and S. Chandra, Opt. Lett. **4**, 170 (1979).

[198] H. Ninomiya, S. Yaeshima, K. Ichikawa, Optical Engineering **46**, 094301 (2007).

[199] W.S. Heaps, J. Burris, and J.A. French, Applied Optics **36**, 9402 (1997).

[200] Y.F. Arshinov, S.M. Bobrovnikov, V.E. Zuev, and V.M. Mitev, Applied Optics **22**, 2984 (1983).

[201] K.P. Huber, and G. Herzberg, *Molecular Spectra and Molecular Structure IV. Constants of Diatomic Molecules* (Van Nostrand, New York, 1979).

[202] J.P. Kuehner, S.V. Naik, W.D. Kulatilaka, N. Chai, N.M. Laurendeau, R.P. Lucht, M.O. Scully, S. Roy, A.K. Patnaik, and J.R. Gord, J. Chem. Phys. **128**, 174308 (2008).

[203] G.L. Eesly, Coherent Raman Spectroscopy (Pergammon Press, New York, 1981).

[204] A.M. Zheltikov, Opt. Lett. **32**, 2052 (2007).

[205] I.V. Fedotov, A.D. Savvin, A.B. Fedotov, and A.M. Zheltikov, Opt. Lett. **32**, 1275 (2007).

[206] L. Essen and J. V. L. Parry, Nature **176**, 280 (1955).

[207] N. F. Ramsey, J. Res. NBS **88**, 301 (1983).

[208] R. Frisch, Z. Phys. **86**, 42 (1933).

[209] J. Brossel, A. Kastler, and J. Winter, J. Phys. Radium **13**, 668 (1952).

[210] W. B. Hawkins and R. H. Dicke, Phys. Rev. **91**, 1008 (1953).

[211] P. Kusch, S. Millman, and I. I. Rabi, Phys. Rev. **57**, 765 (1940).

[212] G. Alzetta, A. Gozzini, L. Moi, and G. Orriols, Nuovo Cimento B **36**, 5 (1976).

[213] E. L. Raab, M. Prentiss, A. Cable, S. Chu, and D. E. Pritchard, Phys. Rev. Lett. **59**, 2631 (1987).

[214] M. H. Anderson, J. R. Ensher, M. R. Matthews, C. E. Wieman, and E. A. Cornell, Science **269**, 198 (1995).

[215] M. Lintz and M. A. Bouchiat, Phys. Rev. Lett. **80**, 2570 (1998).

[216] T. Ban, D. Aumiler, and G. Pichler, A **71**, 022711(2005)

[217] D.H. Sarkisyan, A.S. Sarkisyan, and A.K. Yalanusyan, Appl. Phys. B **66** 241(1998)

[218] E. B. Alexandrov, M. V. Balabas, D. Budker, D. English, D. F. Kimball, C.-H. Li, and V. V. Yashchuk, Phys. Rev. A **66**, 042903 (2002).

[219] M. T. Graf, D. F. Kimball, S. M. Rochester, K. Kerner, C. Wong, D. Budker, E. B. Alexandrov, M. V. Balabas, and V. V. Yashchuk, Phys. Rev. A **72**, 023401 (2005).

[220] V. M. Acosta, A. Jarmola, D. Windes, E. Corsini, M. P. Ledbetter, T. Karaulanov, M. Auzinsh, S. A. Rangwala, D. F. Jackson Kimball, and D. Budker, New J. Phys. **12**, 083054 (2010).

[221] E. Mariotti, S. Atutov, M. Meucci, P. Bicchi, C. Marinelli, and L. Moi, Chem. Phys. **187**, 111 (1994).

[222] R. Gupta, W. Happer, J. Wagner, and E. Wennmyr, J. Chem. Phys. **68**, 799 (1978).

[223] The width of the response of Raman signal against the single photon detuning will be governed by Doppler broadening.

[224] Shaul Mukamel, *Principles of Nonliear Optical Spectroscopy* (Oxford University Press, New York, 1995).

[225] P.M. Morse, *Phys. Rev.* **34**, 57 (1929).

[226] D. Steele, E.R. Lippincott, and J.T. Vanderslice, Rev. Mod. Phys. **34**, 239 (1962).

[227] G. Herzberg, *Molecular Spectra and Molecular Structure. I. Spectra of Diatomic Molecules*, 2nd ed. (D. Van Nostrand Company, New York, 1950).

[228] L. Yuan, G. O. Ariunbold, R. K. Murawski, D. Pestov, X. Wang, A. K. Patnaik, V. A. Sautenkov, A. V. Sokolov, Y. V. Rostovtsev, and M.O.Scully, Phys. Rev. A **81**, 053405 (2010).

[229] An. N. Nesmeyanov, *Vapor Pressure of the Elements* (Academic, New York, 1963).

[230] A. Gozzini, F. Mango, J. H. Xu, G. Alzetta, F. Maccarrone, and R. A. Bernheim, Nuovo Cimento D **15**, 709 (1993).

[231] *Nonlinear Spectroscopy*, Ed. by N. Bloembergen (Societá Italiana di Fisica, Bologna, 1977; Mir, Moscow, 1979).

[232] J. H. Eberly and N. E. Rehler, Phys. Lett. 29A, 142 (1969); Phys. Rev. A **2**, 1607 (1970); **3**, 1735 (1971).

[233] N. Skribanowitz, I. P. Herman, J. C. MacGillivray, and M. S. Feld , Phys. Rev. Lett. **30**, 309 (1973).

[234] J. C. MacGillivray and M. S. Feld, Phys. Rev. A 14, 1169(1976); Phys. Rev. A **23**, 1334(1981).

[235] R. Bonifacio and L. Lugiato, Phys. Rev. A 11, 1507 (1975); Phys. Rev. A **12**, 587 (1975).

[236] R. Bonifacio and P. Schwendimann, Nuovo Cimento Lett. **3**, 509 (1970); **3**, 512 (1970).

[237] I. D. Abella, N. A. Kurnit, and S. R. Hartmann, Phys. Rev. **141**, 391 (1966).

[238] A. V. Andreev, V. I. Emelyanov, and Yu. A. IIinskii, Sov. Phys. Usp. **23**, 493 (1980).

[239] M. F. H. Schuurmans, Q. H. F. Vrehen, D. Polder, and H. M. Gibbs, in *Advances in Atomic and Molecular Physics*, edited by D. Bates and B. Bederson (Academic, New York, 1981), p. 167.

[240] Q. U. F. Vrehen and U. M. Gibbs, in *Dissipative Systems in Quantum Optics*, edited by R. Bonifacio (Springer-Verlag, Berlin, 1982), p. 111.

[241] M. Gross and S. Haroche, Phys. Rep. **93**, 301 (1982).

[242] M. Nagasono, J. R. Harries, H. Iwayama, T. Togashi, K. Tono, M. Yabashi, Y. Senba, H. Ohashi, T. Ishikawa, and E. Shigemasa, Phys. Rev. Lett. **107**, 193603 (2011).

[243] J. H. Brownell, X. Lu and S. R. Hortmann, Phys. Rev. Lett. **75**, 3265 (1995).

[244] Q. H. F. Vrehen and M. F. H. Schuurmans, Phys. Rev. Lett. **42**, 224 (1979).

[245] M. F. H. Schuurmans, D. Polder, and Q. H. F. Vrehen, J. Opt. Soc. Am. **68**, 699 (1978).

[246] C. T. Lee, Phys. Rev. Lett. **43**, 1110 (1979).

[247] G. O. Ariunbold, W. Yang, A. V. Sokolov, V. A. Sautenkov and M. O. Scully, Phys. Rev. A **85**, 023424 (2012).

APPENDIX A

DERIVATION OF HAMILTONIAN FOR THREE-LEVEL ATOM

We consider a three-level atom (ThLA) in cascade Ξ configuration interacting with two non-resonant classical electric field. Here the transitions $c \leftrightarrow a$ and $a \leftrightarrow b$ are dipole allowed while the transition $c \leftrightarrow b$ dipole forbidden. We write the linearly polarized, monochromatic, classical electric field as

$$\vec{E}(t) = \frac{1}{2}\hat{\epsilon}_1\mathscr{E}_1 e^{-i\nu_1 t} + \frac{1}{2}\hat{\epsilon}_2\mathscr{E}_2 e^{-i\nu_2 t} + \frac{1}{2}\hat{\epsilon}_1\mathscr{E}_1 e^{i\nu_1 t} + \frac{1}{2}\hat{\epsilon}_2\mathscr{E}_2 e^{i\nu_2 t} \tag{A.1}$$

where $\hat{\epsilon}$, $\mathscr{E}$, ν are the unit polarization vector, field amplitude and the laser frequency respectively. The interaction Hamiltonian is given as

$$\mathscr{H}_1 = -e\vec{r}\cdot\vec{E}(t) \tag{A.2}$$

where $\vec{r}$ is the position vector of the electron with respect to the nucleus. The free Hamiltonian of ThLA is given as

$$\mathscr{H}_0 = \hbar\omega_a |a\rangle\langle a| + \hbar\omega_b |b\rangle\langle b| + \hbar\omega_c |c\rangle\langle c| \tag{A.3}$$

Using the completeness relation $\sum_{\{j=a,b,c\}} |j\rangle\langle j| = 1$, the interaction Hamiltonian Eq.(A.2) is given as

$$\mathscr{H}_1 = -e(\langle a|\vec{r}|b\rangle|a\rangle\langle b| + \langle b|\vec{r}|a\rangle|b\rangle\langle a| + \langle c|\vec{r}|a\rangle|c\rangle\langle a| + \langle a|\vec{r}|a\rangle|a\rangle\langle c|)\cdot\vec{E}(t) \tag{A.4}$$

Let us define dipole moment as

$$\vec{\wp}_{ab} = e\langle a|\vec{r}|b\rangle, \quad \vec{\wp}_{ca} = e\langle c|\vec{r}|a\rangle \tag{A.5}$$

Substituting Eq(A.5) in Eq(A.4) we get,

$$\begin{aligned}\mathscr{H}_1 = &-(\vec{\wp}_{ab}|a\rangle\langle b| + \vec{\wp}_{ba}|b\rangle\langle a|)\cdot\left[\frac{\hat{\epsilon}_1}{2}\mathscr{E}_1\left(e^{-i\nu_1 t}+e^{i\nu_1 t}\right)+\frac{\hat{\epsilon}_2}{2}\mathscr{E}_2\left(e^{-i\nu_2 t}+e^{i\nu_2 t}\right)\right]\\ &-(\vec{\wp}_{ca}|c\rangle\langle a| + \vec{\wp}_{ac}|a\rangle\langle c|)\cdot\left[\frac{\hat{\epsilon}_1}{2}\mathscr{E}_1\left(e^{-i\nu_1 t}+e^{i\nu_1 t}\right)+\frac{\hat{\epsilon}_2}{2}\mathscr{E}_2\left(e^{-i\nu_2 t}+e^{i\nu_2 t}\right)\right]\end{aligned} \tag{A.6}$$

Without the loss of generality let us consider that the field is polarized along z-direction. Now from Eq(A.6) we get

$$\begin{aligned}H_1 = &-\left[\frac{\wp_{ab}\mathscr{E}_1}{2}|a\rangle\langle b| + \frac{\wp_{ba}\mathscr{E}_1}{2}|b\rangle\langle a|\right]\left(e^{-i\nu_1 t}+e^{i\nu_1 t}\right)-\left[\frac{\wp_{ab}\mathscr{E}_2}{2}|a\rangle\langle b|\right.\\ &\left.+\frac{\wp_{ba}\mathscr{E}_2}{2}|b\rangle\langle a|\right]\left(e^{-i\nu_2 t}+e^{i\nu_2 t}\right)-\left[\frac{\wp_{ca}\mathscr{E}_1}{2}|c\rangle\langle a| + \frac{\wp_{ac}\mathscr{E}_1}{2}|a\rangle\langle c|\right]\left(e^{-i\nu_1 t}+e^{i\nu_1 t}\right)\\ &-\left[\frac{\wp_{ca}\mathscr{E}_2}{2}|c\rangle\langle a| + \frac{\wp_{ac}\mathscr{E}_2}{2}|a\rangle\langle c|\right]\left(e^{-i\nu_2 t}+e^{i\nu_2 t}\right)\end{aligned} \tag{A.7}$$

State vector obeys the Schrödinger equation and can be written as

$$|\Psi\rangle = a(t)e^{-i\phi_a(t)}|a\rangle + b(t)e^{-i\phi_b(t)}|b\rangle + c(t)e^{-i\phi_c(t)}|c\rangle \tag{A.8}$$

The phases $\phi(t)$ are arbitrary, and will be chosen to simplify the description of time dependence at fixed location. The equation of motion for the state b is given as

$$\begin{aligned}i\dot{b}(t) + (\dot{\phi}_b(t)-\omega_b)b(t) = &-\frac{\wp_{ba}\mathscr{E}_1}{2\hbar}\left[e^{-i(\nu_1 t+\phi_a(t)-\phi_b(t))}+e^{i(\nu_1 t-\phi_a(t)+\phi_b(t))}\right]a(t)\\ &-\frac{\wp_{ba}\mathscr{E}_2}{2\hbar}\left[e^{-i(\nu_2 t+\phi_a(t)-\phi_b(t))}+e^{i(\nu_2 t-\phi_a(t)+\phi_b(t))}\right]a(t)\end{aligned} \tag{A.9}$$

Evidently a suitable choice of phases can reduce at least one of the exponentials to unity. This is the first condition we require of the phases. Given that condition, several choices are possible. Let us chose

$$\nu_1 t - \phi_a(t) + \phi_b(t) = 0 \tag{A.10}$$

Equivalently,

$$\dot{\phi}_b(t) = \dot{\phi}_a(t) - \nu_1 \tag{A.11}$$

With this choice the second exponential argument vanishes and the other three argument becomes

$$\begin{aligned} -\nu_1 t - \phi_a(t) + \phi_b(t) &= -2\nu_1 t \\ -\nu_2 t - \phi_a(t) + \phi_b(t) &= -(\nu_2 + \nu_1)t \\ \nu_2 t - \phi_a(t) + \phi_b(t) &= (\nu_2 - \nu_1)t \end{aligned} \tag{A.12}$$

Now $e^{\pm 2i\nu_1 t}, e^{-i(\nu_1 \pm \nu_2)t}$ are rapidly oscillating terms, so in Rotating Wave Approximation, we get neglect these fast oscillating terms by replacing them with their average values, zero. Now we get

$$i\dot{b}(t) = \delta_b b(t) - \Omega_1^* a(t) \tag{A.13}$$

where the coefficient Δ_b

$$\begin{aligned} \delta_b &= \omega_b - \dot{\phi}_b(t) \\ \Omega_b^* &= \frac{\wp_{ba}\mathscr{E}_1}{2\hbar} \end{aligned} \tag{A.14}$$

The equation of motion for the state a is given as

$$\begin{aligned} i\dot{a}(t) + [\dot{\phi}_a(t) - \omega_a]a(t) = -\frac{\wp_{ab}\mathscr{E}_1}{2\hbar}\left[e^{-i(\nu_1 t + \phi_b(t) - \phi_a(t))} + e^{i(\nu_1 t - \phi_b(t) + \phi_a(t))}\right] b(t) \\ -\frac{\wp_{ab}\mathscr{E}_2}{2\hbar}\left[e^{-i(\nu_2 t + \phi_b(t) - \phi_a(t))} + e^{i(\nu_2 t - \phi_b(t) + \phi_a(t))}\right] b(t) - \frac{\wp_{ac}\mathscr{E}_1}{2\hbar}\left[e^{-i(\nu_1 t + \phi_c(t) - \phi_a(t))}\right. \\ \left. + e^{i(\nu_1 t - \phi_c(t) + \phi_a(t))}\right] c(t) - \frac{\wp_{ac}\mathscr{E}_2}{2\hbar}\left[e^{-i(\nu_2 t + \phi_c(t) - \phi_a(t))} + e^{i(\nu_2 t - \phi_c(t) + \phi_a(t))}\right] c(t) \end{aligned} \tag{A.15}$$

Let us choose

$$\nu_2 t - \phi_c(t) + \phi_a(t) = 0 \tag{A.16}$$

Equivalently,

$$\dot{\phi}_a(t) = \dot{\phi}_c(t) - \nu_2 \tag{A.17}$$

With these choices Eq(A.11,A.17), the first and the eighth exponential arguments in Eq(A.15) vanishes and the other two arguments for $b(t)$ are given by Eq(A.12) while for $c(t)$ are given

as

$$\begin{aligned} -\nu_1 t - \phi_c(t) + \phi_a(t) &= -(\nu_1 + \nu_2)t \\ \nu_1 t - \phi_c(t) + \phi_a(t) &= \nu_1 - \nu_2)t \\ -\nu_2 t - \phi_c(t) + \phi_a(t) &= -2\nu_2 t \end{aligned} \tag{A.18}$$

Now $e^{\pm 2i\nu_{(2)}t}$, $e^{-i(\nu_2 \pm \nu_1)t}$ are rapidly oscillating terms, so we replace them with their average values, zero. Now we get

$$i\dot{a}(t) = \delta_a a(t) - \Omega_1 b(t) - \Omega_2^* c(t) \tag{A.19}$$

where the coefficient δ_a, Ω_b and Ω_a^*

$$\begin{aligned} \delta_a &= \omega_a - \dot{\phi}_b(t) - \nu_1 \\ \Omega_b &= \frac{\wp_{ab}\mathscr{E}_1}{2\hbar} \\ \Omega_a^* &= \frac{\wp_{ac}\mathscr{E}_2}{2\hbar} \end{aligned} \tag{A.20}$$

The equation of motion for the state c is given as

$$\begin{aligned} i\dot{c}(t) + [\dot{\phi}_c(t) - \omega_c]c(t) = &-\frac{\wp_{ca}\mathscr{E}_1}{2\hbar}\left[e^{-i(\nu_1 t + \phi_a(t) - \phi_c(t))} + e^{i(\nu_1 t - \phi_a(t) + \phi_c(t))}\right] a(t) \\ &-\frac{\wp_{ca}\mathscr{E}_2}{2\hbar}\left[e^{-i(\nu_2 t + \phi_a(t) - \phi_c(t))} + e^{i(\nu_2 t - \phi_a(t) + \phi_c(t))}\right] a(t) \end{aligned} \tag{A.21}$$

Using Eq(A.17), we get

$$\begin{aligned} -\nu_1 t - \phi_a(t) + \phi_c(t) &= -(\nu_1 - \nu_2)t \\ \nu_1 t - \phi_a(t) + \phi_c(t) &= \nu_1 + \nu_2)t \\ -\nu_2 t - \phi_a(t) + \phi_c(t) &= -2\nu_2 t \end{aligned} \tag{A.22}$$

Now $e^{\pm 2i\nu_{(2)}t}$, $e^{i(\nu_2 \pm \nu_1)t}$ are rapidly oscillating terms, so we replace them with their average values, zero. Now we get

$$i\dot{c}(t) = \delta_c c(t) - \Omega_2 a(t) \tag{A.23}$$

where the coefficient δ_c and Ω_a

$$\begin{aligned} \delta_c &= \omega_c - \dot{\phi}_b(t) - \nu_1 - \nu_2 \\ \Omega_a &= \frac{\wp_{ca}\mathscr{E}_2}{2\hbar} \end{aligned} \tag{A.24}$$

Let us fix the value of ϕ_b as

$$\phi_b(t) = \omega_b t \tag{A.25}$$

From Eq(A.14) we get $\delta_b = 0$. Similarly using Eq.(A.10), we get

$$\phi_a(t) = \omega_b t + \nu_1 t \tag{A.26}$$

Now using Eq.(A.16) we get

$$\phi_c(t) = \omega_b t + \nu_1 t + \nu_2 t \tag{A.27}$$

From Eq.(A.20) and Eq.(A.24) we get

$$\begin{aligned} \Delta_b &= (\omega_a - \omega_b) - \nu_1 \\ \Delta_a + \Delta_b &= (\omega_c - \omega_b) - (\nu_1 + \nu_2) \end{aligned} \tag{A.28}$$

where $\Delta_a = (\omega_c - \omega_a) - \nu_2$. The equation of motion for the states b, a and c can be summarized as

$$\begin{aligned} i\dot{b}(t) &= -\Omega_b^* a(t) \\ i\dot{a}(t) &= \Delta_b a(t) - \Omega_b b(t) - \Omega_a^* c(t) \\ i\dot{c}(t) &= (\Delta_a + \Delta_b)c(t) - \Omega_a a(t) \end{aligned} \tag{A.29}$$

The equivalent Hamiltonian in matrix form is

$$\mathscr{H} = -\begin{pmatrix} 0 & \Omega_1^* & 0 \\ \Omega_1 & -\Delta_1 & \Omega_2^* \\ 0 & \Omega_2 & -\Delta_2 \end{pmatrix}$$

In a more convenient form we will write it as

$$\mathscr{H} = \Delta_b|a\rangle\langle a| + (\Delta_a + \Delta_b)|c\rangle\langle c| - (\Omega_b|a\rangle\langle b| + \Omega_a|c\rangle\langle a| + \text{H.c}) \tag{A.30}$$

Let us choose

$$\nu_2 t - \phi_a(t) + \phi_c(t) = 0 \tag{A.31}$$

Equivalently,

$$\dot{\phi}_a(t) = \dot{\phi}_c(t) + \nu_2 \tag{A.32}$$

With these choices Eq(A.11,A.32), the first and the seventh exponential arguments in Eq(A.15) vanishes and the other two arguments for $b(t)$ are given by Eq(A.12) while for $c(t)$ are given as

$$\begin{aligned} -\nu_1 t - \phi_c(t) + \phi_a(t) &= (-\nu_1 + \nu_2)t \\ \nu_1 t - \phi_c(t) + \phi_a(t) &= (\nu_1 + \nu_2)t \\ \nu_2 t - \phi_c(t) + \phi_a(t) &= 2\nu_2 t \end{aligned} \tag{A.33}$$

Now $e^{\pm 2i\nu_2 t}, e^{i(\nu_2 \pm \nu_1)t}$ are rapidly oscillating terms, so we replace them with their average values, zero. Now we get

$$i\dot{a}(t) = \Delta_a a(t) - \Omega_1 b(t) - \Omega_2 c(t) \tag{A.34}$$

where the coefficient δ_a, Ω_b and Ω_c

$$\begin{aligned} \delta_a &= \omega_a - \dot{\phi}_b(t) - \nu_1 \\ \Omega_b &= \frac{\wp_{ab}\mathscr{E}_1}{2\hbar} \\ \Omega_c &= \frac{\wp_{ac}\mathscr{E}_2}{2\hbar} \end{aligned} \tag{A.35}$$

The equation of motion for the state c is given by Eq(A.21). Using Eq(A.31), we get

$$\begin{aligned} -\nu_1 t - \phi_a(t) + \phi_c(t) &= -(\nu_1 + \nu_2)t \\ \nu_1 t - \phi_a(t) + \phi_c(t) &= (\nu_1 - \nu_2)t \\ \nu_2 t - \phi_a(t) + \phi_c(t) &= 2\nu_2 t \end{aligned} \tag{A.36}$$

Now $e^{\pm 2i\nu_2 t}, e^{-i(\nu_2 \pm \nu_1)t}$ are rapidly oscillating terms, so we replace them with their average values, zero. Now we get

$$i\dot{c}(t) = \delta_c c(t) - \Omega_2^* a(t) \tag{A.37}$$

where the coefficient δ_c and Ω_c^* are given by

$$\begin{aligned} \delta_c &= \omega_c - \dot{\phi}_b(t) - \nu_1 + \nu_2 \\ \Omega_c^* &= \frac{\wp_{ca}\mathscr{E}_2}{2\hbar} \end{aligned} \tag{A.38}$$

Fixing the value of ϕ_b as Eq(A.25), we get $\Delta_b = 0$ and ϕ_a as Eq(A.26). Using the new condition for lambda configuration Eq(A.31), we get

$$\phi_c(t) = \omega_b t + \nu_1 t - \nu_2 t \tag{A.39}$$

From Eq.(A.35) and Eq.(A.38) we get

$$\begin{aligned} \Delta_b &= (\omega_a - \omega_b) - \nu_1 \\ \Delta_b - \Delta_c &= (\omega_c - \omega_b) - (\nu_1 - \nu_2) \end{aligned} \tag{A.40}$$

The equation of motion for the states b, a and c can be summarized as

$$\begin{aligned} i\dot{b}(t) &= -\Omega_1^* a(t) \\ i\dot{a}(t) &= \Delta_1 a(t) - \Omega_1 b(t) - \Omega_2 c(t) \\ i\dot{c}(t) &= \Delta_2 c(t) - \Omega_2^* a(t) \end{aligned} \tag{A.41}$$

The equivalent Hamiltonian in matrix form is

$$\mathscr{H} = \begin{pmatrix} 0 & -\Omega_1^* & 0 \\ -\Omega_1 & \Delta_1 & -\Omega_2 \\ 0 & -\Omega_2^* & \Delta_2 \end{pmatrix}$$

In a more convenient form we will write it as

$$\mathscr{H} = \Delta_b|a\rangle\langle a| + (\Delta_b - \Delta_c)|c\rangle\langle c| - (\Omega_b|a\rangle\langle b| + \Omega_c|c\rangle\langle a| + \text{H.c}) \tag{A.42}$$

APPENDIX B

BACKWARD VS FORWARD GAIN

Let us write the electric fields propagating along the +z and -z direction as

$$\vec{E}_b(z,t) = \frac{\hat{\epsilon}_b^+}{2}\left(\mathcal{E}_b^+ e^{i\theta_b^+} + \mathcal{E}_b^{+*} e^{-i\theta_b^+}\right) + \frac{\hat{\epsilon}_b^-}{2}\left(\mathcal{E}_b^- e^{i\theta_b^-} + \mathcal{E}_b^{-*} e^{-i\theta_b^-}\right) \tag{B.1}$$

Here

$$\theta_b^+ = k_b z - \nu_b t, \quad \theta_b^- = -k_b z - \nu_b t, \tag{B.2}$$

where $\hat{\epsilon}_b, \nu_b$ are the unit polarization vector and the carrier frequency respectively. The interaction of the field $\vec{E}_b(z,t)$ with an two-level atom in the dipole approximation is given as

$$\mathscr{H}_1 = -\left(\vec{\wp}_{ab} \cdot \vec{E}_b(z,t)|a\rangle\langle b| + \text{c.c}\right) \tag{B.3}$$

The unperturbed Hamiltonian of the two-level atom is

$$\mathscr{H}_0 = \omega_a|a\rangle\langle a| + \omega_b|b\rangle\langle b|. \tag{B.4}$$

Incorporating the decay rate γ_b from $a \to b$, the equation of motion for the atomic density matrix is given as $(\hbar = 1)$

$$\frac{\partial \varrho}{\partial t} = -i[\mathscr{H}, \varrho] + \frac{\gamma_b}{2}\left([\sigma_b, \varrho\sigma_b^\dagger] + [\sigma_b\varrho, \sigma_b^\dagger]\right) \tag{B.5}$$

where the atomic lowering (σ_i) and rising operators ($\sigma_i^\dagger$) are defined as

$$\sigma_b = |b\rangle\langle a|, \quad \sigma_b^\dagger = |a\rangle\langle b|. \tag{B.6}$$

From Eq.(B.5) we obtain the equations of motion for the off-diagonal density matrix elements ϱ_{ab} as

$$\dot{\varrho}_{ab} = -\gamma_{ab}\varrho_{ab} - i\vec{\wp}_{ab} \cdot \vec{E}_b(z,t)(\varrho_{aa} - \varrho_{bb}), \tag{B.7}$$

Here $\gamma_{ab} = \gamma_b/2 + i\omega_{ab}$ where $\omega_{ab} = \omega_a - \omega_b$. To eliminate the fast oscillating terms like $e^{i\theta_b^{\pm}}$, let us make a transformation for ϱ_{ab} as

$$\varrho_{ab} = \varrho_{ab}^{+} e^{i\theta_b^{+}} + \varrho_{ab}^{-} e^{i\theta_b^{-}} \tag{B.8}$$

Substituting Eq.(B.8) in Eq.(B.7) we obtain for the forward coherence ϱ_{ab}^{+}

$$\dot{\varrho}_{ab}^{+} + \dot{\varrho}_{ab}^{-} e^{-2ik_b z} = -\Gamma_{ab}\left[\varrho_{ab}^{+} + \varrho_{ab}^{-} e^{-2ik_b z}\right] - i\left[\Omega_b^{+} + \Omega_b^{-} e^{-2ik_b z}\right](\varrho_{aa} - \varrho_{bb}) \tag{B.9}$$

By symmetry, we can write for the backward direction ϱ_{ab}^{-} as

$$\dot{\varrho}_{ab}^{-} + \dot{\varrho}_{ab}^{+} e^{2ik_b z} = -\Gamma_{ab}\left[\varrho_{ab}^{-} + \varrho_{ab}^{+} e^{2ik_b z}\right] - i\left[\Omega_b^{-} + \Omega_b^{+} e^{2ik_b z}\right](\varrho_{aa} - \varrho_{bb}) \tag{B.10}$$

The equations of motion for the population in level a i.e ϱ_{aa} is given by

$$\dot{\varrho}_{aa} = -\gamma_b \varrho_{aa} + i\left(\vec{\wp}_{ab}^{*} \cdot \vec{E}_b \varrho_{ab} - \vec{\wp}_{ab} \cdot \vec{E}_b \varrho_{ab}^{*}\right) \tag{B.11}$$

Substituting Eq.(B.1) in Eq.(B.13) we obtain

$$\begin{aligned}\dot{\varrho}_{aa} = -\gamma_b \varrho_{aa} &+ i\left\{\left[\Omega_b^{+*} + \Omega_b^{-*}\exp(2ik_b z)\right]\varrho_{ab}^{+} - \left[\Omega_b^{+} + \Omega_b^{-}\exp(-2ik_b z)\right]\varrho_{ab}^{+*}\right\} \\ &+ i\left\{\left[\Omega_b^{-*} + \Omega_b^{+*}\exp(-2ik_b z)\right]\varrho_{ab}^{-} - \left[\Omega_b^{-} + \Omega_b^{+}\exp(2ik_b z)\right]\varrho_{ab}^{-*}\right\}\end{aligned} \tag{B.12}$$

The propagation of the probe field $E(z,t)$ is described by the Maxwell-Schrodinger equation

$$\left(\frac{\partial}{\partial z} + \frac{1}{c}\frac{\partial}{\partial t}\right)\left(-\frac{\partial}{\partial z} + \frac{1}{c}\frac{\partial}{\partial t}\right) E_b(z,t) = -\mu_0 \frac{\partial^2 P}{\partial t^2} \tag{B.13}$$

Substituting Eq.(B.1) in Eq.(B.13) we obtain the propagation equation for the probe field $\Omega_b^{\pm}$ as

$$\frac{\partial \Omega_b^{+}}{\partial z} + \frac{1}{c}\frac{\partial \Omega_b^{+}}{\partial t} = i\eta_{ab}\varrho_{ab}^{+} \tag{B.14}$$

$$-\frac{\partial \Omega_b^{-}}{\partial z} + \frac{1}{c}\frac{\partial \Omega_b^{-}}{\partial t} = i\eta_{ab}\varrho_{ab}^{-} \tag{B.15}$$

where $\eta_{ab} = (3/8\pi)N\lambda_{ab}^2\gamma_b(\nu_b/\omega_{ab})$. We have used the definition of Rabi frequency as $\Omega_b = \wp_{ab}\mathcal{E}_b/2\hbar$. Let us discuss a scenario in which we start ($t = 0$) with complete population inversion and study the evolution of the seed pulse in forward (+z) and backward (-z) direction. The temporal shape of the seed pulse entering at $z = 0$ and $z = L$, where L is the length of the gain medium, is identical. From Eq.(B.9), we obtain

$$\dot{\varrho}_{ab}^{+} = -\Gamma_{ab}\varrho_{ab}^{+} - i\Omega_b^{+}(\varrho_{aa} - \varrho_{bb}) \tag{B.16}$$

Similarly, by symmetry, we can write for the backward direction ϱ_{ab}^{-} as

$$\dot{\varrho}_{ab}^{-} = -\Gamma_{ab}\varrho_{ab}^{-} - i\Omega_b^{-}(\varrho_{aa} - \varrho_{bb}) \tag{B.17}$$

and the evolution of the population ϱ_{aa} takes the form

$$\dot{\varrho}_{aa} = -\gamma_b\varrho_{aa} + i\left(\Omega_b^{+*}\varrho_{ab}^{+} - \Omega_b^{+}\varrho_{ab}^{+*}\right) + i\left(\Omega_b^{-*}\varrho_{ab}^{-} - \Omega_b^{-}\varrho_{ab}^{-*}\right) \tag{B.18}$$

From Eqs.(B.14-B.18), we see that the evolution of the seed pulse in the forward and backward direction are identical.

APPENDIX C

GENERATION OF RADIATION BY A TWO-LEVEL ATOMIC MEDIUM WITH EXCITED COHERENCE

Let us assume that a two-level atom has some small initial coherence $\rho_{ab}^0 = \sqrt{\rho_{aa}^0 \rho_{bb}^0}$. Note that in chapter III, we consider the case when there is no population inversion, $\rho_{aa}^0 < \rho_{bb}^0$. The density matrix equations for atomic coherence are

$$\frac{\partial \rho_{ab}}{\partial t} = i\Omega(\rho_{aa} - \rho_{bb}), \text{ and} \tag{C.1}$$

$$\frac{\partial}{\partial t}(\rho_{aa} - \rho_{bb}) = -2i\Omega\rho_{ab}. \tag{C.2}$$

the solution (by neglecting relaxation processes) is

$$\rho_{ab} = i\rho_{ab}^0 \sin\theta. \tag{C.3}$$

Then, for the retarded frame

$$\tau = t - \frac{z}{c}, \tag{C.4}$$

the propagation equation for a resonant field is given by

$$\frac{\partial \Omega}{\partial z} = -i\eta\rho_{ab}, \tag{C.5}$$

where $\eta = 3\lambda^2 N\gamma/(8\pi)$ is the coupling constant. Introducing

$$\theta = 2\int^t \Omega \, dt, \tag{C.6}$$

Eq.(C.5) can be rewritten as

$$\frac{\partial^2 \theta}{\partial z \partial \tau} = -\eta \sin(\theta - \phi), \tag{C.7}$$

where ϕ can be determined from initial condition as

$$\phi \simeq 2\sqrt{\rho_{aa}^{0}}. \tag{C.8}$$

Solution of Eq.(C.7) is given by

$$\theta = \phi[1 - J_0(2\sqrt{\eta z \tau})], \tag{C.9}$$

and the Rabi frequency is

$$\Omega = \phi J_1(2\sqrt{\eta z \tau})\sqrt{\frac{\eta z}{\tau}}. \tag{C.10}$$

The energy of the generated short wavelength pulse can be calculated as

$$\frac{c}{4\pi} A \int_{-\infty}^{\infty} |E|^2 dt = Az\ N\ \rho_{aa}\ \ \hbar\omega_{ab}, \tag{C.11}$$

and it is equal to the energy stored in the medium after excitation. Also it is important to note that the absence of population inversion does not influence much of pulse energy because of coherent interaction of the radiation field with the atomic medium. The time duration of the generated pulse is of the order of

$$\tau_{pulse} = \frac{4\pi}{3N\lambda^2 z\gamma_r}, \tag{C.12}$$

and it gives the power of the pulse be

$$P_{pulse} = \frac{\lambda^2 zN}{4\pi} AzN\gamma_r \rho_{aa} \hbar\omega_{ab}, \tag{C.13}$$

where the factor $\frac{\lambda^2 zN}{4\pi}$ shows the brightness of the source in comparison with spontaneous emission of incoherent source.

APPENDIX D

DENSITY MATRIX VS RATE EQUATIONS FOR TLA

We consider a two level system with a and b as the upper and the lower levels. The density matrix equations are given as

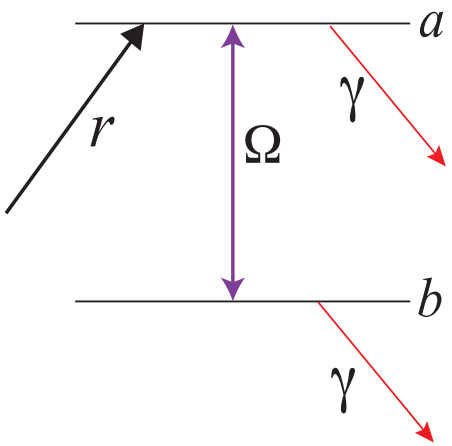

Fig. 67. Two-level model. The decay rate from the levels a and b is given by γ.

$$\dot{\varrho}_{aa} = r - \gamma\varrho_{aa} - i\left(\Omega^*\varrho_{ab} - \Omega\varrho^*_{ab}\right) \tag{D.1}$$

$$\dot{\varrho}_{bb} = -\gamma\varrho_{bb} + i\left(\Omega^*\varrho_{ab} - \Omega\varrho^*_{ab}\right) \tag{D.2}$$

$$\dot{\varrho}_{ab} = -\Gamma_{ab}\varrho_{ab} - i\Omega\left(\varrho_{aa} - \varrho_{bb}\right) \tag{D.3}$$

The propagation equation for the field (Ω) in the slowly varying amplitude approximation as

$$\frac{\partial\Omega}{\partial z} + \frac{1}{c}\frac{\partial\Omega}{\partial t} = i\eta\varrho_{ab} \tag{D.4}$$

where the coupling constant η is

$$\eta = \nu N\wp^2/2\epsilon_0 c\hbar \tag{D.5}$$

Substituting $\dot{\varrho}_{ab} = 0$ in Eq.(D.3) we obtain,

$$\varrho_{ab} = -i\frac{\Omega}{\Gamma_{ab}}\left(\varrho_{aa} - \varrho_{bb}\right) \tag{D.6}$$

Substituting Eq.(D.6) in Eq.(D.1) and Eq.(D.2) we obtain,

$$\dot{\varrho}_{aa} = r - \gamma\varrho_{aa} - \frac{2\Omega^2}{\Gamma_{ab}}\left(\varrho_{aa} - \varrho_{bb}\right) \tag{D.7}$$

$$\dot{\varrho}_{bb} = -\gamma\varrho_{aa} + \frac{2\Omega^2}{\Gamma_{ab}}\left(\varrho_{aa} - \varrho_{bb}\right) \tag{D.8}$$

We obtain,

$$\dot{\varrho}_{aa} - \dot{\varrho}_{bb} = r - \gamma\left(\varrho_{aa} - \varrho_{bb}\right) - \frac{4\Omega^2}{\Gamma_{ab}}\left(\varrho_{aa} - \varrho_{bb}\right) \tag{D.9}$$

Assuming the spatial uniformity of the field and using Eq.(D.6), the propagation equation for the field gives,

$$\frac{d\Omega}{dt} = \frac{c\eta}{\Gamma_{ab}}\left(\varrho_{aa} - \varrho_{bb}\right)\Omega \tag{D.10}$$

Using simple algebra we obtain (for real field)

$$\frac{d\Omega^2}{dt} = \frac{2c\eta}{\Gamma_{ab}}\left(\varrho_{aa} - \varrho_{bb}\right)\Omega^2 \tag{D.11}$$

From the definition of Rabi frequency Ω and field amplitude $\mathcal{E}$ we can write,

$$\Omega = \wp\mathcal{E}/2\hbar, \quad \mathcal{E}^2 = n\hbar\nu/\epsilon_0 V \tag{D.12}$$

Here n is the number of photons. From Eq.(D.11) and Eq.(D.12) we obtain,

$$\frac{dn}{dt} = \frac{\wp^2\nu N}{\epsilon_0\hbar\Gamma_{ab}V}\left(\varrho_{aa} - \varrho_{bb}\right)n \tag{D.13}$$

From Eq.(D.9) and Eq.(D.12) we obtain,

$$\dot{\varrho}_{aa} - \dot{\varrho}_{bb} = r - \gamma\left(\varrho_{aa} - \varrho_{bb}\right) - \frac{\nu\wp^2}{\epsilon_0\hbar\Gamma_{ab}}n\left(\varrho_{aa} - \varrho_{bb}\right) \tag{D.14}$$

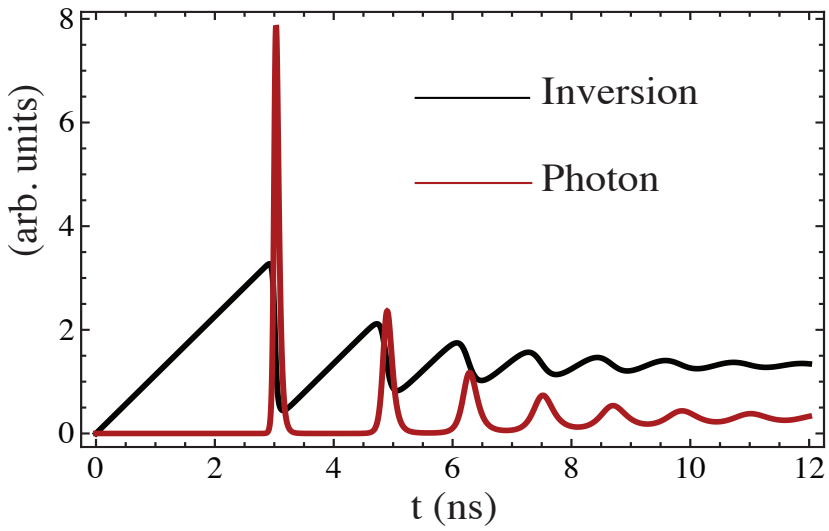

Fig. 68. Numerical simulation using the Rate equations. Using the parameters $\gamma_c = 30$ ns^{-1}.

Let us define some parameters to get our result in consistent with[82]

$$N_{ab} = NV\left(\varrho_{aa} - \varrho_{bb}\right), \quad R_p = NVr, \quad K = \frac{\nu\wp^2}{\epsilon_0\hbar\Gamma_{ab}V} \tag{D.15}$$

Using new parameters, our equations takes the form

$$\frac{dn}{dt} = KN_{ab}n, \quad \dot{N}_{ab} = R_p - \gamma N_{ab} - KnN_{ab} \tag{D.16}$$

To work on the numerical simulations we can use the rate equations derived from the density matrix equations for different choices of T_2. We have also added the cavity decay term in the equation of motion for n phenomenologically we gives us,

$$\frac{dn}{dt} = \frac{\wp^2\nu N}{\epsilon_0\hbar\Gamma_{ab}V}\left(\varrho_{aa} - \varrho_{bb}\right)n - \gamma_c n \tag{D.17}$$

APPENDIX E

DERIVATION OF EMISSION AND ABSORPTION PROBABILITIES USING SCULLY'S DRESSED STATE ANALYSIS

We start with evolution of amplitudes in Eqs. (4.1)-(4.3) for $\gamma_1 = \gamma_2 = \gamma$

$$\dot{v}_2 = -(\gamma + i\Delta)v_2 - p\gamma v_1 - i\Omega_2 c, \tag{E.1}$$

$$\dot{v}_1 = -(\gamma - i\Delta)v_1 - p\gamma v_2 - i\Omega_1 c, \tag{E.2}$$

$$\dot{c} = -i\Omega_2 v_2 - i\Omega_1 v_1 - \Gamma c, \tag{E.3}$$

Writing Eqs. (E.1)-(E.3) in matrix form, we obtain

$$\frac{d}{d\tau}\begin{pmatrix} v_2 \\ v_1 \\ c \end{pmatrix} = -\Gamma_0 \begin{pmatrix} v_2 \\ v_1 \\ c \end{pmatrix} - iV \begin{pmatrix} v_2 \\ v_1 \\ c \end{pmatrix}, \tag{E.4}$$

where $\tau = \gamma t$, and the Fano decay matrix is defined by

$$\Gamma_0 = \begin{pmatrix} 1 + i\tilde{\Delta} & p & 0 \\ p & 1 - i\tilde{\Delta} & 0 \\ 0 & 0 & \Gamma \end{pmatrix}, \tag{E.5}$$

and probe-field interaction is given by

$$V = \begin{pmatrix} 0 & 0 & \tilde{\Omega}_2 \\ 0 & 0 & \tilde{\Omega}_1 \\ \tilde{\Omega}_2 & \tilde{\Omega}_1 & 0 \end{pmatrix}, \tag{E.6}$$

with $\tilde{\Delta} = \Delta/\gamma$ and $\tilde{\Omega}_{1,2} = \Omega_{1,2}/\gamma$. It is intuitive to introduce a basis in which the Fano coupling is transformed away. We proceed from the bare basis via the U, U^{-1} matrices of

diagonalization.

$$U^{-1} = \frac{1}{\sqrt{2}p} \begin{pmatrix} p & p & 0 \\ x - i\tilde{\Delta} & -x - i\tilde{\Delta} & 0 \\ 0 & 0 & \sqrt{2}p \end{pmatrix}, \tag{E.7}$$

$$U = \frac{1}{\sqrt{2}x} \begin{pmatrix} x + i\tilde{\Delta} & p & 0 \\ x - i\tilde{\Delta} & -p & 0 \\ 0 & 0 & \sqrt{2}x \end{pmatrix}. \tag{E.8}$$

Here $x = \sqrt{p^2 - \tilde{\Delta}^2}$. so that the transformed state vector is defined by

$$U \begin{pmatrix} v_2 \\ v_1 \\ c \end{pmatrix} = \begin{pmatrix} V_+ \\ V_- \\ C \end{pmatrix}, \tag{E.9}$$

which implies

$$V_\pm = \frac{(x \pm i\tilde{\Delta})v_2 \pm pv_1}{\sqrt{2}x} \tag{E.10}$$

and thus,

$$\begin{pmatrix} \dot{V}_+ \\ \dot{V}_- \\ \dot{C} \end{pmatrix} = -\Gamma_t \begin{pmatrix} V_+ \\ V_- \\ C \end{pmatrix} - iV_t \begin{pmatrix} V_+ \\ V_- \\ C \end{pmatrix}, \tag{E.11}$$

in which the diagonal Γ_t operator is

$$\Gamma_t = U\Gamma_0 U^{-1} = \begin{pmatrix} 1 + x & 0 & 0 \\ 0 & 1 - x & 0 \\ 0 & 0 & \Gamma \end{pmatrix}, \tag{E.12}$$

and the transformed interaction potential is $V_t = UVU^{-1}$ which yields

$$V_t = \frac{1}{\sqrt{2}p}\begin{pmatrix} 0 & 0 & p[\tilde{\Omega}_2(x+i\tilde{\Delta})+p\tilde{\Omega}_1]/x \\ 0 & 0 & p[\tilde{\Omega}_2(x-i\tilde{\Delta})-p\tilde{\Omega}_1]/x \\ \tilde{\Omega}_2+\tilde{\Omega}_1(x-i\tilde{\Delta}) & \tilde{\Omega}_2-\tilde{\Omega}_1(x+i\tilde{\Delta}) & 0 \end{pmatrix}. \tag{E.13}$$

The equation of motion in terms of $V_\pm$ and C are then found to be

$$\frac{dV_+}{d\tau} = -(1+x)V_+ - \frac{i}{\sqrt{2}x}[\tilde{\Omega}_2(x+i\tilde{\Delta})+p\tilde{\Omega}_1]C, \tag{E.14}$$

$$\frac{dV_-}{d\tau} = -(1-x)V_- - \frac{i}{\sqrt{2}x}[\tilde{\Omega}_2(x-i\tilde{\Delta})-p\tilde{\Omega}_1]C, \tag{E.15}$$

$$\frac{dC}{d\tau} = -\tilde{\Gamma}C - \frac{i}{\sqrt{2}}[p\tilde{\Omega}_2+\tilde{\Omega}_1(x-i\tilde{\Delta})]V_+ - \frac{i}{\sqrt{2}}[p\tilde{\Omega}_2-\tilde{\Omega}_1(x+i\tilde{\Delta})]V_-, \tag{E.16}$$

We start with amplitude equations in dressed basis (E.14) - (E.16). The initial conditions corresponding to the emission from the state C are $V_\pm(0) = 0$, $C(0) = 1$. Assuming the driving fields to be weak ($\tilde{\Omega}_{1,2} << 1$ we can solve Eqs. (E.14) - (E.16) by expansion in perturbation series over $\tilde{\Omega}_{1,2}$. The lowest order solution for $B(\tau)$ of Eq. (E.16) yields $C^{(0)}(\tau) = e^{-\tilde{\Gamma}\tau}$. The latter can be substituted in Eqs. (E.14) and (E.15) to find $V_\pm^{(0)}(\tau)$:

$$V_\pm^{(0)}(\tau) = -i\frac{\tilde{\Omega}_2(x\pm i\tilde{\Delta})\pm p\tilde{\Omega}_1}{\sqrt{2}x(1\pm x-\tilde{\Gamma})}\left(e^{-\tilde{\Gamma}\tau}-e^{-(1\pm x)\tau}\right) \tag{E.17}$$

The exponential approximation or $C(\tau)$ gives relatively good agreement with numerical simulations only for small time. For large time the behavior of the system is far from being exponential. Therefore, we should consider next order correction for $C(\tau)$. It can be done by substituting functions $V_\pm^{(0)}$ from Eq. (E.17) to Eq. (E.16) which yields

$$C^{(1)}(\tau) = \left[\frac{A_+}{1+x-\tilde{\Gamma}}+\frac{A_-}{1-x-\tilde{\Gamma}}-(A_++A_-)\tau\right]e^{-\tilde{\Gamma}\tau}$$
$$+e^{-\tilde{\Gamma}\tau}-\frac{A_+}{1+x-\tilde{\Gamma}}e^{-(1+x)\tau}-\frac{A_-}{1-x-\tilde{\Gamma}}e^{-(1-x)\tau}, \tag{E.18}$$

where

$$A_{\pm} = \frac{[p\tilde{\Omega}_2 \pm (x \mp i\tilde{\Delta})\tilde{\Omega}_1][\tilde{\Omega}_2(x \pm i\tilde{\Delta}) \pm p\tilde{\Omega}_1]}{2px(1 \pm x - \tilde{\Gamma})}. \tag{E.19}$$

Using the definition for emission probability from Eq. (4.5) at large time $\tau \gg 1, 1/\tilde{\Gamma}$, neglecting higher order terms in $\tilde{\Omega}_{1,2}$ the probability of absorption yields

$$P_{\text{emiss}}(\infty|b) = \frac{(\tilde{\Gamma}+1)(|\tilde{\Omega}_1|^2 + |\tilde{\Omega}_2|^2) - 2p\tilde{\Omega}_1\tilde{\Omega}_2}{\tilde{\Gamma}\left[\tilde{\Delta}^2 + (\tilde{\Gamma}+1)^2 - p^2\right]}. \tag{E.20}$$

Similarly one can derive the probability of absorption. We start from absorption from level v_1. The initial conditions for system with population on v_1 in dressed states are $V_{\pm}(0) = \pm p/\sqrt{2}x$, $C(0) = 0$ (see Eq. (E.10)). In lowest order of $\tilde{\Omega}_{1,2}$, Eqs. (E.14) and (E.15) yield

$$V_{\pm}^{(0)}(\tau|v_1) = \pm\frac{p}{\sqrt{2}x}e^{-(1\pm x)\tau}. \tag{E.21}$$

Corresponding zero order solution of $C^{(0)}(\tau)$ of Eq. (E.16) is given by

$$C^{(0)}(\tau|v_1) = B_+e^{-(1+x)\tau} - B_-e^{-(1-x)\tau} + (B_- - B_+)e^{-\tilde{\Gamma}\tau}, \tag{E.22}$$

where

$$B_{\pm} = i\frac{p\tilde{\Omega}_2 \pm \tilde{\Omega}_1(x \mp i\tilde{\Delta})}{2x(1 \pm x - \tilde{\Gamma})} \tag{E.23}$$

Therefore, probability of absorption form level v_1 for large time $\tau \gg 1, 1/\tilde{\Gamma}$ given by Eq. (4.7) reads

$$P_{\text{abs}}(\infty|v_1) = \frac{(\tilde{\Gamma}+2)|\tilde{\Omega}_1 - p\tilde{\Omega}_2|^2 + [\tilde{\Gamma}(1-p^2) + 2\tilde{\Delta}^2(\tilde{\Gamma}+1)]|\tilde{\Omega_1}|^2}{2(1+\tilde{\Delta}^2-p^2)[\tilde{\Delta}^2 + (\tilde{\Gamma}+1)^2 - p^2]} \tag{E.24}$$

The probability of absorption from level v_2 can be derived in the same way as for the level v_1. In this case, the initial conditions according to Eq. (E.10) read $V_{\pm}(0) = (x \pm i\tilde{\Delta})/\sqrt{2}x$, $C(0) = 0$. In lowest order of $\tilde{\Omega}_{1,2}$, Eqs. (E.14) and (E.15) have the following solution:

$$V_{\pm}^{(0)}(\tau|a_2) = \frac{x \pm i\tilde{\Delta}}{\sqrt{2}x}e^{-(1\pm x)\tau}. \tag{E.25}$$

Corresponding zero order solution of $C^{(0)}(\tau)$ of Eq. (E.16) yields

$$C^{(0)}(\tau|v_1) = D_+ e^{-(1+x)\tau} + D_- e^{-(1-x)\tau} + (D_+ + D_-)e^{-\tilde{\Gamma}\tau}, \tag{E.26}$$

where

$$D_\pm = i\frac{[p\tilde{\Omega}_2 \pm \tilde{\Omega}_1(x \mp i\tilde{\Delta})](x \pm i\tilde{\Delta})}{2px(1 \pm x - \tilde{\Gamma})} \tag{E.27}$$

Therefore, probability of absorption from level v_2 for $\tau \gg 1, 1/\tilde{\Gamma}$ given by Eq. (4.7) yields

$$P_{\text{abs}}(\infty|v_2) = \frac{(\tilde{\Gamma}+2)|\tilde{\Omega}_2 - p\tilde{\Omega}_1|^2 + [\tilde{\Gamma}(1-p^2) + 2\tilde{\Delta}^2(\tilde{\Gamma}+1)]|\tilde{\Omega_2}|^2}{2(1+\tilde{\Delta}^2-p^2)[\tilde{\Delta}^2 + (\tilde{\Gamma}+1)^2 - p^2]}, \tag{E.28}$$

which becomes Eq. (E.24) if $\tilde{\Omega}_1 \leftrightarrow \tilde{\Omega}_2$.

APPENDIX F

ANALYSIS OF GAIN IN THREE-LEVEL CONFIGURATION: UNI AND BI-DIRECTION PUMPING

Our model consists of a three-level atomic system in cascade configuration with energy levels labelled as a, b and c as shown in Fig. 30(b). The atomic system is driven by a strong laser field of Rabi frequency Ω which couples the level $a \leftrightarrow c$ in resonance. It also interacts with a weak probe field of Rabi frequency Ω_l coupling the level $b \leftrightarrow a$. The Hamiltonian in the interaction picture can be written as

$$\mathscr{H} = -\Omega_l \left|a\right\rangle\left\langle b\right| - \Omega \left|c\right\rangle\left\langle a\right| - \Omega_l^* \left|b\right\rangle\left\langle a\right| - \Omega^* \left|a\right\rangle\left\langle c\right|, \tag{F.1}$$

The decay in the channel ab is quantified by the rate γ respectively. Incorporating these decay rates, the equation of motion for the atomic density matrix, in rotating wave approximation is given as

$$\dot{\rho} = -i[\mathscr{H}, \rho] + \frac{\gamma}{2}\left([\sigma_b, \rho\sigma_b^\dagger] + [\sigma_b\rho, \sigma_b^\dagger]\right) \tag{F.2}$$

where,

$$\sigma_b = \left|b\right\rangle\left\langle a\right|, \sigma_b^\dagger = \left|a\right\rangle\left\langle b\right|, \tag{F.3}$$

The density matrix equations for the populations and the polarization of the atomic system can be written as

$$\dot{\rho}_{ab} = -\frac{\gamma}{2}\rho_{ab} + i\Omega_l(\rho_{bb} - \rho_{aa}) + i\Omega^*\rho_{cb} \tag{F.4}$$

$$\dot{\rho}_{cb} = -i\Omega_l\rho_{ca} + i\Omega\rho_{ab} \tag{F.5}$$

$$\dot{\rho}_{ca} = -\frac{\gamma}{2}\rho_{ca} - i\Omega(\rho_{cc} - \rho_{aa}) - i\Omega_l^*\rho_{cb} \tag{F.6}$$

$$\dot{\rho_{bb}} = \gamma\rho_{aa} + i(\Omega_l^*\rho_{ab} - \Omega_l\rho_{ba}) \tag{F.7}$$

$$\dot{\rho_{aa}} = -\gamma\rho_{aa} - i(\Omega_l^*\rho_{ab} - \Omega_l\rho_{ba}) + i(\Omega^*\rho_{ca} - \Omega\rho_{ac}) \tag{F.8}$$

$$\dot{\rho_{cc}} = -i(\Omega^* \rho_{ca} - \Omega \rho_{ac}) \tag{F.9}$$

The exact analytical solutions of the coupled differential equation given be Eqs. (F.4-F) is very difficult to obtain. So let us take some approximations and see if we can find analytic solutions which agree with the numerical simulation to good extent. Let us take a simple model as show in in which we neglect the effect of the weak probe field Ω_l. The equation of motion for the population and the polarization is given as

$$\dot{\rho}_{ca} = -\frac{\gamma}{2}\rho_{ca} + i\Omega(\rho_{aa} - \rho_{cc}) \tag{F.10}$$

$$\dot{\rho_{aa}} = -\gamma \rho_{aa} + i(\Omega^* \rho_{ca} - \Omega \rho_{ac}) \tag{F.11}$$

$$\dot{\rho_{cc}} = -i(\Omega^* \rho_{ca} - \Omega \rho_{ac}) \tag{F.12}$$

The exact solution of Eqs. (F.10-F.12) is given as

$$\begin{aligned} \rho_{cc} = e^{-\gamma t/2} \Big\{ & 16\alpha^2(\rho_{cc}(0) + \rho_{aa}(0))\text{sinh}^2(\tilde{\Omega}t/4) \\ & + \rho_{cc}(0)[\text{cosh}(\tilde{\Omega}t/2) + (\gamma/\tilde{\Omega})\text{sinh}(\tilde{\Omega}t/2)] \Big\} \end{aligned} \tag{F.13}$$

$$\begin{aligned} \rho_{aa} = e^{-\gamma t/2} \Big\{ & 16\alpha^2(\rho_{cc}(0) + \rho_{aa}(0))\text{sinh}^2(\tilde{\Omega}t/4) \\ & + \rho_{aa}(0)[\text{cosh}(\tilde{\Omega}t/2) - (\gamma/\tilde{\Omega})\text{sinh}(\tilde{\Omega}t/2)] \Big\} \end{aligned} \tag{F.14}$$

$$\begin{aligned} \rho_{ca} = -4i\alpha e^{-\gamma t/2} \text{sinh}(\tilde{\Omega}t/4) \Big\{ & (\rho_{cc}(0) - \rho_{aa}(0))\text{cosh}(\tilde{\Omega}t/4) \\ & + (\gamma/\tilde{\Omega})(\rho_{cc}(0) + \rho_{aa}(0))\text{cosh}(\tilde{\Omega}t/4) \Big\} \end{aligned} \tag{F.15}$$

where, $\tilde{\Omega}^2 = \gamma^2 - 16\Omega^2$ and $\alpha = \Omega/\tilde{\Omega}$. Taking help from solutions from simple two-level model Eqs. (F.10-F.12) and using the normalization condition of the population

$$\rho_{bb} + \rho_{aa} + \rho_{cc} = 1 \tag{F.16}$$

ρ_{bb} is given as

$$\rho_{bb} = 1 - e^{-\gamma t/2}\left\{(\rho_{cc}(0)+\rho_{aa}(0))\left[\cosh(\tilde{\Omega}t/2) + 32\alpha^2\sinh^2(\tilde{\Omega}t/4)\right] + (\rho_{cc}(0)-\rho_{aa}(0))\left[(\gamma/\tilde{\Omega})\sinh(\tilde{\Omega}t/2)\right]\right\} \tag{F.17}$$

Eliminating ρ_{cb} from Eqs. (F.4,F.5) gives the differential equation governing the time evolution of ρ_{ab} as

$$\ddot{\rho}_{ab} + \frac{\gamma}{2}\dot{\rho}_{ab} + \Omega^2\rho_{ab} - \Omega\Omega_l\rho_{ca} + i\Omega_l(\dot{\rho}_{aa} - \dot{\rho}_{bb}) = 0 \tag{F.18}$$

Using the population normalization condition Eqs. (F.16), Eq(F.18) can be written in more informative form as

$$\ddot{\rho}_{ab} + \frac{\gamma}{2}\dot{\rho}_{ab} + \Omega^2\rho_{ab} - \Omega\Omega_l\rho_{ca} + i\Omega_l(2\dot{\rho}_{aa} + \dot{\rho}_{cc}) = 0 \tag{F.19}$$

Using Eqs. (F.13-F.15) in Eq. (F.19) gives

$$\ddot{\rho}_{ab} + \frac{\gamma}{2}\dot{\rho}_{ab} + \Omega^2\rho_{ab} = f(t) \tag{F.20}$$

where,

$$f(t) = 2i\Omega_l e^{-\gamma t/2}\{\gamma\rho_{aa}(0)\cosh(\tilde{\Omega}t/2) + 10\gamma(\rho_{cc}(0)+\rho_{aa}(0))\alpha^2\sinh^2(\tilde{\Omega}t/4) - \tilde{\Omega}[\rho_{aa}(0) + (3\rho_{cc}(0)+13\rho_{aa}(0))\alpha^2]\sinh(\tilde{\Omega}t/2)\} \tag{F.21}$$

In the limit $\tilde{\Omega} \to 4i\Omega$, Eqs.(F.13-F.15,F.18) takes a simple form

$$\rho_{cc}(t) = e^{-\gamma t/2}\left\{\left[\frac{\rho_{cc}(0)+\rho_{aa}(0)}{2}\right] + \left[\frac{\gamma\rho_{cc}(0)}{4\Omega}\right]\sin(2\Omega t) + \left[\frac{\rho_{cc}(0)-\rho_{aa}(0)}{2}\right]\cos(2\Omega t)\right\} \tag{F.22}$$

$$\rho_{aa}(t) = e^{-\gamma t/2}\left\{\left[\frac{\rho_{cc}(0)+\rho_{aa}(0)}{2}\right] - \left[\frac{\gamma\rho_{aa}(0)}{4\Omega}\right]\sin(2\Omega t) - \left[\frac{\rho_{cc}(0)-\rho_{aa}(0)}{2}\right]\cos(2\Omega t)\right\} \tag{F.23}$$

$$\rho_{ca}(t) = -ie^{-\gamma t/2}\text{sin}(\Omega t)\,\{[\rho_{cc}(0) - \rho_{aa}(0)]\text{cos}(\Omega t) + [\rho_{cc}(0) + \rho_{aa}(0)](\gamma/4\Omega)\text{sin}(\Omega t)\} \tag{F.24}$$

$$\rho_{bb}(t) = 1 - e^{-\gamma t/2}\,\{[\rho_{cc}(0) + \rho_{aa}(0)] + [\rho_{cc}(0) - \rho_{aa}(0)](\gamma/4\Omega)\text{sin}(2\Omega t)\} \tag{F.25}$$

Using $\tilde{\Omega} \to 4i\Omega$ and neglecting the terms $\propto (\gamma/\Omega)^2$ thus Eq.(F.21) gets simplified as

$$f(t) = i(\Omega_l/8)e^{-\gamma t/2}\,\{5\gamma[\rho_{cc}(0) + \rho_{aa}(0)] + \gamma[11\rho_{aa}(0) - 5\rho_{cc}(0)]\text{cos}(2\Omega t) + 12\Omega[\rho_{aa}(0) - \rho_{cc}(0)]\text{sin}(2\Omega t)\} \tag{F.26}$$

Solving for ρ_{ab} gives

$$\begin{aligned}\rho_{ab} =& i(\Omega_l/24\Omega^2)e^{-\gamma t/2}\,\{15\gamma[\rho_{cc}(0) + \rho_{aa}(0)] + \gamma[\rho_{cc}(0) - 7\rho_{aa}(0)]\text{cos}(2\Omega t) \\ &+12\Omega[\rho_{cc}(0) - \rho_{aa}(0)]\text{sin}(2\Omega t) - 8e^{\gamma t/4}[\gamma(2\rho_{cc}(0) + \rho_{aa}(0))\text{cos}(\Omega t) \\ &+3\Omega(2\rho_{cc}(0) + \rho_{aa}(0) - 1)]\text{sin}(\Omega t)\}\end{aligned} \tag{F.27}$$

Thus using a simple two-level atom toy model we are able to find approximate analytical solutions for a three level atom in Ξ configuration for constant Ω, Ω_l when $\Gamma/\gamma \ll 1$ and $\Omega \gg \gamma, \Omega_l$.

APPENDIX G

CALCULATION OF PROBABILITY AMPLITUDE FOR SINGLE AND MULTI-PHOTON EXCITATION

In this appendix we have calculated the probability amplitude for single and multi-photon excitation using perturbation theory. We show the strength of the off-resonant excitation is not negligible when the Rabi frequency is large. The wave function of a two-level atom can be written in the form

$$|\psi(t)\rangle = C_a(t)e^{-i\omega_a t}|a\rangle + C_b(t)e^{-i\omega_b t})|b\rangle, \tag{G.1}$$

where C_a and C_b are the probability amplitudes of finding the atom in the states a and b, respectively. The equation of motions for C_a and C_b are given by,

$$\dot{C}_a(t) = i\Omega(t)e^{i\omega t}C_b(t) \tag{G.2}$$

$$\dot{C}_b(t) = i\Omega^*(t)e^{-i\omega t}C_a(t). \tag{G.3}$$

Integrating Eq.(G.2) we obtain

$$C_a(t) = i\int_{-\infty}^{t} \Omega(t')e^{i\omega t'}C_b(t')dt' \tag{G.4}$$

In the limit $t \to \infty$ Eq.(G.4) gives,

$$C_a(\infty) = i\int_{-\infty}^{\infty} \Omega(t')e^{i\omega t'}C_b(t')dt' \tag{G.5}$$

Substituting Eq.(G.4) in Eq.(G.3) and using the initial condition $C_b(0) = 1$ we get,

$$C_b(t') = 1 - \int_{-\infty}^{t'} \left[\Omega^*(t'')e^{-i\omega t''}\left(\int_{-\infty}^{t''} \Omega(t''')e^{i\omega t'''}C_a(t''')dt'''\right)dt''\right] \tag{G.6}$$

Plugging back Eq.(G.6) in Eq.(G.4), we get

$$C_a(t) = i\int_{-\infty}^{t}\Omega(t')e^{i\omega t'}\left\{1-\int_{-\infty}^{t'}\left[\Omega^*(t'')e^{-i\omega t''}\left(\int_{-\infty}^{t''}\Omega(t''')e^{i\omega t'''}C_a(t''')dt'''\right)dt''\right]\right\}dt' \tag{G.7}$$

Thus from Eq.(G.7) we get,

$$C_a(\infty) = i\int_{-\infty}^{\infty}\Omega(t')e^{i\omega t'}\left\{1-\int_{-\infty}^{t'}\left[\Omega^*(t'')e^{-i\omega t''}\left(\int_{-\infty}^{t''}\Omega(t''')e^{i\omega t'''}C_a(t''')dt'''\right)dt''\right]\right\}dt' \tag{G.8}$$

In the perturbation theory $C_b(t) \cong 1$, we are looking for a solution of the form $C_a(\infty) = C_a^{(1)}(\infty) + C_a^{(3)}(\infty)$, where the first term $C_a^{(1)}(\infty)$ is given by

$$C_a^{(1)}(\infty) = i\int_{-\infty}^{\infty}\Omega(t')e^{i\omega t'}dt' \tag{G.9}$$

The second term can be found as

$$C_a^{(3)}(\infty) = -i\int_{-\infty}^{\infty}\left\{\Omega(t')e^{i\omega t'}\int_{-\infty}^{t'}\left[\Omega^*(t'')e^{-i\omega t''}\int_{-\infty}^{t''}\Omega(t''')e^{i\omega t'''}dt'''\right]dt''\right\}dt' \tag{G.10}$$

Let us consider that the Rabi frequency $\Omega(t)$ is given as

$$\Omega(t) = e^{-\alpha^2t^2}\{\Omega_1\text{cos}(\nu_1t+\phi_1) + \Omega_2\text{cos}(\nu_2t+\phi_2)\}, \tag{G.11}$$

(i) Absorption of one-photon of frequency ν_1. The transition probability amplitude is given as

$$C_{a,(\nu_1)}^{(1)}(\infty) = i\left(\frac{\sqrt{\pi}}{2\alpha}\right)\Omega_1e^{-[(\omega-\nu_1)/2\alpha]^2}e^{-i\phi_1} \tag{G.12}$$

Similarly we can find $C_{a,(\nu_2)}^{(1)}(\infty)$ using the substitution $\Omega_1 \to \Omega_2, \nu_1 \to \nu_2$ and $\phi_1 \to \phi_2$.

(ii) Absorption of three-photon of frequency ν_2. The transition probability amplitude

is given as

$$C^{(3)}_{a,(\nu_2,\nu_2,\nu_2)}(\infty) = -i\left[\frac{\sqrt{\pi}}{16\sqrt{3}\alpha\nu_2(\omega-\nu_2)}\right]\Omega_2^3 e^{-(1/3)[(\omega-3\nu_2)/2\alpha]^2}e^{-3i\phi_2} \tag{G.13}$$

(iii) Absorption of two-photon of frequency ν_1 and emission of one-photon of frequency ν_2 in the order:

(iii.a) $\nu_1 \rightarrow \nu_1 \rightarrow \nu_2$. The transition probability amplitude is given as

$$C^{(3)}_{a,(\nu_1,\nu_1,\nu_2)}(\infty) = -i\left[\frac{\sqrt{\pi}}{16\sqrt{3}\alpha\nu_1(\omega-\nu_1)}\right]\Omega_1^2\Omega_2 e^{-(1/3)[(2\nu_1-\nu_2-\omega)/2\alpha]^2}e^{-i[2\phi_1-\phi_2]} \tag{G.14}$$

(iii.b) $\nu_1 \rightarrow \nu_2 \rightarrow \nu_1$. The transition probability amplitude is given as

$$C^{(3)}_{a,(\nu_1,\nu_2,\nu_1)}(\infty) = -i\left[\frac{\sqrt{\pi}}{8\sqrt{3}\alpha(\nu_1-\nu_2)(\omega-\nu_1)}\right]\Omega_1^2\Omega_2 e^{-(1/3)[(2\nu_1-\nu_2-\omega)/2\alpha]^2}e^{-i[2\phi_1-\phi_2]} \tag{G.15}$$

(iii.c) $\nu_2 \rightarrow \nu_1 \rightarrow \nu_1$. The transition probability amplitude is given as

$$C^{(3)}_{a,(\nu_2,\nu_1,\nu_1)}(\infty) = -i\left[\frac{\sqrt{\pi}}{8\sqrt{3}\alpha(\nu_1-\nu_2)(\nu_2+\omega)}\right]\Omega_1^2\Omega_2 e^{-(1/3)[(2\nu_1-\nu_2-\omega)/2\alpha]^2}e^{-i[2\phi_1-\phi_2]} \tag{G.16}$$

The resonant three-photon excitation we studied in chapter VII are given by (iii.a), (iii.b) and (iii.c). Ratio of the amplitudes R_α for the processes (iii.a) and (iii.b) defined as

$$R_\alpha = \frac{\left|C^{(3)}_{a,(\nu_1,\nu_1,\nu_2)}(\infty)\right|}{\left|C^{(3)}_{a,(\nu_1,\nu_2,\nu_1)}(\infty)\right|} \tag{G.17}$$

is given by

$$R_\alpha = \frac{\nu_1-\nu_2}{2\nu_1} \tag{G.18}$$

This ratio $R_\alpha \rightarrow 0$ in the limit $\nu_1 \rightarrow \nu_2$ i.e Doppleron type process given by Eq.(G.15) dominates over the hyper-Raman type process given by Eq.(G.14) and other resonant and non-resonant processes. Similarly the ratio of the amplitudes R_β for the processes (iii.c)

and (iii.b) defined as

$$R_\beta = \frac{|C^{(3)}_{a,(\nu_2,\nu_1,\nu_1)}(\infty)|}{|C^{(3)}_{a,(\nu_1,\nu_2,\nu_1)}(\infty)|} \tag{G.19}$$

is given by

$$R_\beta = \frac{\omega - \nu_1}{\omega + \nu_2} \tag{G.20}$$

In this case smaller the one photon detuning $\omega - \nu_1$, higher will be the probability of the Doppleron type process. The ratio of the amplitudes R_γ for the processes (ii) and (i) defined as

$$R_\gamma = \frac{|C^{(3)}_{a,(\nu_2,\nu_2,\nu_2)}(\infty)|}{|C^{(1)}_{a,(\nu_1)}(\infty)|} \tag{G.21}$$

is given by

$$R_\gamma = \frac{\Omega_2^3 e^{[(\omega-3\nu_2)^2/6\alpha^2]}}{8\sqrt{3}\Omega_1\nu_2(\omega-\nu_2)} \tag{G.22}$$

Ratio of the amplitudes R_δ for the processes (i) and (iii.b) defined as

$$R_\delta = \frac{|C^{(1)}_{a,(\nu_1)}(\infty)|}{|C^{(3)}_{a,(\nu_1,\nu_2,\nu_1)}(\infty)|} \tag{G.23}$$

is given by

$$R_\delta = \frac{4\sqrt{3}(\nu_1-\nu_2)(\omega-\nu_1)e^{[-(\omega-\nu_1)^2/4\alpha^2]}}{\Omega_1\Omega_2} \tag{G.24}$$

For small α, this ratio is very small and we can neglect the contribution of the non-resonant one-photon excitation with respect to the resonant three-photon excitation to a good approximation. But for large α i.e small pulse duration we should be careful. Let us consider $\Omega_2 \approx 0.3\nu_1, \Omega_1 \approx 0.4\nu_1, \nu_2 = 0.6\nu_1, \omega = 1.4\nu_1$ and $\alpha \approx 0.128\nu_1$. Using this parameters we obtain $R_\delta \approx 0.8$; thus absorption of one-photon of ν_1 followed by emission of one-photon of ν_2 followed by absorption of one-photon of ν_1 is comparable to one-photon absorption of ν_1. Thus we can see the contribution of off-resonant one-photon absorption to Peak ③ is not negligible.

APPENDIX H

STIMULATED RAMAN SCATTERING: SEMICLASSICAL APPROACH

In this appendix we have presented a semi-classical derivation of the stimulated Raman scattering.

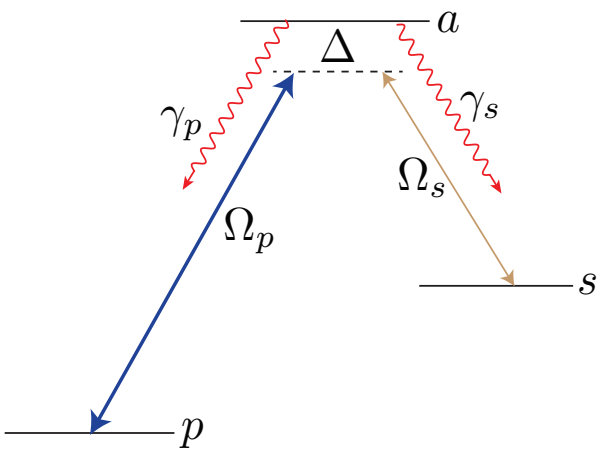

Fig. 69. Level diagram for the three-level model. The spontaneous decay rates $a \rightarrow s$ and $a \rightarrow p$ are give by γ_s, γ_p respectively. Ω_p and Ω_s are the pump and stokes field Rabi frequencies respectively.

The electric field can be written as

$$\vec{E}(z,t) = \frac{\hat{\epsilon}_p}{2}\mathscr{E}_p(z,t)\exp[i(k_p z - \nu_p t)] + \frac{\hat{\epsilon}_s}{2}\mathscr{E}_s(z,t)\exp[i(k_s z - \nu_s t)] + \text{c.c} \tag{H.1}$$

where $\hat{\epsilon}$, $\mathscr{E}$, ν are the unit polarization vector, field envelope and the carrier frequency respectively. The free Hamiltonian of the three-level model is

$$H_0 = \hbar\omega_a |a\rangle\langle a| + \hbar\omega_s |s\rangle\langle s| + \hbar\omega_p |p\rangle\langle p| \tag{H.2}$$

The interaction Hamiltonian in the dipole approximation is given as

$$H_1 = -(\vec{\wp}_{as}|a\rangle\langle s| + \vec{\wp}_{sa}|s\rangle\langle a| + \vec{\wp}_{ap}|a\rangle\langle p| + \vec{\wp}_{pa}|p\rangle\langle a|) \cdot \vec{E}(z,t) \tag{H.3}$$

Equation of motion for the density matrix equations is given by

$$\frac{\partial \rho(z,t)}{\partial t} = -\frac{i}{\hbar}\left[\mathscr{H},\rho\right] + \frac{\gamma_s}{2}\left(\left[\sigma_s,\rho\sigma_s^\dagger\right] + \left[\sigma_s\rho,\sigma_s^\dagger\right]\right) + \frac{\gamma_p}{2}\left(\left[\sigma_p,\rho\sigma_p^\dagger\right] + \left[\sigma_p\rho,\sigma_p^\dagger\right]\right) \quad \text{(H.4)}$$

where the atomic lowering (σ) and raising ($\sigma^\dagger$) operators are defined as

$$\sigma_s = |s\rangle\langle a|\,, \sigma_s^\dagger = |a\rangle\langle s|\,;\; \sigma_p = |p\rangle\langle a|\,, \sigma_p^\dagger = |a\rangle\langle p|\,. \quad \text{(H.5)}$$

From Maxwell's equation, the propagation equation for the electric field in slowly varying envelope approximation (SVEA) we obtain,

$$\left(\frac{\partial}{\partial z} + \frac{1}{c}\frac{\partial}{\partial t}\right)\left(-\frac{\partial}{\partial z} + \frac{1}{c}\frac{\partial}{\partial t}\right)\vec{E}(z,t) = -\mu_0\frac{\partial^2}{\partial t^2}\vec{P}(z,t) \quad \text{(H.6)}$$

If we neglect the higher harmonics, the polarization of the medium can be written as

$$\vec{P}(z,t) = N\vec{\wp}_{pa}\varrho_{ap}(z,t)\exp[i(k_p z - \nu_p t)] + N\vec{\wp}_{sa}\varrho_{as}(z,t)\exp[i(k_s z - \nu_s t)] + \text{c.c} \quad \text{(H.7)}$$

Substituting Eq.(H.1,H.7) in Eq.(H.6) we obtain propagation equation for the pump and the stokes field as

$$\left(\frac{\partial}{\partial z} + \frac{1}{c}\frac{\partial}{\partial t}\right)\mathscr{E}_s(z,t) = i\left(\frac{N\wp_{sa}\nu_s}{\epsilon_0 c}\right)\varrho_{as}(z,t) \quad \text{(H.8)}$$

$$\left(\frac{\partial}{\partial z} + \frac{1}{c}\frac{\partial}{\partial t}\right)\mathscr{E}_p(z,t) = i\left(\frac{N\wp_{pa}\nu_p}{\epsilon_0 c}\right)\varrho_{ap}(z,t) \quad \text{(H.9)}$$

We obtain the equation of motion for $\rho_{ij}(z,t)$

$$\begin{aligned}\frac{\partial \rho_{as}(z,t)}{\partial t} = &-\left(\gamma_{as} + i\omega_{as}\right)\rho_{as}(z,t) - i\frac{\vec{\wp}_{as}\cdot\vec{E}(z,t)}{\hbar}\left[\rho_{aa}(z,t) - \rho_{ss}(z,t)\right] \\ &+ i\frac{\vec{\wp}_{ap}\cdot\vec{E}(z,t)}{\hbar}\rho_{sp}^*(z,t)\end{aligned} \quad \text{(H.10)}$$

$$\begin{aligned}\frac{\partial \rho_{ap}(z,t)}{\partial t} = &-\left(\gamma_{ap} + i\omega_{ap}\right)\rho_{ap}(z,t) - i\frac{\vec{\wp}_{ap}\cdot\vec{E}(z,t)}{\hbar}\left[\rho_{aa}(z,t) - \rho_{pp}(z,t)\right] \\ &+ i\frac{\vec{\wp}_{as}\cdot\vec{E}(z,t)}{\hbar}\rho_{sp}(z,t)\end{aligned} \quad \text{(H.11)}$$

$$\frac{\partial \rho_{sp}(z,t)}{\partial t} = -\left(\gamma_{sp} + i\omega_{sp}\right)\rho_{sp}(z,t) - i\frac{\vec{\wp}_{sa}\cdot\vec{E}(z,t)}{\hbar}\rho_{ap}(z,t) - i\frac{\vec{\wp}_{ap}\cdot\vec{E}(z,t)}{\hbar}\rho^{*}_{as}(z,t) \tag{H.12}$$

Let us make a transformation

$$\rho_{as}(z,t) = \varrho_{as}(z,t)\exp[i(k_s z - \nu_s t)] \tag{H.13}$$

$$\rho_{ap}(z,t) = \varrho_{ap}(z,t)\exp[i(k_p z - \nu_p t)] \tag{H.14}$$

$$\rho_{sp}(z,t) = \varrho_{sp}(z,t)\exp[i(\Delta k\, z - \Delta\nu\, t)] \tag{H.15}$$

where $\Delta k = k_p - k_s$ and $\Delta\nu = \nu_p - \nu_s$. Using the transformation Eqs.(H.13,H.14,H.15) in Eqs.(H.10,H.11,H.12) we obtain,

$$\frac{\partial \varrho_{as}(z,t)}{\partial t} = -\left(\gamma_{as} + i\Delta\right)\varrho_{as}(z,t) - i\Omega_s(z,t)\left[\varrho_{aa}(z,t) - \varrho_{ss}(z,t)\right] + i\Omega_p(z,t)\varrho^{*}_{sp}(z,t) \tag{H.16}$$

$$\frac{\partial \varrho_{ap}(z,t)}{\partial t} = -\left(\gamma_{ap} + i\Delta\right)\varrho_{ap}(z,t) - i\Omega_p(z,t)\left[\varrho_{aa}(z,t) - \varrho_{pp}(z,t)\right] + i\Omega_s(z,t)\varrho_{sp}(z,t) \tag{H.17}$$

$$\frac{\partial \varrho_{sp}(z,t)}{\partial t} = -\gamma_{sp}\varrho_{sp}(z,t) + i\Omega^{*}_s(z,t)\varrho_{ap}(z,t) - i\Omega_p(z,t)\varrho^{*}_{as}(z,t) \tag{H.18}$$

We obtain the steady-state solution for $\varrho_{as}(z,t)$ and $\varrho_{ap}(z,t)$ as

$$\bar{\varrho}_{as}(z) = -i\frac{\Omega_s(z)}{\mathcal{M}}\left[\left(\Gamma_{pa}\gamma_{ps} + |\Omega_s(z)|^2\right)\left(\bar{\varrho}_{aa}(z) - \bar{\varrho}_{ss}(z)\right) - |\Omega_p(z)|^2\left(\bar{\varrho}_{aa}(z) - \bar{\varrho}_{pp}(z)\right)\right] \tag{H.19}$$

$$\bar{\varrho}_{ap}(z) = -i\frac{\Omega_p(z)}{\mathcal{M}^{*}}\left[\left(\Gamma_{sa}\gamma_{sp} + |\Omega_p(z)|^2\right)\left(\bar{\varrho}_{aa}(z) - \bar{\varrho}_{pp}(z)\right) - |\Omega_s(z)|^2\left(\bar{\varrho}_{ss}(z) - \bar{\varrho}_{aa}(z)\right)\right] \tag{H.20}$$

where

$$\mathcal{M} = \Gamma_{as}\Gamma_{pa}\gamma_{ps} + \Gamma_{pa}|\Omega_p|^2 + \Gamma_{as}|\Omega_s|^2 \tag{H.21}$$

Thus for $\Omega_p \ll \Delta$ we can assume that in the steady-state the population in the level are

same as thermal equilibrium values i.e $\bar{\varrho}_{aa}(z) \sim 0$ and $\bar{\varrho}_{ss}(z) = \varrho_{ss}^{(0)},\ \bar{\varrho}_{pp}(z) = \varrho_{pp}^{(0)}$.

$$\bar{\varrho}_{as}(z) = i\frac{\Omega_s}{\mathcal{M}}\left[\left(\Gamma_{pa}\gamma_{ps} + |\Omega_s(z)|^2\right)\varrho_{ss}^{(0)} - |\Omega_p(z)|^2\varrho_{pp}^{(0)}\right] \tag{H.22}$$

$$\bar{\varrho}_{ap}(z) = i\frac{\Omega_p}{\mathcal{M}^*}\left[\left(\Gamma_{sa}\gamma_{sp} + |\Omega_p(z)|^2\right)\varrho_{pp}^{(0)} - |\Omega_s(z)|^2\varrho_{ss}^{(0)}\right] \tag{H.23}$$

For stimulated Raman scattering we will only consider the terms which are responsible for energy exchange between the pump and stokes waves. Thus we can write Eqs.(H.22,H.23)

$$\frac{\partial}{\partial z}\Omega_s(z) = \left(\frac{N|\wp_{as}|^2\nu_s n_{ps}^{(0)}}{2\epsilon_0 c\hbar\Delta^2\gamma_{sp}}\right)|\Omega_p(z)|^2\Omega_s(z) \tag{H.24}$$

$$\frac{\partial}{\partial z}\Omega_p(z) = -\left(\frac{N|\wp_{ap}|^2\nu_p n_{ps}^{(0)}}{2\epsilon_0 c\hbar\Delta^2\gamma_{sp}}\right)|\Omega_s(z)|^2\Omega_p(z) \tag{H.25}$$

where $n_{ps}^{(0)} = \varrho_{pp}^{(0)} - \varrho_{ss}^{(0)}$. Using the definition of intensity as

$$I(z) = 2\epsilon_0 c\frac{\hbar^2}{|\wp|^2}|\Omega(z)|^2 \tag{H.26}$$

We obtained the coupled-differential equation for the stokes and pump waves intensities as

$$\frac{d}{dz}I_s(z) = \left(\frac{N|\wp_{ap}|^2|\wp_{as}|^2\nu_s n_{ps}^{(0)}}{2\epsilon_0^2 c^2\hbar^3\Delta^2\gamma_{sp}}\right)I_s(z)I_p(z) \tag{H.27}$$

$$\frac{d}{dz}I_p(z) = -\left(\frac{N|\wp_{ap}|^2|\wp_{as}|^2\nu_p n_{ps}^{(0)}}{2\epsilon_0^2 c^2\hbar^3\Delta^2\gamma_{sp}}\right)I_s(z)I_p(z) \tag{H.28}$$

The extension of this result to include both forward and backward stimulated Raman signal is trivial and we obtain

$$\frac{d}{dz}I_s^f(z) = \left(\frac{N|\wp_{ap}|^2|\wp_{as}|^2\nu_s n_{ps}^{(0)}}{2\epsilon_0^2 c^2\hbar^3\Delta^2\gamma_{sp}}\right)I_s^f(z)I_p(z) \tag{H.29}$$

$$\frac{d}{dz}I_s^b(z) = -\left(\frac{N|\wp_{ap}|^2|\wp_{as}|^2\nu_s n_{ps}^{(0)}}{2\epsilon_0^2 c^2\hbar^3\Delta^2\gamma_{sp}}\right)I_s^b(z)I_p(z) \tag{H.30}$$

$$\frac{d}{dz}I_p(z) = -\left(\frac{N|\wp_{ap}|^2|\wp_{as}|^2\nu_p n_{ps}^{(0)}}{2\epsilon_0^2 c^2\hbar^3\Delta^2\gamma_{sp}}\right)\left[I_s^f(z) + I_s^b(z)\right]I_p(z) \tag{H.31}$$

APPENDIX I

THREE-PHOTON EXCITATION RABI FREQUENCY

In this Appendix, we will discuss how to calculate effective Rabi-frequency for the three-photon excitation by ultra-short pulses as shown in Fig. (70).

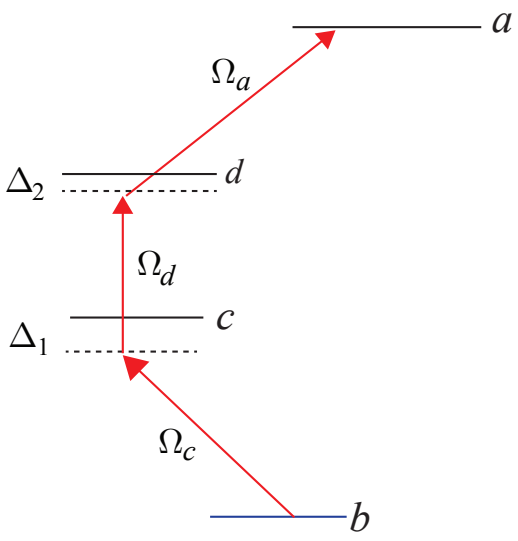

Fig. 70. Three-photon excitation

We will write the interaction picture Hamiltonian in the rotating-wave approximation as

$$\begin{aligned}\mathscr{H}_1 = &-\Omega_c e^{i\Delta_1 t}|c\rangle\langle b| - \Omega_d e^{i(\Delta_2-\Delta_1)t}|d\rangle\langle c| - \Omega_a e^{-i\Delta_2 t}|a\rangle\langle d| \\ &- \Omega_c^* e^{-i\Delta_1 t}|b\rangle\langle c| - \Omega_d^* e^{-i(\Delta_2-\Delta_1)t}|c\rangle\langle d| - \Omega_a^* e^{i\Delta_2 t}|d\rangle\langle a|.\end{aligned} \tag{I.1}$$

Here $\Delta_1 = \omega_{cb} - \nu_p$ and $\Delta_2 = \omega_{db} - 2\nu_p$. The time scale of the three-photon excitation is much shorter than the spontaneous decay time from the levels and any coherence relaxation rates $\gamma_{\alpha\beta}$. At any instant of time $t > 0$, the wave function for the four-level atom can be written as

$$|\Psi(t)\rangle = C_a|a\rangle + C_b|b\rangle + C_c|c\rangle + C_d|d\rangle. \tag{I.2}$$

where C_α is the probability amplitude of finding the atom in state $|\alpha\rangle$. Using the Schrodinger equation $i\hbar|\dot{\Psi}(t)\rangle = \mathscr{H}_1|\Psi(t)\rangle$. and Eqs.(I.1,I.2) we obtain coupled differential equations governing the evolution of the probability amplitudes C_α,

$$\dot{C}_a = i\Omega_a e^{-i\Delta_2 t} C_d, \tag{I.3}$$

$$\dot{C}_b = i\Omega_c^* e^{-i\Delta_1 t} C_c, \tag{I.4}$$

$$\dot{C}_c = i\Omega_c e^{i\Delta_1 t} C_b + i\Omega_d^* e^{-i(\Delta_2-\Delta_1)t} C_d, \tag{I.5}$$

$$\dot{C}_d = i\Omega_d e^{i(\Delta_2-\Delta_1)t} C_c + i\Omega_a^* e^{i\Delta_2 t} C_a. \tag{I.6}$$

To solve for C_α, we first write the equation of motion for the slowly varying amplitudes,

$$C_\alpha = c_\alpha e^{i\phi_\alpha t}. \tag{I.7}$$

From Eqs. (I.3-I.7) we obtain,

$$\dot{c}_a = -i\phi_a c_a + i\Omega_a c_d, \tag{I.8}$$

$$\dot{c}_b = -i\phi_b c_b + i\Omega_c^* c_c, \tag{I.9}$$

$$\dot{c}_c = -i\phi_c c_c + i\Omega_c c_b + i\Omega_d^* c_d, \tag{I.10}$$

$$\dot{c}_d = -i\phi_d c_d + i\Omega_d c_c + i\Omega_a^* c_a, \tag{I.11}$$

where the phase factors ϕ_α obey the conditions

$$\phi_d - \phi_a = \Delta_2. \tag{I.12}$$

$$\phi_b - \phi_a = 0. \tag{I.13}$$

$$\phi_b - \phi_c = -\Delta_1. \tag{I.14}$$

$$\phi_c - \phi_d = -\Delta_2 + \Delta_1. \tag{I.15}$$

Solving Eqs. (I.12-I.14) gives,

$$\phi_a = 0, \quad \phi_b = 0, \quad \phi_c = \Delta_1, \quad \phi_d = \Delta_2. \tag{I.16}$$

Using these phase factors in Eqs. (I.8-I.11), we obtain

$$\dot{c}_a = i\Omega_a c_d, \tag{I.17}$$

$$\dot{c}_b = i\Omega_c^* c_c, \tag{I.18}$$

$$\dot{c}_c = -i\Delta_1 c_c + i\Omega_c c_b + i\Omega_d^* c_d, \tag{I.19}$$

$$\dot{c}_d = -i\Delta_2 c_d + i\Omega_d c_c + i\Omega_a^* c_a. \tag{I.20}$$

Let us consider a weak excitation regime in which $\Omega \ll \Delta$. We can adiabatically eliminate the levels c and d i.e solve for c_c and c_d from Eqs. (I.19-I.20) in the steady state approximation and obtain

$$c_c = \left(\frac{\Omega_a^*\Omega_d^*}{\Delta_1\Delta_2}\right) c_a + \left(\frac{\Omega_c}{\Delta_1}\right) c_b, \tag{I.21}$$

$$c_d = \left(\frac{\Omega_a^*}{\Delta_2}\right) c_a + \left(\frac{\Omega_c\Omega_d}{\Delta_1\Delta_2}\right) c_b. \tag{I.22}$$

From Eqs. (I.17,I.18) and Eqs. (I.21, I.22) we obtain,

$$\dot{c}_a = i\left(\frac{|\Omega_a|^2}{\Delta_2}\right) c_a + i\left(\frac{\Omega_a\Omega_c\Omega_d}{\Delta_1\Delta_2}\right) c_b, \tag{I.23}$$

$$\dot{c}_b = i\left(\frac{|\Omega_c|^2}{\Delta_1}\right) c_b + i\left(\frac{\Omega_a^*\Omega_c^*\Omega_d^*}{\Delta_1\Delta_2}\right) c_a. \tag{I.24}$$

If we compare Eqs. (I.23,I.24) with standard two-level model, we obtain the effective three-photon Rabi frequency Ω_{eff}

$$\Omega_{\text{eff}} = \frac{\Omega_a\Omega_c\Omega_d}{\Delta_1\Delta_2}, \tag{I.25}$$

Here $|\Omega_a|^2/\Delta_2$ and $|\Omega_c|^2/\Delta_1$ are the off-resonant Stark shifts in the levels a and b respec-

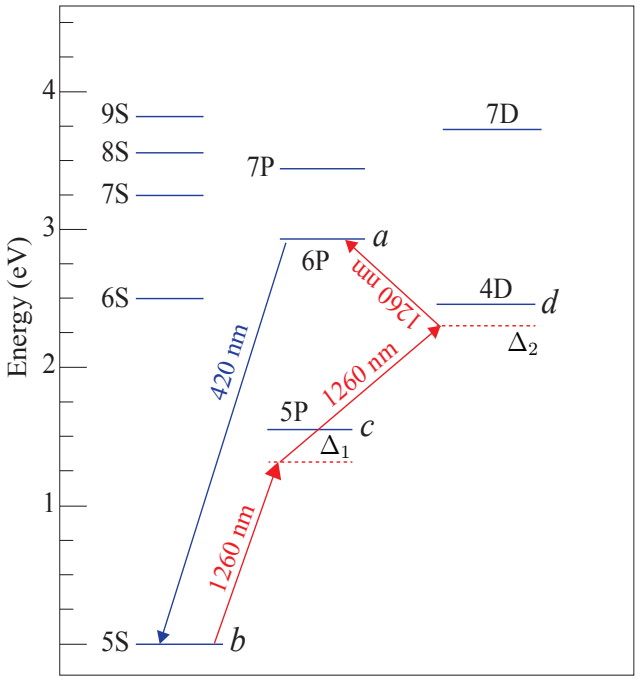

Fig. 71. Three-photon (at 1260nm) induced superradiant emission at 420nm

tively.

In the second part of this section we will discuss the effective three-photon Rabi frequency recently reported [247]. Let us calculate Δ_1 and Δ_2 for the excitation mechanism shown in Fig.(71). We have pump wavelength $\lambda_p = 1260$nm, $\lambda_{5^2P_{1/2}\to 5^2S_{1/2}} = 795$nm and $\lambda_{4^2D_{3/2}\to 5^2P_{1/2}} = 1475$nm. We define $\Delta_1 = \omega_{cb} - \nu$ and $\Delta_2 = \omega_{db} - 2\nu_p$ which gives

$$\Delta_1 = 1.39 \times 10^{14}\,\mathrm{s}^{-1}, \quad \Delta_2 = 1.05 \times 10^{14}\,\mathrm{s}^{-1}. \tag{I.26}$$

Using the definition

$$\gamma = \frac{1}{4\pi\epsilon_0}\frac{4\omega^3\wp^2}{\hbar c^3} \tag{I.27}$$

we obtain the expression for the dipole moment as

$$\wp = \left[(4\pi\epsilon_0)\frac{3\hbar c^3}{4\omega^3}\gamma\right]^{1/2} \tag{I.28}$$

We will use the definition of Rabi frequency as $\Omega = \wp\mathcal{E}/2\hbar$. In our experiment, we use ultrashort pulse $\tau_{\text{FWHM}} \sim 120$fs, center wavelength $\lambda_p = 1260$nm and energy per pulse is $\mathscr{E} = 1\mu$J. The unfocused beam diameter is $D \sim 2.5$mm which gives the size of the focal spot $d = 4\lambda_p f/\pi D \sim 128\mu$m where f is the focal length of the converging lens and we used $f = 20$cm. The corresponding area $A = \pi d^2/4$ is $\sim 1.29 \times 10^{-8}$m^2. The average energy per pulse is $\mathscr{E} = 1\mu$J, thus the average electric field $\mathcal{E} = \sqrt{\mathscr{E}/c\epsilon_0 A\tau_{FWHM}}$ is $\sim 4.92\times10^8$V/m. From Eq.(I.27) and the atomic parameters, we obtain the dipole moment for the transition $5^2P_{1/2} \leftrightarrow 5^2S_{1/2}$ where the spontaneous decay rate is $\gamma = 3.613\times10^7$s^{-1}

$$\wp_{cb} = 2.5356 \times 10^{-29}\,\text{C.m} \tag{I.29}$$

Hence the Rabi frequency for the transition $5^2P_{1/2} \leftrightarrow 5^2S_{1/2}$ is

$$\Omega_c \sim 5.92 \times 10^{13}\,\text{s}^{-1} \tag{I.30}$$

Similarly we obtain the dipole moment from the $4^2D_{5/2} \leftrightarrow 5^2P_{1/2}$ where the spontaneous decay rate is $\gamma = 1.11 \times 10^7$s^{-1}

$$\wp_{dc} = 3.556 \times 10^{-29}\,\text{C.m} \tag{I.31}$$

Hence the Rabi frequency for the transition $5^2P_{1/2} \leftrightarrow 4^2D_{5/2}$ is

$$\Omega_d \sim 8.30 \times 10^{13}\,\text{s}^{-1} \tag{I.32}$$

Similarly we obtain the dipole moment from the $6^2P_{1/2} \leftrightarrow 4^2D_{5/2}$ where the spontaneous decay rate is taken as $\gamma = 2.204 \times 10^6\,\text{s}^{-1}$

$$\wp_{ad} = 3.0716 \times 10^{-29}\,\text{C.m} \tag{I.33}$$

Hence the Rabi frequency for the transition $6^2P_{1/2} \leftrightarrow 4^2D_{5/2}$ is

$$\Omega_a \sim 7.17 \times 10^{13}\,\mathrm{s}^{-1} \tag{I.34}$$

Thus the effective Rabi frequency for the three-photon excitation is

$$\Omega_{\text{eff}} \sim 2.42 \times 10^{13}\,\mathrm{s}^{-1} \tag{I.35}$$

Thus the effective area (Θ) of the pulse if $\Omega_{\text{eff}}\tau_{FWHM}$ which is $\Theta \sim 2.905$. Thus with these estimates, we see that the three-photon excitation under these conditions is not weak.

VITA

Name: Pankaj Kumar Jha.

Address: Department of Physics and Astronomy, Texas A&M University, College Station, TX 77843-4242.

Email: pkjha@physics.tamu.edu

EDUCATION:

2012: Ph.D., Physics, Department of Physics and Astronomy, Texas A&M University.

2006: M.Sc., Physics (Integrated), Indian Institute of Technology Kanpur, India.

PROFESSIONAL EXPERIENCE:

2012(Fall)-: Postdoctoral Scholar, Department of Mechanical Engineering, University of California, Berkeley.

2012 (Spring): Teaching Assistant, Department of Mechanical and Aerospace Engineering, Princeton University.

2009-2012: Visiting student, Department of Mechanical and Aerospace Engineering, Princeton University.

2006-2012: Research and Teaching assistant, Department of Physics and Astronomy, Texas A&M University.

HONORS:

Robert A. Welch Foundation, Graduate Fellowship: 2009-2012.

American Physical Society, Travel Grant: 2011

Research and Presentation Grant, Texas A&M University: 2010.

HEEP Foundation Graduate Fellowship: 2010.

Center of Teaching Excellence Texas A&M University, Mentor: 2007-2012.

The typist for this dissertation was Pankaj Kumar Jha.